Imperial College London

Phenomenological Modelling of Molten Salt Reactors with Coupled Point Nuclear Reactor Kinetics and Thermal Hydraulic Feedback Models

Academic Supervisors:

Dr Matthew Eaton (principal)

Prof. Berend van Wachem (co-supervisor)

Industrial Supervisors:

Prof. Alan Copestake

Mr. Chris Jackson

Dr. Vittorio Badalassi (former)

Author:

Gareth Owen Morgan

Department of Mechanical Engineering

A thesis submitted in partial fulfillment of the requirements for the degree of Doctor of Philosophy and the Diploma of Imperial College London

September 2018

Abstract

The Molten Salt Reactor Experiment (MSRE) was a small circulating fuel reactor operated at Oak Ridge National Laboratory (ORNL) between 1965 and 1969. To do date it remains the only molten salt reactor (MSR) that has been operated for extended periods, on diverse nuclear fuels. Reactor physics in MSRs differs from conventional solid-fuelled reactors due to the circulation of hot fuel and delayed neutron precursors (DNPs) in the primary circuit. This alters the steady state and time-dependent behaviours of the system.

A coupled point kinetic-thermal hydraulic feedback model of an MSRE-like system was constructed in order to investigate the effect of uncertainties in the values of key physical parameters on the model's response to step and ramp reactivity insertions. This information was used to determine the parameters that affected the steady state condition and transient behaviours.

The model was also used to investigate features identified in the frequency response, in particular a feature corresponding to fuel recirculation. Greater than expected mixing in the primary circuit has been previously proposed as an explanation for the lack of observation of this feature. A velocity-dependent turbulent dispersion term is proposed to increase dispersion of the fuel temperature field in order to suppress the recirculation feature in the frequency response. An additional semi-analytical model was constructed as a part verification of the mixing hypothesis - this model was also used to examine the stability of an MSRE-like design.

Finally the validated coupled system model was used to establish the just-safe combination of intrinsic source and ramp rate that does not exceed an estimated maximum permissible vessel temperature. The CALLISTO-SPK stochastic point kinetics code is used to demonstrate that the intrinsic source in an MSRE-like design is sufficient to reduce the probability of a rogue startup transient to an acceptably small value from the point of view of regulatory safety analysis. Such analyses may be used to support the case for extrinsic source deletion in future MSR designs.

Declaration of Originality

The content of this thesis is solely the work of the author unless indicated otherwise, in which case it has been reproduced with permission and appropriately cited. Works kindly placed in the public domain have been cited in the manner requested by the original owner.

Copyright Declaration

Acknowledgements

I would like to express my thanks to my principal supervisor, Dr. Matthew Eaton, my co-supervisor, Prof. Berend van Wachem, and my industrial supervisors Prof. Alan Copestake, Dr. Vittorio Badalassi and Mr. Chris Jackson. In addition I would like to thank the Nuclear Engineering Group's post-doctoral research assistants Dr. Chris Cooling and Dr. Jozsef Kópházi, plus the PhD students within the Nuclear Engineering Group at the Rolls-Royce Nuclear UTC, Imperial College London. Thank you also to Emeritus Professor Mike Williams for teaching me a number of useful analytical techniques. I acknowledge Rolls-Royce and the Engineering and Physical Sciences Research Council (EPSRC) for their financial support of my industrial CASE studentship, the Imperial College London Research Computing Service and the Wood Plc ANSWERS Software Service for their technical support.

Contents

Nomenclature

Abbreviations

BeF_2 Beryllium fluoride

Gd_2O_3 Gadolinium oxide

ZrF_4 Zirconium fluoride

ARE Aircraft Reactor Experiment

BeO Beryllium oxide

BWR Boiling Water Reactor

CALLISTO-SPK CALculation of Low Intensity STartup Operations - Stochastic Point Kinetics

DNPs Delayed neutron precursors

DOS Density of States

EVENT EVEn parity Neutral particle Transport

FSI Flow-Structure Interaction

HEU Highly Enriched Uranium

HTRE Heat Transfer Reactor Experiment

LEU Low Enriched Uranium

LiF Lithium fluoride

LTI Linear Time-Invariant

MC Monte Carlo

MCNP Monte Carlo N-Particle

MSBR Molten Salt Breeder Reactor

MSRE Molten Salt Reactor Experiment

NIST National Institute of Standards and Technology

ODE Ordinary Differential Equation

ORNL Oak Ridge National Laboratory

PDE Partial Differential Equation

PRBS Pseudo-Random Binary Sequence

PWR Pressurised water reactor

RTG Radioisotope Thermoelectric Generator

WIMS Winfrith Improved Multigroup Scheme

List of Symbols

α_f Fuel temperature coefficient of reactivity, 8.46×10^{-5} K^{-1}.

α_g Graphite temperature coefficient of reactivity, 4.68×10^{-5} K^{-1}.

$\bar{\nu}$ Average number of neutrons emitted per fission event.

β Delayed neutron fraction.

β_i Delayed neutron precursor yield in group i.

$\chi_{fission}$ Energy released per fission event [J].

Λ Mean generation time of neutrons in core [s].

λ_i Decay constant for delayed neutron precursor group i [s^{-1}].

ψ Flux shape function.

$\rho_g =$ Graphite density [kg m^{-3}].

ρ_T Temperature-dependent reactivity.

ρ_{fuel} Fuel density [kg m^{-3}].

ξ Deposited power density [m^{-3}].

$A_{f,g}$ Interfacial area between fuel and graphite [m^2].

$A_{H.E.}$ Heat exchanger interfacial area [m^2].

C_i''' concentration of delayed neutron precursors in group i [m^{-3}]

C_i''' concentration of delayed neutron precursors in group i [m^{-3}]

$C_{p,fuel}$ Fuel specific heat capacity [$\mathrm{J\,kg^{-1}\,K^{-1}}$].

$C_{p,graphite}$ Graphite specific heat capacity [$\mathrm{J\,kg^{-1}\,K^{-1}}$].

$f_{fission}$ Fraction of fissions occurring in vessel region.

$f_{vol,fuel}$ Volume fraction of fuel in core.

$f_{vol,g}$ Volume fraction of graphite in the core.

H Core height [m].

$h_{f,g}$ Heat transfer coefficient between fuel and graphite [$\mathrm{W\,m^{-2}\,K^{-1}}$].

$h_{H.E.}$ Heat transfer coefficient [$\mathrm{W\,m^{-2}}$].

K Turbulent dispersion parameter [W/m/K].

$L_{H.E.}$ Heat exchanger length [m].

n Number of neutrons in the core.

P Reactor power [W]

p_g Fraction of fission power deposited in graphite.

p_{dep} Deposited power fraction in vessel region.

T_g Graphite temperature [K].

$T_{coolant}$ Temperature of the coolant salt in the secondary circuit [K].

T_{ref} Reference temperature of the system [K].

u Fuel velocity [$\mathrm{m\,s^{-1}}$].

z Circuit coordinate [m].

List of Figures

List of Tables

Chapter 1

Introduction and Overview of Molten Salt Reactors

1.1 A Brief Review of Early Molten Salt Reactor History

In the early days of the Cold War, when ballistic missile technology was still in its infancy, the United States military investigated the potential for compact high-temperature nuclear reactors for the purposes of powering nuclear-armed bombers with near unlimited range and loiter time [15]. Circulating fuel reactors were identified as promising candidates for aircraft propulsion due to their high power density and neutron economy [16]. A liquid fuel offered advantages in terms of safety and simplicity - a negative temperature coefficient, load following, low pressure operation; and the potential for simplified (even continuous) fuel processing [17].

Selection of suitable fuel liquids and reactor materials was a significant materials science and chemical challenge. The chosen mixture had to satisfy criteria in terms of nuclear physics, thermal hydraulics, chemical compatibility, fuel solubility and fission product retention.

Candidate molten oxides and hydroxides were eliminated on the basis of corrosion and chemical stability under intense irradiation. The experience gained from aqueous homogeneous reactor operation [18] at Oak Ridge National Laboratory highlighted the desirability of working fluid with a low vapour pressure and stability under intense ionising radiation flux. For example,

D_2O, while a good moderator can be radiolytically split into D_2 and O_2 gases, constituting an explosion hazard in confined spaces [19].

Solutions of uranium in molten bismuth or bismuth-lead eutectic have been examined as potential fuels. Attractive properties include a low neutron absorption cross section, large working temperature range and low vapour pressure. Molten bismuth has a poorer specific heat capacity compared to other candidate liquids and limited uranium solubility. Thorium solubility is extremely poor, to the extent that slurries of thorium bismuthide ($ThBi_2$) have been considered for breeding. Neutron capture by ^{209}Bi produces ^{210}Bi which decays into the intense alpha emitter ^{210}Po which is a biological hazard. Corrosion of steels by molten bismuth can be severe [20].

Molten fluoride salts of lithium and beryllium are stable under irradiation by virtue of their strong ionic bonding. This results in high melting points (7-800 K) and very high boiling points (approx. 1700 K) [21], permitting a large working range of temperatures and high thermodynamic efficiency. In addition, the salts are sufficiently reactive to retain most fission products in the event of spills or leaks, however they do not react violently with water (unlike liquid sodium or the sodium-potassium eutectic mixture known as 'NaK'). Low vapour pressures reduce the need for components rated for high pressures, and the fluid dynamic properties are of the same order of magnitude as water, simplifying the design process. In addition, molten salts exhibit strong thermal expansion resulting in a negative temperature coefficient of reactivity of the order of $10^{-4}\Delta k/k$ per Kelvin.

A lithium-beryllium-zirconium fluoride mixture offers the appropriate blend of properties as a solvent for a uranium fluoride fuel. Lithium fluoride (LiF) offers the best fluid dynamic properties, however beryllium fluoride (BeF_2) is added to reduce the melting point and zirconium fluoride (ZrF_4) to avoid precipitation of uranium oxide in the event of air ingress or other oxidising materials [2, 12].

Lithium in the salt must be isotopically enriched in the ^{7}Li isotope to avoid neutron capture by ^{6}Li and to reduce the undesirable production of tritium. Fuel salt in the MSRE was enriched to more than 99.99% ^{7}Li [7]. The ^{19}F nucleus has a low capture cross section and a low resonance integral which contribute to neutron economy, however its moderating power alone is poor.

Additional moderation in the core is required for a critical mass of practical size, for example with beryllium oxide (BeO) or graphite. Chloride salts would be preferable over their fluoride counterparts in a fast reactor, but only ^{37}Cl would be suitable due to the large absorption cross section of ^{35}Cl. For thermal neutrons (0.025 eV), the absorption cross sections are approximately 0.4 barns for ^{37}Cl and 40 barns for ^{35}Cl [22]. Isotopic enrichment in ^{37}Cl may be prohibitively costly on the scale required for a reactor.

A molten fuel requires no fabrication of fuel structures or cladding and continuous reprocessing of diverse fuel cycles may be carried out on site. A range of fuels are available (Pu, isotopes of U including the potential for a ^{232}Th-^{233}U breeding cycle) and any undesirable fission products (primarily xenon, rare earths, semi noble and noble metals) may be removed via a combination of gas sparging, distillation, fluorination, and the slow discarding and replenishment of the salt [23].

Early designs focused on the thermal expansion of a stagnant volume of molten salt to reduce the density of fissile material in the reactor core. If the fuel expanded above a 'neutron curtain' above the core, the neutron leakage would increase providing negative power feedback. An example of a successful static molten salt reactor was the PWAR-1 experiment - a hot zero-power design with a beryllium reflector-moderator and NaF-ZrF_4-UF_4 fuel that went critical in February 1957 [24].

For higher power experiments, the thermal conductivity of the molten salt was deemed too low to distribute the heat on its own and in order to avoid a boiling of the fuel near the cooling tube walls, the design was changed to include fuel circulation. This resulted in the Aircraft Reactor Experiment (ARE), in 1954. It consisted of a high temperature NaF-ZrF_4-UF_4 fuel salt circulated in pipes that repeatedly entered and exited the BeO reflector-moderator structure (Figure 1.1). Among the achievements of the experiment was the demonstration of the negative temperature coefficient and low buildup of noble gas fission products [25, 26].

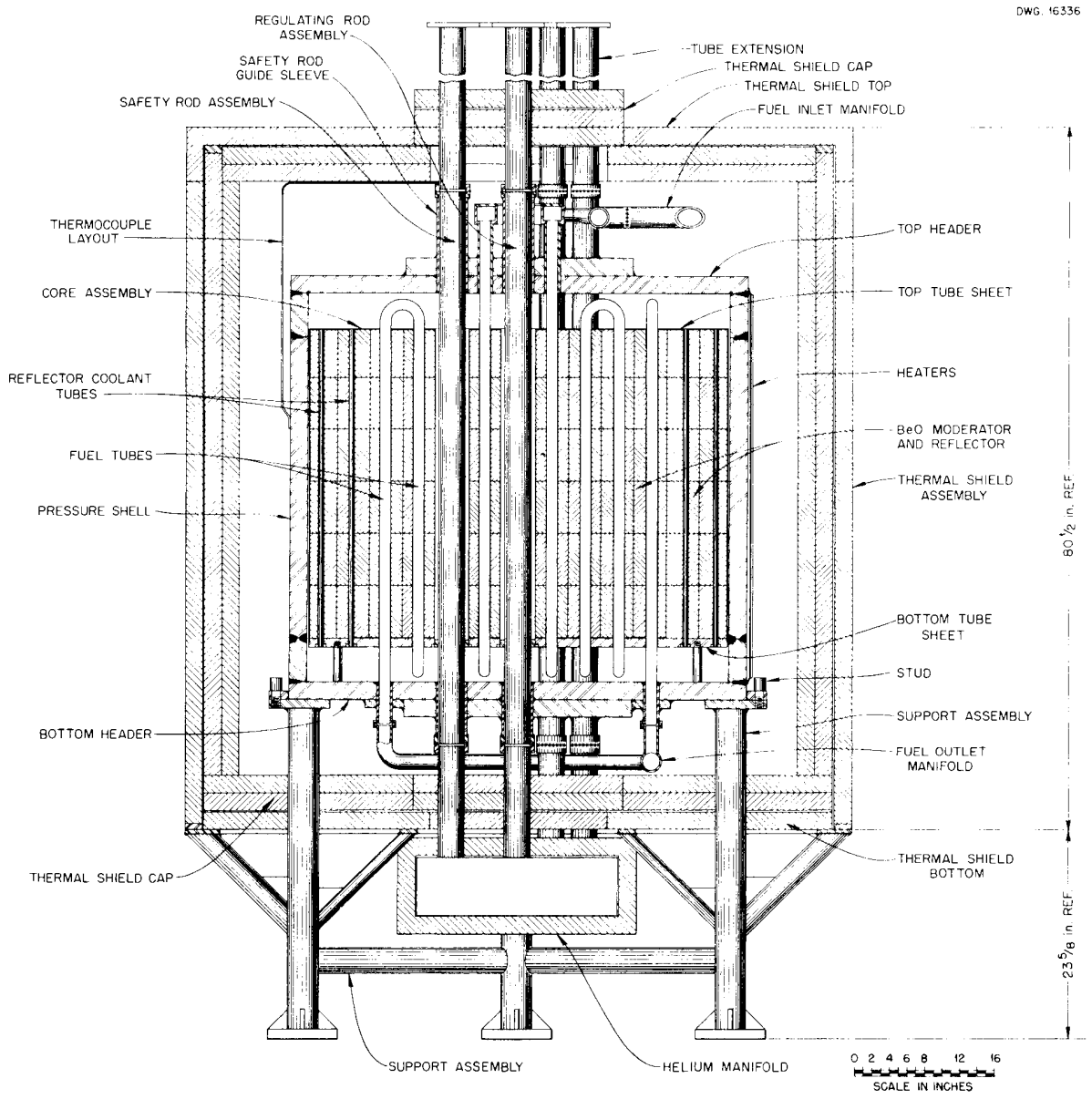

Figure 1.1: Aircraft Reactor Experiment, viewed from the side. Adapted with permission, courtesy of U.S. Dept. of Energy [1].

Due to the piping geometry in the ARE, it was not possible to repair a gas leak that was identified in the circuit or drain the system via gravity if an accident were to occur. Excessive helium consumption and the desire for a molten salt-based design that could be safely operated for extended periods led to the Molten Salt Reactor Experiment.

Work on direct-cycle aircraft nuclear propulsion systems continued in the United States, culminating in the successful Heat Transfer Reactor Experiment No. 3 (HTRE No. 3) [27]. This experiment demonstrated the feasibility of running two turbojets with a high temperature nuclear reactor as the heat source. The configuration was similar to that planned for a prototype nuclear-powered aircraft that would have flown in the early 1960s. HTRE No. 3 ran for extended periods and demonstrated startup under nuclear power, instead of starting the gas turbines on chemical fuel and then switching over to the nuclear heat source. Ultimately, the development of the ballistic missile as the primary deterrent platform doomed the Aircraft Nuclear Propulsion programme and it was cancelled in March 1961 [28]

1.2 Description of the MSRE

The Molten Salt Reactor Experiment (MSRE) was authorised at Oak Ridge National Laboratory, Tennessee in 1960, with design work beginning in May of that year. Construction began in 1962 with the reactor taken critical in 1965. The objectives of the program were:

(i) to evaluate the feasibility of extended operation of a low pressure, thermal spectrum molten salt reactor.

(ii) to demonstrate the ability to run on diverse fuel mixtures, including ^{233}U fuel.

(iii) to demonstrate the remote service and replacement of components in the reactor cell.

(iv) to demonstrate the online processing of the working fluid, including scrubbing of fission product gases.

(v) to evaluate suitable materials for use in later molten salt reactor designs.

The MSRE ran on ^{235}U fuel for 9000 full-power equivalent hours, with a further 2500 h running on ^{233}U as the fissile material [29]. To date, it remains the only molten salt reactor operated for extended periods.

An overview of the MSRE facility is shown in Figure 1.2 with major components numbered. A flow schematic with full power design temperatures and flow rates is shown in Figure 1.3. The

fuel salt circulated in the primary circuit from the reactor vessel (1), upwards to the primary circuit fuel pump and pump bowl (3) where it was discharged a short distance to the heat exchanger (2). After exchanging heat with the secondary circuit it returned to the vessel via (5). Upon vessel reentry, the fuel salt flowed into a distributor ring and down an annulus outside the core, also referred to as the 'downcomer' (Fig. 1.4). The lower head redirected the flow upwards and into the graphite moderating structure that formed the core, completing the primary circuit flow path.

The secondary circuit contained an unfuelled molten salt. Heat was discharged to the atmosphere at the secondary circuit radiator (7), that was cooled by a pair of large fans (9). No electrical power was generated from the MSRE. The design also included a unique passive safety feature - a constriction in a pipe from the reactor vessel formed a valve that would be frozen shut in normal operation. In the event of external power loss, the fuel would melt through the plug (13) allowing the primary circuit to drain in to a tank in a subcritical configuration (10).

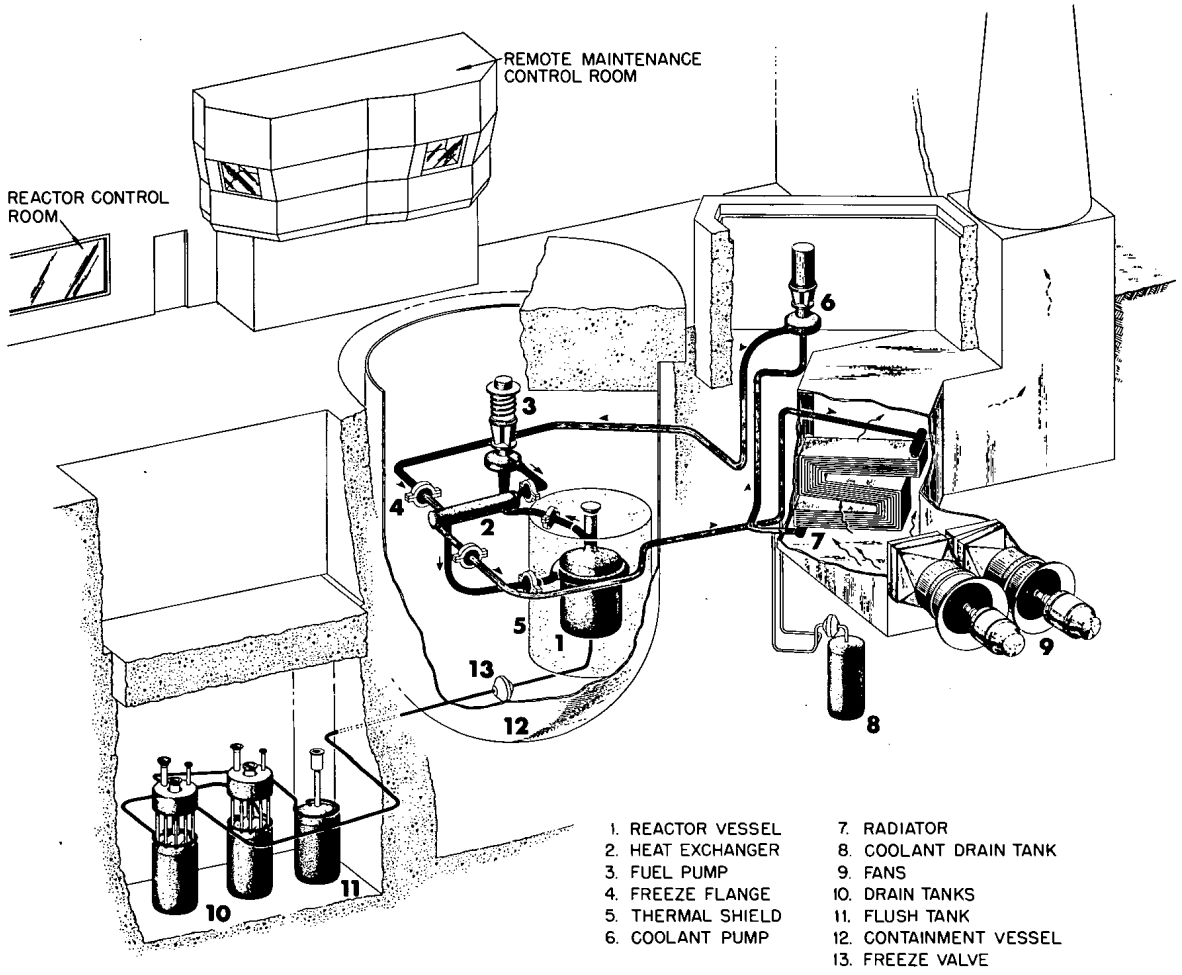

Figure 1.2: Overview of the MSRE reactor pit, cooling systems and drain tanks. Adapted with permission, courtesy of the U.S. Dept. of Energy [2].

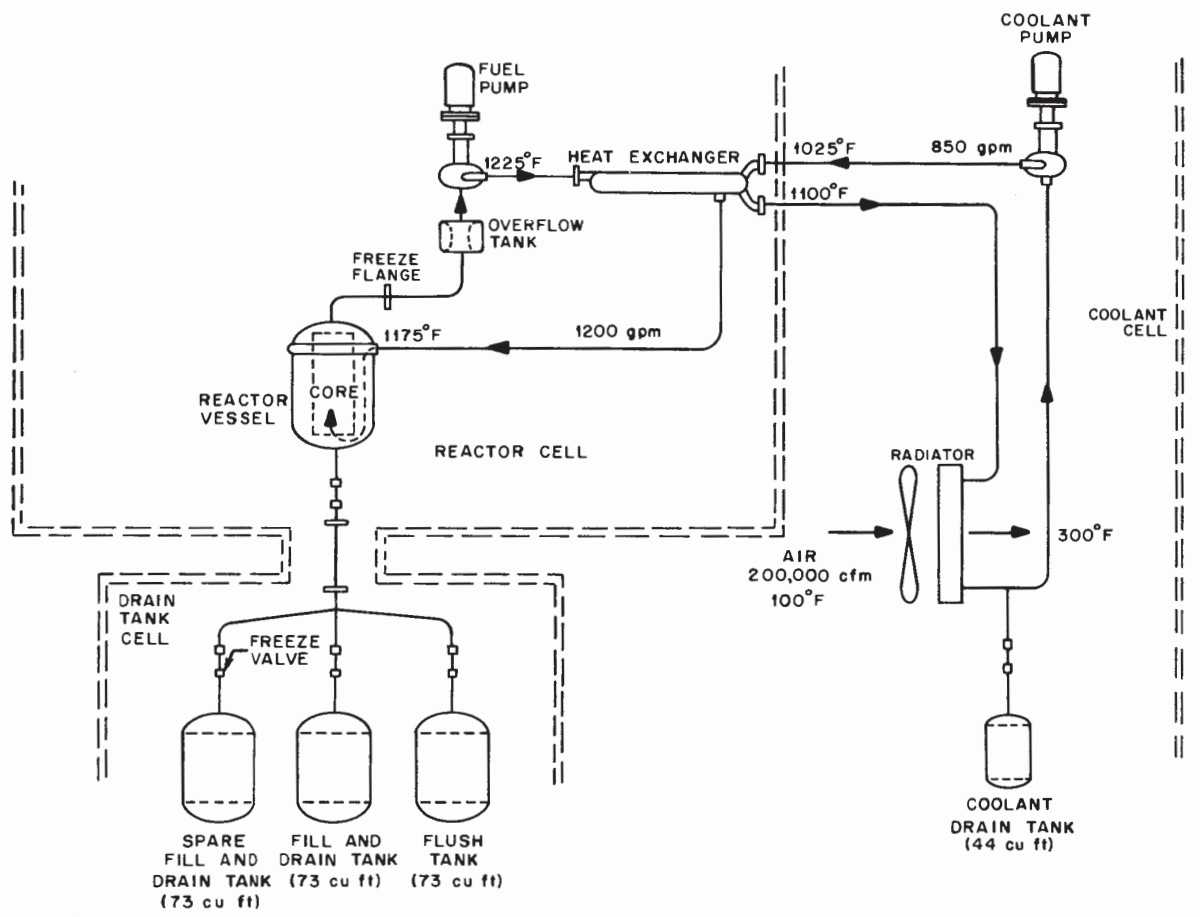

Figure 1.3: MSRE flow schematic with average full operating power temperatures and flow rates. Adapted with permission, courtesy of the U.S. Dept. of Energy [3].

The reactor pressure vessel was approximately cylindrical, 2.4 m high and 1.5 m in diameter, containing a graphite moderating structure consisting of over 600 graphite bars (also referred to as 'stringers'). A cutaway representation of the reactor vessel is shown in Figure 1.4. The graphite stringers had machined edges so that gaps were left in the moderating structure when they were pressed together - these gaps formed the channels for salt flow (see the plan view at upper left in Fig. 1.5). The fuel salt volume fraction in the core was approx. 22% and the total moderated region in the core was ~ 2.5 m^3.

The vessel was suspended from the upper biological shield in the reactor cell. The space between the walls of the reactor cell was filled with steel shot and water to form a thermal and ionising radiation shield.

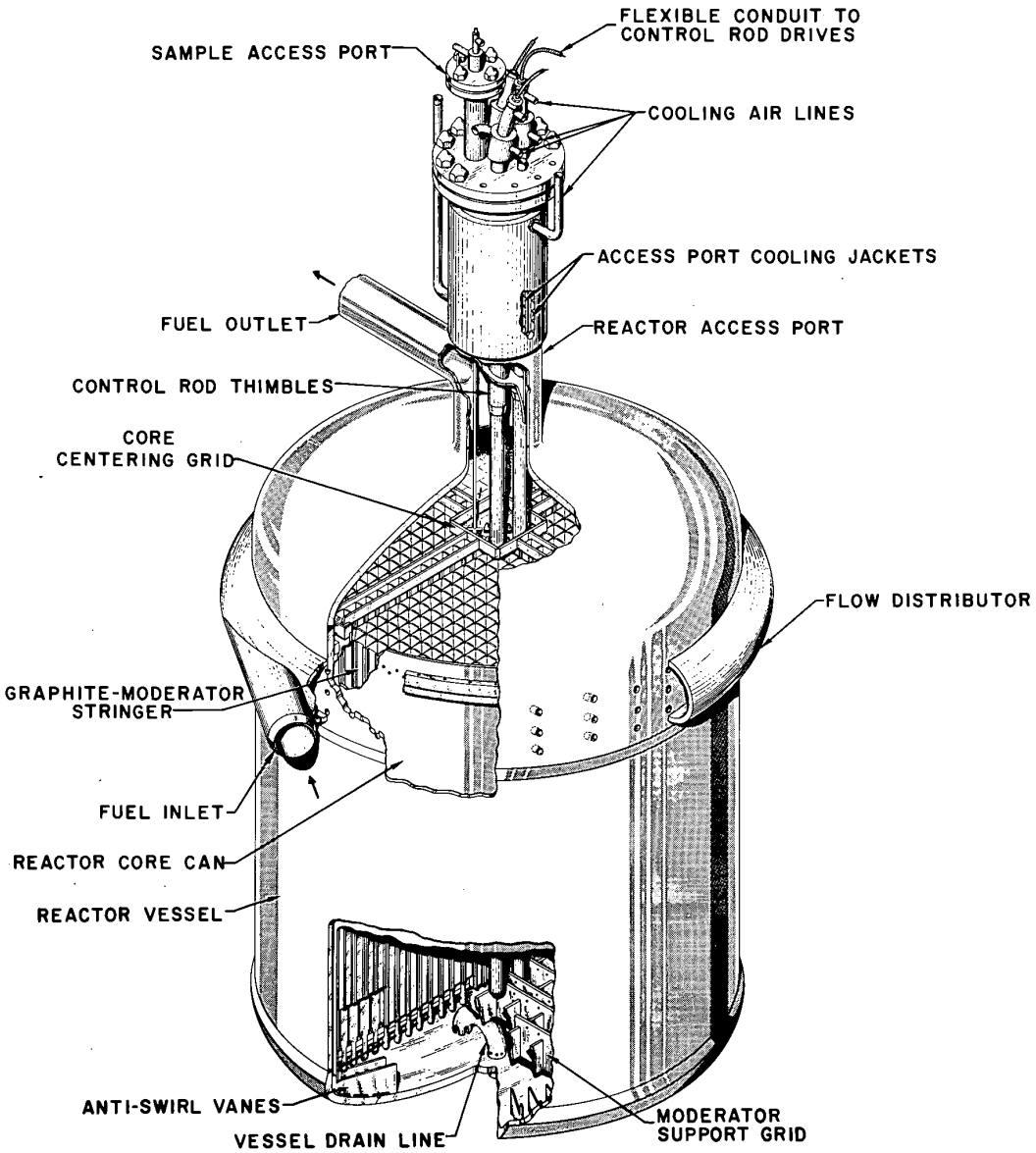

Figure 1.4: Cutaway view of the MSRE core, adapted with permission, courtesy of the U.S. Dept. of Energy [2].

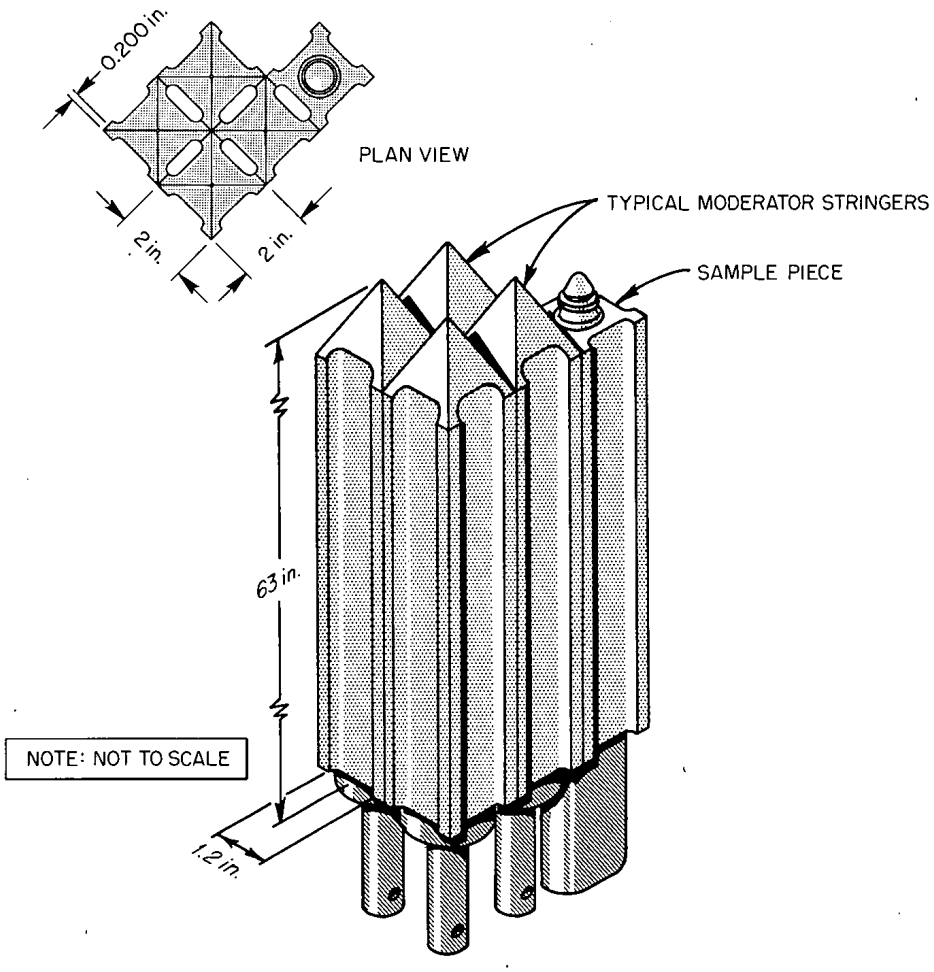

Figure 1.5: Graphite bar/stringer arrangement in moderating structure showing channels between them. Reproduced with permission, courtesy of the U.S. Department of Energy [2]

The core was originally designed for a power of 10 MW, however in practice this was approx. 8 MW. There is uncertainty over the true maximum core power due to disagreement between heat balance calculations ($P_{max} = 8.2 \pm 0.16$ MW) and fuel isotopic analysis ($P_{max} = 7.34 \pm 0.09$ MW) [30]. Design temperatures were approx. 908 K (635 °C, 1175 °F) at the vessel inlet and approx. 936 K (663 °C, 1225 °F) at the vessel outlet.

The primary circuit fuel pump was a sump-type centrifugal pump, discharging fuel salt at approx. 170 kg/s (1200 gallons per minute), with a head of approx. 3.4 bar (50 psi). A notable feature was the sparging of some of the salt flow back into the pump bowl using helium gas in order to separate out fission product gases (Figure 1.6) [2]. The gaseous fission products

were filtered through charcoal bed with a long residence time before discharge to the atmosphere.

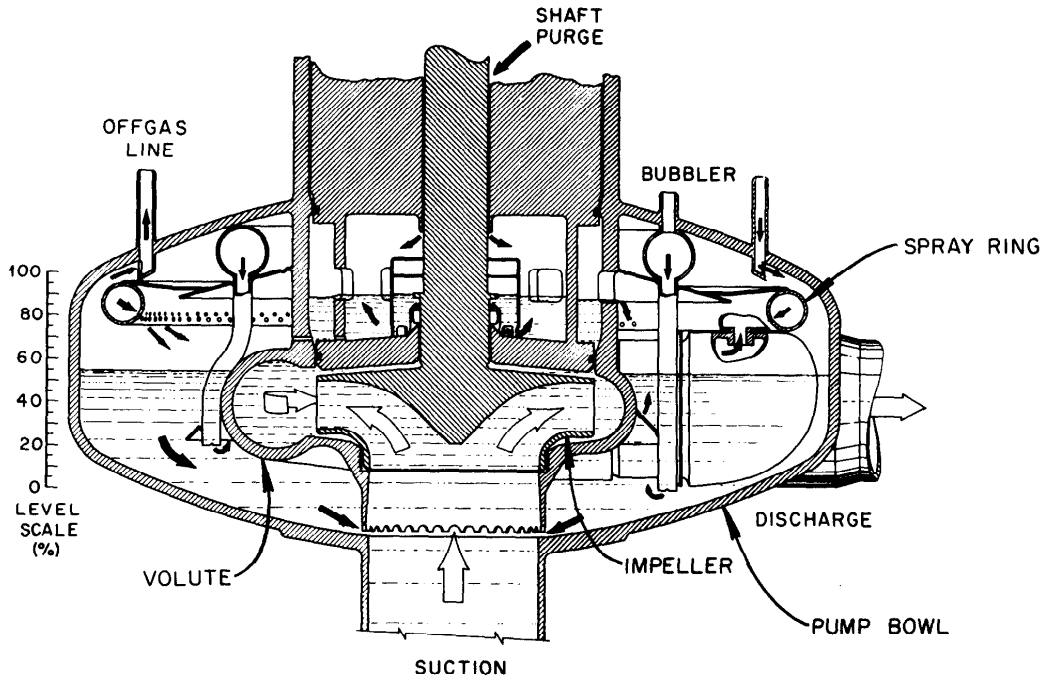

Figure 1.6: MSRE primary circuit pump with associated pump bowl. Note the spray ring used for sparging of fission product gases. Adapted with permission, courtesy of the U.S. Dept. of Energy [4].

The vessel, heat exchanger and major connecting components consisted of INOR-8 (also known as Hastelloy N), a nickel-based high-performance alloy that is resistant to attack by molten fluoride salts [14]. Primary circuit piping was constructed from 5in schedule-40 INOR-8 pipe. Under typical MSRE operating conditions, total fuel circulation time was approx. 25 seconds.

The primary heat exchanger (Fig. 1.7) was a shell-and-U-tube configuration with the secondary coolant salt flowing through the tubes and the primary salt flowing through the outer shell around a series of baffles. The contact area between primary salt and secondary tube was estimated to be $23.6\,\mathrm{m}^2$, with a measured average heat transfer coefficient of $3725\,\mathrm{W/m^2/K}$. This is lower than than the $6734\,\mathrm{W/m^2/K}$ predicted at the design phase and may be due to incorrect data on salt thermal conductivity used early in the programme. Measurements suggested the cause was not scale buildup or trapped gas pockets in the heat exchanger [31, 30].

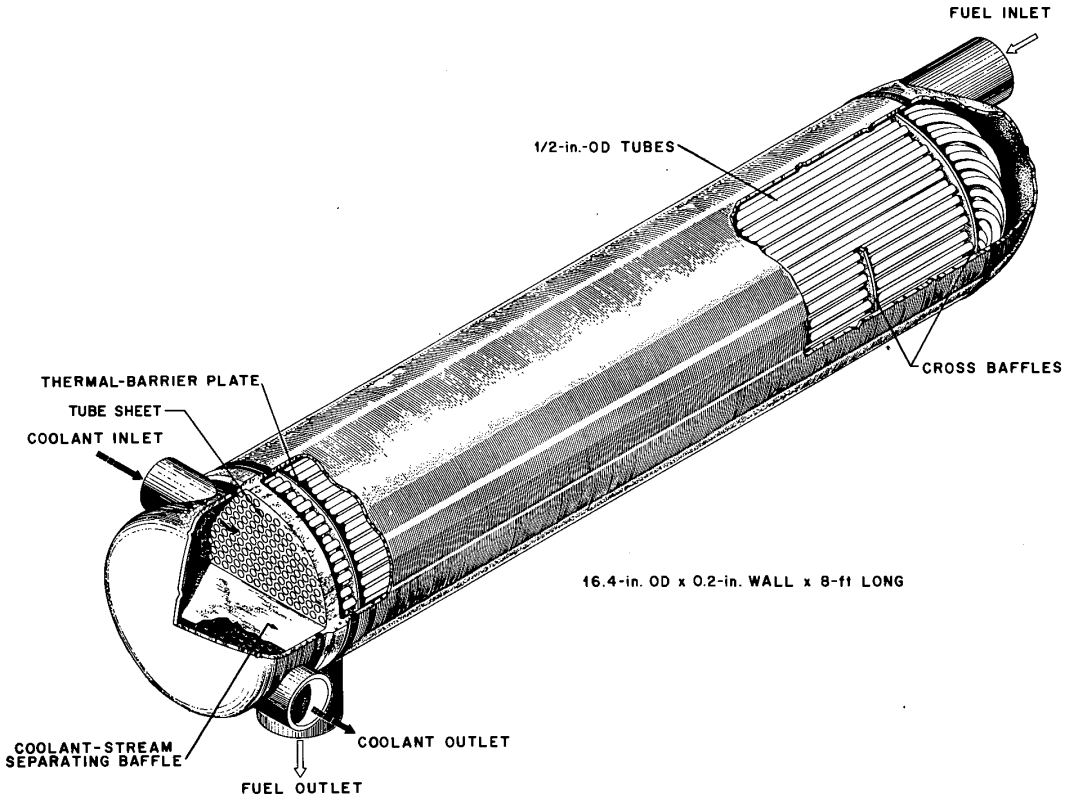

Figure 1.7: Schematic of the MSRE primary circuit heat exchanger, adapted with permission, courtesy of the U.S. Dept. of Energy [2].

The fuel salt was a lithium-beryllium fluoride salt with small amounts of zirconium fluoride acting as a solvent for enriched uranium fluoride fuel, with a final ^{235}U enrichment of approx. 30% by weight. The typical composition of the fuel salt for full power operations is shown in Table 1.1. A more detailed isotopic breakdown of a fuel mixture used for neutronic calculations

during initial criticality operations can be found in Table C.7, and a thorough accounting of the enriched salt additions throughout the MSRE operational programme may be found in Reference [32].

Species	**Mole %**
LiF	65.0
BeF_2	29.1
ZrF_4	5.0
UF_6	0.9

Table 1.1: Typical chemical composition of clean MSRE fuel salt [12].

The secondary coolant was an unfuelled LiF-BeF_2 mixture with a lower flow rate than the fuel salt. Coolant circulation time was 23 seconds, and the average temperature of the coolant salt at the heat exchanger inlet was approx. 825 K when operating at full power (Fig. 1.3).

The secondary circuit radiator (Component 7 in Fig. 1.2) consisted of ¾ inch tubes arranged in banks of 12, with axial flow fans and a sliding door to control the heat load taken off the secondary circuit (Figure 1.8). In addition, heaters were installed to prevent uncontrolled freezing of the coolant salt in the event of a pump shutdown.

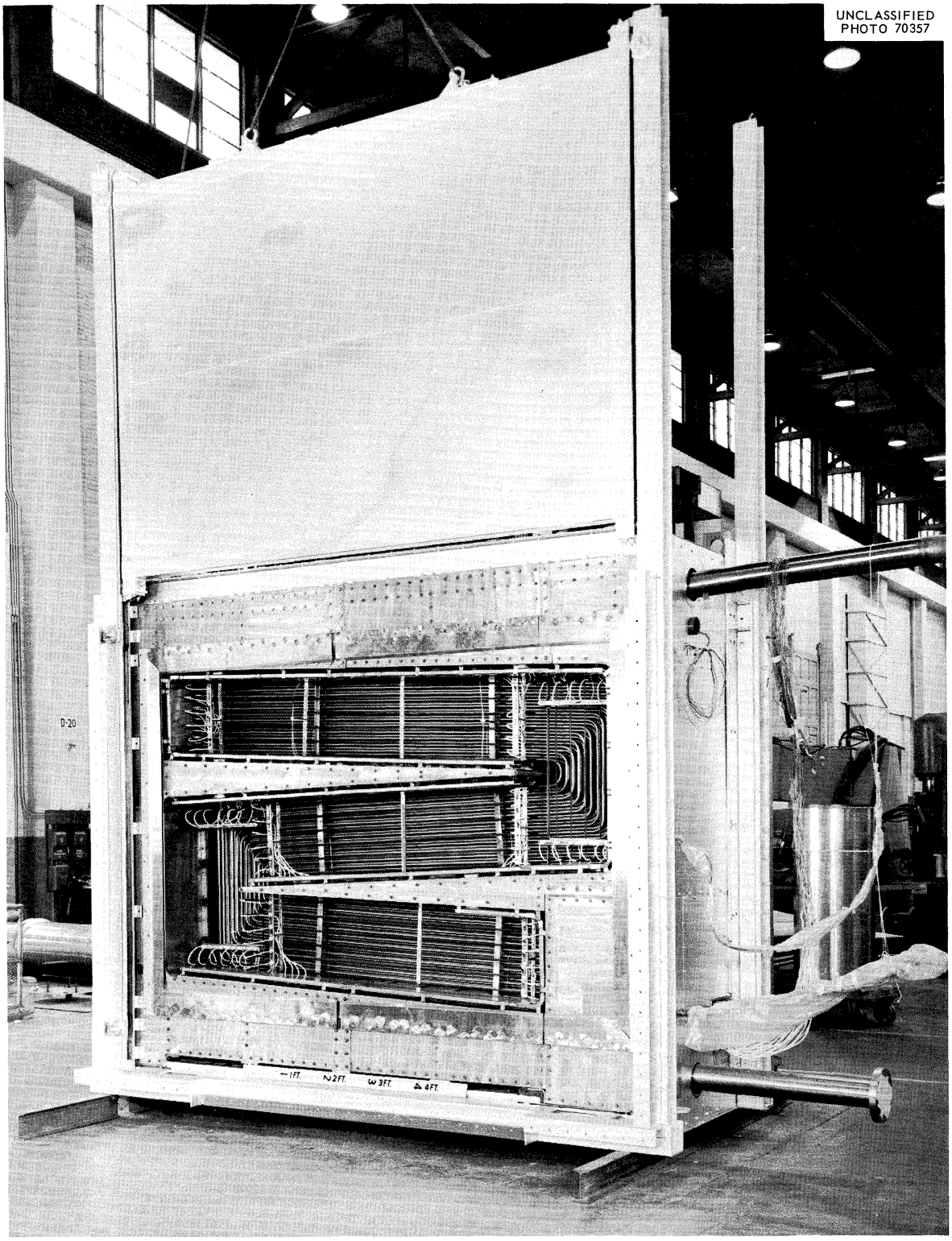

Figure 1.8: Secondary circuit heat exchanger upon delivery to the MSRE site. Note the raised door above the radiator banks for controlling air flow and scale (denoting 0 to 4 feet) at bottom centre. Reproduced with permission, courtesy of the U.S. Dept. of Energy [5].

1.2.1 Control and Safety Systems

Four of the graphite stringers at the centre of the core were replaced with guide tubes for the three identical control rods and a sample testing port. The control rods consisted of a flexible chain of gadolinium oxide (Gd_2O_3) poison elements to allow off-axis placement of the control rod drives (Fig. 1.9) as the vessel flow outlet and pump occupied the central axis. Under normal operation, two of the control rods were used as shim rods for coarse reactivity adjustment, with the third acting as the regulating rod. The position of the regulating rod could be controlled by computer in order to input reactivity signals for experiments. The use of such signals for determining the frequency response of MSRE is discussed in detail in Chapter 5.

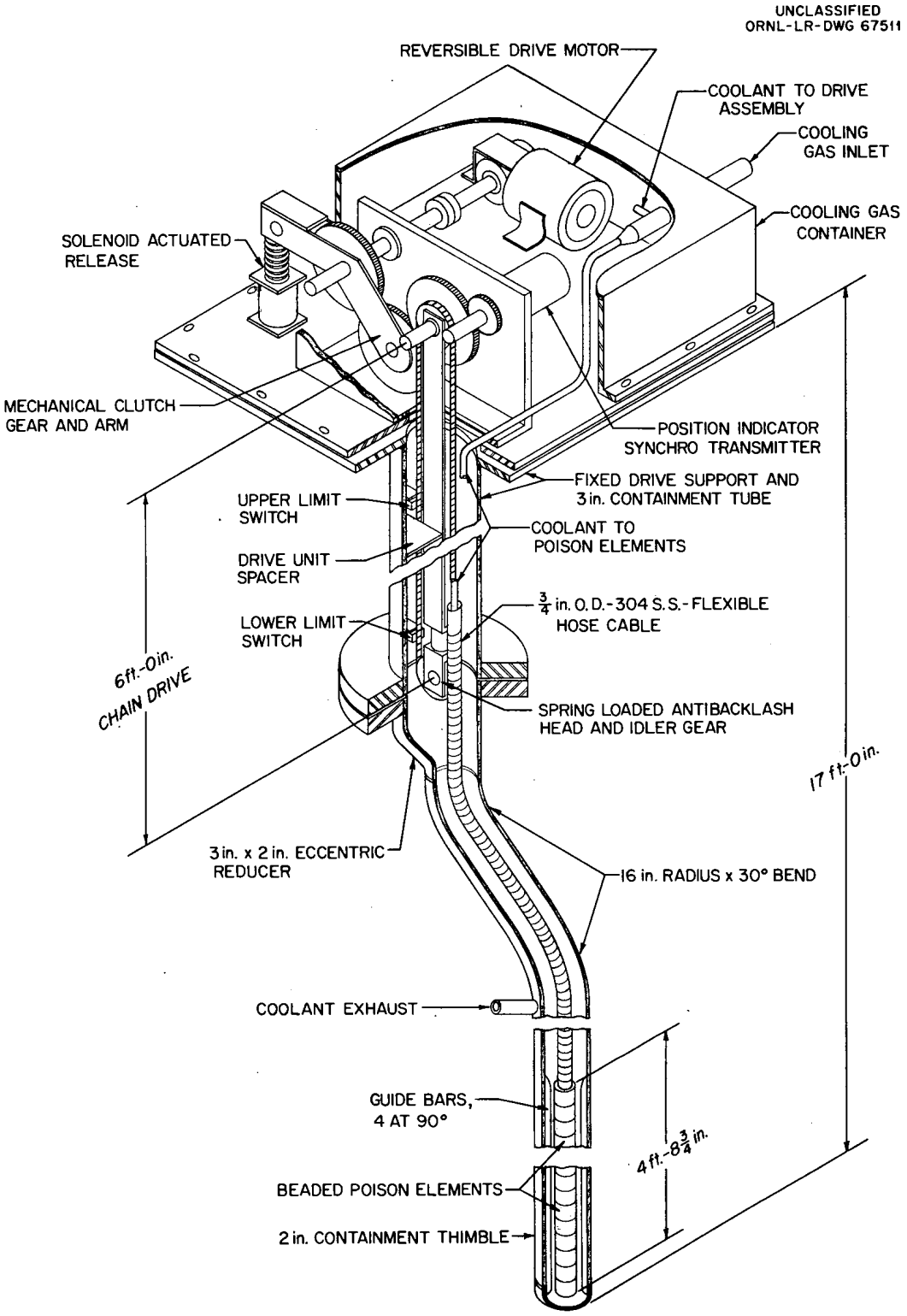

Figure 1.9: Control rod assembly with drive mechanism and cooling. Adapted with permission [2], courtesy of the U.S. Dept. of Energy.

Additional control of the core power in the MSRE was provided by secondary circuit heat rejection [33]. Raising or lowering the air inlet doors (Figure 1.8) to the secondary circuit radiator controlled the airflow which resulted in a change in the temperature of the coolant salt returning to the primary heat exchanger. Due to the strong negative temperature coefficient in the core, a cooling of the fuel salt returning to the core would result in an increase in reactivity and therefore core power.

In the event of an unanticipated primary circuit pump shutdown, the radiator airflow could be reduced to 20% of normal flow rate, or the radiator door dropped quickly in order to prevent the coolant salt freezing in the radiator tubes [34]. Overcooling of the secondary circuit could also result in a cool fuel slug on the primary circuit side of the heat exchanger. If the fuel pump was suddenly restarted, the cool slug could enter the core and cause an unanticipated large increase in core reactivity [35].

1.3 Later Proposed Designs

Later work in the ORNL molten salt reactor programme focused on designs for a molten salt breeder reactor (MSBR) running a ^{232}Th-^{233}U fuel cycle in single fluid, or two-fluid configurations. A two-fluid design with a fissile fuel liquid separated from a fertile breeding liquid by graphite channels was considered, however newer data on the stability of graphite under prolonged irradiation plus the development of new chemical processing methods favoured a single-liquid approach. Development of a separation process involving reduction in molten bismuth enabled this process [36]. Capture of a neutron by ^{232}Th followed by β^- decay yields ^{233}Pa. This is a neutron poison and so must be separated into order to decay into fissile ^{233}U with a half-life of 27.4 days [37, 38, 12]. The use of U and Th in the salt plus undermoderation of the fuel salt towards the reactor edge increases breeding via Th capture [23], also facilitating the use of a single salt rather than two liquids.

1.4 Modern Developments in MSR Technology

Interest in molten salt reactors is experiencing something of a resurgence at the time of writing, with new designs such as the Stable Salt Reactor by Moltex Energy [39] and the Integral Molten

Salt Reactor by Terrestrial Energy Inc. in early regulatory stages with the Canadian Nuclear Safety Commission [40]. The Stable Salt Reactor does not make use of a flowing fuel salt and therefore will not be discussed further in this work.

In addition there is a programme of works in the People's Republic of China on solid-fuelled reactors cooled by molten salt and molten salt-fuelled reactors. The candidate designs are known as TMSR-SF1 and -LF1 for the solid fuelled and liquid fuelled variants, respectively. The design of TMSR-LF1 is similar to MSRE and planned operations will increase the amount of thorium in the salt to progressively move towards a ^{232}Th-^{233}U breeding cycle [41].

Reactors with a high output temperature are desirable from the perspective of thermodynamic efficiency. Use of the Brayton cycle for power generation has been proposed for high-temperature reactors. In addition, they may be used to supply heat for industrial chemical processes, such as the production of hydrogen from water using a sulphur-iodine process, either exclusively or in conjunction with electrical power generation.

1.5 General MSR Physics

Circulating fuel reactors differ from their solid-fuelled cousins in the following fundamental ways.

(i) *Delayed neutron precursor movement* - In a conventional solid-fueled reactor, such as a pressurised water reactor (PWR), delayed neutron precursors (DNPs) are born and decay in the same location in the fuel. In a reactor with molten fuel salt, delayed neutron precursors are transported away from their point of birth to decay in another location. The decay in regions of minimal importance (away from the core region) to the chain reaction will reduce the effective delayed neutron fraction. In addition, neutrons emitted by precursor decay as they are transported may cause fissions altering the power distribution in the reactor.

As the flow rate increases (and residence time outside the core decreases), this effect becomes less severe as some of the precursors may re-enter the core and contribute to the power [42].

(ii) *Thermal feedbacks* - Fuel flow through the core reduces the rate of fuel and moderator heating when the core undergoes transients [43]. In addition, there is a negative reactivity feedback due to thermal expansion of the salt which reduces its density and displaces fissile material from the core.

The recirculation of delayed neutron precursors and hot fuel back into the reactor vessel contributes to positive and negative feedbacks, respectively, that can give rise to oscillating behaviours. These are investigated in detail in Chapter 5.

(iii) *Moderation differences* - In a PWR, it is the moderator (water) which is the coolant and responsible for removal of heat from the core. In a circulating fuel reactor, it is the fuel that is responsible for the heat removal. In the case of MSRE, the moderator was stationary (graphite) and the fuel salt also possessed a degree of moderation ability.

(iv) *Fuel voids* - In the case of a MSRE-like design, sparging in the pump bowl introduces gas bubbles which are entrained in the flow and account for approx. 1-2% of the volume fraction upon entry to the core. These bubbles reduce the local density of fissile material causing fluctuations in power as they pass through the core [44]. It was expected that changing the system temperature would induce changes in pressure that would affect the void volume fraction due to the compressibility of the helium gas [7]. Voids may occur in other types of reactor, e.g. boiling water reactors (BWRs) , however this will affect the coolant/moderator density not that of the fuel.

(v) *Removal of fission products and neutron poisons* - Molten fuel allows gaseous fission products, some of which may be neutron poisons, (for example, ^{135}Xe) to escape, improving the neutron economy and reactivity control of the core. Continuous reprocessing has been proposed [45] for the removal of non-volatile fission products that may be neutron poisons.

1.6 MSRE-Specific Physics

Reactivity Compensation for Fuel Movement and Pump Transients

As discussed above, a circulating fuel design will exhibit a reduced delayed neutron fraction and an altered distribution of the delayed neutron source due to fuel movement. More detailed

discussion of the delayed neutron source distribution with comparison between models including that developed in this work may be found in Section 3.1.

An early prediction of the loss in reactivity due to fuel circulation in MSRE (fuelled with ^{235}U) gave a value of -0.3 % $\Delta k/k$ [46], however this was later refined to -0.222 % with consideration of the large salt volume fractions and residence times in the upper and lower plena.

Experiments measured this reactivity change by comparing rod positions with static and circulating fuel, over a range of fuel loads during the fuelling process. Titrations with enriched ^{235}U buckets yielded a reactivity change of -0.212 ± 0.004 % $\Delta k/k$ (see Fig. 1.10). This is consistent with values obtained during independent measurements of pump startup and coastdown transients, shown in Fig. 1.11 [6].

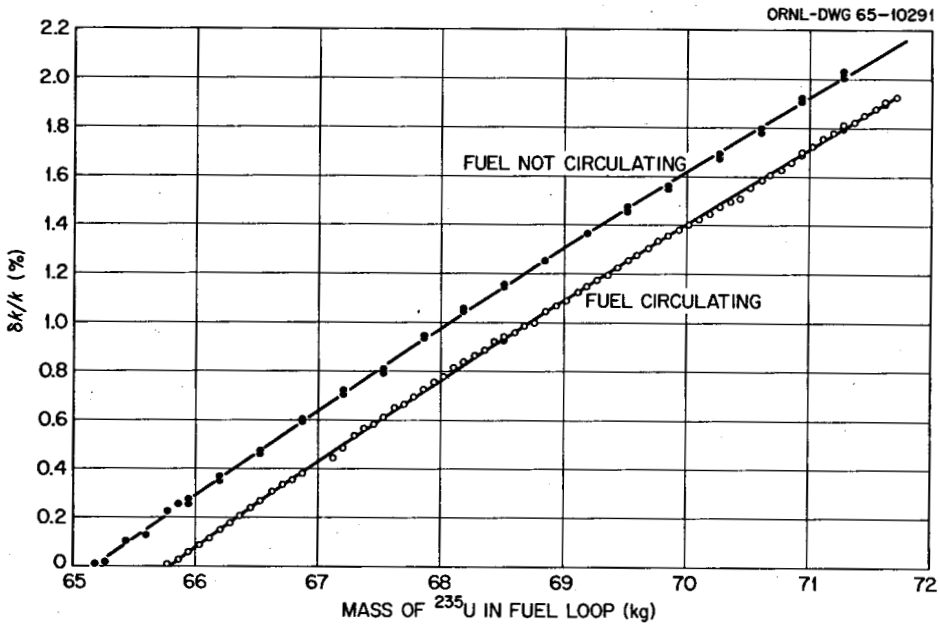

Figure 1.10: Difference in reactivity between static and circulating fuel conditions, over various fuel loads. Reproduced with permission, courtesy of U.S. Dept. of Energy [6].

An alternative method for measuring the change in reactivity due to fuel movement is by stopping or starting the pump and observing the change in rod position required to maintain criticality. Theoretically, a cessation of fuel salt movement through the core would result in more precursors decaying in the core than at the previous, flowing, steady state. This can

be represented as a positive change in reactivity ρ. In order for the reactor to remain in a critical state, some external negative change in reactivity (*e.g.* rod movement) must take place to compensate. Conversely, if the pumps were to start salt flow again, the loss of precursor-derived neutrons from the core would require a positive reactivity insertion in order to maintain criticality.

Fig. 1.11 shows regulating rod positions during MSRE pump transients. The total change in reactivity at the conclusion of the transient is approx. 0.2 % $\Delta k/k$ in agreement with the fuel titration method shown in Fig. 1.10.

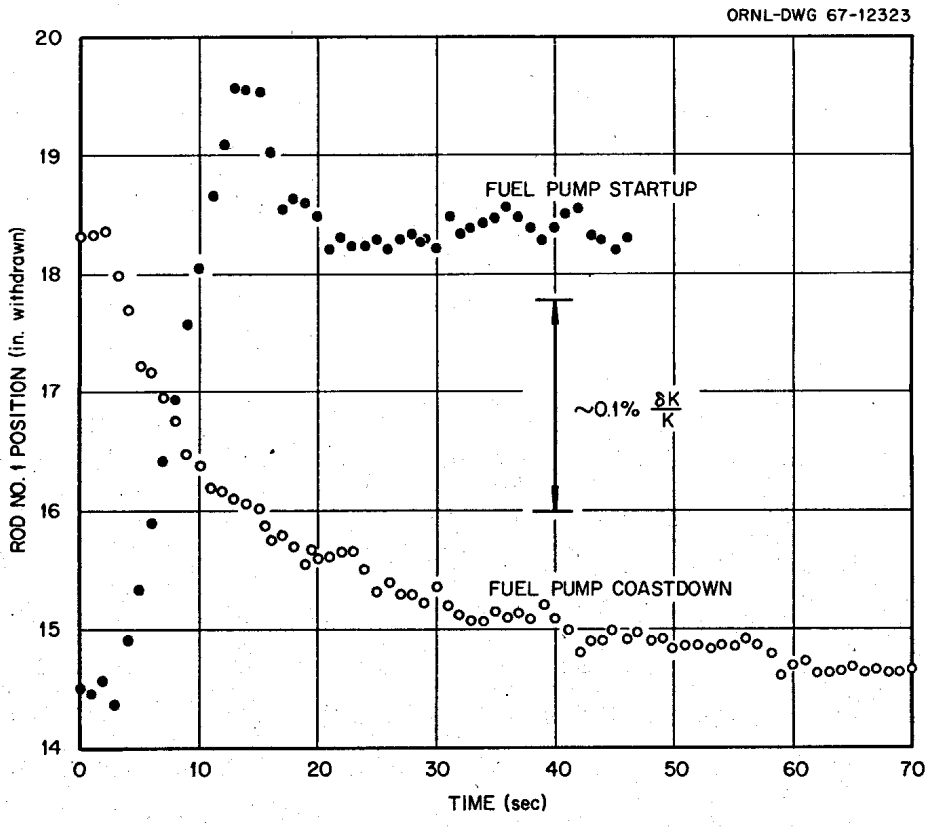

Figure 1.11: Change in rod MSRE control rod position in response to pump startup and coast-down transients. Reproduced with permission, courtesy of U.S. Dept. of Energy [6].

1.6.1 General Reactivity Feedback Mechanisms in MSRE

When operating at low powers, the salt temperature is held constant by the resistive heating circuit while fission power is governed by control rod position. At high power, the negative

temperature coefficient of the system plays the major role in regulating power - therefore the reactor is controlled by modification of the amount of heat extracted from the coolant circuit. Power will increase if cooler fuel reenters the core [7]. Temperature feedback is assumed to be immediate in response to changes in core power as the fuel as it hosts the majority of fission power production. The graphite moderator will heat up more slowly due to the small fraction of fission power deposited in it and the limited rate of fuel-graphite heat transfer.

Pressure can also influence the reactivity of MSRE through the gas volume fraction - gas is entrained in the fuel by the spray ring in the pump bowl, designed to purge a portion of the salt flow of ^{135}Xe. This volume fraction (1.7 - 2.0 %) reduces to approx. 1.2 % by the time the salt enters the core. Transients in pressure can alter reactivity by changing the gas volume fraction (and therefore density) of the salt-gas mixture. A rapid pressure increase is expected to result in a positive contribution to reactivity as the gas volume fraction will decrease, increasing the local fuel concentration.

1.7 Point Kinetics as a Methodology for Reactor Analysis

The 'point kinetic' equations are a useful approximation to the behaviour of the neutrons and delayed neutron precursors in a nuclear reactor core. Integration of the neutron transport equation in a multiplying medium, over the reactor volume, neutron energies and angles, yields the point kinetic equations for a zero-dimensional reactor core [47].

A common assumption is that the flux, ϕ as a function of time and location may be decomposed into the product of an amplitude N (a function of time, representing the number of neutrons), and a shape function ψ (a function of space).

$$\phi(\mathbf{r}, t) = N(t)\psi(\mathbf{r})$$

This permits fixing the shape of the flux in the core and solving for N as a function of time. This assumption is valid for a compact core (dimensions of only a few neutron diffusion lengths), where the flux profile can adjust quickly to local fluctuations.

The advantages of using a point kinetic model for reactor analysis include simplicity and ease of coupling to other physical models and speed of computation. For rapid changes in reactivity or geometry, when higher order modes may be present, models including neutron transport in the core may give more accurate results.

1.8 Modelling of MSRE and Other MSRs

A recent and comprehensive review [48] compares a variety of methods for modelling MSR behaviours in terms of accuracy, developmental complexity and computational cost. An outline of the discussion will be reproduced here, with additional references to MSRE programme-specific models developed at ORNL.

1.8.1 Point Kinetic Models with Simplified Thermal Hydraulic Feedback

The very simplest models of a molten salt reactor are based on the point kinetic equations with modifications to the delayed neutron fraction β and emission of delayed neutrons using the residence times in the core and the primary circuit external loop. Early simulations of the behaviour of circulating fuel reactors solved these equations using analytical methods, analog computers [49] and later digital computers running numerical algorithms.

For example, Zhang *et al.* [50] [1] account for the loss of precursors using an effective delayed neutron fraction reduced on the basis of respective residence times inside and outside the core. The authors investigate a pump shutdown, sudden overcooling of fuel salt and two transient increases in reactivity, sufficient to take the reactor supercritical and prompt supercritical, respectively. Some models suggest that an increase in delayed neutron precursor decay outside of the core (*i.e.* a reduction in the effective value of β) would result in faster response to reactivity transients, with higher peak powers [51, 52].

[1] The author suspects a typographical error in Eq. 4 (erroneous factor of 2 in '2w') in [50], however the results look plausible.

1.8.2 Point Kinetic Models with Detailed Models of Nuclear Thermal Hydraulic Feedback

Explicit modelling of the transport of delayed neutron precursors and the fuel temperature field provides a useful increase in model fidelity. Transient peaks and troughs in power, pressure and temperature may be observed in response to reactivity changes, an appropriate addition needed for safety analyses. Early investigations focussed on the stability of circulating fuel systems [53]. Ergen [54] discusses the stability of a circulating fuel system, outlining an argument in which oscillations would have to be bounded, but this does not rule out the possibility of those oscillations being large enough in amplitude to destroy a reactor.

These models may be further enhanced with importance functions for the decay of precursors with respect to decay location - the desirability of updating the adjoint flux to account for fuel movement in the core was highlighted in analytical models at the end of the MSRE programme [55].

These coupled point kinetic-thermal hydraulic models were used extensively in the MSRE programme for the reactor safety case in the event of unanticipated reactivity steps and ramps, fuel enrichment and temperature changes, starting from a range of initial power conditions [56]. The temperature coefficients of reactivity, mean generation time, and total heat capacities used were significantly different from later analysis, therefore they are not suitable for direct comparison with the models developed in this work. Additional safety analysis for a separate MSRE run fuelled by ^{233}U, was performed using analog models to investigate startup and enriched slug accidents [57].

Similar distributed point kinetic models with updated parameters were used to predict the stability and frequency response of the MSRE. It was predicted that the reactor would become more stable as the power level increased [33]. Theoretical analysis of oscillatory behaviours is discussed in [43] and comparison with measurements in [58]. Further discussion of oscillatory behaviours and stability in an MSRE-like design may be found in Chapter 5.

Analysis of molten salt reactor designs continued after the end of the MSRE programme, including the notable example of a hybrid analog-digital computer system used to simulate the

core and heat exchanger (in detail) of a 1000 MW(e) MSBR design [59].

1.8.3 Spatially-Dependent Nuclear Reactor Kinetics with Detailed Nuclear Thermal Hydraulic Feedback or Computational Fluid Dynamics (CFD)

The most detailed of molten salt reactor models account for neutron transport in the core, and the coupling between DNP distribution, movement, and the neutron flux. Typically neutron diffusion is used, but there exists at least one documented case of a Monte Carlo model being adapted to account for precursor drift [42]. One dimensional [60] and three-dimensional [61] models have been developed, both providing good agreement with the experimental data for pump transients and a recirculation experiment in MSRE. Other codes have incorporated multi-phase hydrodynamic models for modelling of severe accidents [62]. Recent models have extended the modelling of neutron transport in the core to multigroup neutron diffusion [63, 64].

'Quasi-static' approaches exist where the flux and importance distributions are updated in an adaptively timestepped fashion to account for changes in the thermal hydraulic conditions. The amplitude of the shape function or flux (depending on implementation [65]) is updated on a short timescale while the shape is updated less frequently. It is argued they are most appropriate for rapid power and/or flow transients, however point methods are still able to predict the final states after conclusion of the transient. These models provide the best agreement with MSRE experimental data, however they are underdeveloped at the time of writing. They have the potential to provide a balance between computational cost and accuracy for modelling MSR behaviours, though Wooten & Powers [48] warn the reader of poor implementations as these could consume more computing resources than a fully coupled model.

Chapter 2

Modelling an MSRE-like Reactor with Point Kinetics

2.1 Motivation

As discussed in Section 1.8, modified point kinetic models have been used to represent the majority of MSR system behaviours. They are efficient, capable of representing many physical processes and quick to modify, making them amenable to statistical sampling using modest computing resources.

This chapter outlines the derivation of a coupled point kinetic-thermal hydraulic model of an MSRE-like system for investigation of reactor physics phenomena highlighted by the Molten Salt Reactor Experiment. A series of coupled ordinary differential equations (ODEs) and partial differential equations (PDEs) were derived (Section 2.2) to describe the behaviour of the reactor core, primary circuit and control systems.

The equations were discretised and solved using an object-oriented program written using the Fortran 2003 standard with ODE solver subroutines originally developed by Shampine & Gordon [66]. Frequency response calculations and Monte Carlo sampling were performed using the MPI parallel framework.

2.2 Physics and Modelling Assumptions

The model of the MSRE-like system used a one-dimensional representation of the core due to its simplicity and speed of calculation, with an assumed sinusoidal axial flux distribution. Modelling of the secondary circuit was neglected in order to reduce computational demands and data on ^{235}U-fuelled behaviour was not conclusive and had no discernible effect on the frequency response at the frequencies of interest (see Section 5.5). A recent review [48] discusses the advantages of including a secondary circuit in MSR kinetic analyses - more accurate damping after reactivity insertion is shown but the effect is slight.

A proportion of fissions were expected to occur outside the moderated region of the core - in the vessel downcomer, lower and upper heads. It was assumed that production of delayed neutron precursors in these regions was proportional to the fraction of fissions that occur in that region. Table 2.1 lists the proportions of total fissions in the four fissioning regions as calculated by Haubenreich *et al.* [7] using the EQUIPOISE-3 two-group diffusion code [13]. All neutrons produced by the decay of precursors in these regions were assumed to contribute to the chain reaction. The contribution to fuel salt heating from decay of delayed neutron precursors is ignored.

Distribution of Fissions	
Section	% of total fissions
Downcomer	2.9
Lower head	2.4
Core	89.1
Upper head	5.6

Table 2.1: Percentage of fissions in vessel regions [7]. Calculated using the two-group diffusion code EQUIPOISE-3 two-group code [13].

The primary circuit was modelled as a 1D pipe through which salt properties (temperature and concentrations of delayed neutron precursors) will be advected (Figure 2.1). Additional dispersion of the fuel temperature field to mimic the effect of hydrodynamic mixing in the circuit was modelled using a velocity-dependent turbulent dispersion term, based on oil pipe line experiments [67]. Mixing of the delayed neutron precursors would also be expected to occur, however was neglected in this model due to disparity in the magnitude of the gradients and

subsequent effect on the ODE solver, and a lack of comparable data for turbulent mass transfer in molten salts, as acknowledged in the review by Wooten and Powers [48]. Some numerical dispersion of the precursors was still expected to occur.

A one-dimensional periodic circuit coordinate system was defined with the bottom of the graphite moderator in the core corresponding to $z = 0$, and end of the circuit corresponding to $z = L = 16.37$ m.

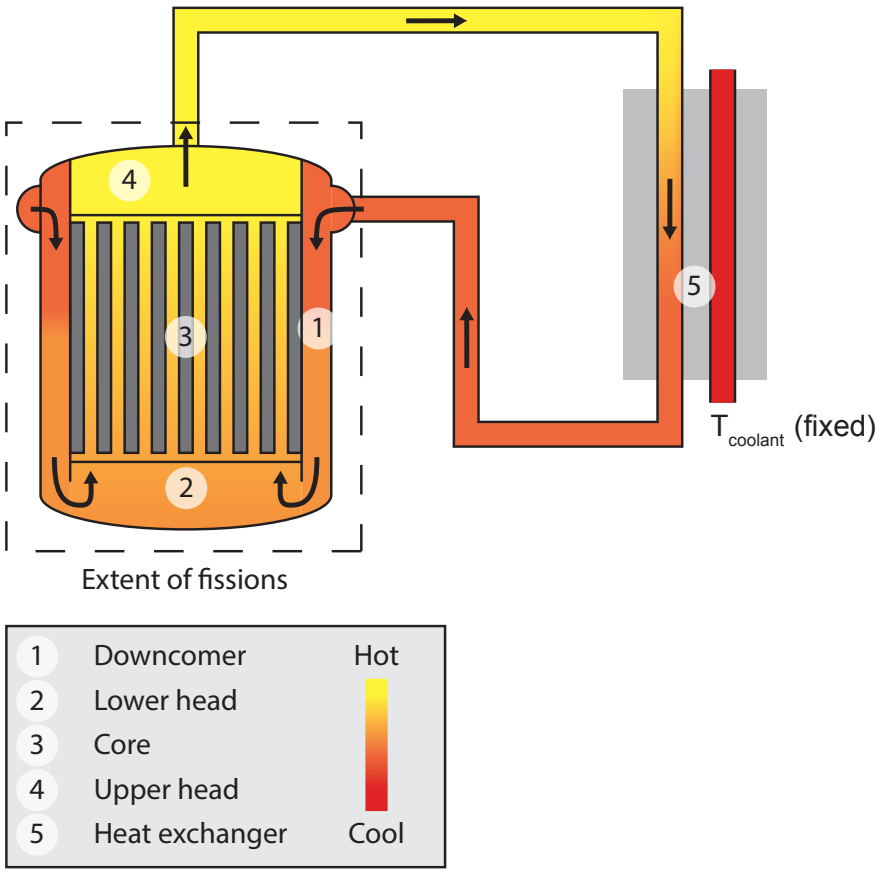

Figure 2.1: Schematic of the primary circuit with regions undergoing fission and primary heat exchanger labelled.

2.2.1 Core and Fissioning Regions

The behaviour of the core is described by modified point-kinetic equations coupled to the thermal hydraulic behaviours of the primary circuit. The kinetics of any surrounding reflector material,

for example the reactor cell thermal shield, were not considered.

The rate of change of the number of neutrons in the core, n, neglecting spatial variations in flux, is described by

$$\frac{dn(t)}{dt} = \frac{\rho(t, T_f, T_g) - \beta}{\Lambda} n(t) + \sum_{i=1}^{6} \lambda_i \int\limits_{\substack{core,LH,\\ UH,DC}} f_{vol,fuel}(z)\ CSA(z)\ C_i'''(z)\ dz \tag{2.1}$$

where ρ = reactivity (in non-Dollar units), β = delayed neutron fraction, $\Lambda = \frac{1}{v\Sigma_a}$ = mean neutron generation time [s], λ_i = decay constant for precursor group i [s^{-1}], $f_{vol,fuel}$ = volume fraction of fuel, CSA = cross-sectional area of primary circuit and C_i''' = concentration of delayed neutron precursors in group i [m^{-3}], and z = circuit coordinate [m].

The rate of change of precursor concentration, C_i''', is described by

$$\frac{\partial C_i'''(t,z)}{\partial t} = \frac{f_{fission}\psi(z)\beta_i n(t)}{\Lambda CSA(z) f_{vol,fuel}(z)} - \lambda_i C_i'''(z) - u(z)\frac{\partial C_i'''}{\partial z} \tag{2.2}$$

where $f_{fission} = \{f_{core},\ f_{D.C.},\ f_{U.H.},\ f_{L.H.}\}$, *i.e.*, the fraction of total fissions in the core, downcomer, upper head and lower head, respectively, $\psi = sin\left[\frac{\pi}{1.985}(z+0.145)\right]$, the distribution of fissions across the moderated core region with height z, β_i = the production yield of precursor group i, and u = the fuel velocity [$m\,s^{-1}$].

The distribution of fissions in the core was calculated using the EQUIPOISE-3 diffusion code, as described in [7]. The calculation used a core height of 1.985 m and axial extrapolation distance of 0.145 m into the upper and lower vessel plena.

The rate of change of fuel temperature, T_f, is described by

$$\frac{\partial T_f(t,z)}{\partial t} = \frac{P(t)\ p_{dep}\ \xi(z)}{f_{vol,fuel}(z)\rho_{fuel}\ C_{p,fuel}} + \frac{h_{f,g}A_{f,g}\Big(T_g(z) - T_{f,core}(z)\Big)}{H\ CSA(z)f_{vol,fuel}(z)\rho_{fuel}\ C_{p,fuel}} - u(z)\frac{\partial T_f}{\partial z} + \frac{\partial}{\partial z}\left(u(z)K\frac{\partial T_f}{\partial z}\right) \tag{2.3}$$

where P = reactor power [W], $p_{dep} = \{p_{core},\ p_{D.C.},\ p_{U.H.},\ p_{L.H.}\}$, the fraction of fission power deposited in the core, downcomer, upper head and lower head, respectively; ξ = deposited power density [m^{-3}], ρ_{fuel} = fuel density [$\mathrm{kg\,m}^{-3}$], $C_{p,fuel}$ = fuel specific heat capacity [$\mathrm{J\,kg}^{-1}\,\mathrm{K}^{-1}$], $h_{f,g}$ = heat transfer coefficient between fuel and graphite [$\mathrm{W\,m}^{-2}\,\mathrm{K}^{-1}$], $A_{f,g}$ = interfacial area between fuel and graphite [m^2], T_g = graphite temperature [K] and H = core height [m], u = fuel velocity [$\mathrm{m\,s}^{-1}$], and K = turbulent dispersion parameter [W/m/K].

The rate of change of graphite temperature is described by

$$\frac{dT_g(t,z)}{dt} = \frac{P(t)p_g\xi(z)}{f_{vol,g}\rho_g C_{p,g}} + \frac{h_{f,g}A_{f,g}(T_{f,core}(z) - T_g(z))}{H\ CSA(z)f_{vol,g}\rho_g C_{p,g}} \tag{2.4}$$

with reactor power $P(t)$,

$$P(t) = \frac{n(t)\chi_{fission}}{\Lambda\ \bar{\nu}} \quad , \tag{2.5}$$

where p_g = fraction of fission power deposited in the graphite, $f_{vol,g}$ = volume fraction of graphite in the core, ρ_g = graphite density [$\mathrm{kg\,m}^{-3}$], and $C_{p,graphite}$ = graphite specific heat capacity [$\mathrm{J\,kg}^{-1}\,\mathrm{K}^{-1}$], $\chi_{fission}$ = energy released per fission event [J], and $\bar{\nu}$ = average number of neutrons emitted per fission event.

Reactivity in the core is represented by Equation 2.6, which is comprised of a temperature-dependent term (Equations 2.7 through 2.10) and an external reactivity term. The external reactivity term usually represents any movement of the control rods as a function of time, while the temperature-dependent reactivity contribution is calculated using the nuclear average temperatures of the fuel and graphite in the core relative to a reference temperature (usually

chosen to be the inlet temperature of the coolant salt during full power operation, 825 K). The selection of temperature coefficients of reactivity based on available experimental and modelling data is discussed in Appendix A.4.

The nuclear average temperatures are the temperatures of fuel and graphite (Eqs. 2.8 and 2.9) are weighted with respect to an importance function. Small changes in temperature in a region of high flux may induce the same reactivity change as a larger temperature change in a region of low flux. The model assumes a sine-squared importance function with total height 2.017 m and an extrapolation distance outside the graphite-moderated region of 0.1196 m (Eq. 2.10). This function was based on a two group adjoint calculation using the EQUIPOISE-3A two-group diffusion calculation performed by Prince & Engel [68].

$$\rho(t, T_f, T_g) = \rho_T(T_f, T_g) + \rho_{external}(t) \tag{2.6}$$

$$\rho_T(t) = \alpha_f \left(T_f^*(t) - T_{ref} \right) + \alpha_g \left(T_g^*(t) - T_{ref} \right) \tag{2.7}$$

where ρ_T = temperature-dependent reactivity term, α_f = fuel temperature coefficient of reactivity, 8.46×10^{-5} K^{-1} and α_g = graphite temperature coefficient of reactivity, 4.68×10^{-5} K^{-1}; and T_{ref} = reference temperature of the system, 825 K.

$$T_f^* = \frac{\int_{z=0}^{z=H} I_f(z)\ T_f(z)\ dz}{\int_{z=0}^{z=H} I_f(z)\ dz} \tag{2.8}$$

$$T_g^* = \frac{\int_{z=0}^{z=H} I_g(z)\ T_g(z)\ dz}{\int_{z=0}^{z=H} I_g(z)\ dz} \tag{2.9}$$

$$I_{f,g} = sin^2 \left[\frac{\pi}{2.017} (z + 0.1196) \right] \tag{2.10}$$

2.3 Primary Circuit Pipework

The rate of change of precursor concentration, C_i''', in the primary circuit pipework and heat exchanger is described by

$$\frac{\partial C_i'''(t,z)}{\partial t} = -\lambda_i C_i'''(z) - u(z)\frac{\partial C_i'''}{\partial z} \tag{2.11}$$

The rate of change of fuel temperature, T_f, in the piping outside the core (excluding the heat exchanger) is described by

$$\frac{\partial T_f(t,z)}{\partial t} = -u(z)\frac{\partial T_f}{\partial z} + \frac{\partial}{\partial z}\left(u(z)K\frac{\partial T_f}{\partial z}\right) \tag{2.12}$$

2.4 Equations in the Primary Heat Exchanger

The rate of change of fuel temperature in the primary circuit heat exchanger is described by

$$\frac{\partial T_{f,\ H.E.}}{\partial t} = \frac{h_{H.E.}A_{H.E.}\big(T_{coolant} - T_f(z)\big)}{L_{H.E.}\ CSA(z)\rho_{fuel}\ C_{p,fuel}} - u(z)\frac{\partial T_f}{\partial z} + \frac{\partial}{\partial z}\left(u(z)K\frac{\partial T_f}{\partial z}\right) \tag{2.13}$$

where $h_{H.E.}$ = heat transfer coefficient [$\mathrm{W\,m^{-2}}$], $A_{H.E.}$ = heat exchanger interfacial area [$\mathrm{m^2}$], $T_{coolant}$ = temperature of the coolant salt in the secondary circuit [K] and $L_{H.E.}$ = heat exchanger length [m].

2.5 Closures and Periodic Boundary Conditions

The following relations are defined for the sum of the fission fractions in all fissioning regions, and the sum of the deposited power fractions, both of which must sum to 1.0:

$$f_{core} + f_{U.H.} + f_{D.C.} + f_{L.H.} = 1 \tag{2.14}$$

$$p_{core} + p_{graphite} + p_{U.H.} + p_{D.C.} + p_{L.H.} = 1 \tag{2.15}$$

The reentry of fuel and precursors from the lower head into the bottom of the core are represented by periodic boundary conditions that equate the values at the beginning and end of the primary circuit,

$$T_f(z = 0) = T_f(z = L) \tag{2.16}$$

$$C_i'''(z = 0) = C_i'''(z = L) \tag{2.17}$$

where L = total primary circuit path length [m].

2.6 Summary of Equations

Core

$$\frac{dn(t)}{dt} = \frac{\rho(t, T_f, T_g) - \beta}{\Lambda} n(t) + \sum_{i=1}^{6} \lambda_i \int\limits_{\substack{core,LH,\\ UH,DC}} f_{vol,fuel}(z)\ CSA(z)\ C_i'''(z)\ dz \tag{2.1}$$

$$\frac{\partial C_i'''(t,z)}{\partial t} = \frac{f_{fission}\psi(z)\beta_i n(t)}{\Lambda CSA(z) f_{vol,fuel}(z)} - \lambda_i C_i'''(z) - u(z)\frac{\partial C_i'''}{\partial z} \tag{2.2}$$

$$\begin{aligned}\frac{\partial T_f(t,z)}{\partial t} = &\frac{P(t)\ p_{dep}\ \xi(z)}{f_{vol,fuel}(z)\rho_{fuel}\ C_{p,fuel}} \\ &+ \frac{h_{f,g}A_{f,g}\Big(T_g(z) - T_{f,core}(z)\Big)}{H\ CSA(z) f_{vol,fuel}(z)\rho_{fuel}\ C_{p,fuel}} \\ &- u(z)\frac{\partial T_f}{\partial z} + \frac{\partial}{\partial z}\left(u(z)K\frac{\partial T_f}{\partial z}\right)\end{aligned} \tag{2.3}$$

$$\frac{dT_g(t,z)}{dt} = \frac{P(t)p_g\xi(z)}{f_{vol,g}\rho_g C_{p,g}} + \frac{h_{f,g}A_{f,g}(T_{f,core}(z) - T_g(z))}{H\ CSA(z) f_{vol,g}\rho_g C_{p,g}} \tag{2.4}$$

$$\rho(t, T_f, T_g) = \rho_T(T_f, T_g) + \rho_{external}(t) \tag{2.6}$$

$$\rho_T(t) = \alpha_f\Big(T_f^*(t) - T_{ref}\Big) + \alpha_g\Big(T_g^*(t) - T_{ref}\Big) \tag{2.7}$$

Primary Circuit Pipework

$$\frac{\partial C_i'''(t,z)}{\partial t} = -\lambda_i C_i'''(z) - u(z)\frac{\partial C_i'''}{\partial z} \tag{2.11}$$

$$\frac{\partial T_f(t,z)}{\partial t} = -u(z)\frac{\partial T_f}{\partial z} + \frac{\partial}{\partial z}\left(u(z)K\frac{\partial T_f}{\partial z}\right) \tag{2.12}$$

Heat Exchanger

$$\frac{\partial T_{f,\ H.E.}}{\partial t} = \frac{h_{H.E.}A_{H.E.}\big(T_{coolant} - T_f(z)\big)}{L_{H.E.}\ CSA(z)\rho_{fuel}\ C_{p,fuel}} - u(z)\frac{\partial T_f}{\partial z} + \frac{\partial}{\partial z}\left(u(z)K\frac{\partial T_f}{\partial z}\right) \tag{2.13}$$

Closures and Periodic Boundary Conditions

$$f_{core} + f_{U.H.} + f_{D.C.} + f_{L.H.} = 1 \tag{2.14}$$

$$p_{core} + p_{graphite} + p_{U.H.} + p_{D.C.} + p_{L.H.} = 1 \tag{2.15}$$

$$T_f(z = 0) = T_f(z = L) \tag{2.16}$$

$$C_i'''(z = 0) = C_i'''(z = L) \tag{2.17}$$

2.7 Discretisation & Convergence

The primary circuit was discretised into smaller sections according to a target Δz with the temperature and precursor advection term discretised using an upwind scheme and the velocity-dependent dispersion discretised using a central difference scheme. The precise Δz was adjusted to maintain the same residence time in each component as measured in a full-scale hydrodynamic mockup of the MSRE vessel [2, 69].

ORNL theoretical models predicted a peak in response at approx. $\omega = 0.3$ rad s^{-1}, however this feature was not observed in later experiments. The full investigation of this feature is the subject of Chapter 5, however some results from the author's Fortran code are reproduced here. The convergence study sought to identify the appropriate combination of mesh resolution (via target Δz) and mixing (via the velocity-dependent dispersion parameter K) required for a convergent solution in the frequency range of interest while closely matching the MSRE experimental data [10]. The frequency response of the model for oscillating reactivities between 0.1 and ~ 0.6 rad s^{-1} was measured relative to a highly-refined reference case.

There are competing effects in the mesh convergence study - a higher degree of mesh refinement counteracts numerical dispersion in the model and preserves advection of temperature and precursor gradients around the primary circuit. In addition, a higher degree of turbulent dispersion

(represented by the parameter K) will enhance dispersion of fuel temperature gradients in the primary circuit.

Figures 2.2 and 2.3 show the convergence of the model's frequency response with increasing mesh resolution, at four different levels of dispersion from $K = 0$ to $K = 3 \times 10^5$ W/m/K. The dip in gain/peak in phase shift at ~ 0.25 rad s^{-1}, corresponding to the recirculation time of the reactor is apparent at lower K as the mesh becomes more refined. This is consistent with hot fuel reentering the core and inducing a drop in power output due to negative temperature feedbacks. A corresponding out-of-phase increase in gain is observed at slightly higher frequency (~ 0.3 rad s^{-1}).

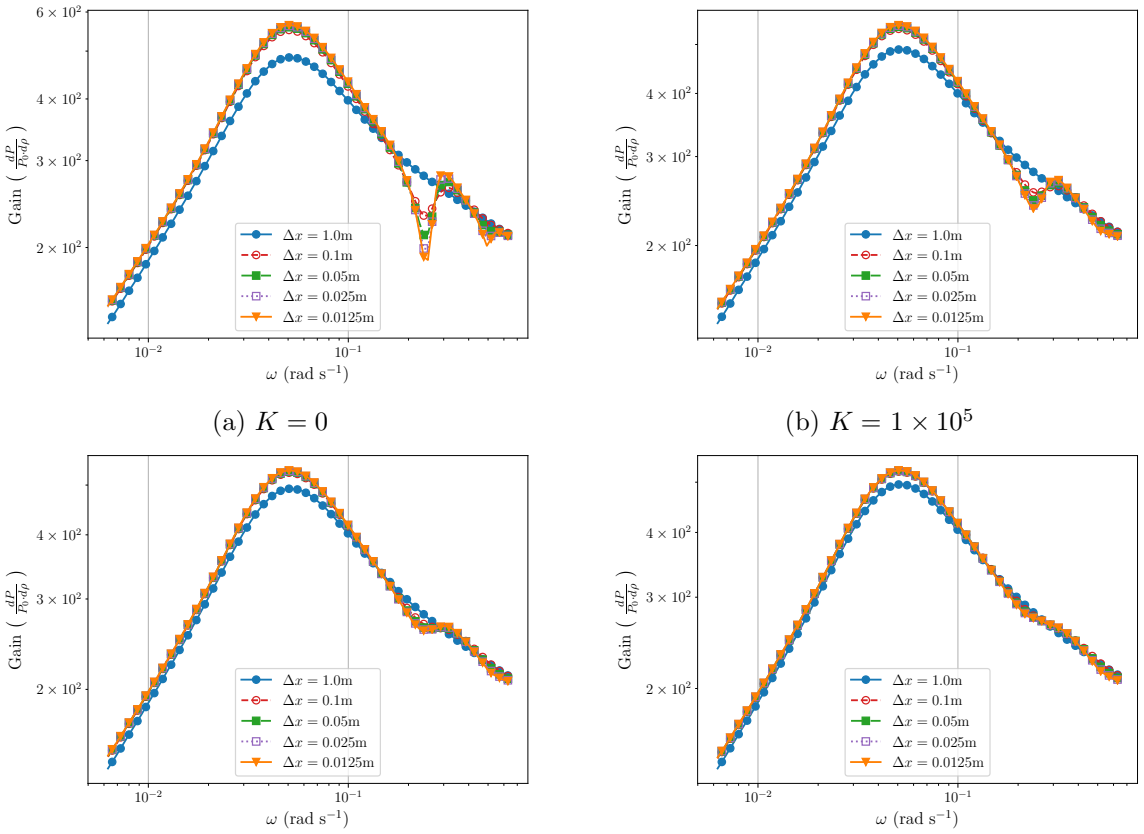

(a) $K = 0$

(b) $K = 1 \times 10^5$

(c) $K = 2 \times 10^5$

(d) $K = 3 \times 10^5$

Figure 2.2: Convergence of model frequency response for K values between 0.0 and 3×10^5 W/m/K. Power = 7.5 MW.

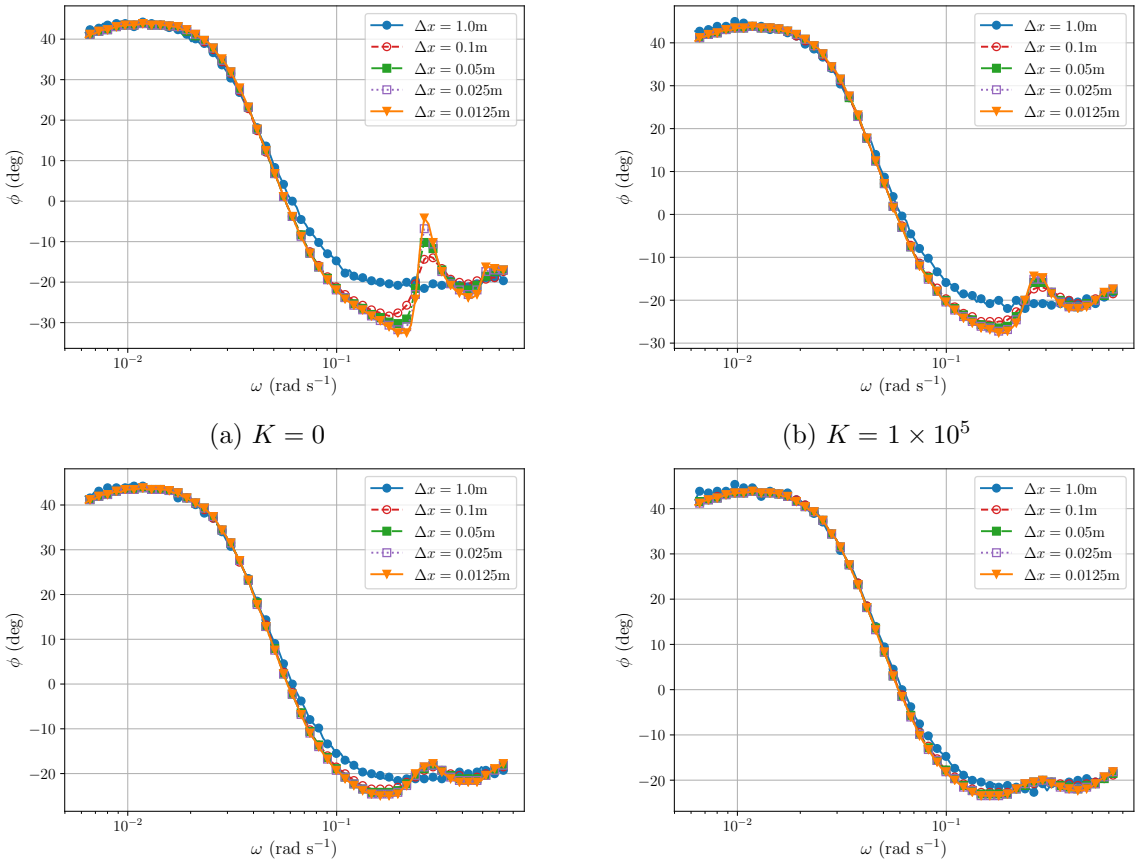

(a) $K = 0$

(b) $K = 1 \times 10^5$

(c) $K = 2 \times 10^5$

(d) $K = 3 \times 10^5$

Figure 2.3: Convergence of model phase shift for K values between 0.0 and 3×10^5 W/m/K . Power = 7.5 MW.

Figure 2.4 shows the convergence of relative error $\bar{\epsilon}$ (in the vicinity of the recirculation peak) on a highly-refined reference case. The final combination of mesh and dispersion parameter was chosen based on qualitative similarity to the experimental data (*i.e.* no peak in response at ~ 0.25 rad s^{-1}) and computational efficiency. It was found that a target Δz of 0.05 m and $K = 3 \times 10^5$ W/m/K provided sufficient turbulent dispersion to remove the recirculation peak and sufficient convergence in the frequency range of interest (a monotonically-decreasing $\bar{\epsilon}$ less than 10^{-2} was deemed sufficient). A more detailed discussion of the model frequency response and comparison with experimental data is presented in Chapter 5.

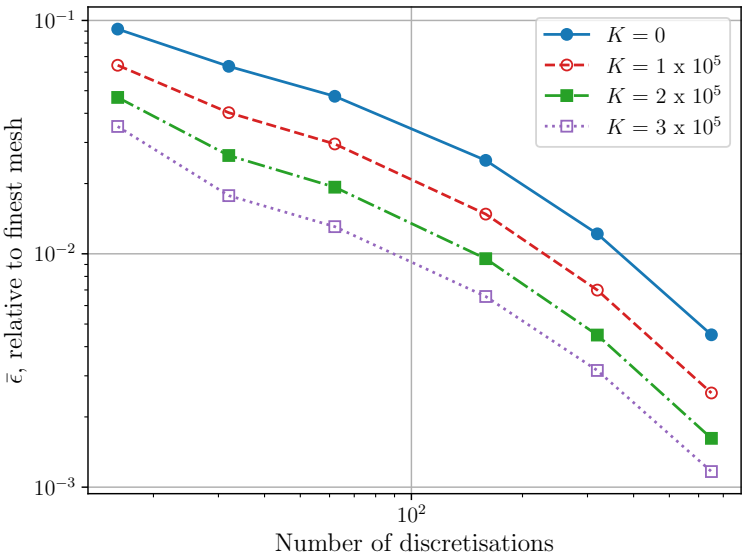

Figure 2.4: Convergence plot with increasing levels of turbulent dispersion. $\bar{\epsilon} = L_2$ norm of deviation from a highly-refined reference case.

Chapter 3

Numerical Model Behaviour

This chapter analyses the steady state conditions and transient behvaviours of the numerical model developed in Chapter 2. Parameters were chosen to best approximate the behaviour of the Molten Salt Reactor Experiment. This data served as the basis for interpreting the frequency response and sensitivity analyses discussed in subsequent chapters.

3.1 Steady State Conditions

3.1.1 Circuit Temperatures, P = 8 MW

The deterministic model of MSRE was initialised in a steady-state condition and power output of 8 MW $\left(\frac{dP}{dt} = 0\right)$. The distribution of fuel temperature around the primary circuit loop is shown in Fig. 3.1. The circuit coordinate represents the distance around the primary circuit with zero representing the bottom of the graphite-moderated portion of the core.

Fissions in the power-producing regions of the loop (downcomer, lower head, core and upper head) contribute to an increase in the temperature of the fuel as it flows through these regions. Primary circuit pipework was treated as adiabatic, therefore the rate of temperature change is zero in these regions. Transfer of heat from the primary to secondary coolant causes a rapid decrease in temperature in the heat exchanger (between $z = 6$ and $z = 10$ m).

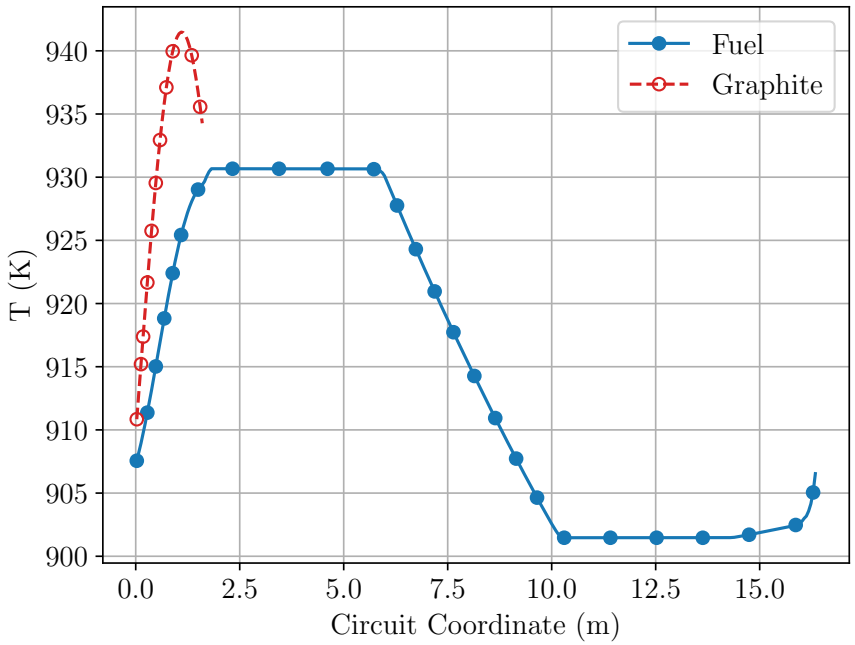

Figure 3.1: Temperature distributions in the primary circuit under steady state conditions, $P = 8$ MW.

The steady-state vessel inlet and outlet fuel temperatures were 901.5 K (628.4 °C, 1,163 °F), and 930.7 K (657.6 °C, 1216 °F), respectively. These temperatures are slightly different to those observed during typical MSRE operation (1170 °F inlet and 1210 °F outlet [29]).

3.1.2 Comparison Against ORNL Design Data, P = 10 MW

Figure 3.2 compares the fuel and graphite temperatures in the core at the original design power of 10 MW against a predicted temperature distribution using an MSRE design model [70].

The temperature of the graphite moderator is higher than that of the core fuel under steady state operation as the only mechanism for the graphite to lose deposited power is via conduction to the salt flowing past. Peak T_g occurs at $z = 1.11$ m, approximately two-thirds of the way up the moderated portion of the core.

The ORNL data was calculated for the channel predicted to be the hottest in the core, in an annulus at $r = 21$ cm that surrounds the central axis (off-centre due to the control rods

locally depressing the flux slightly and thus the fission power density). Figure 3.2 shows a greater temperature increase for the ORNL model compared to this work, which is based on the volumetric average fission power density across the entire moderated core region, hence the lower peak temperatures compared to the ORNL hot channel data. The axial position that corresponds to peak graphite and fuel temperatures is at a higher position in the ORNL data compared to the model. This may be due to the calculation with a neutron diffusion code [13] which would permit a more accurate estimation of the fission power distribution however was not pursued in this work due to software development time constraints.

In addition, a portion of the total fission power was distributed in the downcomer, lower and upper heads which may account for the higher temperature at beginning of core and smaller increase across it. Indeed it is noted in the documentation for the ORNL design model [70] that the heating in the inlet is neglected and $T_f(z = 0)$ is taken to be the vessel inlet temperature. The predicted ORNL temperature distributions are close to the design temperatures of approx. 1175 °F and 1125 °F, for inlet and outlet temperatures, respectively. In addition, turbulent and numerical dispersion in the model will reduce gradients including those across the core.

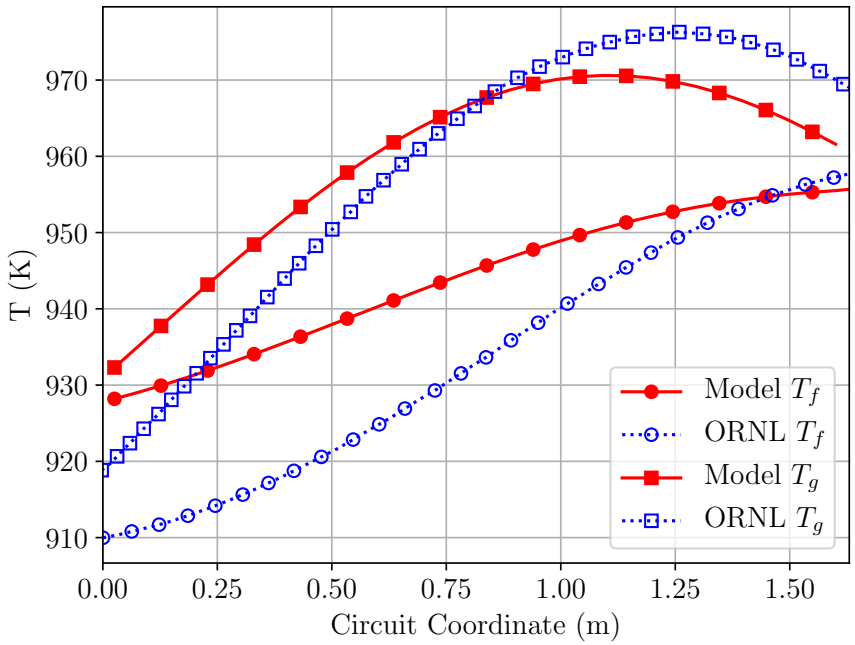

Figure 3.2: Temperature distributions across the moderated core region in fuel and graphite, compared with predicted ORNL data for hottest channel in core [7]. $P = 10$MW.

3.1.3 Delayed Neutron Precursor Distribution, P = 8MW

Distribution of delayed neutron precursors around the circuit at steady-state power of 8 MW is shown in Figure 3.3. This power level was chosen as it is close to the true maximum operating power of the MSRE. The concentration of short-lived precursors mimics the distribution of fissions in the power-producing regions, as their short half lives mean they can only persist in regions undergoing fission (for example, observe the rapid equilibration of the concentration of short-lived precursors in the downcomer, starting at $z = 14.5$ m). In contrast, long-lived precursors may be transported from their point of origin before a significant proportion can decay. This is evidenced by a shift in the peak into the upper head of the reactor vessel, as precursors accumulate in the fuel during its transit through fissioning regions. Thereafter, significant amounts persist in the loop. The steepening of the negative gradient late in the loop corresponds to the greater residence time in the downcomer and lower head (thus giving greater time for precursors to decay).

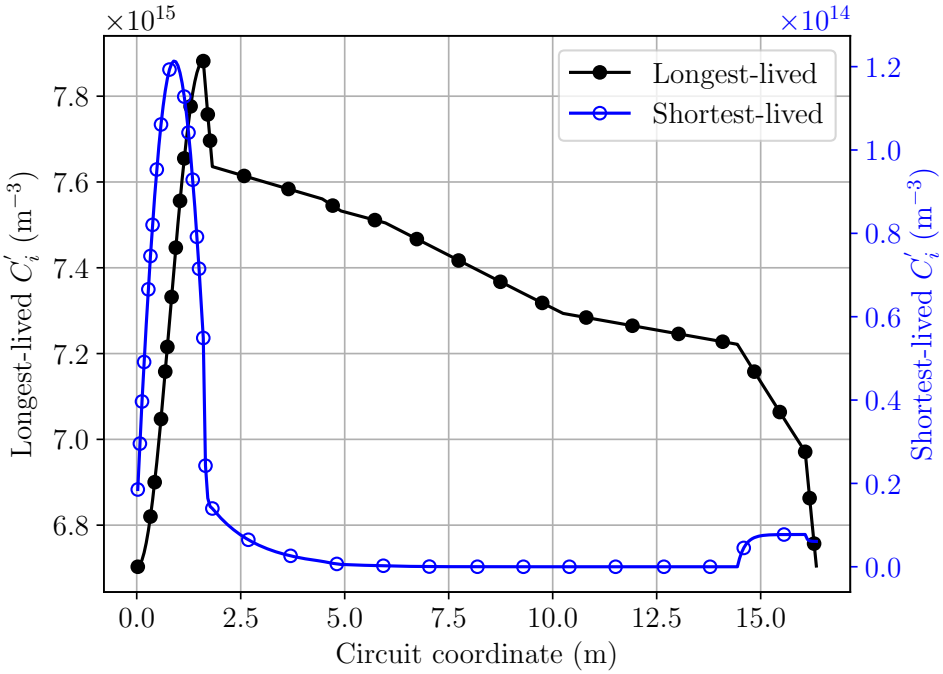

Figure 3.3: Distributions of precursors around the loop under steady state conditions, power = 8 MW.

Figures 3.4 and 3.5 compare the total (across all precursor groups) delayed neutron source distributions at steady state and supercritical with stable period. The overall shapes and relative source magnitudes (between critical and supercritical states) are very similar, with both models showing the adjustment of the delayed neutron source distribution in response to increasing power - a reduction in the magnitude and a shift towards the centre of the reactor.

The general shift of the delayed neutron source towards the top of the core is due to fuel movement transporting precursors upwards before they decay. The reduction in source intensity when supercritical with constant period is due to the delayed neutron emission rate not having a chance to catch up with the power as the delayed neutron precursors were released by past fissions at a lower power level.

The very slight decrease in delayed neutron source entering the moderated region in Figure 3.5 is likely due to the higher fraction of fissions present in the downcomer vs. the lower head (see Table 2.1).

The delayed neutron source distribution under circulating supercritical conditions is slightly shifted towards the centre of the core compared to the circulating critical condition. It is a combination of the precursors emitted at a lower power level which have been transported upwards and the newly generated delayed neutrons from the now-higher power level closer to the centre of the core.

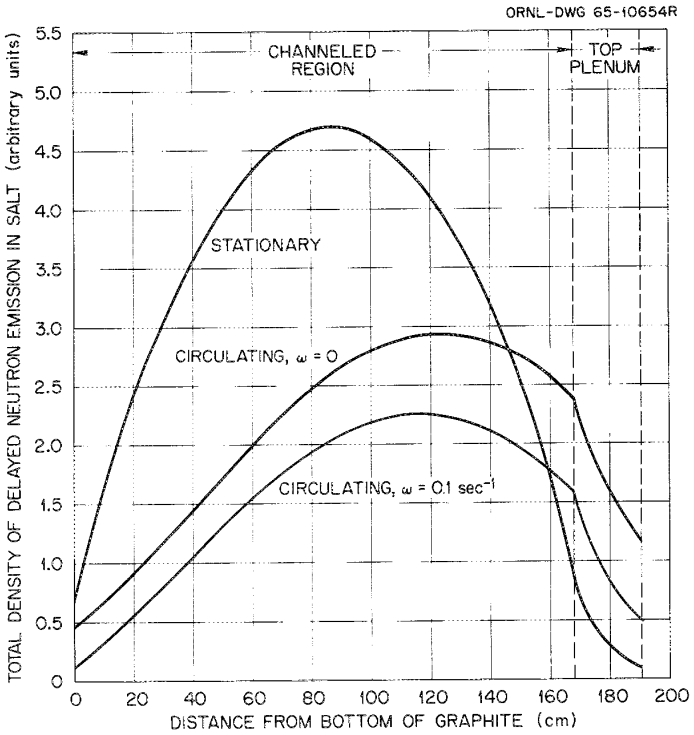

Figure 3.4: Distribution of delayed neutron source in core and upper head, as calculated by the ORNL code EXTERMINATOR [8]. Adapted with permission, courtesy of the U.S. Dept. of Energy [9].

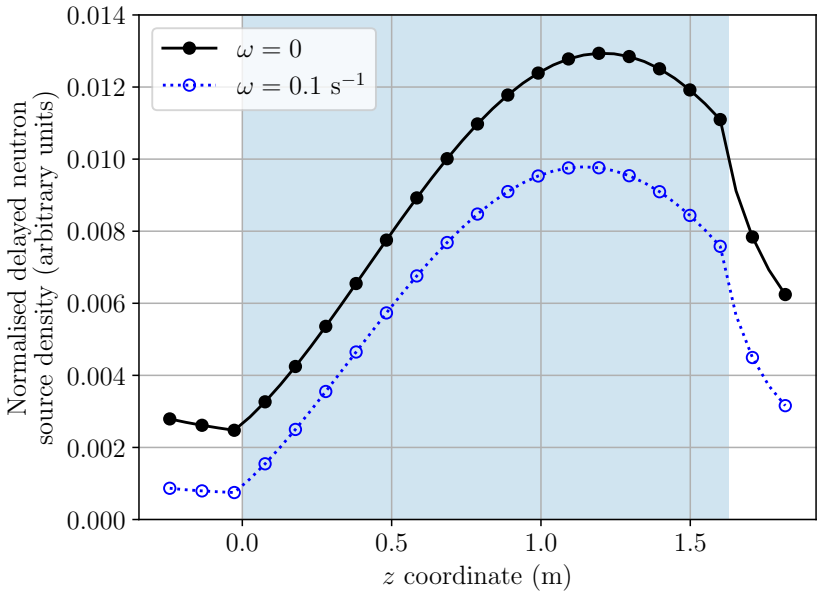

Figure 3.5: Distribution of delayed neutron source in core and plena with fuel circulating as calculated by the model for critical state and a supercritical state with stable reactor period of 10s. Shaded region indicates extent of graphite-moderated region.

3.2 Transient Behaviour in Response to Reactivity Insertions

3.2.1 Half Dollar Reactivity Ramp

The numerical model was initialised at a steady-state power of 8 MW, before a 60 s half dollar reactivity ramp starting at $t = 5$s. This is equivalent to an operator withdrawing a control rod at a constant rate for one minute, assuming constant rod reactivity worth along its length.

Initial steady-state reactivity is non-zero due to two reasons. First, the transport and decay of delayed neutron precursors outside of the core reduces the neutrons available for the chain reaction, and second the core is operating with a steady-state temperature above the reference temperature (set to the temperature of the secondary coolant circuit). In order to compensate for the delayed neutron loss and the negative temperature feedback extra reactivity must be added to the system. This initial external reactivity compensation is approximately 2.1 dollars.

At the start of the ramp, the core becomes delayed supercritical, with power peaking at 15.9 MW

at $t = 65$ s (Fig. 3.6a). Total reactivity (the sum of the external and temperature-dependent contributions) peaks at approx. \$0.22 at $t = 30.5$s, beyond which the contribution of ρ_T exceeds the external reactivity ramp as the increasing number of fissions deposit energy in the core fuel and graphite regions. The rate of increase of the core power lessens slightly towards the end of the ramp, becoming significantly subcritical at the conclusion of the reactivity ramp ($t = 65$ s).

Between approx. $t = 100$ and $t = 250s$ the core exhibits some strongly-damped oscillatory behaviour. This may be due to the fuel salt cooling after the end of the reactivity ramp, evidenced by a simultaneous reduction in the magnitude of ρ_T. The reactor then settles to a new steady-state power level at just under 10 MW. The extra external reactivity added to the system during the ramp permits steady-state operation at a higher average core temperature.

Concentrations of the shortest-lived precursors in the core follow the power level (Fig. 3.6f). The concentration of the longest-lived precursors, with a half-life of just under one minute, continue to increase after the end of the reactivity ramp while the power remains relatively high, peaking between $t = 90$ and $t = 100s$ depending on vessel region. The concentrations then decay throughout the remainder of the simulation, tending to a higher steady state level, but with relative concentrations in the vessel regions the same as prior to the transient. This constitutes a new post-transient steady state condition.

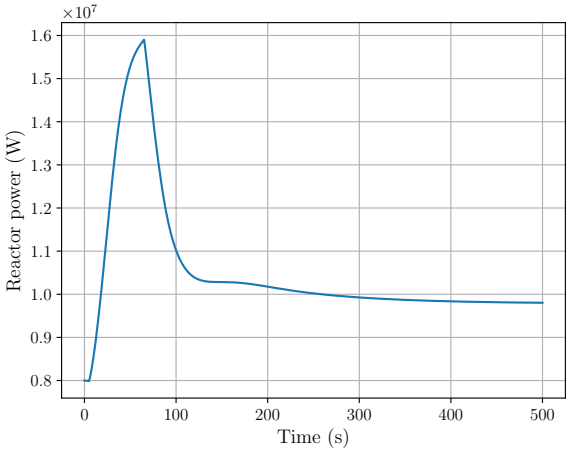

(a) Reactor power

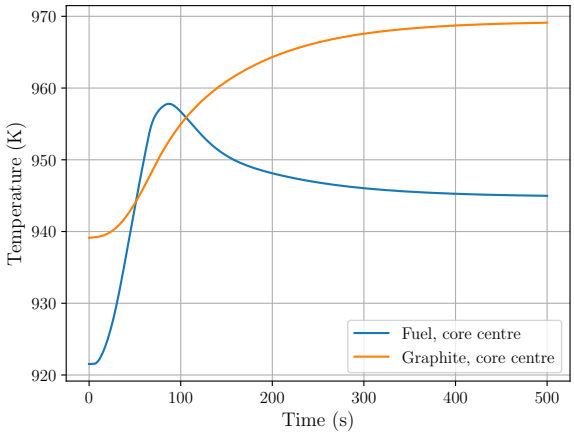

(b) Fuel & graphite temperatures

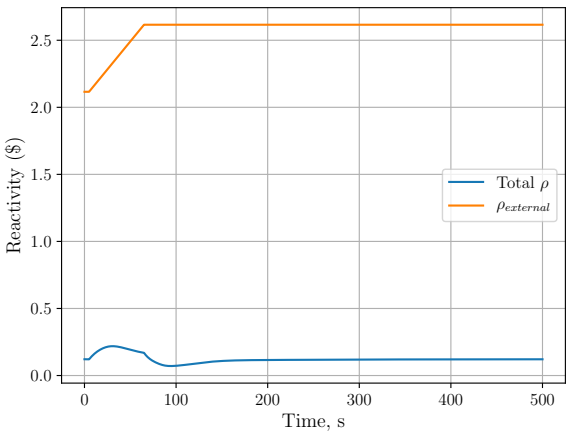

(c) Total and external reactivity contributions

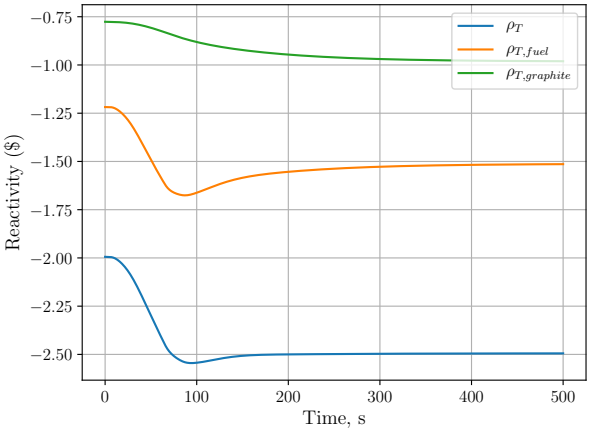

(d) Temperature-dependent reactivity contributions

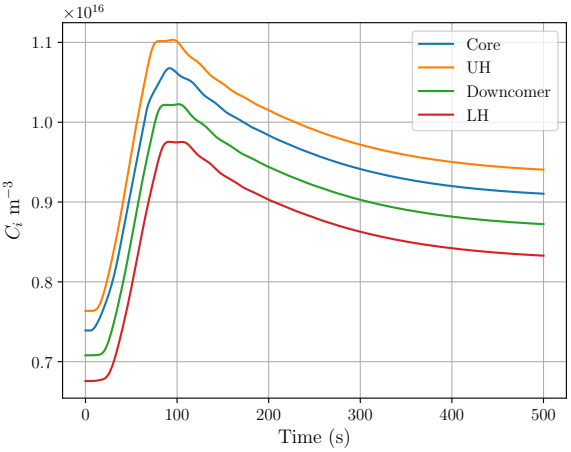

(e) Longest-lived delayed neutron precursors

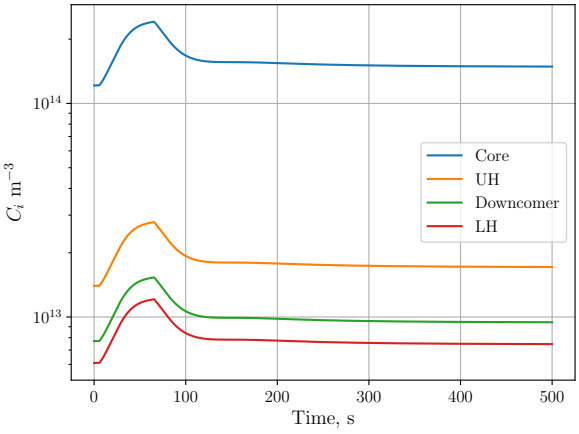

(f) Shortest-lived delayed neutron precursors

Figure 3.6: $ 0.5 ramped reactivity insertion resulting in delayed supercritical transient.

3.2.2 $1.5 Reactivity Step Insertion

As in the previous section, the model was initialised with a steady state power of 8 MW, before a $ 1.5 step reactivity insertion at $t = 5$ s. The core immediately becomes prompt supercritical achieving a peak power of 1.35 GW, 0.3 seconds after the reactivity insertion. Beyond this point, the increase in the magnitude of ρ_T exceeds the reactivity insertion and the power ceases to increase. The timescale of the initial transient is too short for the decay of delayed neutron precursors to make a significant contribution to the reactivity of the system.

The power level then decreases rapidly, dropping below 100 MW just after $t = 6$ s. The power deposited during the initial burst is sufficient to raise the fuel temperature at the centre of the core to just over 1057 K by $t = 6.5$ s.

Between $t = 10$ and 15s, with power around 48 MW, the hot salt from the burst is departing the core and cool fuel salt from the external loop is reentering, resulting in an increase in reactivity (Fig. 3.7c) sufficient to sustain the core at/near criticality for a few seconds. Such an effect has been observed in other models of MSRE [71].

The large number of fissions early in the transient generate delayed neutron precursors in the the downcomer. 4.5 seconds later there is a rapid increase in the concentration ($t \sim 11$ s). This delay corresponds to the residence time of the fuel as it is pumped out to the heat exchanger and back to a power-producing region, bringing with it a large number of precursors from the upper head and shortly after, the core that were generated in the initial fission burst. A similar effect can be observed a few seconds later in the lower head. Flow times between vessel regions are detailed in Appendix A.3. The concentrations of long-lived precursors undergo substantial oscillations for several minutes after the reactivity insertion as they are transported around the primary circuit, decay and are dispersed.

The reentry of hot fuel salt into the vessel and increasing graphite temperature (Fig. 3.7b) drive the total reactivity to its lowest at $t = 31$s.

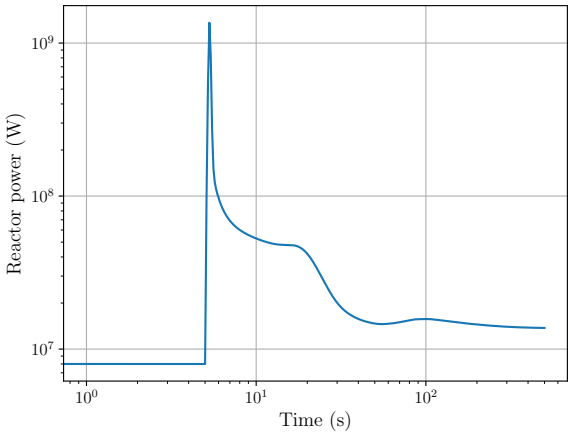

(a) Reactor power

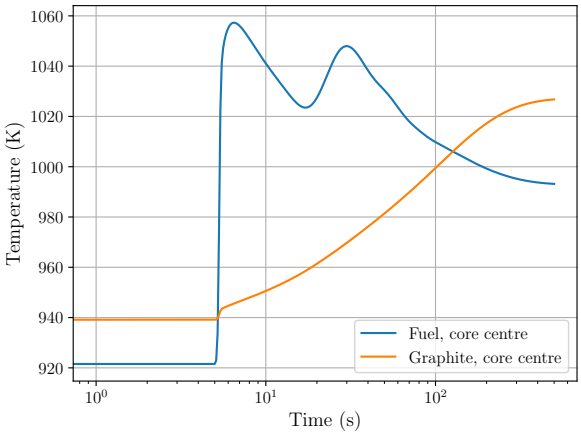

(b) Vessel temperatures

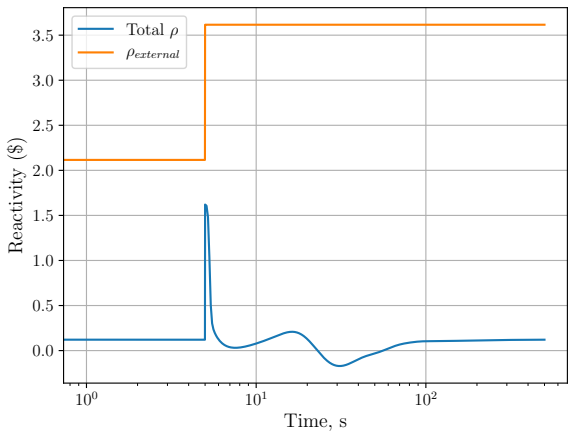

(c) Total and external reactivity contributions

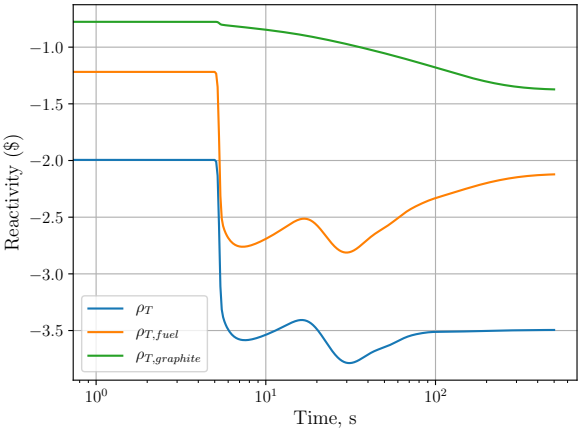

(d) Temperature-dependent reactivity contributions

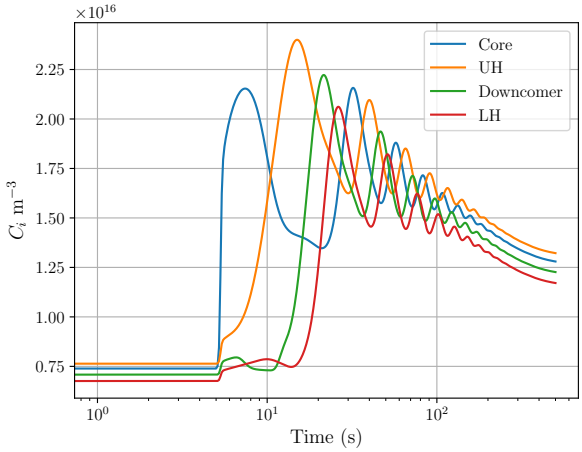

(e) Longest-lived delayed neutron precursors

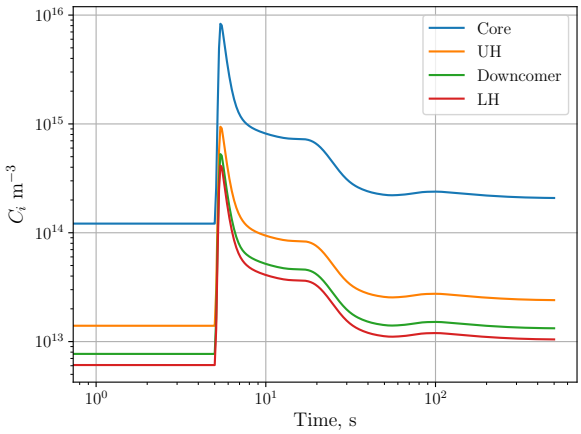

(f) Shortest-lived delayed neutron precursors

Figure 3.7: Overview of \$1.5 step reactivity insertion resulting in prompt supercritical transient.

3.3 Conclusions

This chapter demonstrated that the numerical model could be initialised in a steady state at an operational power level, with physically-plausible distributions of fuel and graphite temperatures, and of delayed neutron precursors. Good agreement with ORNL predictions was shown for the distribution of the delayed neutron source under critical and supercritical conditions with a constant period. The temperature rise across the core was slightly different to that predicted by ORNL for an equivalent core power (10 MW in that case).

The response and feedbacks in the model are as expected under steady state, delayed supercritical and prompt supercritical conditions. Heating and cooling of the fuel salt, plus transport of delayed neutron precursors in the primary circuit leads to positive and negative feedbacks and some oscillatory behaviour. The results and performance of the model were deemed acceptable for use in subsequent investigations.

Chapter 4

Sensitivity Analysis of Step Reactivity Insertion Transients Using the Numerical Model

This chapter examines the sensitivity of the numerical model introduced in Chapter 2 to changes in key physical parameters in order to gain physical insights into the workings of the MSRE system. This understanding will be used to interpret phenomena observed in MSRE experiments and simulations in subsequent chapters.

Monte Carlo (MC) simulation was used to sample distributions of the parameters under investigation, followed by transient simulations with a \$1.5 step reactivity insertion (the same transient as Section 3.2.2). Statistical information was gathered on the reactor power as a function of time; the spatially-averaged graphite and fuel temperatures as a function of time peak power; time of peak power; maximum spatially-averaged core temperature (fuel and graphite); and the times of the maximum average fuel temperature.

Parameters under investigation were sampled independently from a uniform distribution between 50% and 150% of the original value, followed by a 1000s steady state equilibration. Other parameters were kept constant unless otherwise stated. The parameters varied were:

(i) heat transfer coefficient between the fuel and graphite ($h_{f,g}$)

(ii) temperature-dependent reactivity coefficient of the graphite (α_g)

(iii) distribution of fissions in the upper head, lower head and the downcome ($f_{fission}$)

(iv) heat transfer coefficient in the primary heat exchanger ($h_{H.E.}$)

(v) temperature-dependent reactivity coefficient of the fuel (α_f)

(vi) specific heat capacity of the fuel ($C_{p,fuel}$)

The parameters were sampled a minimum of 1024 times unless otherwise stated - in most cases this was sufficient to produce converged distributions. For the purposes of this discussion, the standard deviation of the population of Monte Carlo realisations will be interpreted as a measure of the sensitivity of the system to an uncertain input parameter.

4.1 Sensitivity of Power Profiles Over Time

Figure 4.1 shows the mean and standard deviations of the power over the simulation time for a \$1.5 step reactivity insertion for the reactor at a steady state power of 7.5 MW. Figures 4.2 and 4.3 show the standard deviations with enhanced time resolution near the step reactivity insertion.

From initiation of the transient up to $t = 45$ s, the systems with uncertain $C_{p,fuel}$ and α_f exhibit the largest sensitivity in the power observed, with standard deviations of approx. 500 MW at the time of peak reactor power. The sensitivity of the peak power is less pronounced for the remaining parameters, with standard deviations between 48 MW ($f_{fission}$) and 140 kW ($h_{H.E.}$).

Beyond $t = 45$ s, the sensitivity to uncertain $h_{H.E.}$ grows to become the most influential parameter for the rest of the simulation. The standard deviation of the realisations with uncertain $C_{p,fuel}$ undergoes a decay with damped oscillations reaching $\approx$ 150 kW by $t = 500$s. The standard deviations of $h_{f,g}$ and $f_{fission}$ also exhibit some oscillatory behaviour, the latter less pronounced. The remaining parameters approach asymptotes in a largely monotonic

fashion.

As the majority of the fission power is generated in the fuel, the combination of the rate of heating (dependent on $C_{p,fuel}$) and the reactivity feedback (dependent on α_f) will strongly govern the feedback via the fuel temperature and nuclear average temperature, T_f^* (see Eq. 2.8) during the early part of the transient.

On the second to minutes timescale, it is possible for heat transfer through the heat exchanger, heat transfer between fuel and graphite, and the reactivity feedback of the graphite to exert an effect. As the system settles onto a new equilibrium state at the longest timescales, the core power must equal the power rejected through the heat exchanger. As this power rejection is dependent on $h_{H.E.}$, changes to this parameter will influence the equilibrium power (note the increased uncertainty in the power denoted by increased standard deviation in Fig. 4.1d and Fig. 4.2 after $t = 30$ s). Controlling heat rejection via the secondary circuit was used in practice as a means of controlling core power when above 1 MW in the Molten Salt Reactor Experiment [2].

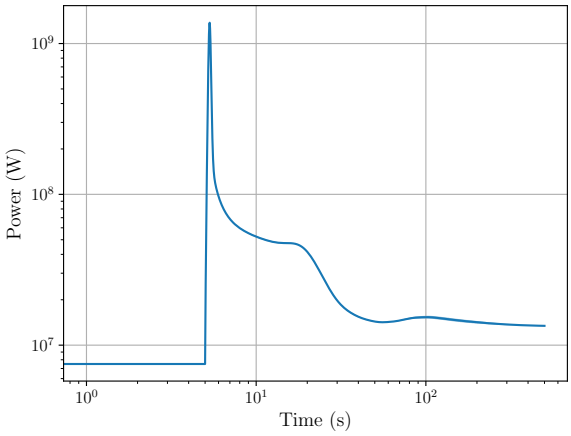

(a) $h_{f,g}$

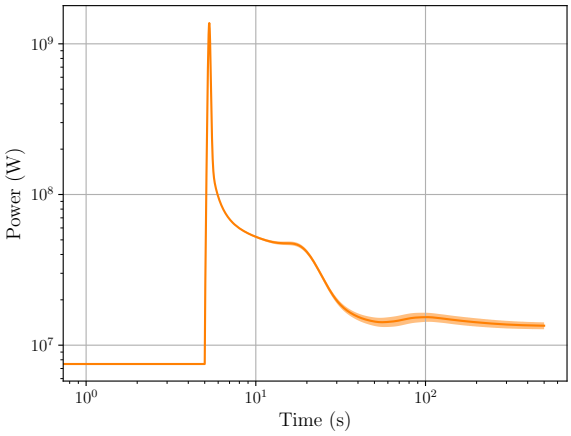

(b) α_g

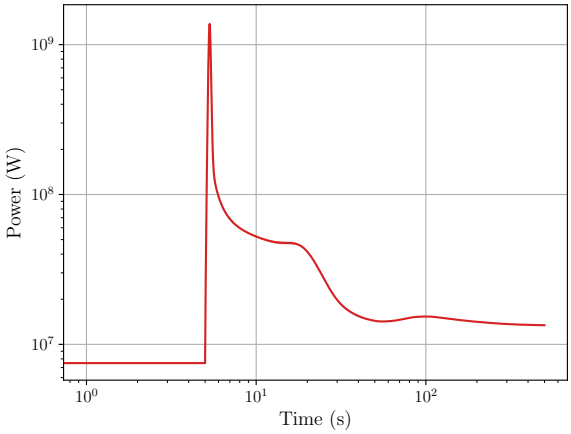

(c) $f_{fission}$

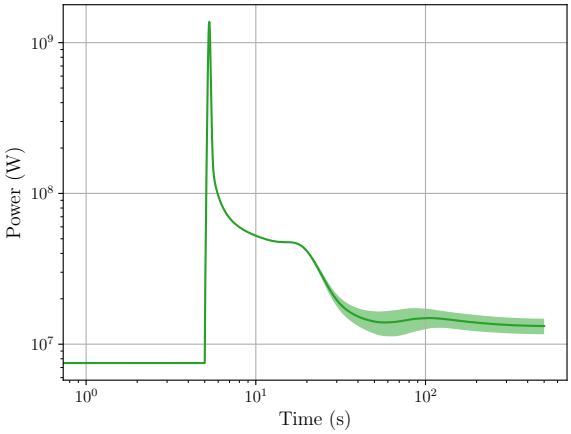

(d) $h_{H.E.}$

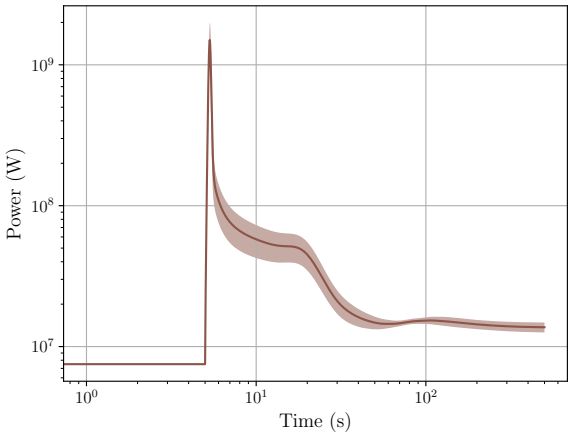

(e) α_f

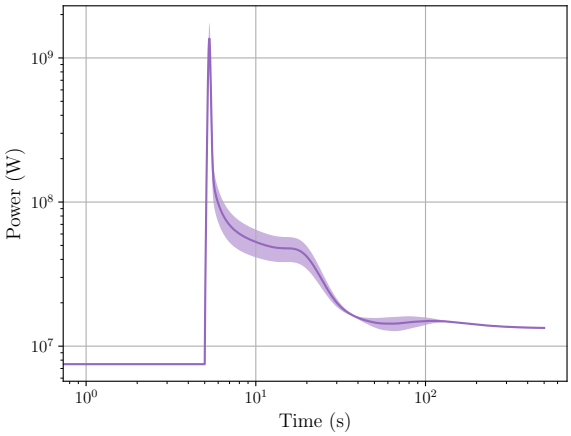

(f) $C_{p,fuel}$

Figure 4.1: Mean power profiles (bold lines) for transients performed after Monte Carlo sampling on uncertain model parameter distributions. Standard deviations ($\pm 1\sigma$) shaded.

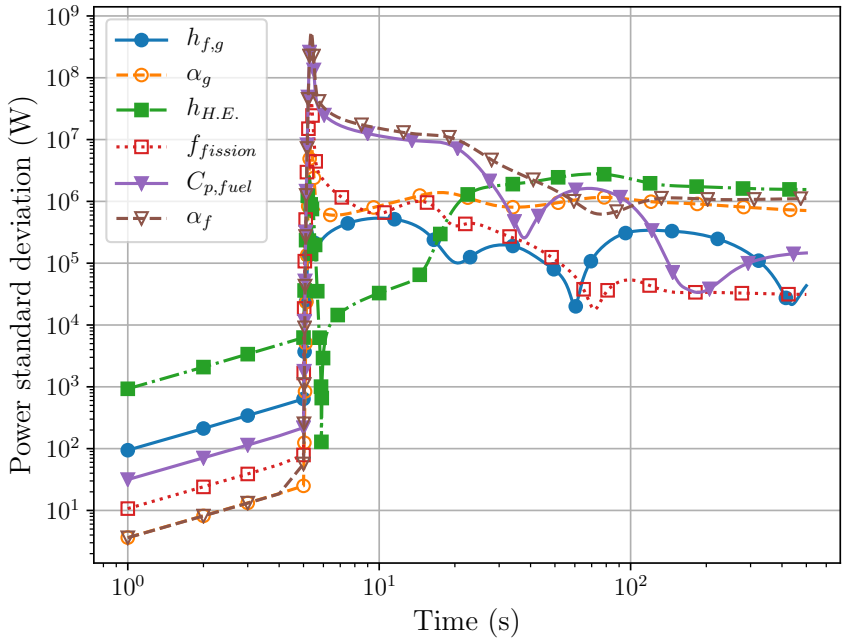

Figure 4.2: Standard deviations of power profiles for each uncertain parameter over time.

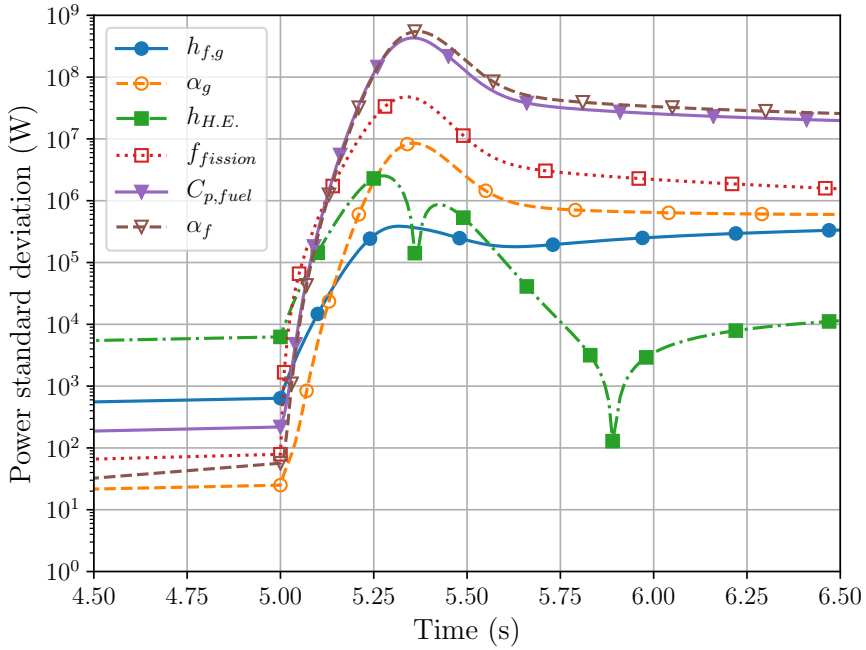

Figure 4.3: Standard deviations of power profiles in the first 2.5 seconds after initiation of the transient.

4.2 Sensitivity of Spatially-Averaged Core Temperatures Over Time

The sensitivity of the spatially-averaged core temperatures to variations in the parameters was then investigated. Figures 4.4 and 4.5 show the means and standard deviations of the spatially-averaged fuel temperature over the course of the MC simulations.

Figures 4.6 and 4.7 show the corresponding means and standard deviations of the spatially-averaged graphite temperatures through the MC simulations.

4.2.1 Spatially-Averaged Core Fuel Temperature

Prior to the initiation of the transient, the initial sensitivity to changes in $h_{H.E.}$ is much greater than for the other parameters. This is a consequence of the steady state calculation at fixed power to produce a critical initial condition. As discussed in Ch. 3, under steady state conditions the core power must be equalled by the power rejected through the heat exchanger. If $h_{H.E.}$ is reduced, then the average fuel temperature must increase in order to maintain the rejection power, hence the high observed standard deviation of the initial average core fuel temperature. Similarly, at the end of the simulations as the reactor is settling towards a new equilibrium state post-transient, it is again most sensitive to the heat transfer across the primary heat exchanger (Fig. 4.4d).

Upon the reactivity insertion at $t = 5$ s, the standard deviation of the α_f and $C_{p,fuel}$ runs jump sharply, and then oscillate in the first 100s of the simulation. Oscillations with uncertain α_f have a period approx. equal to the primary circuit recirculation time. This is consistent with the power burst depositing energy in the fuel, creating a hot slug which travels through the primary circuit, exerting its reactivity effects primarily through α_f. In this period, the standard deviation of the runs with an uncertain heat exchanger heat transfer coefficient also rises slightly.

Correlated behaviour between α_f and $C_{p,fuel}$ is to be expected as both may influence, and are dependent on, the reactor power. Variation in $C_{p,fuel}$ will affect the magnitude of fuel temperature oscillations in the primary circuit while variation in $h_{H.E.}$ and α_f will influence the

rate of decay of these temperature fluctuations. For example, a higher value of $h_{H.E.}$ will cause fuel in the heat exchanger to tend to the temperature of the secondary circuit more rapidly, while a high value of α_f would result in a larger negative value of ρ_{T_f} leading to reduced reactor power and reduced heating of the fuel as it passes through the core.

By $t = 50$ s, the temperature of the core is steadying due to dispersive effects in the primary circuit and the sensitivity to α_f drops significantly from its peak value. The standard deviations of the $h_{H.E.}$ and $C_{p,fuel}$ are no longer fluctuating by $t = 100$s.

Due to the limited rate at which heat can be transferred between fuel and moderator, MC runs with uncertain α_g take longer to diverge. The standard deviation of these realisations plateaus by $t = 200$s.

The sensitivities to changes in the distribution of $f_{fission}$ and $h_{f,g}$ remain low throughout the simulations. This may be due to the relatively low proportion of fission power deposited in the graphite (on average less than seven percent). The standard deviation of runs with uncertain $h_{f,g}$ reaches a maximum around $t = 100$ s and a minimum around $t = 400$ s before increasing slightly towards the end of the simulations.

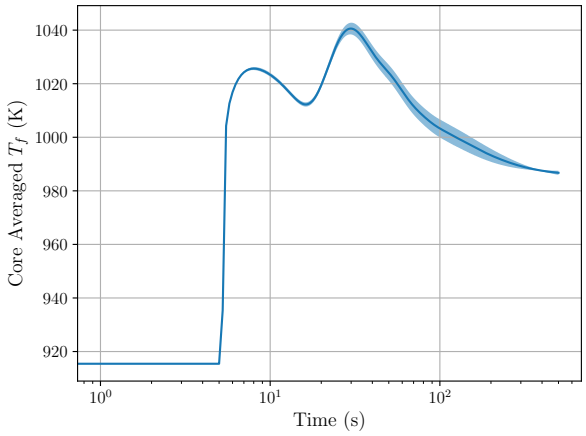

(a) $h_{f,g}$

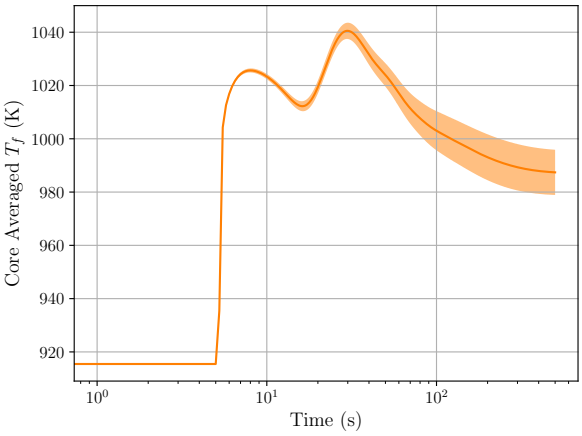

(b) α_g

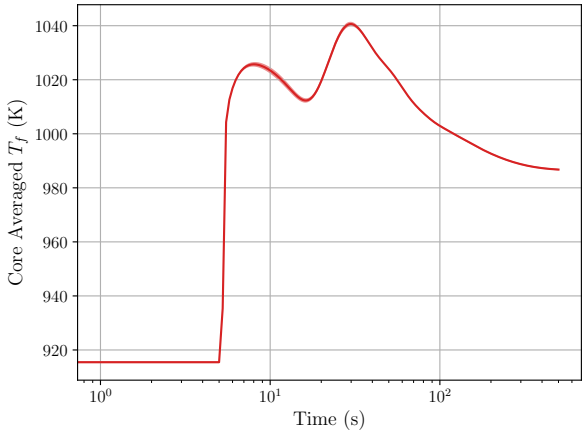

(c) Fission distribution

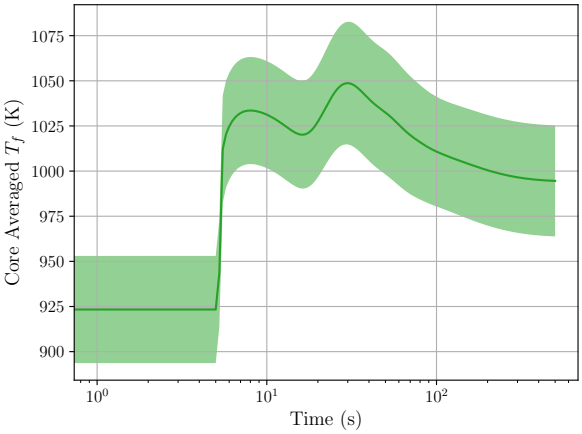

(d) $h_{H.E.}$

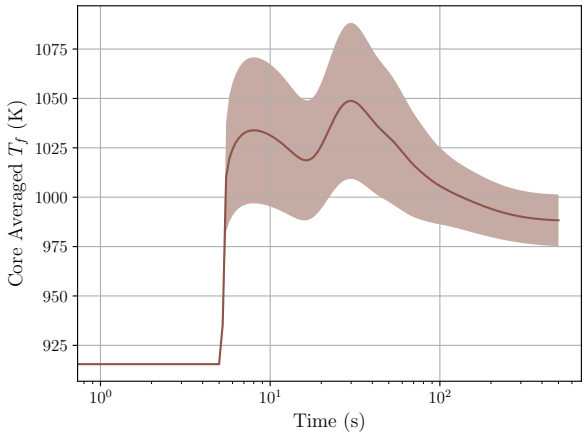

(e) α_f

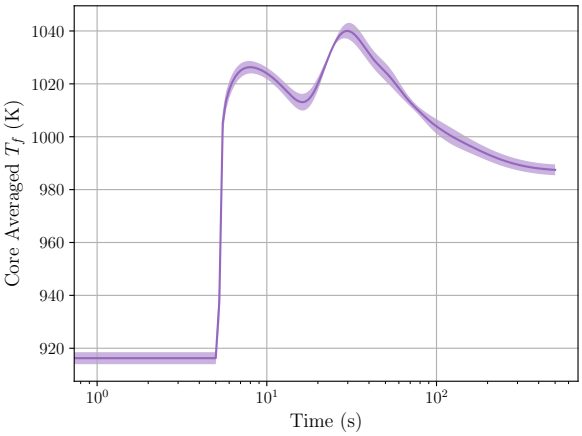

(f) $C_{p,fuel}$

Figure 4.4: Mean of spatially-averaged core fuel T profiles for each set of Monte Carlo runs with $\pm 1\sigma$ shaded.

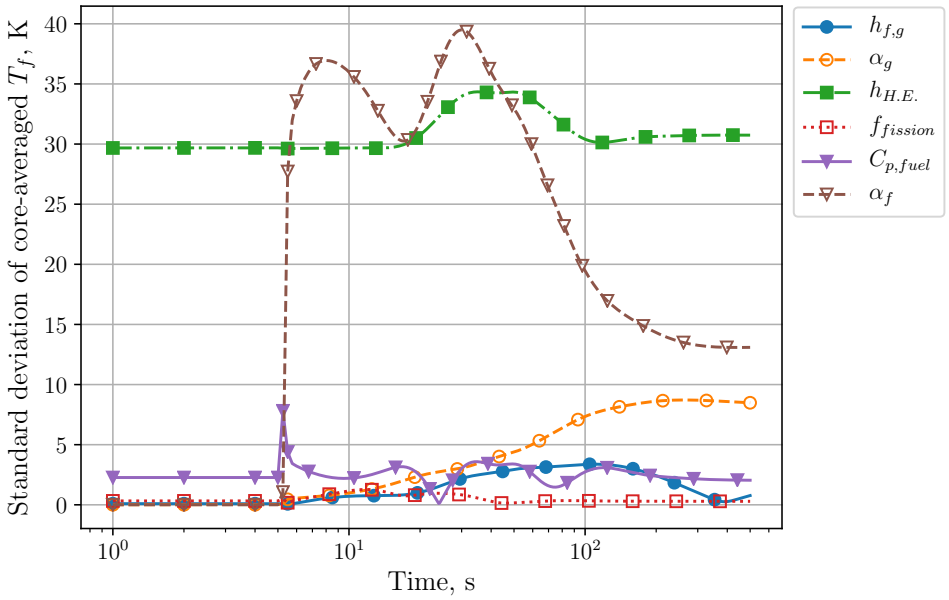

Figure 4.5: Standard deviations of mean core fuel T profiles for each uncertain parameter over time.

4.2.2 Spatially-Averaged Graphite Temperature

The sensitivity of the realisations to $h_{H.E.}$ is consistently the highest of the parameters tested with only a small increase occurring after the prompt supercritical transient. This supports the previous discussion that the heat exchanger is highly influential in the steady state but exerts little influence on the average graphite temperature during a step reactivity transient. The distribution of fissions in the core exerts little influence on the average graphite temperature, as evidenced by the low standard deviation over the entire run time (Figure 4.6).

Sensitivity to changes in α_f and α_g rises after the reactivity insertion, with the latter taking longer. The effect of changes to the graphite temperature feedback manifests itself later due to the limited rate of heat transfer between the fuel and graphite in the core (see Figure 4.7).

Sensitivity to changes in $h_{f,g}$ fluctuates through the simulation, being a prominent parameter at the beginning and end of the simulations. At steady state powers the average temperature of the graphite is expected to be higher than the fuel which will drive conduction across the interface - this explains the sensitivity to $h_{f,g}$ near the end of the simulation as the reactor

approaches a new steady state (a core average ΔT of approx. 25 K is observed at $t = 500$s - see also steady state temperature distributions in Fig. 3.1).

Figure 4.8 aids interpretation of the $h_{f,g}$ Monte Carlo sampling data. It shows the mean (among MC realisations) spatially-averaged graphite temperature through the simulation (with shaded standard deviations), in addition to the deterministic runs conducted with the upper and lower bounds of $h_{f,g}$. With the lower bound value, the initial steady-state graphite temperature is higher as the heat deposited in the graphite can only be transferred to the fuel at a low rate. After the reactivity insertion, the rate of T_g increase is lower than the mean (among MC realisations) as hot fuel cannot easily transfer energy to the graphite in order to raise the average T_g.

For the deterministic simulation with the upper bound of $h_{f,g}$, increased heat transfer between the fuel and graphite results in an initial average graphite temperature which is closer to that of the fuel (lower than the Monte Carlo mean). The average graphite temperature rises quickly but settles on a lower value than the low bound $h_{f,g}$ simulation. In a similar fashion to the initial condition, fuel and graphite temperatures are closer in this new quasi-steady state condition than the low bound $h_{f,g}$ case.

The times at which the average temperature for the bounding cases cross over ($t \sim 40$ s and 200 s) correspond to the times of minimal variance in the MC populations in Fig. 4.7.

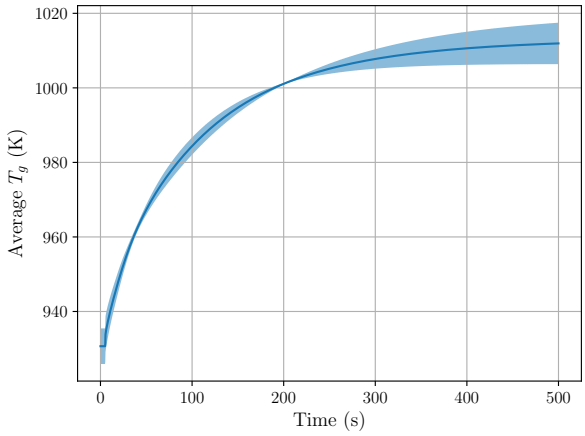

(a) $h_{f,g}$

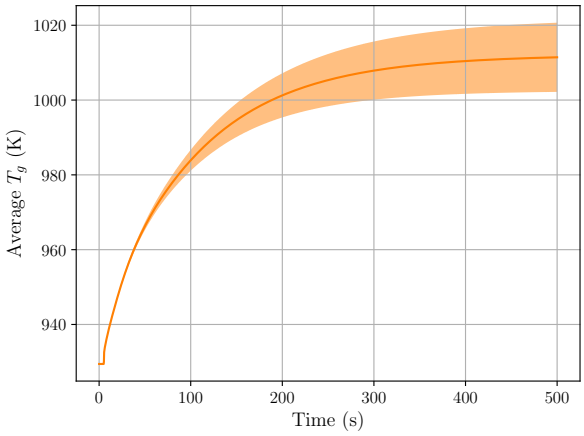

(b) α_g

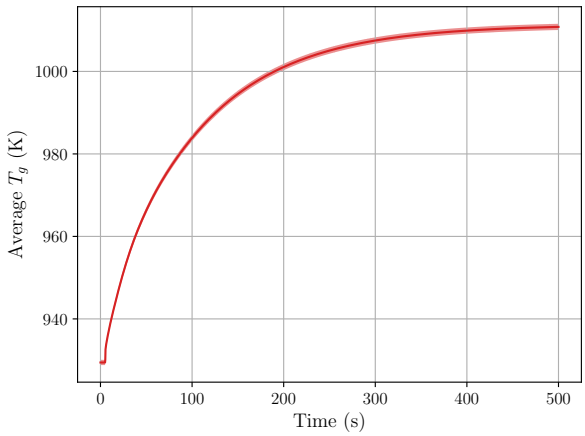

(c) $f_{fission}$

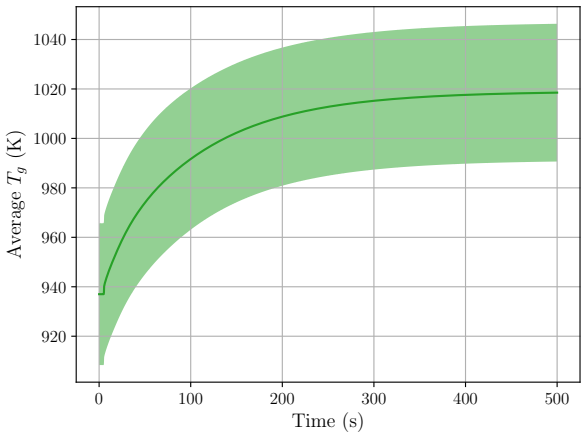

(d) $h_{H.E.}$

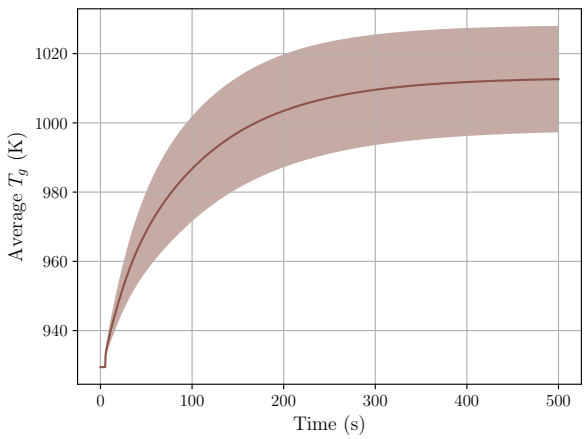

(e) α_f

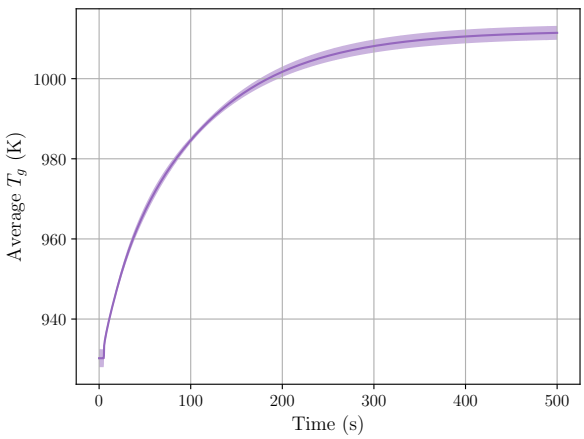

(f) $C_{p,fuel}$

Figure 4.6: Mean graphite T profiles for each set of Monte Carlo runs with $\pm 1\sigma$ shaded.

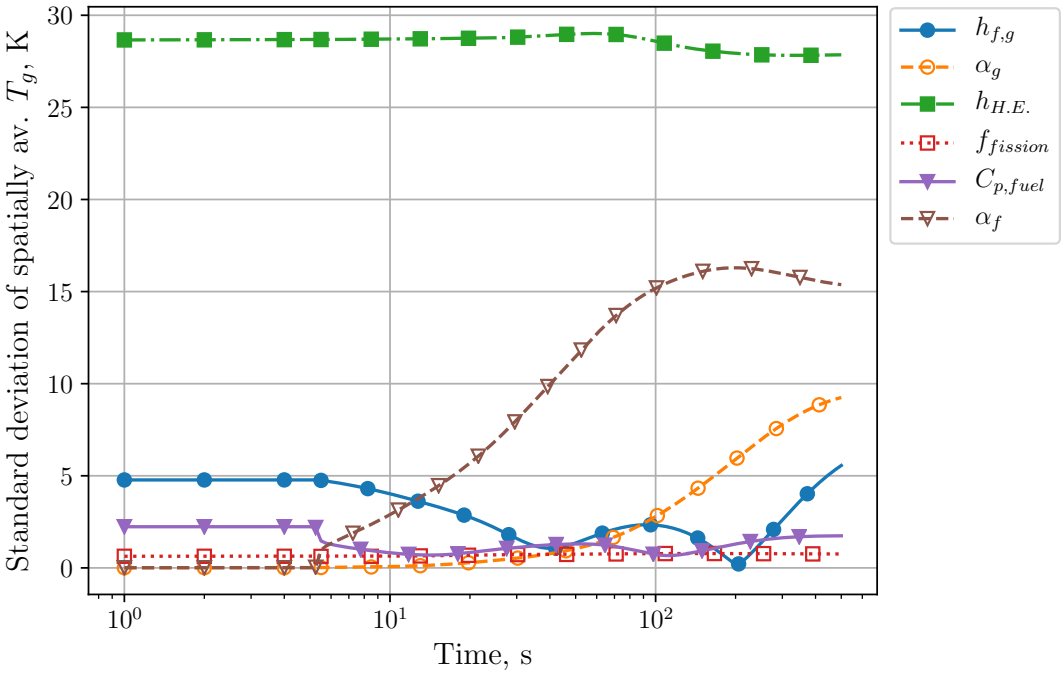

Figure 4.7: Standard deviations of mean graphite T profiles.

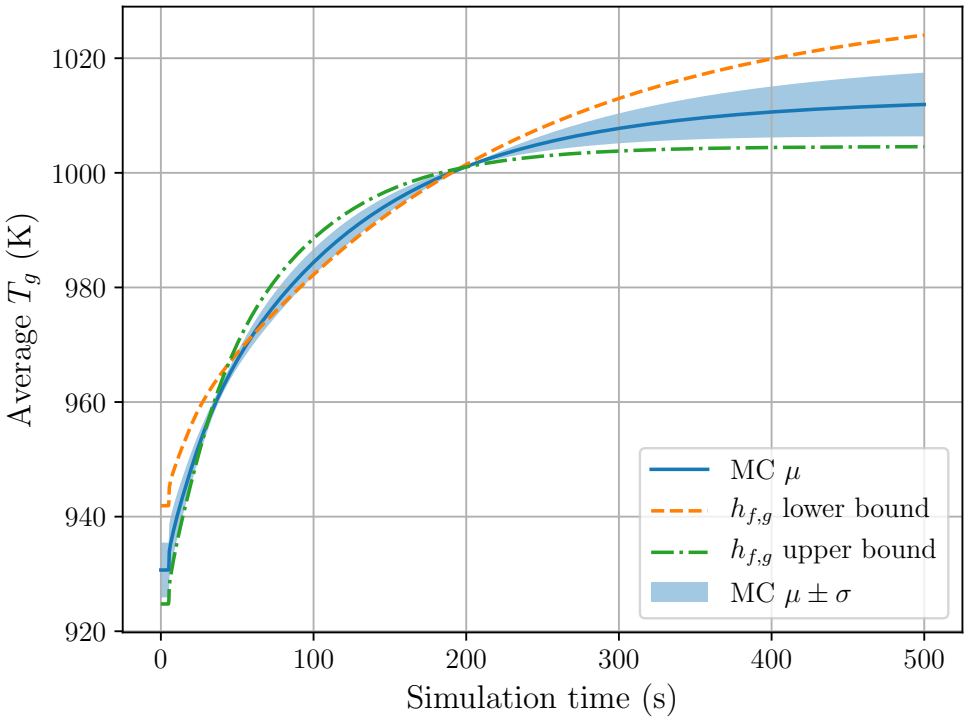

Figure 4.8: Comparison of upper and lower bounds for $h_{f,g}$ with Monte Carlo average ($\pm 1\sigma$ shaded).

The standard deviation in the simulations with uncertain $C_{p,fuel}$ drops sharply just after the time of reactivity insertion ($t = 5$s, see Fig. 4.7). Subsequent investigation of the bounding cases (Fig. 4.16e) shows the core-averaged graphite temperatures converging (particularly the lower bound and mean cases) leading to the drop in observed variance. A case with a lower average T_g prior to the transient would permit the power to rise further before negative reactivity stopped it, however the integrated energy of this burst would raise the temperature of the graphite faster. This is observed in Fig. 4.16e, where the lower bound and mean case average T_g curves cross over at $t = 10$ s.

4.3 Sensitivity of the Peak Power

Figures 4.9 through 4.14 use Knuth's rule [72] implemented as part of the Astropy package [73] for optimal fixed-width binning for the histograms representing each data set.

Figure 4.9 shows the distributions of peak powers in response to the step reactivity insertion. The mean peak power is 1.375 GW. The system is most sensitive to changes in α_f and $C_{p,fuel}$, with moderate sensitivity to changes in the distribution of fissions. Changes to these parameters will alter the rate of temperature change in the vessel regions with the strongest reactivity feedback (via $C_{p,fuel}$ and $f_{fission}$), and the magnitude of that reactivity feedback (via α_f), and consequently the amount of time available for power increase before ρ_T compensates for the step reactivity insertion, ending the rise in power - see Equations 2.7, 2.8 & 2.9 in Section 2.2.

Minimal sensitivity is exhibited to variations in α_g, $h_{H.E.}$ and $h_{f,g}$ (shown with an enlarged scale in Fig. 4.10). The timescales over which heating of the graphite, fuel-graphite heat transfer and heat transfer at the heat exchanger occur are much longer than the duration of the transient, hence their small influence on peak power which occurs only a fraction of a second after the step reactivity insertion.

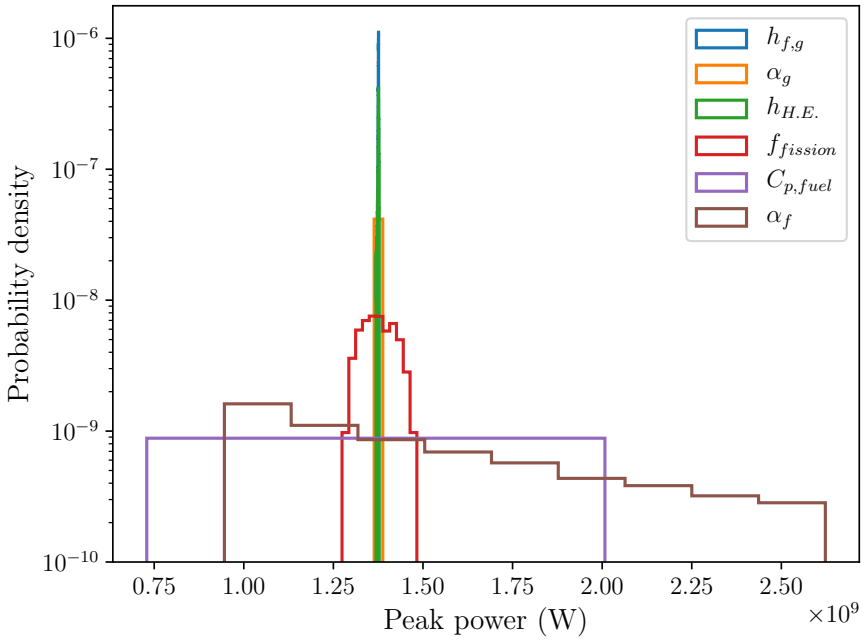

Figure 4.9: Sensitivity of the peak core power to variations in system parameters.

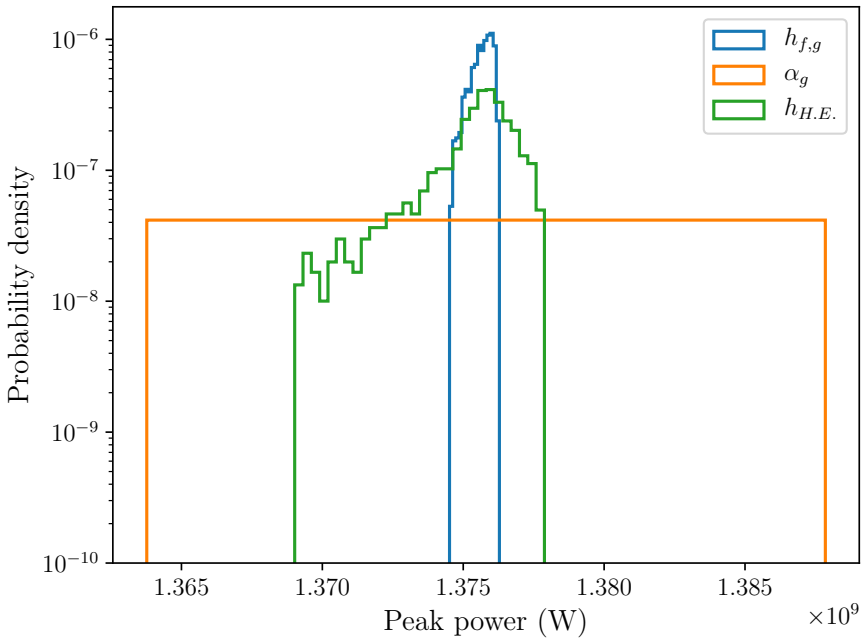

Figure 4.10: Expanded power scale showing the distributions with low standard deviations.

4.4 Sensitivity of the Time-to-Peak Power

A similar pattern of sensitivities is observed for the distributions of the time required to reach maximum power (Figure 4.11). Changes to $C_{p,fuel}$ and α_f exhibit the greatest effect. The minimum time to peak power is 0.28 s after the initiation of the transient, with a maximum time of 0.352 s. The distributions for uncertain $h_{f,g}$, α_g, $h_{H.E.}$ and $f_{fission}$ have much lower variances and are clustered around $t = 5.316$ s. As discussed in Section 4.3, only those parameters connected to physical processes operating on a short timescale may exert a significant effect on the time of peak power as it occurs soon after the reactivity insertion.

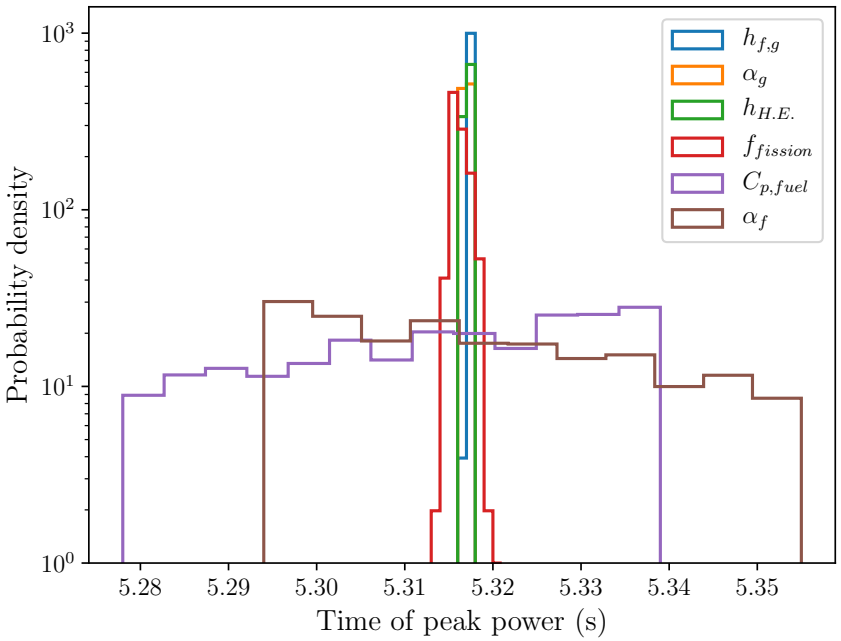

Figure 4.11: Distribution of times at which peak power occurs.

4.5 Sensitivities of the Maximum Spatially-Averaged Core Temperatures

Figure 4.12 shows the distributions of the maximum spatially-averaged temperatures in the core. The general trends of sensitivity are similar between fuel and graphite, with α_f and $h_{H.E.}$ exerting the greatest influence over the maximum average temperatures. Several of the distributions are between 100 and 150 K wide. The distributions of the other parameters are located closer to the mean, around 1040 K.

The means of the maximum temperatures in the fuel exceed those of the maximum temperatures in the graphite - this is in contrast to the steady state distributions discussed in Section 3.1, where the graphite is hotter than the fuel. The times of maximum fuel temperature all occur approximately one circulation time after the initiation of the transient (Fig. 4.13). This may be due to the energy deposited during the plateau in power observed between $t = 10$ and 20 s, where the reactor is briefly delayed supercritical in the deterministic case (representing the

average of the sampled MC distribution).

Large variability in the maximum average temperatures is observed in the $h_{H.E.}$ MC runs - this parameter was shown to exert little influence on the peak power (see Section 4.3), instead strongly affecting the steady state conditions. Examination of the bounding $h_{H.E.}$ values in Fig. 4.17 show that a high initial average temperature will result in a high peak average temperature.

The times of maximum graphite temperature are consistently recorded at the end of the 500 s simulations, for all the parameters under investigation (data not shown).

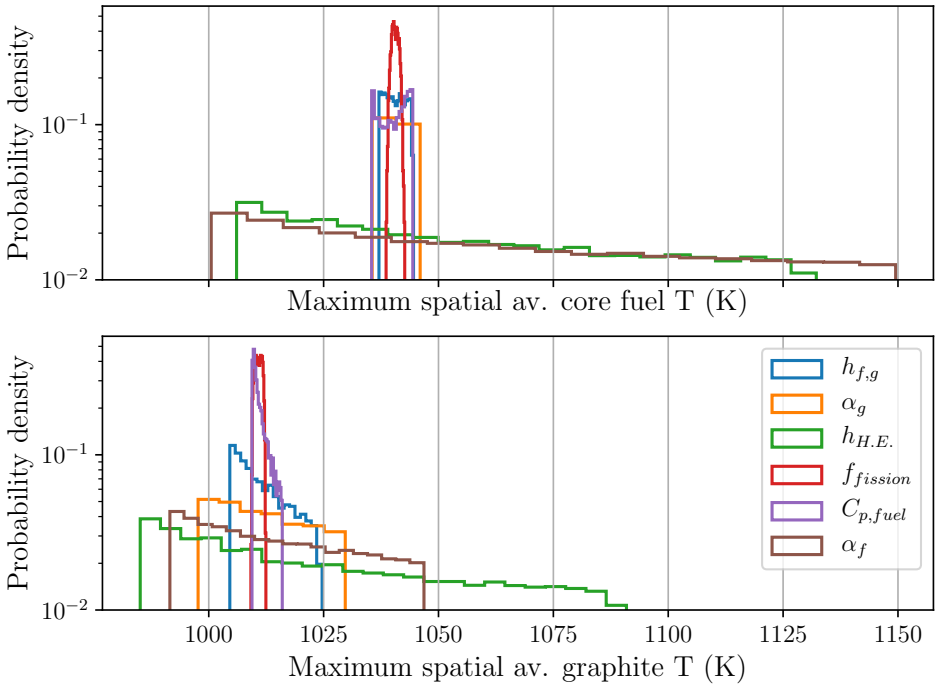

Figure 4.12: Distribution of the temporal maximum of spatially-averaged core temperatures. Number of MC realisations = 4096.

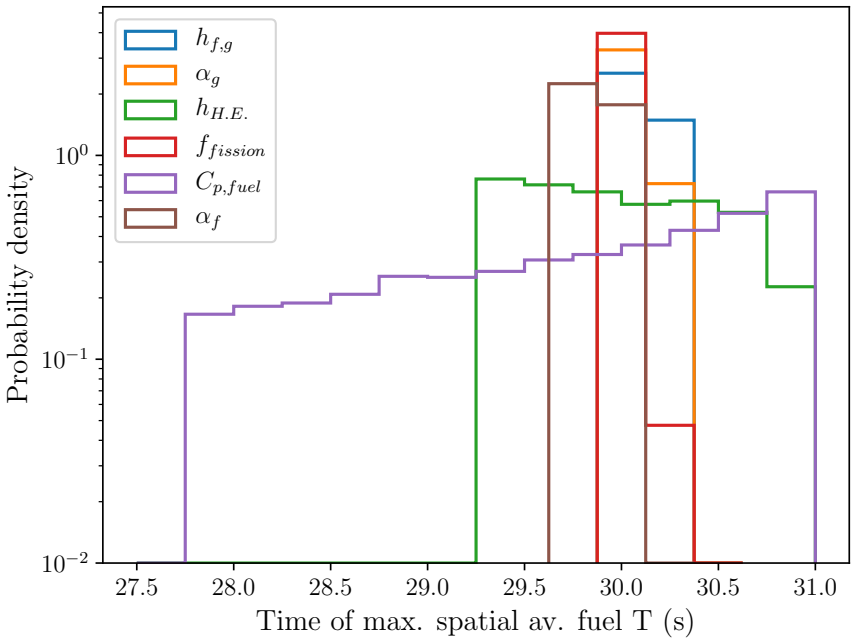

Figure 4.13: Distribution of times of maximum spatially-averaged core fuel temperatures. Number of MC realisations = 4096.

Closer examination of the distributions close to the mean (Fig. 4.14) reveals a bimodal $C_{p,fuel}$ distribution. In order to investigate this feature, a series of deterministic cases were simulated, incrementing $C_{p,fuel}$ from the lower bound (50 % of original $C_{p,fuel}$ value) to the upper bound (150%). The maximum average fuel temperature for these cases are plotted in Fig. 4.15. In the first portion of the sampled distribution, the rate of change of maximum temperature with respect to $C_{p,fuel}$ is negative leading to a buildup in probability density at the around 1036 K in Figures 4.12 and 4.14.

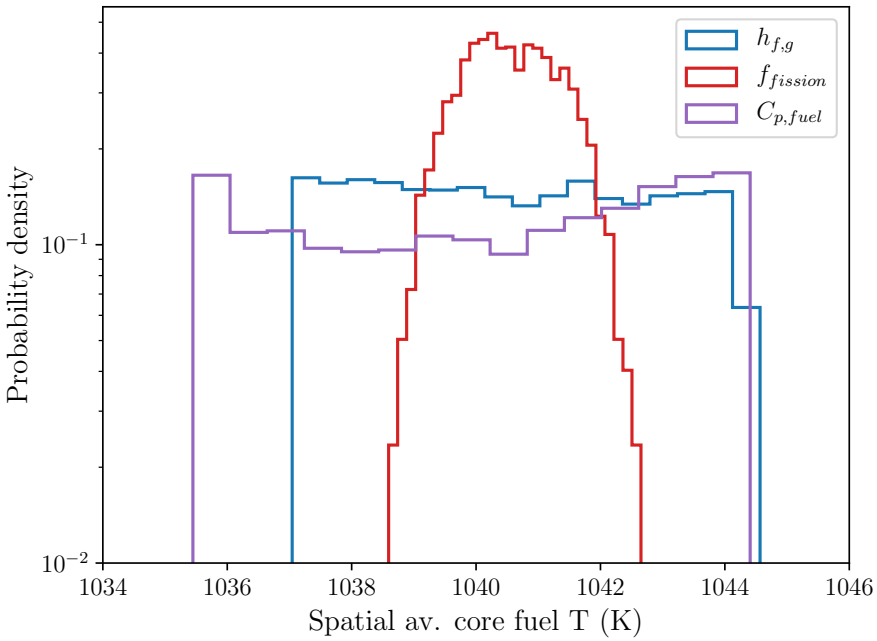

Figure 4.14: Distribution of maximum of core averaged fuel temperatures for $h_{f,g}$, $f_{fission}$ and $C_{p,fuel}$ sampling. Number of MC realisations = 4096.

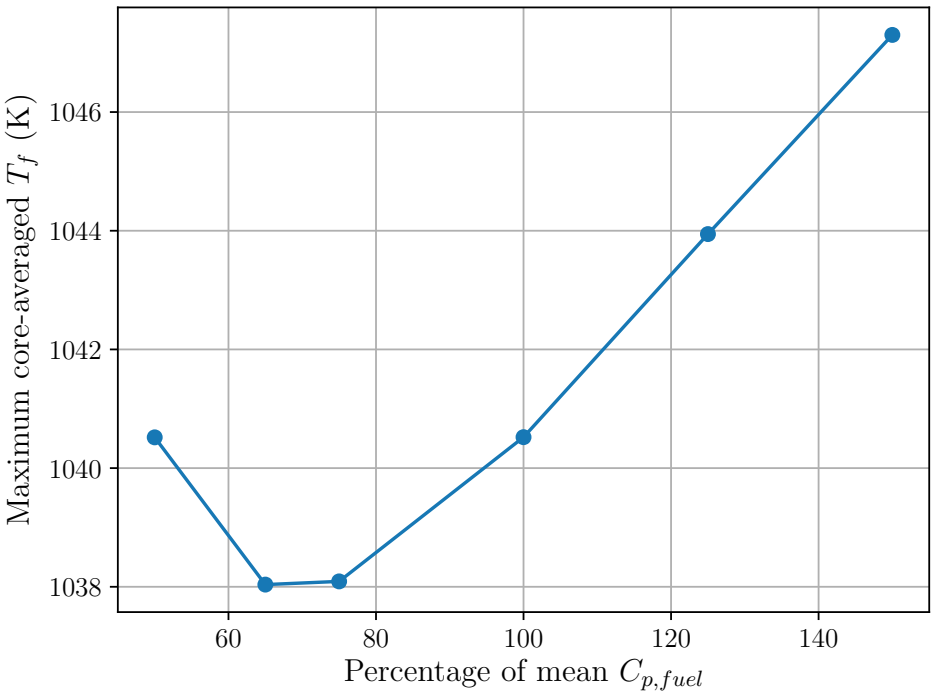

Figure 4.15: $C_{p,fuel}$ vs. maximum core average fuel temperature in the range sampled in the MC simulations.

Power, core-averaged T_f and reactivity contributions over time provide further insight into reactor behaviour with uncertain $C_{p,fuel}$. Figure 4.16 displays this data for the cases at the two bounds and the mean $C_{p,fuel}$ case for the \$1.5 step transient. For the lower bound case, reduced core heat capacity results in a larger increase in average temperature and consequently larger negative reactivity contribution. This causes the reactor power to drop lower than the mean case, to around 30 MW in the $t = 10$ to 20 s time frame.

For the upper bound case, temperature rise in the core is more limited leading to a smaller increase in negative thermal feedback. Core power remains high between $t = 10$ and 20s (around 60 MW) resulting in a higher maximum average temperature at $t \sim 30$ s due to the deposited power up to this time. Simultaneously, the maximum negative temperature-dependent reactivity contribution is observed for the fuel, and ρ_{T_g} at a greater negative magnitude than the $C_{p,fuel}$ mean and lower bound cases.

This increased negative reactivity feedback causes the power (and consequently the average core

temperature) to drop more rapidly towards $t = 60$ s, leading the upper bound case to cross over the mean and lower bound cases. Generally the system appears more strongly damped at lower values of $C_{p,fuel}$ due to the greater temperature increases and greater negative value of ρ_T.

The relationship between the $C_{p,fuel}$ cases is similar in the initial steady state prior to the reactivity insertion and the final quasi-steady state at $t = 500$ s, that is a higher average core temperature for a lower specific heat capacity. This is a function of the temperature increase as the fuel passes through the core; and of the temperature decrease during flow through the primary heat exchanger. Reduced $C_{p,fuel}$ will result in a greater temperature increase in the core, but also a more rapid cooling at the heat exchanger. There is a limit to the latter effect as the primary circuit cannot become colder than the secondary circuit, however this difference in ρ_T may still be sufficient to cause the reactor to become prompt supercritical ($\Delta\rho_T = \$1.995$ for uncontrolled cooling of a reactor at $P = 7.5$ MW to a uniform 825 K, the reference temperature in these simulations).

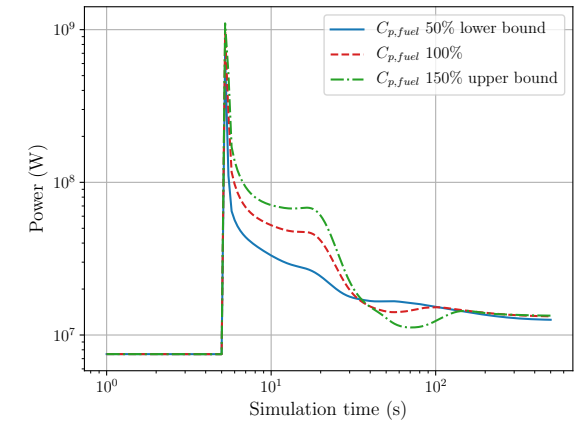

(a) Power

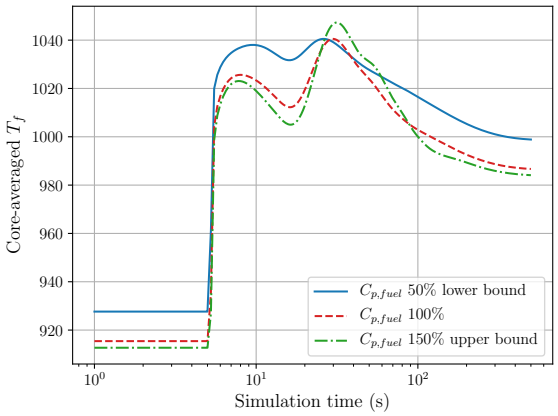

(b) Core-averaged T_f

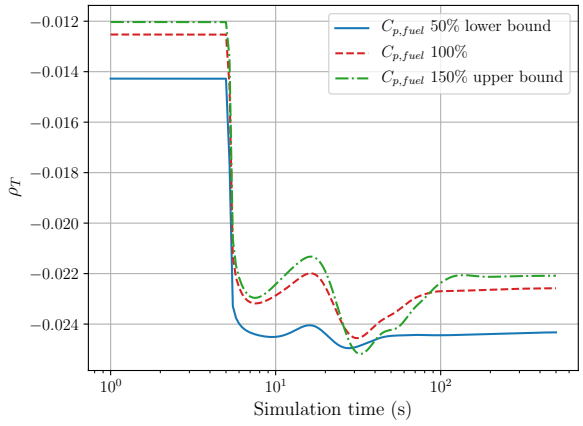

(c) Temperature-dependent reactivity

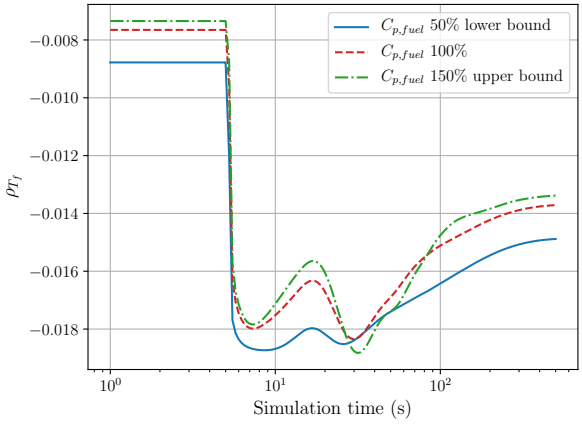

(d) Fuel T-dependent reactivity

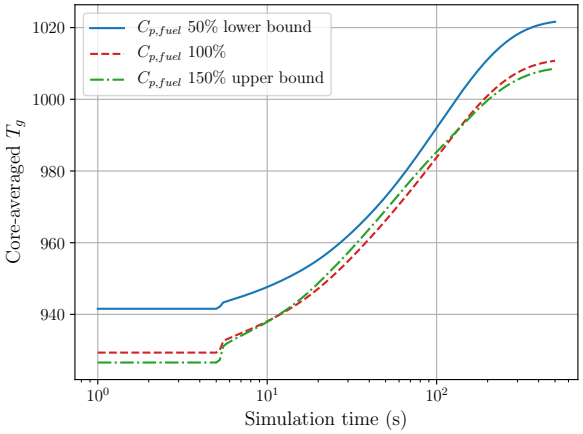

(e) Core-averaged T_g

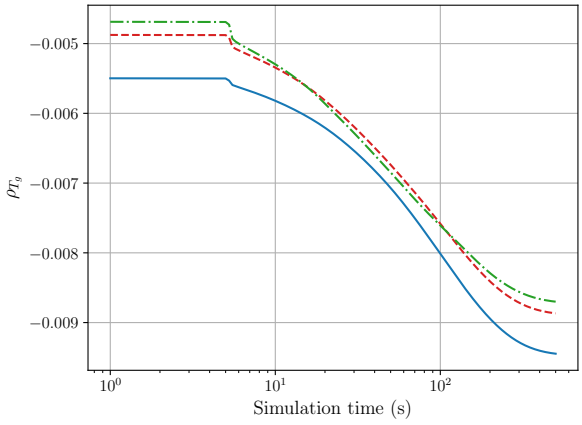

(f) Graphite T-dependent reactivity

Figure 4.16: Power and reactivity contributions for lower bound, mean and upper bound $C_{p,fuel}$ runs.

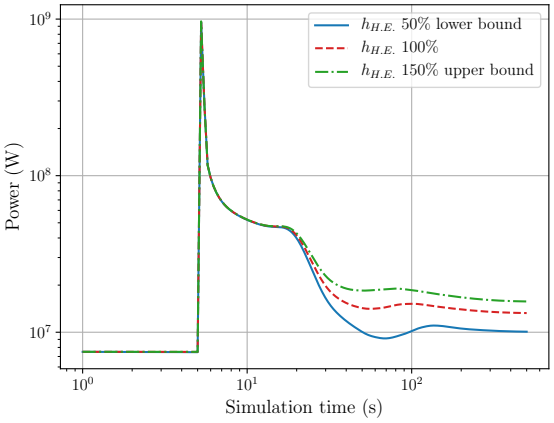

(a) Power

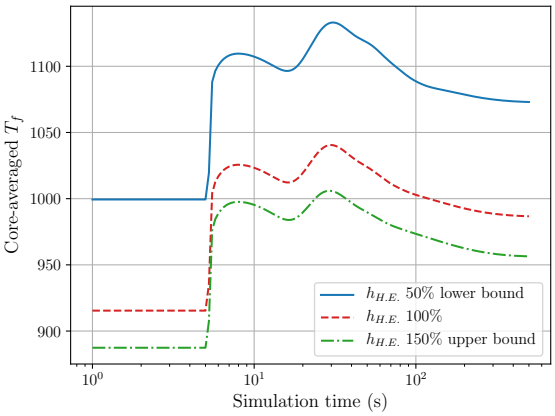

(b) Core-averaged T_f

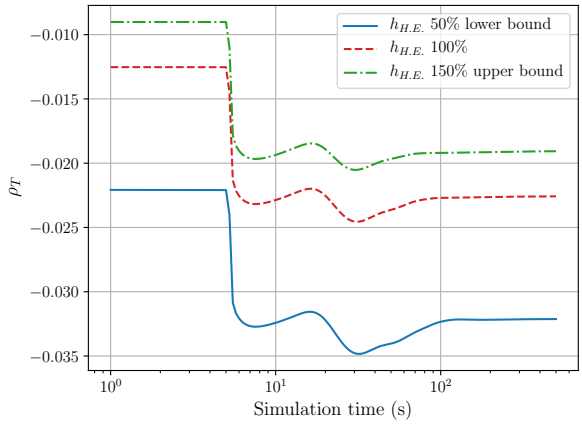

(c) Temperature-dependent reactivity

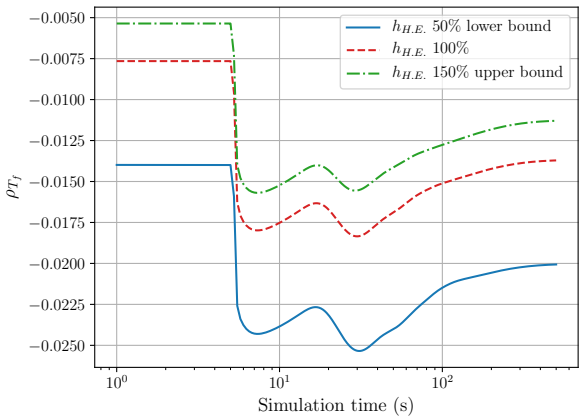

(d) Fuel T-dependent reactivity

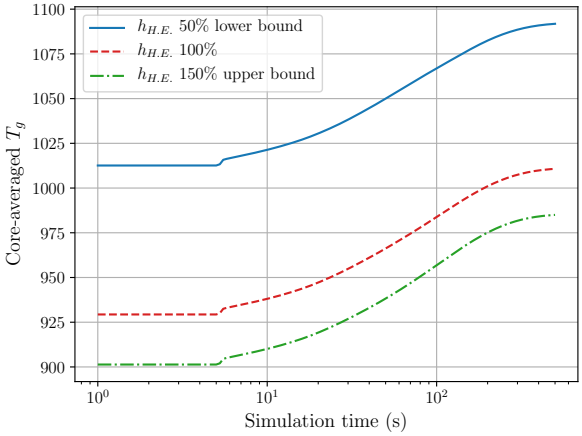

(e) Core-averaged T_g

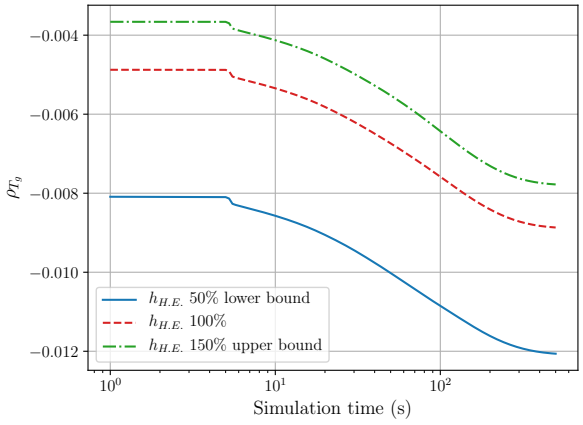

(f) Graphite T-dependent reactivity

Figure 4.17: Power and reactivity contributions for lower bound, mean and upper bound $h_{H.E.}$ runs.

4.6 Summary of Sensitivity Analyses

This chapter has explored the sensitivity of the numerical model to changes in physical parameters using MC sampling of the parameter distributions. In addition, the value of deterministic runs for exploring features in distributions or oscillating standard deviations has been shown. The deterministic simulations were essential for the correct interpretation of the statistical data obtained from the MC simulations, as evidenced by investigations into the effect of $h_{f,g}$ on the average graphite temperature, and the effect of $C_{p,fuel}$ on the average core fuel temperature.

Some parameters exert the greatest influence at or near steady state conditions, particularly $h_{H.E.}$. Other parameters will become influential under transient conditions, particularly when the power (and consequently the core temperatures) are changing on a short timescale, for example α_f and $C_{p,fuel}$ influencing the temperature-dependent reactivity. Differences between the temperature of core fuel and graphite will permit changes in $h_{f,g}$ and α_g to influence system behaviour. Changes to the value of α_f may influence both steady state conditions and transients. Parameters relating to physical processes occurring on longer timescales (due to limited rates, e.g. $h_{f,g}$ or remote location, e.g. $h_{H.E.}$) exert only limited influence during fast transients.

Chapter 5

Frequency Response and Stability with Increasing Reactor Power

This chapter explores the frequency response and stability of the MSRE. In general, frequency and stability modelling is an important part of the safety analysis of nuclear power plants [74]. The frequency response of the numerical model described in Chapter 2 is compared against experimental data obtained during the MSRE programme. A turbulent dispersion parameter is proposed to account for mixing in the primary circuit and its effect on a frequency response feature related to fuel recirculation is discussed. Additionally, a semi-analytical model of the system is constructed as a part-verification of the frequency response, including the capability for sensitivity analysis for changes to key model parameters. The semi-analytical model is also used to perform stability analysis of the MSRE-like system.

5.1 Definitions & Motivation

The time dependent behaviours of a circulating fuel system with feedbacks are well suited to investigation using the system's response in the frequency domain. The frequency response consists of two parts - the gain, defined as the ratio of the output to input amplitude signals; and the phase shift between the input and output signals. These can provide useful information on the physics of the system and stability analysis.

For the purposes of this discussion, the gain will be defined as the fraction by which the power increases from the average in response to a driving reactivity signal. In practice it is a measure of the extent to which the power will fluctuate in response to some some reactivity signal at a certain frequency. This is of engineering interest as a high gain could lead to violation of temperature or pressure limits in the system.

The phase shift is calculated from the time difference between the peak reactivity and peak power, divided by the period of the oscillating reactivity signal. It is a measure of the lag in system response with respect to the driving signal. Both gain and phase shift are functions of the physical feedback processes occurring in the reactor system and can provide insights into system stability. Stability analysis is discussed further in Section 5.9.

The gain is calculated from the following equation,

$$G(\omega) = \frac{\Delta P}{P_0 \Delta \rho} \tag{5.1}$$

where $G(\omega)$ = gain [dimensionless] at angular frequency ω [rad s^{-}1], ΔP = difference in power from average to peak [W], P_0 = average power in final period and $\Delta\rho$ = driving reactivity amplitude [dimensionless] (equal to 1.25×10^{-4} in this case).

The phase shift is calculated using the following equation,

$$\phi(\omega) = \frac{t_{peak\ \rho} - t_{peak\ power}}{\tau} \tag{5.2}$$

where $\phi(\omega)$ = phase shift [radians] at angular frequency ω, $t_{peak\rho}$ = time of peak driving reactivity [s], $t_{peak\ power}$ = time of peak power [s] and τ = reactivity period [s].

Gain and phase shift were measured during the final complete wavelength after any initial transients had decayed. Simulation times were set long enough to permit a minimum of three complete cycles of the driving reactivity and a sufficient number of half lives of the longest delayed neutron precursor group to pass.

Fig. 5.1 shows an example transient simulation using the numerical model derived in Chapter 2. This data will be used as an example from which the gain and phase change can be calculated.

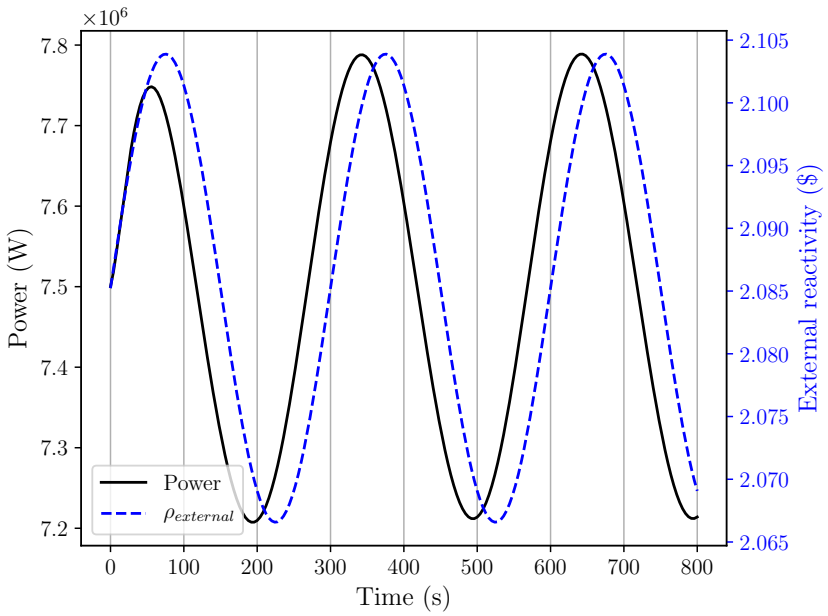

Figure 5.1: Reactor power and driving external reactivity for a sinusoidal reactivity profile, amplitude $= 1.25 \times 10^{-4}$. Average power $= 7.5$ MW.

The average power in the final complete period shown in Fig. 5.1 was 7.4959 MW, with a peak of 7.7888 MW. Using Eq. 5.1, this yields a gain of 312.6. The time of peak reactivity was $t =$ 675.5 s, and the time of peak power was $t = 643.8$ s. Substituting the times of peak power, peak reactivity and the reactivity signal period (300 s) into Eq. 5.2 yields a phase shift of 0.106 rad (6 degrees).

5.2 Original Theoretical Predictions of MSRE Frequency Response

Numerical models of the MSRE were developed by ORNL in order to predict the performance and stability of candidate designs with respect to changes in design parameters [75]. The original theoretical frequency responses discussed in this section were generated using the ORNL MSFR code with 9 graphite regions and 18 fuel regions in the core plus delay terms for the upper head,

primary and secondary circuit loops [33]. This model predicted the reactor becoming more stable with increasing power (evidenced by the reduction in the maximum gain as the reactor power increased in Fig. 5.2 [33, 43]).

Related models included MATEXP for transient calculations [33] and SFR-III for frequency response prediction with ^{233}U fuel [76],. This code was also used for sensitivity analysis of the frequency response to changes in design parameters [43].

A feature was predicted in the frequency response at approx. $\omega = 0.25$ rad s^{-1} - a dip in gain, and increase in phase shift, respectively, at the recirculation frequency. It is believed to be the result of recirculation of fuel with a temperature and delayed neutron precursor history that resonates with the driving external reactivity. At high power levels the heat exchanger will not be capable of removing all the excess energy added to a fuel volume as it passes through the power-producing regions. When this hotter fluid reenters the core it causes a decrease in reactivity, and therefore a decrease in response to any rising external reactivity input hence the reduction in gain. An increase in the strength of the feedback will manifest itself as an increase in phase shift as the power will cease rising with the reactivity at an earlier point in the reactivity cycle.

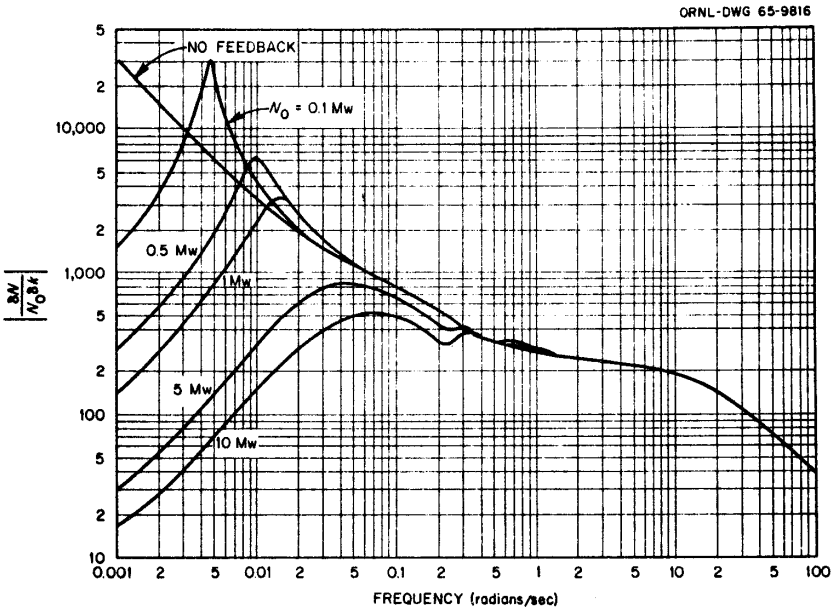

Figure 5.2: Theoretical gain for ^{235}U-fuelled MSRE. Reproduced with permission, courtesy of U.S. Dept. of Energy [10]

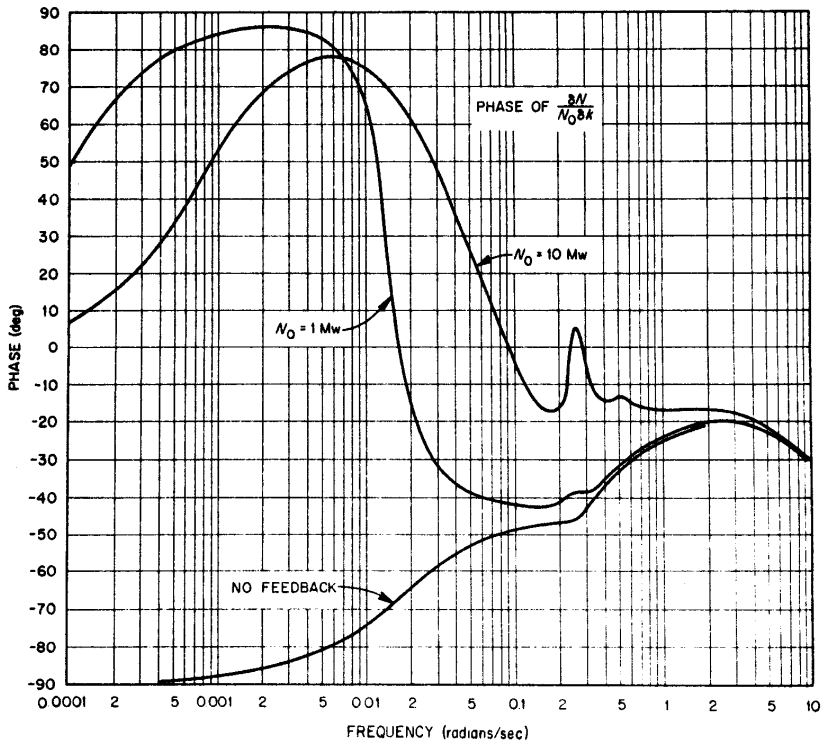

Figure 5.3: Theoretical phase shift for ^{235}U-fuelled MSRE. Reproduced with permission, courtesy of U.S. Dept. of Energy [10]

Other investigations into MSRE frequency response have been performed at zero power (with no temperature feedback) [77] - this investigation showed good agreement with MSRE experimental zero-power response.

5.3 Experimental Measurement of MSRE Frequency Response

Subsequent experimental observations confirmed the dampening of the system with respect to power. Figures B.1 and B.2 in Appendix B show the experimental frequency response for MSRE with ^{235}U fuel at a range of power levels from zero power (with fuel circulating) up to 7.5 MW. Also plotted are the theoretical responses predicted by the MSFR code, which are generally in agreement.

5.3.1 Experimental Methods

A pseudo-random binary sequence (PRBS) of rod movements was generated by computer and used to control the movement of one of the control rods. These sequences were designed to perturb the reactor across a wide range of frequencies simultaneously. The rod movement corresponded to a reactivity amplitude ($\Delta\rho$) of 0.02 to 0.03% (peak to peak) [10].

The frequency response function is calculated from the ratio of the cross-spectral power density to the input power spectral density. Two different methods are used to generate these power spectral densities - a 'direct' method based on digital filters with variable filter shape to compute the spectral power densities, using the CPSD code [10, 3] and an 'indirect' method based on autocorrelation and cross correlation functions to compute the spectral power densities, using the CABS code [78]. This method has been used to validate theoretical predictions of frequency response and stability in other engineering systems, for example the Hawker Hunter jet fighter. An electronic light system directed the pilot to input a PRBS of pitch signals via the control column, while the aircraft pitch rate was recorded for later processing [79].

5.3.2 Experimental Results

As the reactor power increases, the magnitude of the gain peak decreases, and the frequency at which peak gain is recorded increases. This implies that transients decay more rapidly and with a higher frequency as the power increases. This is supported by observations of the power transients at the conclusion of the frequency response tests (Figure 5.4). At low power levels, the transients have a larger relative magnitude and take longer to decay (over two hours to return to equilibrium in the case of the 75 kW experiment). As the power increased, the transients were smaller and decayed faster [10].

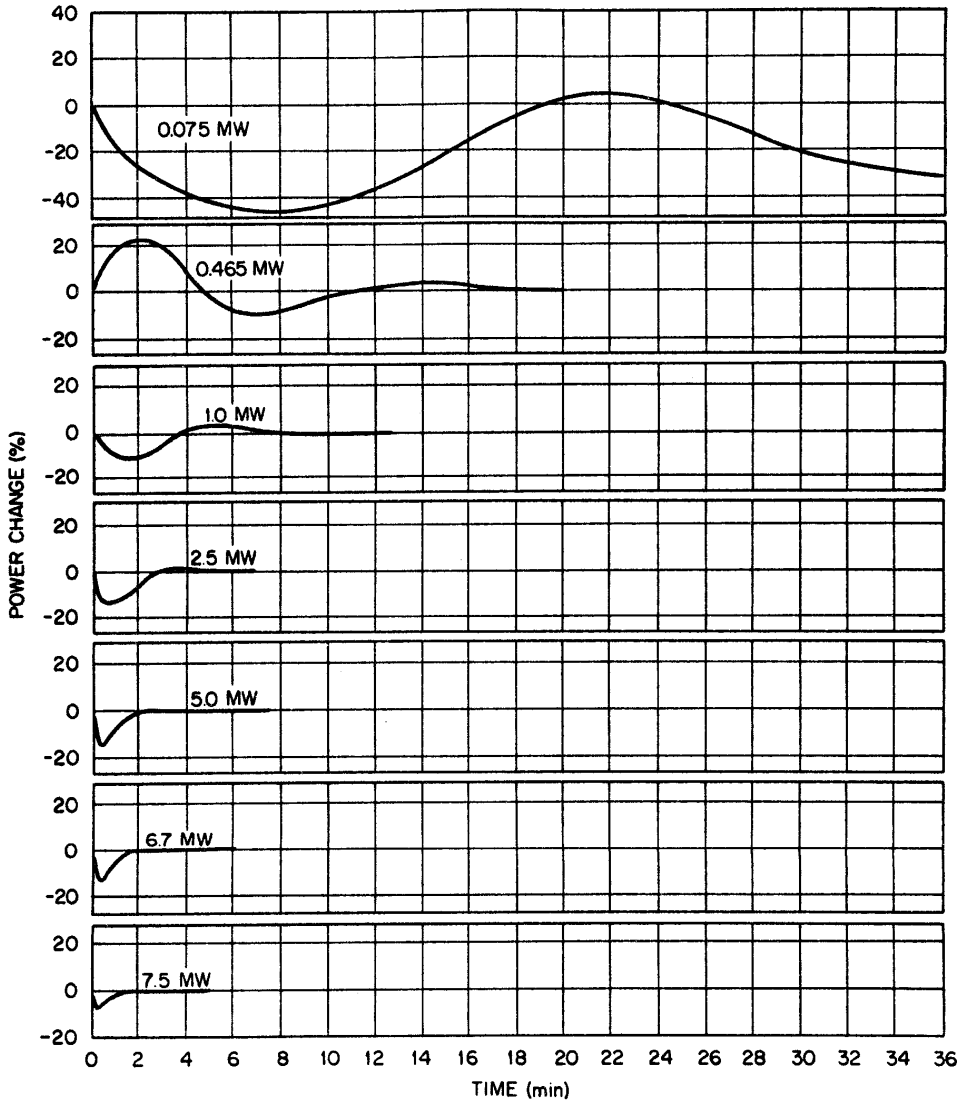

Figure 5.4: MSRE power level transients after the conclusion of frequency response tests. Reproduced with permission, courtesy of the U.S. Dept of Energy [10].

5.4 Frequency Response of the Numerical Model

5.4.1 Methodology

The numerical model described in Chapter 2 was used to determine the frequency response at power levels corresponding to the MSRE experiments running on ^{235}U fuel. 192 transient simulations driven by sinusoidal external reactivity of amplitude 1.25×10^{-4} were simulated to construct the frequency response at each power level, across a frequency band between 10^{-3}

and 10 rad s^{-1}.

This method was chosen over a pseudo-random binary sequence due to the simplicity of implementation. It is equivalent to a 'white' input spectrum as power is evenly distributed over the range of frequencies tested.

5.4.2 Results

Figure 5.5 shows an overview of the response and phase shifts from the numerical model across the range of operational powers. The trend of reduced magnitude of response and an increase in the frequency at which it is recorded is present, in agreement with the experimental data shown in Figure B.1. The trends are similar (cf. Figs. 5.7, 5.8, 5.9, 5.10, 5.11, 5.12, 5.13 and 5.14), however the frequencies at which they occur are shifted relative to experiment (Figure 5.6) and the gain is lower compared to the experimental data. At high powers there is only a small difference in the natural period of the system (defined as the period corresponding to the frequency at which the highest gain is recorded). At low powers, the difference is larger, for example in the $P = 75$ kW case, the natural period for the numerical model is substantially longer than the experiment (83 minutes vs. 30 minutes).

Figure 5.6 shows the natural oscillation periods of the system at different power levels, for the ORNL theoretical model, MSRE experimental data, and the numerical model discussed in this section. The natural oscillation period for MSRE was either measured directly at the conclusion of a PRBS test, or determined from the frequency at which maximum gain was recorded. The latter method was used to estimate the oscillation period for the numerical model. At powers above about 2 MW, the difference in natural period between the ORNL data and the model under discussion is about one minute. At low powers, the period predicted by the numerical model diverges from the experimental data and ORNL model.

5.4.3 Discussion of Natural Oscillation Periods

Figure 5.6 showed a divergence of the natural oscillation period of the model from experimental data at low powers. Close inspection of the experimental data points suggests some uncertainty over the oscillation periods quoted. For example, at $P = 75$ kW (Fig. 5.8) - there is no experimental data below 0.0035 rad s^{-1}, yet the trend of the experimental gain appears to be

increasing. This suggests the true peak response lies at a lower frequency, resulting in a smaller discrepancy between the presented model and the experimental result at this power level.

Possible explanations for the difference in oscillation periods include an absence of xenon in the model. Ball & Kerlin (1965) [33] included iodine decay into xenon, burnup of the xenon and diffusion into the graphite in the most detailed model tested (referred to as the 'complete' model in [33]), however removal of this effect only resulted in a small phase shift of approx. $+1.5°$ at a simulated power of 10 MW. An increase in the phase shift ϕ implies an increase in system stability as increases in power are curtailed more rapidly after an increase in the driving reactivity.

5.4.4 Comparisons of Frequency Responses at Each Power Level

Figure 5.5 shows an overview of the numerical system responses for power levels between 1 μW and 7.5 MW. At frequencies (below 0.01 rad s^{-1}), the model is less damped in the experiment, with the gain flattening out compared to experiment. This is particularly evident for the lower power levels. At high frequencies (above 0.3 rad s^{-1}) the responses converge on gain of approx. 200, in agreement with ORNL theoretical predictions and experiment.

A small feature in the phase shift at approx. 0.25 rad s^{-1} is observed at all power levels. A feature at the same frequencies is sometimes observed in the experimental phase shifts, for example at $P = 1$ MW (Fig. 5.10) and $P = 6.7$ MW (Fig. 5.13). Noise in the data makes assessment at other power levels difficult.

Near zero power (1 μW) and low frequency, phase shift is approximately -90° and rises steadily as the frequency of the oscillating external reactivity increases. This is consistent with almost zero reactivity feedback at this very low power level. The phase shift for the 75 kW case at the lowest frequencies is near zero, decreasing to a minimum of just under $-70°$ at 0.007 rad s^{-1}, before tending to the 1 μW curve (see also Fig. 5.8). At frequencies below about 8×10^{-3} rad s^{-1} the phase shift is closer to zero as the system has time to heat up and thermal feedbacks to exert an effect.

At power levels at or exceeding 465 kW, the phase shift begins above zero, and increases to a maximum before dipping towards the zero power curve. Higher power levels result in a greater

maximum phase shift, which also occurs at a higher frequency. A change in phase shift is observed for power levels above 2.5 MW at a frequency of 0.3 rad s^{-1}. This feature is examined further in Section 5.5.

The gains and phase shifts converge for all power levels at high frequencies (above $\sim$ 0.4 rad s^{-1}).

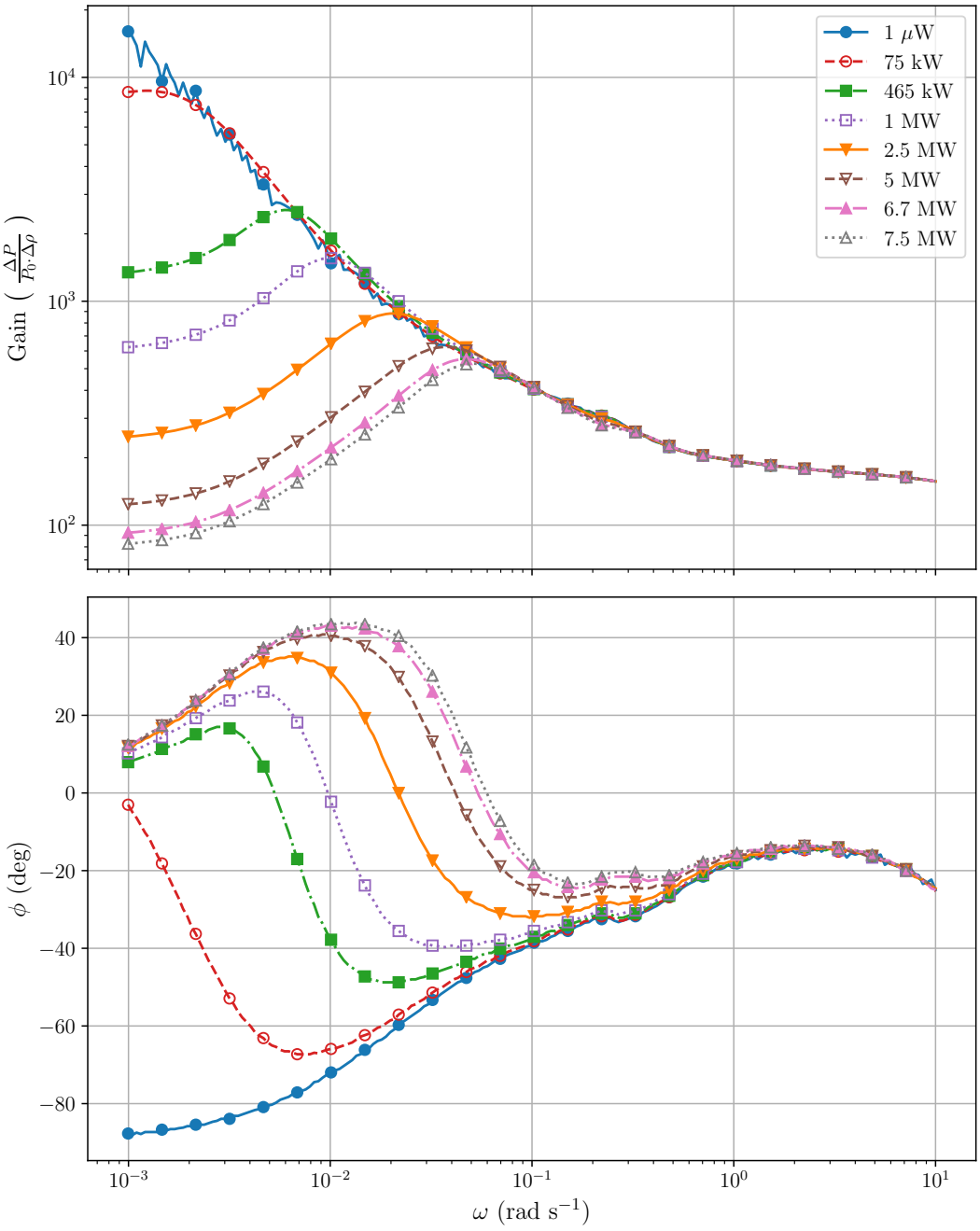

Figure 5.5: Overview of model frequency response and phase shift, ϕ for power levels between 10^{-6} W and 7.5 MW. Markers correspond to every eighth data point.

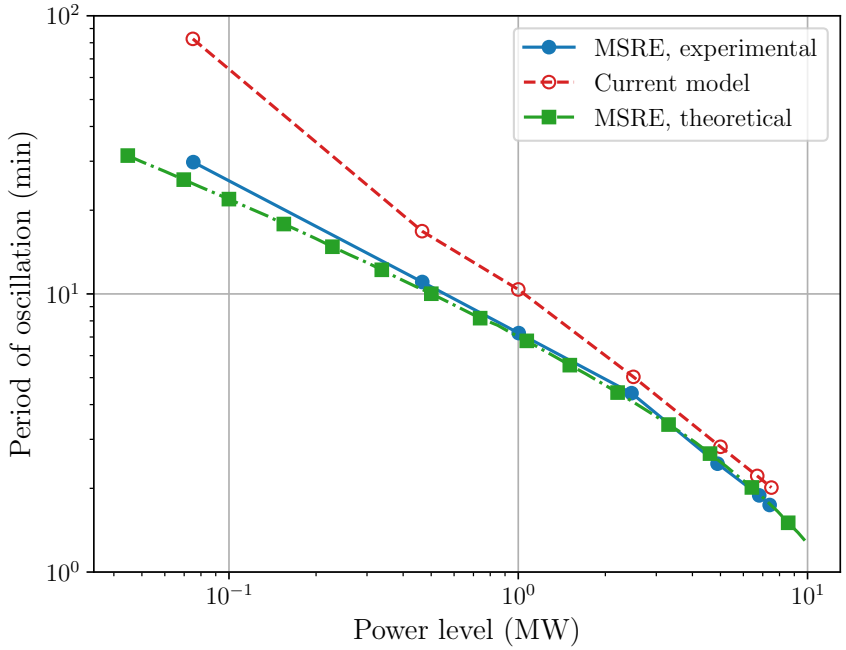

Figure 5.6: Natural oscillation period for theoretical MSRE model and MSRE experiment [10] and the model presented in this work.

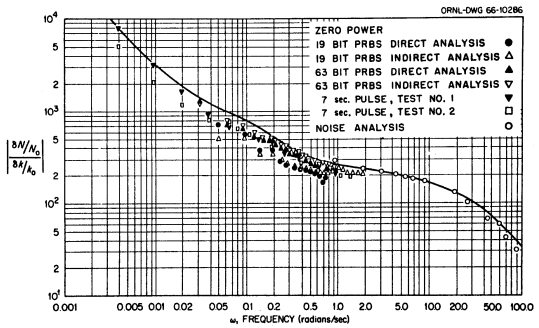

(a) Experimental response

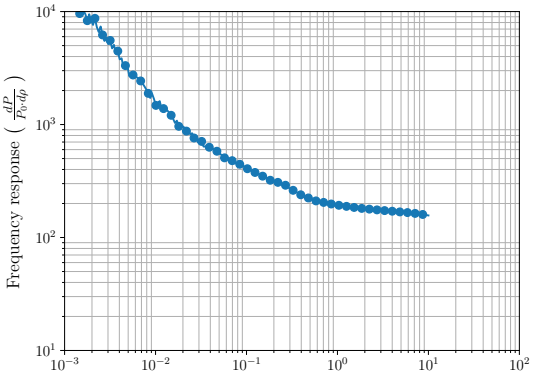

(b) Model response

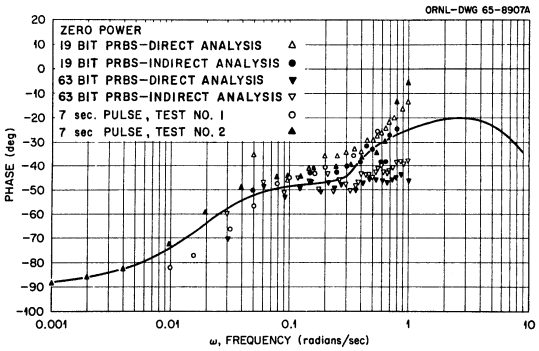

(c) Experimental phase shift

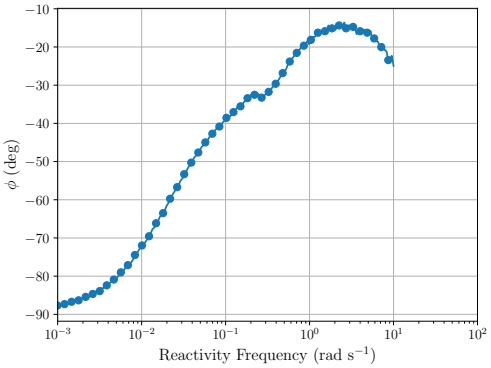

(d) Model phase shift

Figure 5.7: Experimental and model frequency responses near zero power.

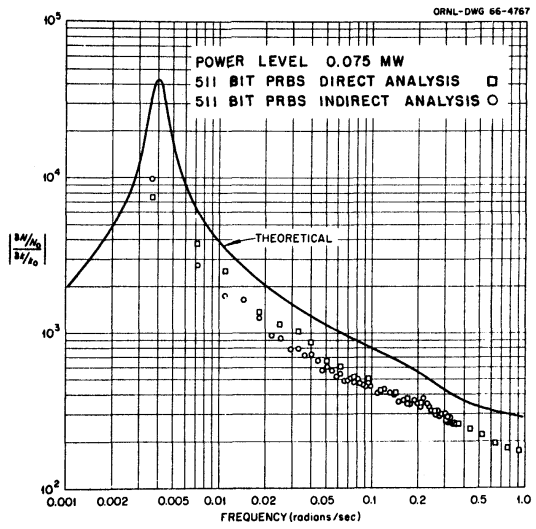

(a) Experimental response

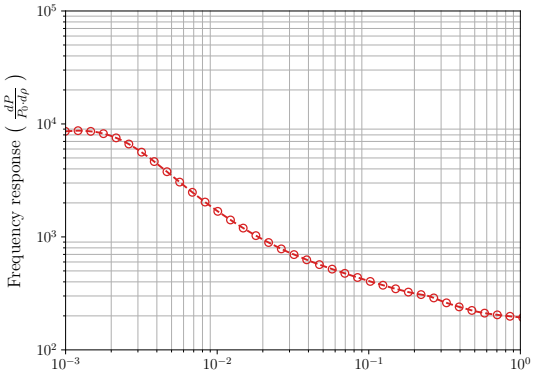

(b) Model response

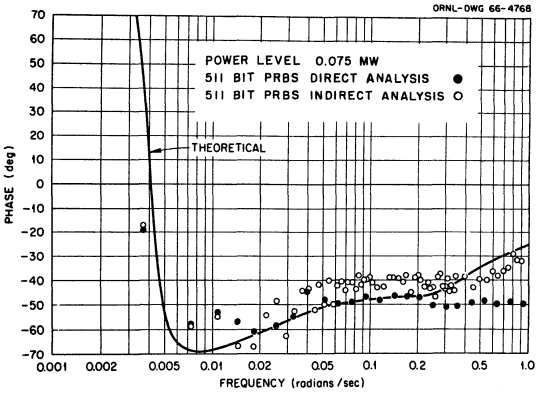

(c) Experimental phase shift

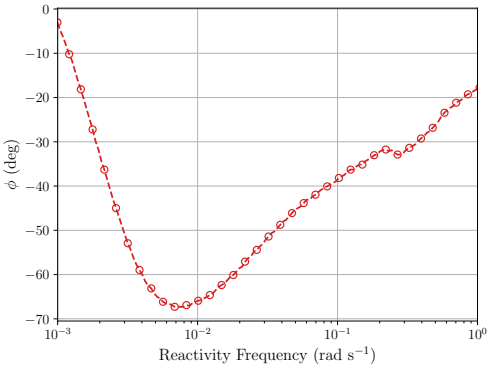

(d) Model phase shift

Figure 5.8: Experimental and model frequency responses at $P = 75$ kW.

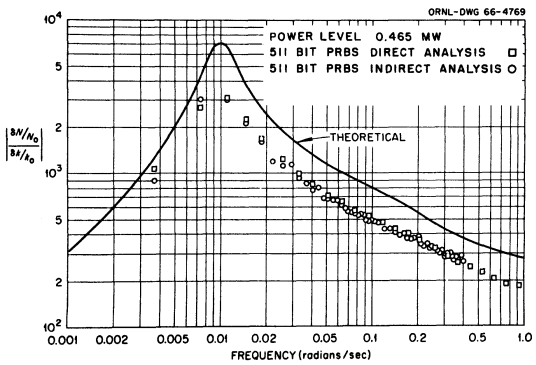

(a) Experimental response

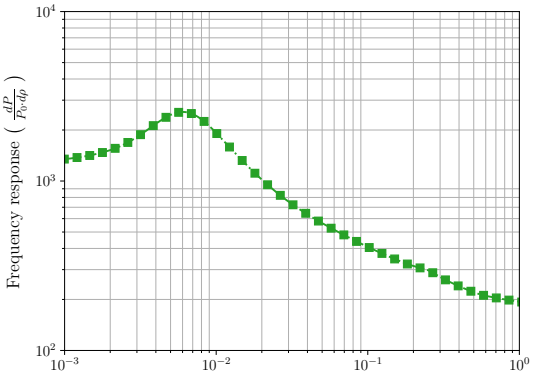

(b) Model response

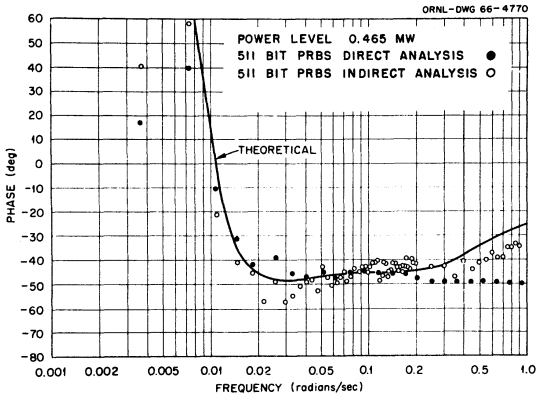

(c) Experimental phase shift

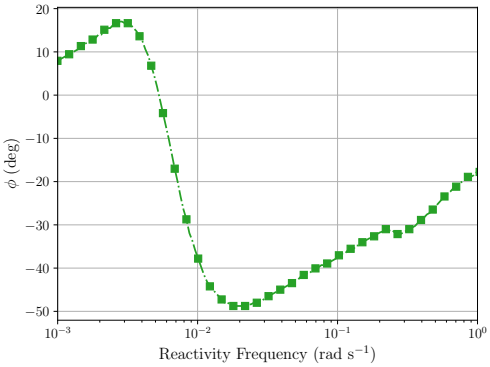

(d) Model phase shift

Figure 5.9: Experimental and model frequency responses at $P = 465$ kW.

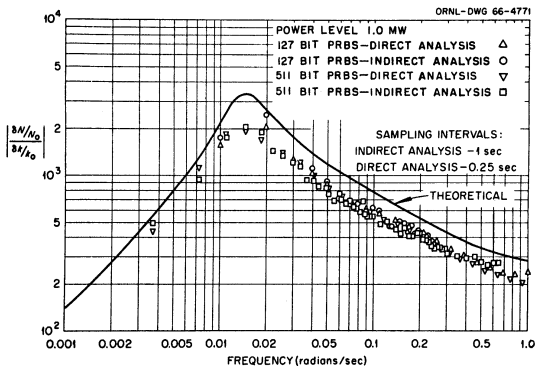

(a) Experimental response

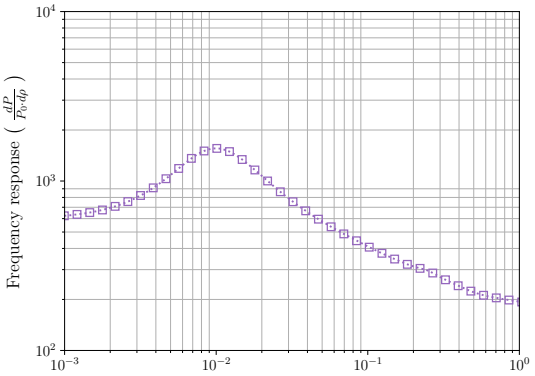

(b) Model response

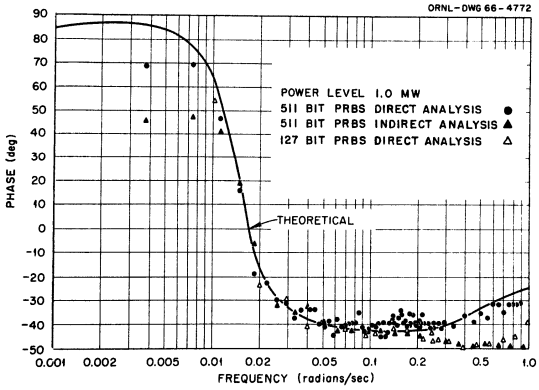

(c) Experimental phase shift

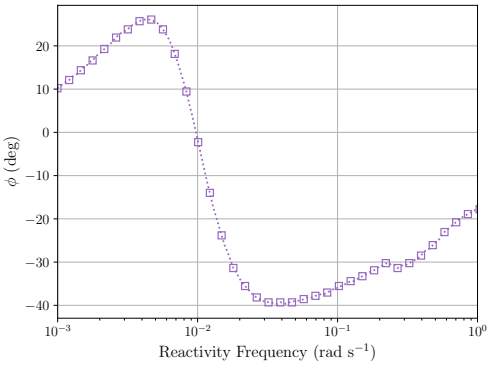

(d) Model phase shift

Figure 5.10: Experimental and model frequency responses at $P = 1$ MW.

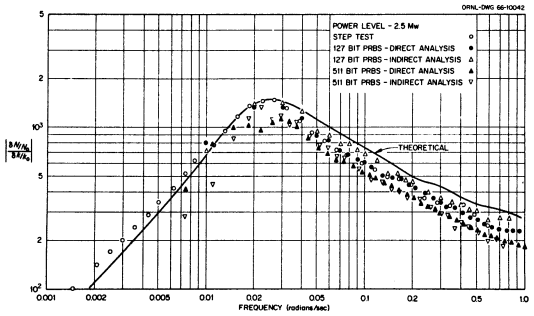

(a) Experimental response

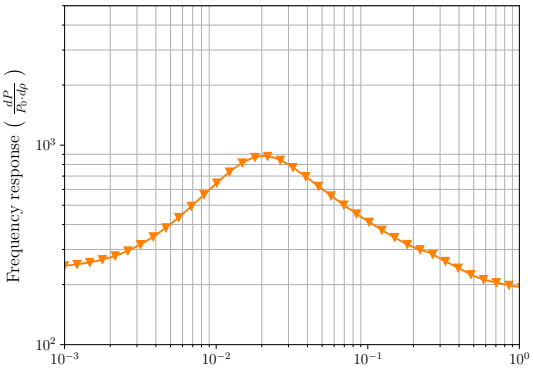

(b) Model response

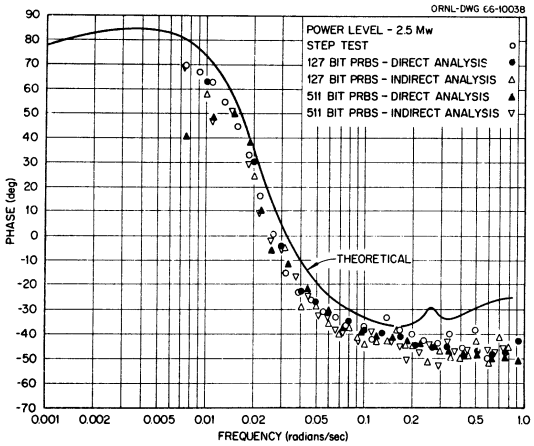

(c) Experimental phase shift

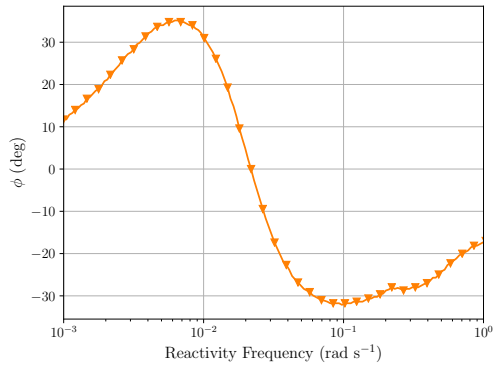

(d) Model phase shift

Figure 5.11: Experimental and model frequency responses at $P = 2.5$ MW.

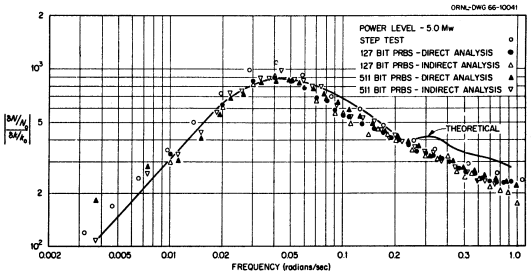

(a) Experimental response

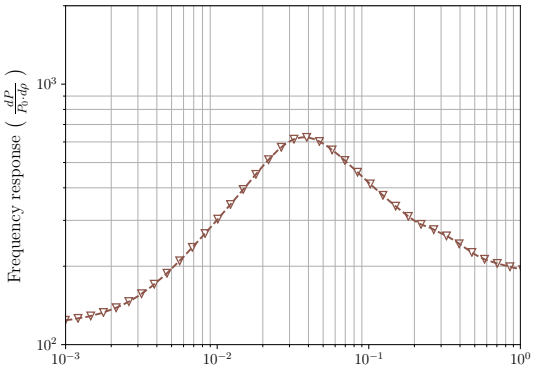

(b) Model response

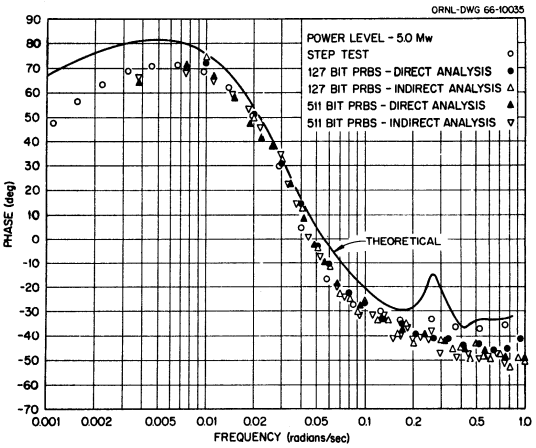

(c) Experimental phase shift

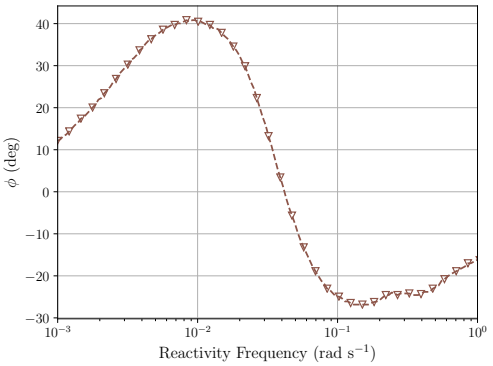

(d) Model phase shift

Figure 5.12: Experimental and model frequency responses at $P = 5$ MW.

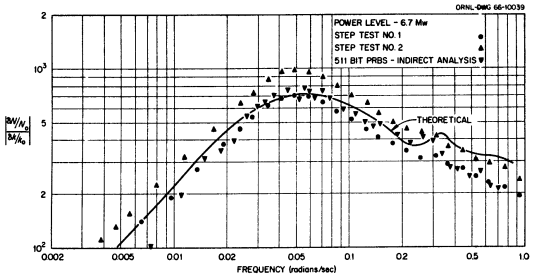

(a) Experimental response

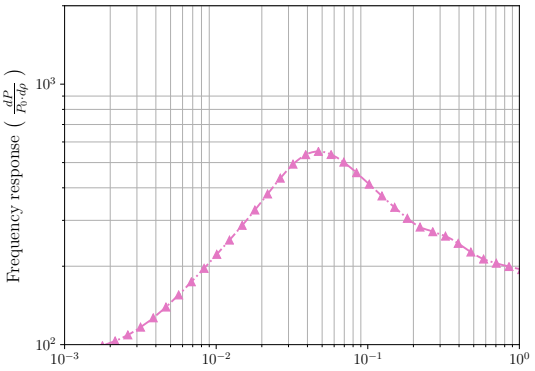

(b) Model response

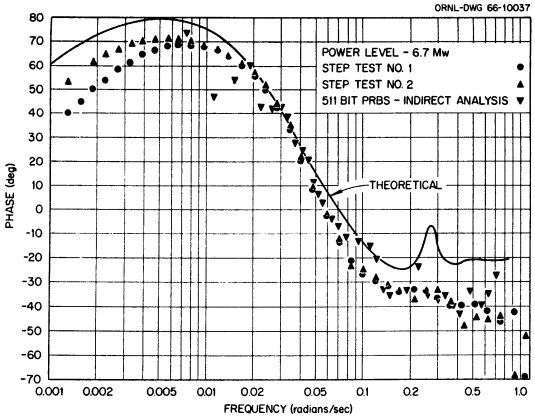

(c) Experimental phase shift

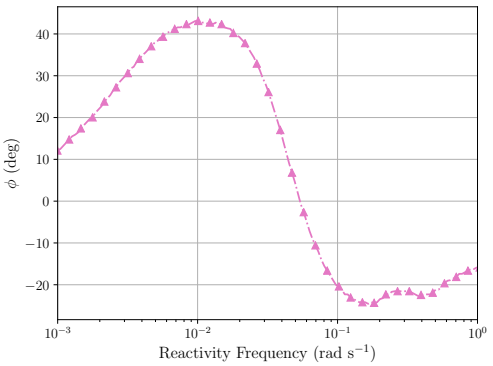

(d) Model phase shift

Figure 5.13: Experimental and model frequency responses at $P = 6.7$ MW.

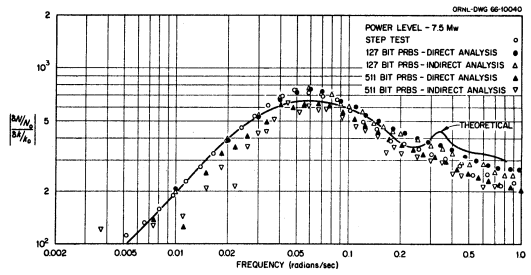

(a) Experimental response

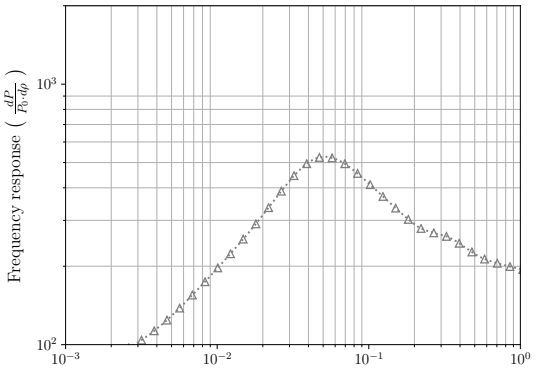

(b) Model response

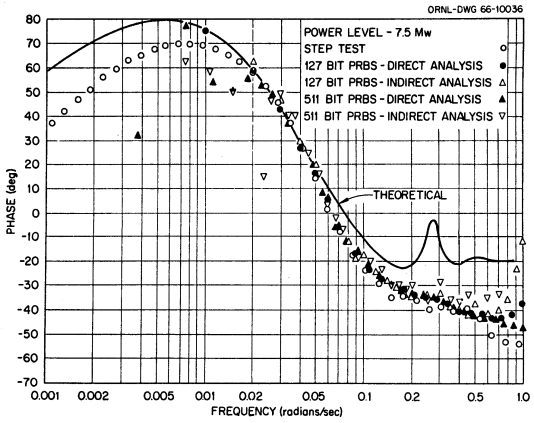

(c) Experimental phase shift

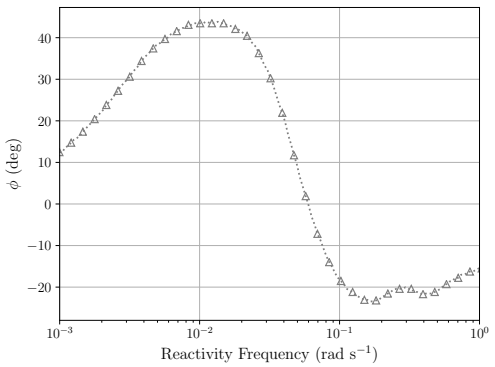

(d) Model phase shift

Figure 5.14: Experimental and model frequency responses at $P = 7.5$ MW.

5.5 Frequency Response with Turbulent Dispersion

The recirculation feature predicted by the MSFR model (the bump in the solid line in Figs. 5.2 and 5.3 at $\omega \approx 0.25$ rad s^{-1}) was not generally observed in the experimental frequency response. Close examination of the frequency response for the P = 5 MW and 6.7 MW cases do show small features at frequencies corresponding to the recirculation period in the primary circuit (for example, see the experimental phase shift in Fig. 5.13c). Underestimation of mixing in the primary circuit has been suggested as an explanation for this difference [58]. Theoretical models with additional mixing in the primary circuit through the use of first order lag 'mixing pots' [80] over-predicted the size of the recirculation feature when compared to experimental results using ^{233}U fuel [58, 3]. Later models with well-mixed regions match experimental data in

the vicinity of the recirculation feature but deviated from experiment at higher frequencies [81]. Other modelling efforts suggest that the influence of the secondary circuit maybe contributing to the damping of the recirculation feature, however neglect of the secondary circuit only partially suppressed the feature in that case [82]. A detailed three-dimensional model coupling neutron diffusion to thermal hydraulics incorporated some mixing in the external circuit but the system frequency response was not examined in that investigation [83].

A model that introduced mixing in a gradual fashion around the circuit in a similar fashion to the fluid dynamics of the MSRE system was desirable from the standpoint of the neutronic coupling of regions via fission and delayed neutron emission. For example, if a large well-mixed region in the upper head was used to disperse temperature and delayed neutron precursors it would not reproduce the sequencing of subsequent influences on the power when that slug reentered the vessel after passing around the external part of the primary circuit. The effect of the sequenced heating and precursor production in vessel regions in response to the step reactivity transient was discussed in Ch. 3.

It was instead decided to introduce the mixing in proportion to the component fuel velocity using a turbulent dispersion parameter (Reynolds number estimated at 240,000 in the primary circuit [33]). This velocity-dependent parameter is inspired by experiments on the dispersion of conductive salt solutions in oil pipelines [67]. A similar mixing term has been employed in analysis of the ^{235}U-fuelled MSRE pump startup transient. Additional mixing reduced the magnitude of control rod oscillations in response to pump startup but the frequency response was not examined as part of that investigation [84].

Therefore the relationship between the amount of mixing in the primary circuit and the $\omega = 0.25$ rad s^{-1} feature in the frequency response was investigated. The frequency responses for four cases, all at $P = 7.5$ MW, with increasing amounts of mixing (via the velocity-dependent dispersion term in Eqs. 2.11 and 2.12) are presented in Figs. 5.15 through 5.18 with comparison to experimental measurements of the MSRE frequency response.

The maximum gain was recorded at a similar, though slightly lower frequency (ORNL: 0.057 vs. model: 0.052 rad s^{-1}, see Fig. 5.15). At higher frequencies the model has a similar trend but lower overall gain than the ORNL experimental data points. Model phase shift is close to

the experimental data between $\omega = 0.03$ and 0.1 rad s^{-1}, however at the edges of the frequency domain the model differs from the ORNL experiment (Fig. 5.16).

Figures 5.17 and 5.18 show the frequency response close to the recirculation feature. Setting the turbulent dispersion parameter, K, to 3×10^5 W/m/K was found to introduce sufficient mixing in the primary circuit to qualitatively reproduce the frequency response in the frequency range corresponding to the recirculation peak.

Some other aspect of the model physics must be responsible for the discrepancy in the phase shift at high and low frequencies between the model and experiment, as this difference exists independently of the degree of turbulent dispersion.

Differences between the physics represented in the model and the observed physics of the experiment include no modelling of the secondary circuit, a uniform delayed neutron importance with respect to location, and no explicitly modelled heating due to precursor decay (this energy was assumed to be deposited at the time of fission). ORNL documents from the MSRE programme note that the reactor response from controlling heat rejection at the secondary heat exchanger was sluggish (also see Fig. 5.4) - this may explain the difference in frequency response at low frequencies.

The numerical model assigns an equal importance to all delayed neutrons regardless of the vessel location at which they decay. This is different to the actual reactor where the physics of neutron transport influence likelihood of a delayed neutron being able to cause additional fissions and contribute to the overall neutron population. This likelihood will be dependent on the location of decay, direction and energy of the neutron that is emitted. On the timescale of only a few seconds it is possible for a precursor to be born and then be advected from a region of relatively high importance to low importance (e.g. from upper head to pump), where a subsequent decay has a very low probability of causing further fissions due to a lack of moderation. This effect may explain the notable difference in response above $\omega = 10^{-1}$ rad s^{-1}.

Accurate assignment of importance to regions outside the core would require modelling neutron transport throughout the whole vessel using multiple neutron energy groups, for example via neutron diffusion, the Boltzmann transport equation, or Monte Carlo methods. For example,

the SERPENT Monte Carlo code has been used to generate importance functions for delayed neutrons which were then used in point kinetic models, with good agreement for some of the ^{233}U-fuelled data sets from MSRE [81, 85]. Such approaches were not pursued in this work due to the computational cost.

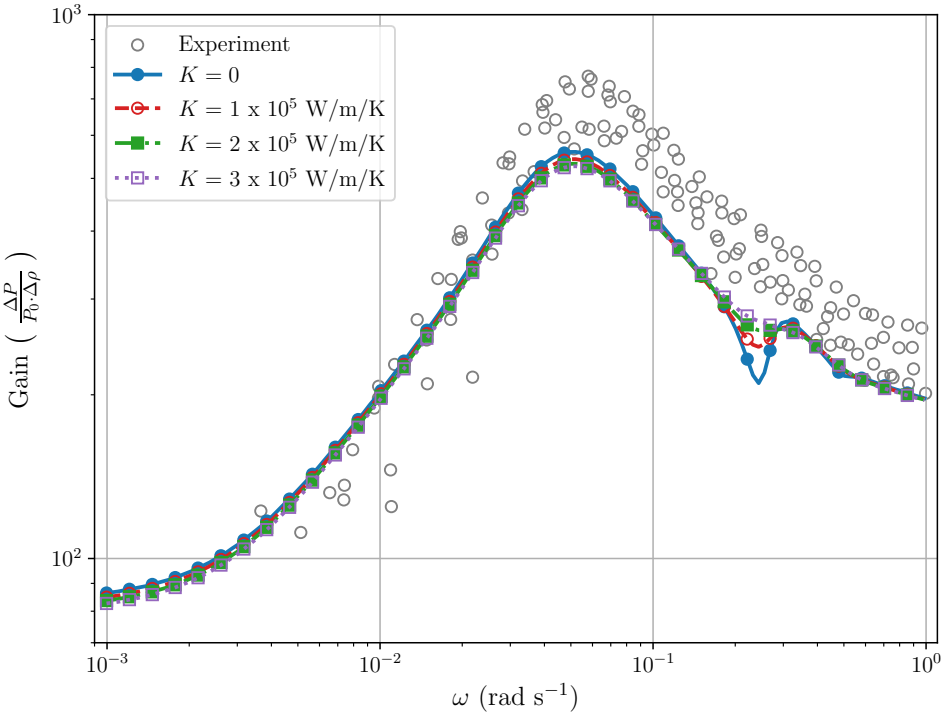

Figure 5.15: System gain for increasing amounts of turbulent dispersion, with experimental data points [10].

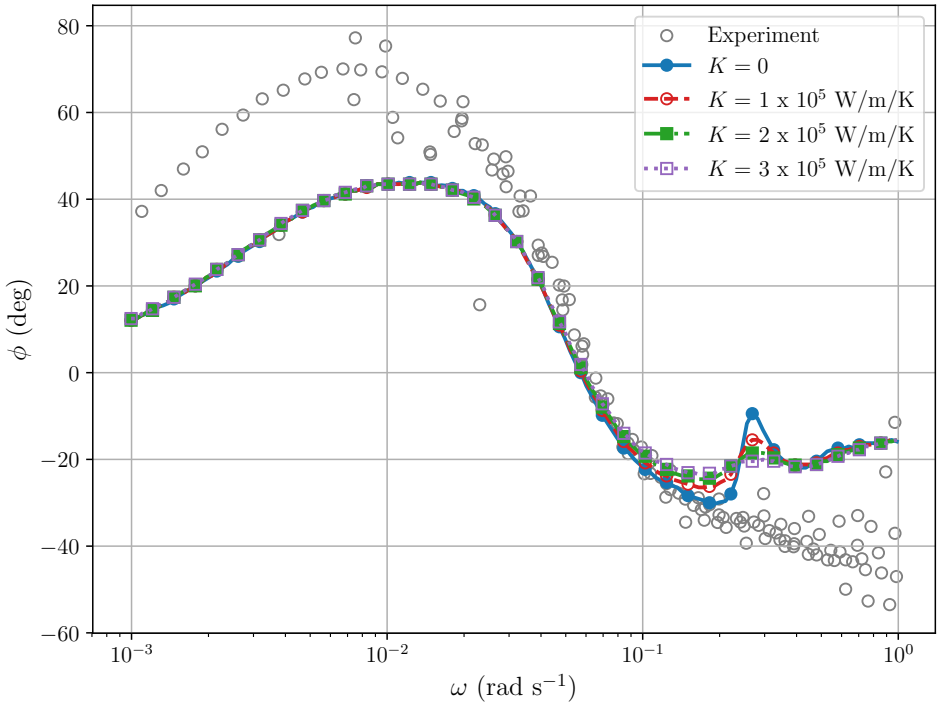

Figure 5.16: System phase shift for increasing amounts of turbulent dispersion, with experimental data points [10].

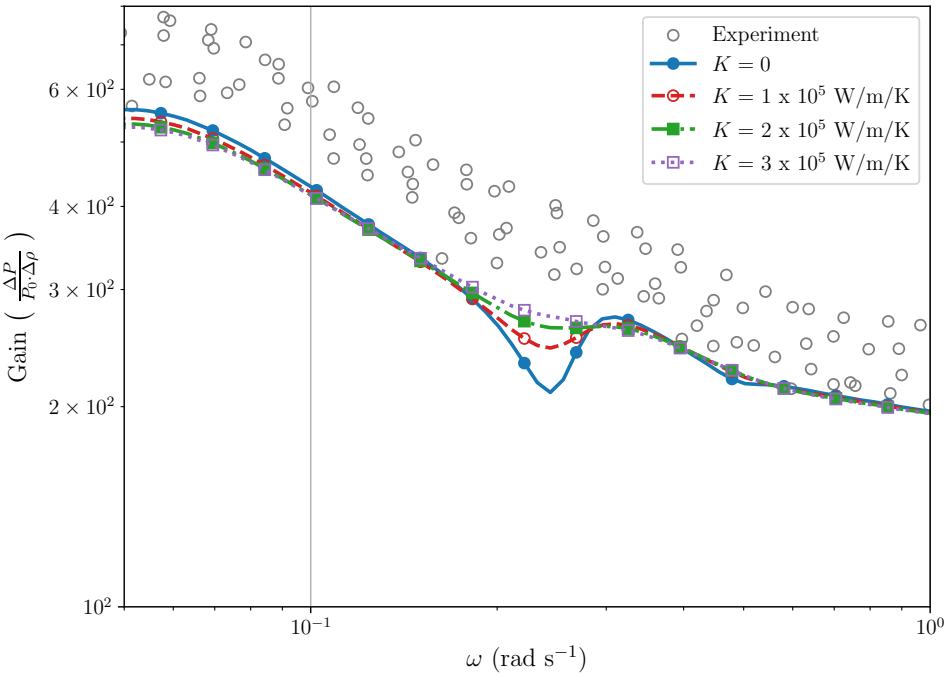

Figure 5.17: Gain in vicinity of recirculation peak.

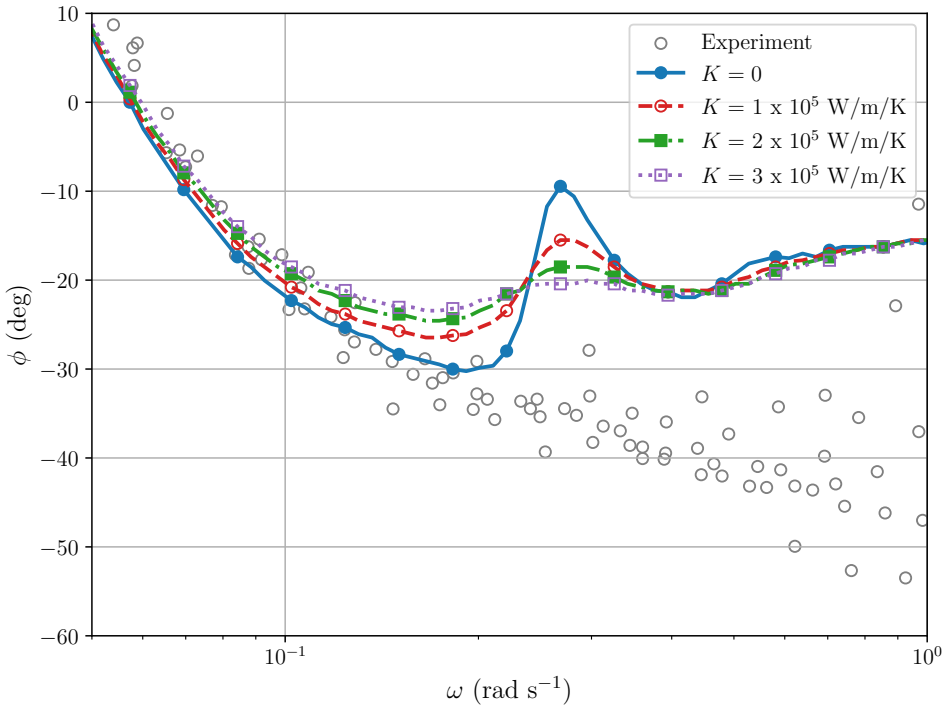

Figure 5.18: Phase shift in vicinity of recirculation peak.

Comparison of Numerical Model Response With and Without Mixing

Figure 5.19 compares the gain and phase for the numerical model with no additional mixing and the maximum mixing tested ($K = 3 \times 10^5$ W/m/K) introduced via the dispersion term. The magnitude of the recirculation feature is proportional to the power level in both cases. Increased heating of the fuel salt as it passes through the core may be responsible for this trend - the proportion of precursors reentering the core is expected to be a fixed proportion of the number departing the core, with the ratio dependent on the external loop residence time.

The size of the recirculation feature is greatly reduced in the case of additional mixing (right hand side of Fig. 5.19), providing better agreement with the experimental data at frequencies close to that of the primary circuit recirculation. Fig. 5.20 shows the vicinity of the recirculation feature with enlarged scales. The frequency response at core powers below 1 MW is almost unchanged as a result of the turbulent dispersion.

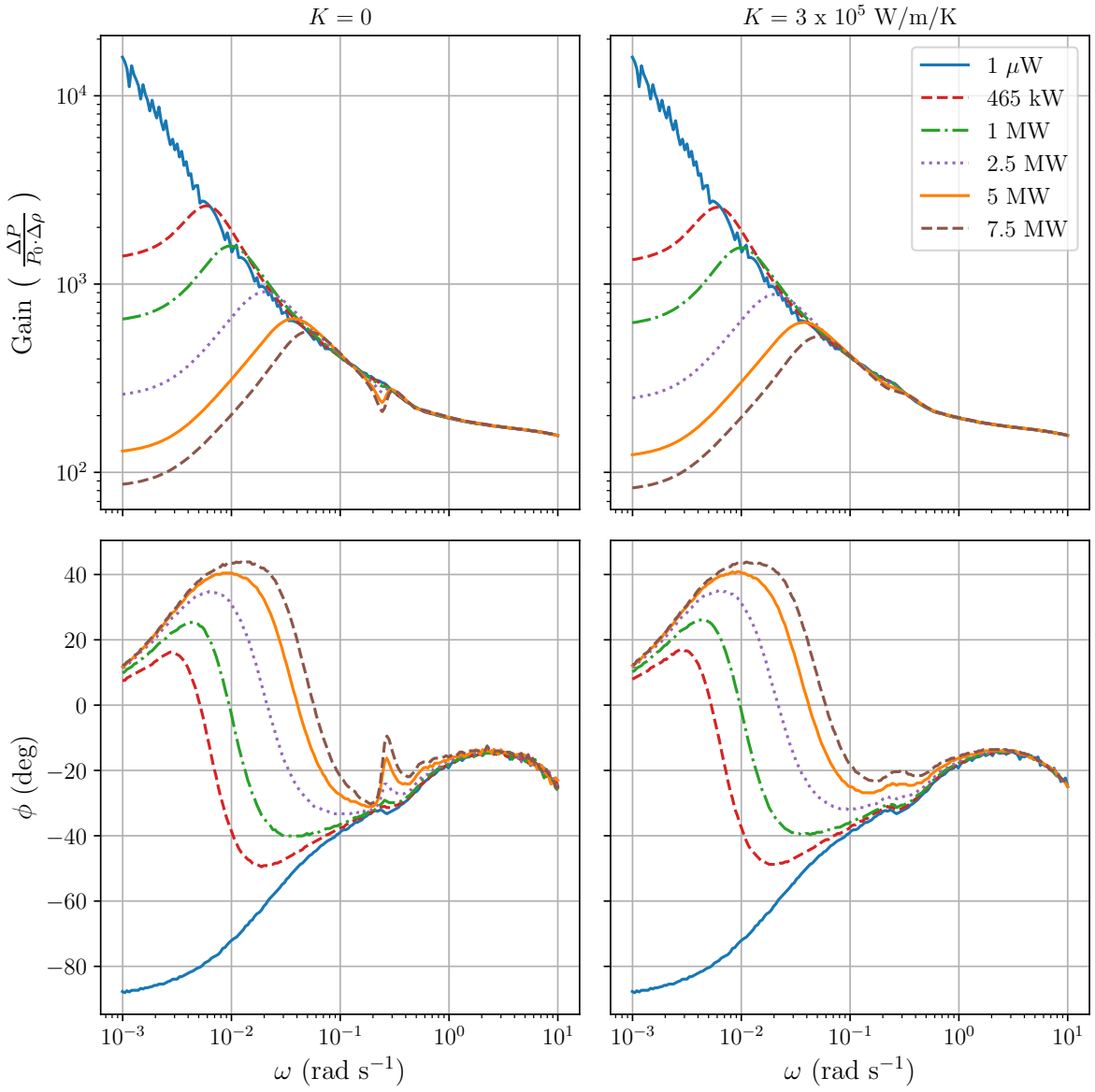

Figure 5.19: Comparison of frequency response for models with zero and maximum turbulent dispersion tested ($K = 3 \times 10^5$ W/m/K), for a subset of the power levels simulated between 10^{-6} W and 7.5 MW.

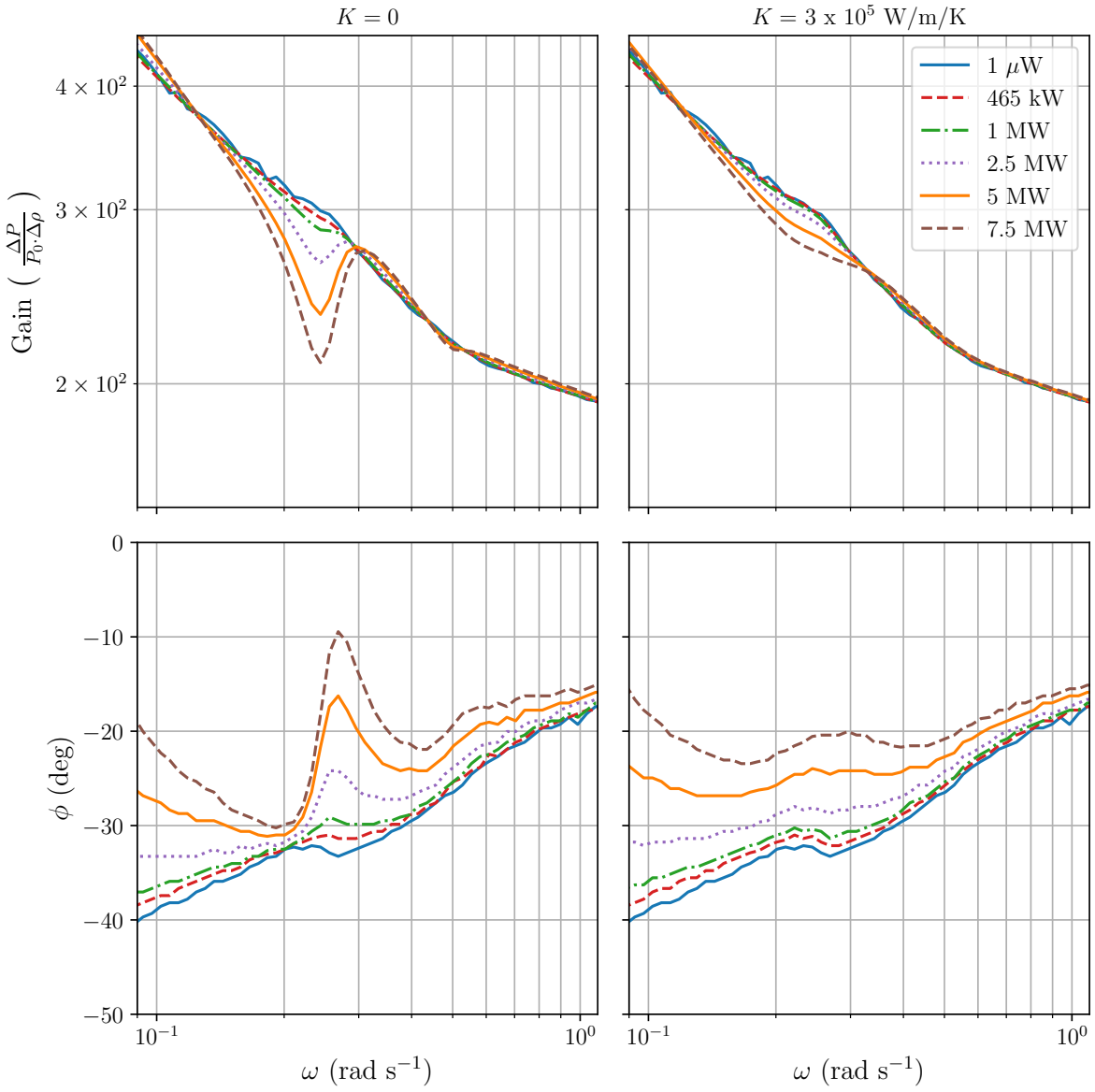

Figure 5.20: Enlarged scale frequency response for models with zero and maximum turbulent dispersion tested ($K = 3 \times 10^5$ W/m/K), for a subset of the power levels simulated between 10^{-6} W and 7.5 MW.

5.6 Semi-analytical Model

An additional semi-analytical model of MSRE frequency response was developed from similar equations to the numerical model derived in Ch. 2; This served as a verification of the multiple transient simulation method presented above. The semi-analytical method was faster than the numerical model and required fewer computing resources. The derivation and more detailed testing of the semi-analytical model is discussed in Appendix A.5.

Figure 5.21 shows an overview of the semi-analytical system frequency response across the range of operational power levels. The overall features of the frequency response are similar to the numerical model discussed in the previous section, albeit with some slight differences to the trends of phase shifts at high power levels at frequencies around 10^{-3} rad s^{-1}. The recirculation feature at approx. 0.25 rad s^{-1} is again present, with the size of the feature increasing as the reactor power increases.

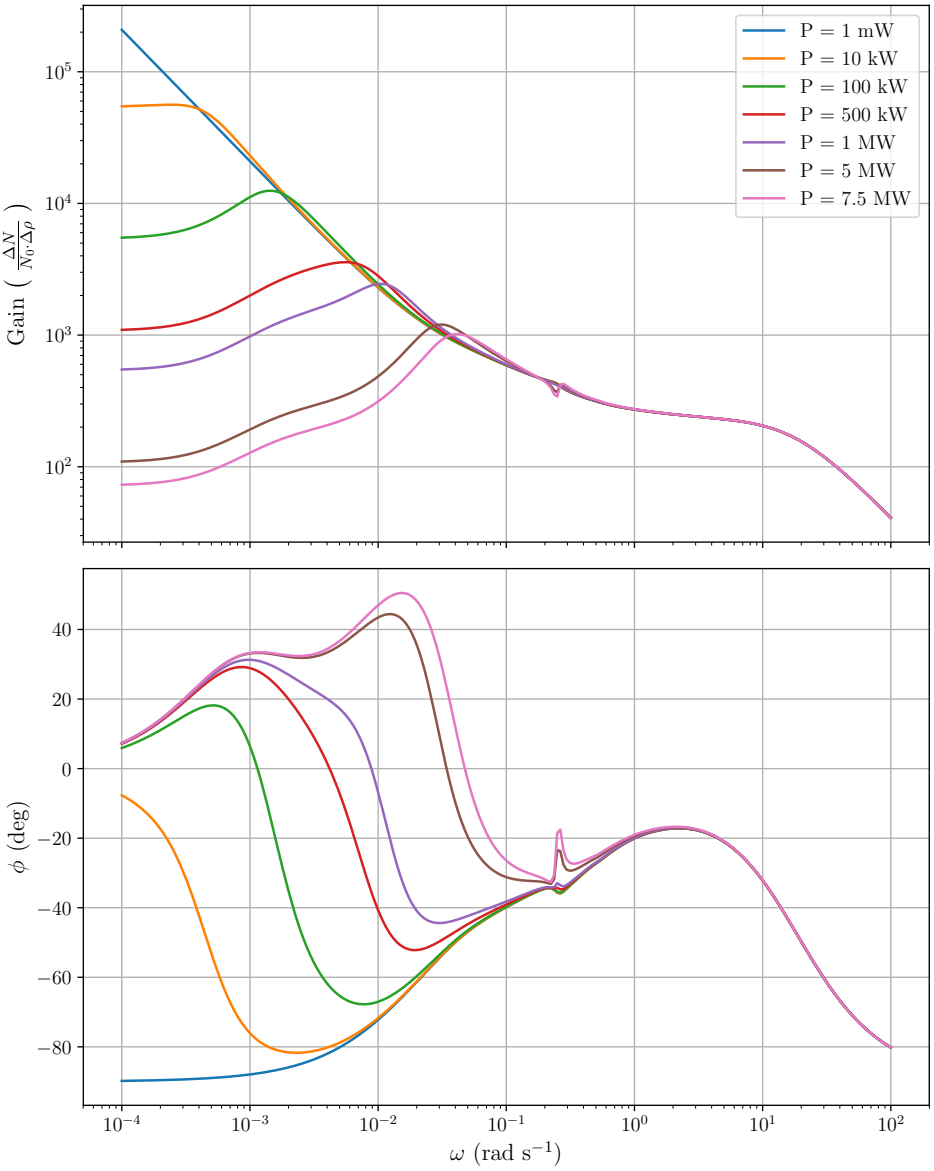

Figure 5.21: Overview of frequency response for semi-analytical model.

5.7 Comparison of Frequency Response Between Models and Conclusions

Figure 5.22 shows a comparison of the frequency responses for the numerical model, the semi-analytical model, an ORNL semi-analytical model and multiple experimental datasets, with and without deliberate additional mixing. The frequency responses of the numerical model and

the semi-analytical model are qualitatively similar to the ORNL model and experimental data; however, differences are present in the magnitude of the gains and at the extremities of the frequency range tested. Differences at low frequencies may be due to neglect of the secondary circuit, (for example the semi-analytical model has significantly higher gain than the others below $\omega \sim 10^{-2}$ rad s^{-1}) but the numerical model is closer to experiment despite also lacking a secondary circuit.

At higher frequencies, the phase shifts for the numerical and semi-analytical models deviate from the clustering of experimental data points but are just within the overall extent. Most experimental data points show a phase shift more negative than that predicted by the models at higher frequencies. This suggests the models exhibit higher feedbacks at these frequencies than existed in the real reactor, as the power may continue increasing for a greater proportion of the first half of a reactivity cycle while $\rho > 0$. Rapid processes that redistribute energy throughout the system, *i.e.* neutron transport and thermal conduction, may be responsible for this behaviour. This also supports the case for more detailed coupled neutronic-thermal hydraulic investigations of this reactor across a wide range of driving frequencies.

While exhibiting some error relative to the numerical model and experimental data, the semi-analytical model captures the behaviour in the frequency range while being cheap to run and was deemed suitable for stability analysis in Section 5.9.

5.7.1 Addition of a Well-Mixed Region in the Upper Head

Kerlin et al. [86] attempted to introduce extra mixing into models of the MSRE circuit by including a single well-mixed region after the core into a model of the ^{233}U-fuelled MSRE frequency response. Residence times of 2 seconds and 5 seconds were tested but neither was able to suppress the recirculation feature.

A region with mass equal to the upper head (residence time 3.9 s) was introduced into the semi-analytical model to verify the effect of this change to the model. Overall ratio of core to loop residence times and mass flow rate was maintained by shortening the section of pipework between the heat exchanger and core. Inclusion of this mixing region had only minor effect on the frequency response. The frequency response of the semi-analytical model with mixing pot

is shown on the right hand side of Fig. 5.22, compared against the experimental results and the numerical model with additional dispersion. The addition of the upper head mixing pot has only a small effect on the size of the recirculation feature.

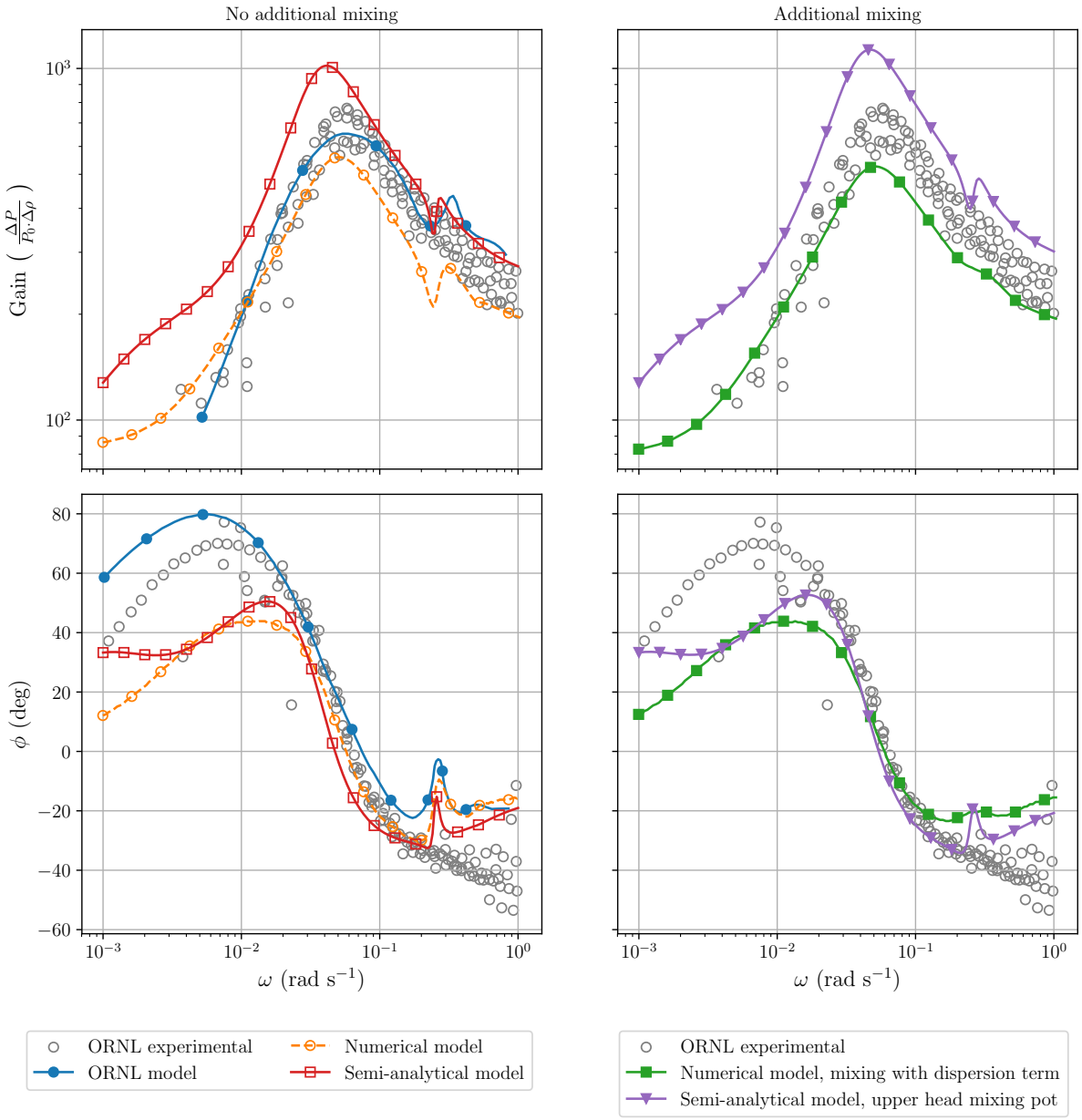

Figure 5.22: Comparison of frequency responses at P = 7.5 MW for semi-analytical model with and without mixing, the numerical model from Ch. 2, an ORNL model and step test experimental data.

5.7.2 Discussion

A K value of 3×10^5 W/m/K or greater was found to introduce sufficient mixing in the numerical model primary circuit in order to suppress the recirculation feature. Testing higher K values was not pursued due to increasing computational cost and an apparent asymptotic response to further increases in K.

Some aspect of the model physics other than mixing must be responsible for the discrepancy in the maximum gain and the phase shift at high and low frequencies between the model and experiment, as this difference exists independently of the degree of turbulent dispersion.

The difference in maximum gain may be due to the thermal feedback coefficients as this will dictate the extent to which the power can rise with the reactivity before thermal feedback effects counteract the driving reactivity signal. This may also explain the discrepancy between the phase shift of the model and experiment at low frequencies. In the limiting case of no thermal feedback, phase shift will be -90 degrees as the reactor power can increase for a full 180 degrees of the driving external reactivity signal until the net reactivity drops below zero. In the case of strong feedback, the power will stop increasing soon after the reactivity rises above zero, similar to the example shown in Fig. 5.1.

Parametric sensitivity analysis on the temperature feedback coefficients for the fuel and graphite, α_f and α_g, was performed using the semi-analytical model in order to ascertain the effect of changing the overall temperature feedback on the frequency response. These results are presented in the next section.

An additional difference between the model and experiment is the neglect of a secondary circuit in the models. Comparison of models with and without the secondary circuit for MSRE on ^{233}U fuel [85] showed a change in frequency response below approx. 0.05 rad s^{-1}. The effect of including the secondary circuit was to decrease the maximum magnitude of the gain and a more negative phase shift, which if applied to this ^{235}U-fuelled system would increase the difference between model and experimental results. Furthermore, sensitivity analysis conducted on a model with a secondary circuit showed sensitivity to the secondary circuit radiator heat transfer coefficient at low frequencies [33].

Assignment of a uniform delayed neutron importance with respect to location may explain the difference in phase shift at higher frequencies (above $\omega = 10^{-1}$ rad s^{-1}). Currently the decay of a precursor contributes equally to the total neutron population regardless of the decay location. A more accurate reactor model using spatially-dependent neutron kinetics would be capable of modelling these processes - for example solution of the neutron diffusion equation with multiple energy groups, or the Boltzmann transport equation. Such approaches were not pursued in this work primarily due to the software development cost. Other modelling efforts have used these more detailed models of reactor kinetics but have not combined them with more detailed models of primary circuit mixing discussed above [87, 88, 64, 89], or have only accounted for mixing between radial segments of the flow exiting a channelled core [61]. Attempts at coupling CFD models to neutron transport for MSRE have encountered modelling issues [90]. However a detailed discussion of these issues is beyond the scope of this thesis.

Another investigation has been performed at relatively high frequencies on ^{233}U fuel [81], however the phase shift when compared with the ORNL model and later analysis of experimental results [3, 86] decreased rapidly towards -90° above $\omega = 0.5$ rad s^{-1}, in contrast to the model presented in this work.

A possible improvement to the numerical model could be to use pseudo-random binary sequences (PRBS) in order to perturb the system. This may shorten the runtime and therefore the computational cost. Techniques exist to boost the signal-to-noise ratio at the frequencies of interest and to minimise non-linear effects during measurements [91]. Minimising non-linear effects is relevant to the stability analysis discussed in Section 5.9, which is based on the theory of linear time-invariant (LTI) systems. Linearisations of the governing equations are only valid for small deviations from a steady state.

5.8 Sensitivity Analysis of Frequency Response Using Semi-Analytical Model

The sensitivity of the semi-analytical frequency response to changes in model parameters was assessed at multiple power levels. This was achieved by varying all the parameters around their nominal values and recording the fractional change in response relative to the fractional change

in the parameter under study.

The parameters varied were:

(i) temperature-dependent reactivity coefficient of the fuel (α_f)

(ii) temperature-dependent reactivity coefficient of the graphite (α_g)

(iii) specific heat capacity of the fuel ($C_{p,fuel}$)

(iv) rate of heat transfer between the fuel and graphite ($h_{f,g}$)

(v) heat transfer coefficient in the primary heat exchanger ($h_{H.E.}$)

(vi) fraction of fission energy deposited in the fuel (p_f)

(vii) fraction of fission energy deposited in the graphite (p_g)

(viii) mean neutron generation time (Λ)

5.8.1 Sensitivity to Changes in Fuel Temperature Coefficient of Reactivity (α_f)

Figure 5.23 shows the sensitivity of frequency response to changes in the fuel temperature coefficient of reactivity (α_f). The general effect of increased temperature-dependent feedback in the fuel is a reduction in gain with corresponding increase in phase shift at most frequencies tested. This effect becomes more pronounced at higher power levels, as the fuel is heated to a greater degree as it passes through the fissioning regions of the vessel.

For driving reactivities close to the the recirculation frequency ($\omega \sim 0.25$ rad s^{-1}), hotter fuel reenters the vessel coinciding with a rising reactivity in the core, however temperature-dependent feedback reduces the total reactivity and so the power drops. This causes a decrease in gain - the stronger the negative feedback, the greater the reduction in gain.

Some frequencies exhibit a slight increase in gain in response to increased α_f. In these cases, the driving reactivity may be out-of-phase with the circulation in the primary circuit where greater feedback leads to a decrease in power and cooling of the core which permits the power

to rise higher at a different point in the reactivity cycle before thermal feedbacks can override the reactivity insertion.

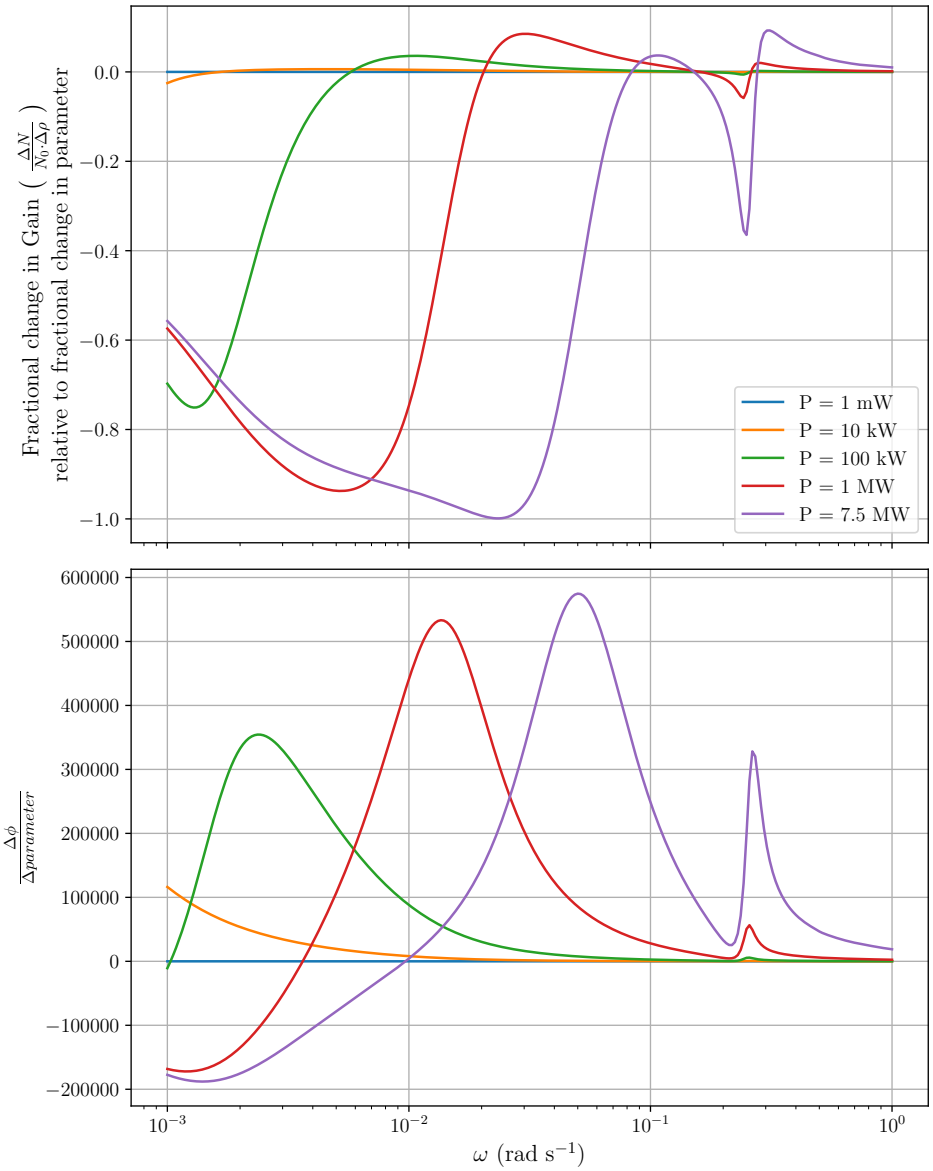

Figure 5.23: Frequency response sensitivity to change in α_f, with increasing reactor power. $\frac{\Delta \phi}{\Delta parameter}$ = absolute change in phase shift with respect to absolute change in parameter. This was chosen to avoid a singularity in the equation for relative change in phase shift with respect to relative change in parameter.

5.8.2 Sensitivity to Changes in Graphite Temperature Coefficient of Reactivity (α_g)

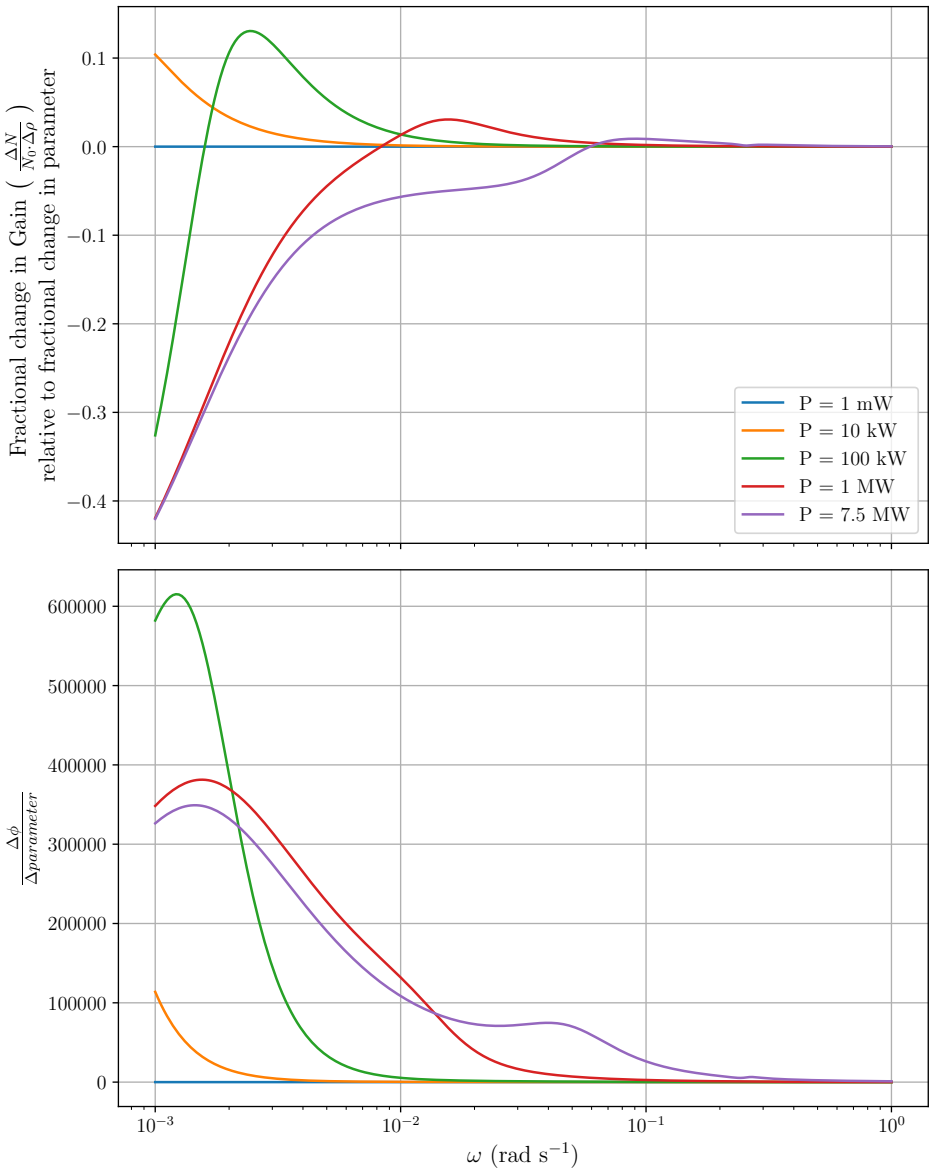

Figure 5.24: Frequency response sensitivity to change in α_g, with increasing reactor power. $\frac{\Delta\phi}{\Delta parameter}$ = absolute change in phase shift with respect to absolute change in parameter.

Similarly, the general effect of increasing the temperature feedback in the graphite is a decrease in gain as shown in Figure 5.24, with some slight increases at certain frequencies.

5.8.3 Sensitivity to Changes in Fuel Specific Heat Capacity ($C_{p,fuel}$)

The changes in frequency response with respect to $C_{p,fuel}$ are shown in Fig. 5.25. Increased specific heat capacity generally leads to an increase in gain as the system takes longer to heat up and negative reactivity feedbacks take longer to kick in. A difference in behaviour is observed between the gain and phase sensitivities at low frequencies, and those observed at higher frequencies close to the recirculation frequency. In the former case, increased $C_{p,fuel}$ leads to an increase in gain and phase shift, but for the latter, an increase in $C_{p,fuel}$ leads to an increase in gain but decrease in phase shift. This is indicative of lower feedback.

The difference in phase shift sensitivity between these frequency regions may be due to competing effects in the core and at the primary heat exchanger - at higher frequencies, around 0.06 rad s^{-1}, an increase in $C_{p,fuel}$ leads to the aforementioned slower heating of the core and primary circuit. The reduced feedback leads to a more negative phase shift as the power may increase for a larger proportion of the first (positive) half of the driving reactivity cycle. At lower frequencies, around 10^{-2} rad s^{-1}, reduced cooling of the fuel at the heat exchanger leads to increased feedback and therefore more positive phase shift. This effect is however out-competed by the reduced heating of the core so the gain sensitivity is still positive at this frequency.

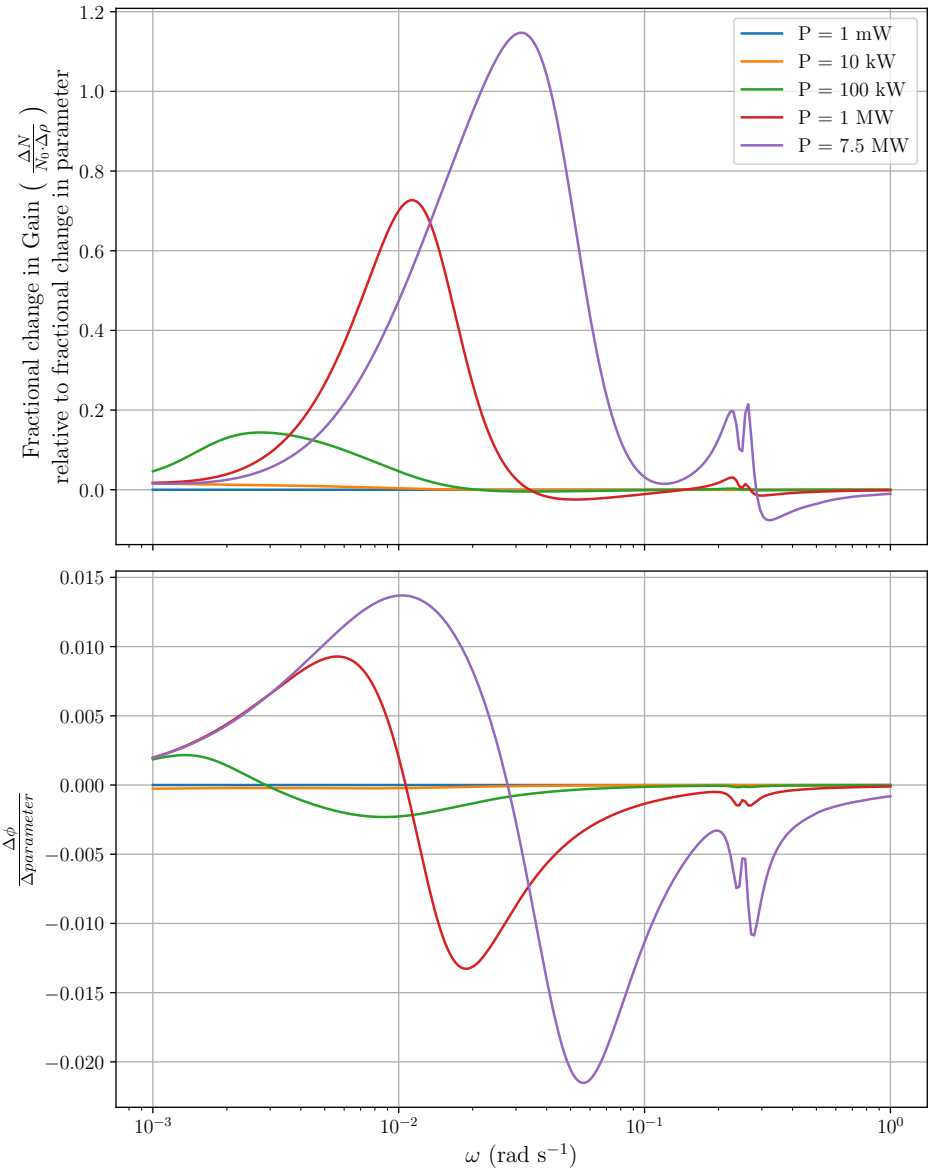

Figure 5.25: Frequency response sensitivity to change in $C_{p,fuel}$, with increasing reactor power. $\frac{\Delta \phi}{\Delta parameter}$ = absolute change in phase shift with respect to absolute change in parameter.

5.8.4 Sensitivity to Changes in Fuel-Graphite Heat Transfer Coefficient ($h_{f,g}$)

Figure 5.26 shows the sensitivity to changes in the fuel-graphite heat transfer coefficient, $h_{f,g}$. As discussed in Section 4.2.2, changes to $h_{f,g}$ influence the steady state difference in temperature between the fuel and the graphite. At the lowest frequencies tested, near 10^{-3} rad s^{-1}, the system has time to reach a quasi-equilibrium with the slowly-increasing reactivity, hence the

system has greatest sensitivity at these low frequencies.

A greater rate of heat conduction between fuel and graphite leads to a reduced equilibrium graphite temperature (and therefore by conservation of energy hotter fuel). Given the greater magnitude of α_f vs α_g this leads to an overall increase in negative feedback and the subsequent reduction in gain observed in Fig. 5.26.

This effect is most pronounced at 100 kW, with the reduction in gain becoming less severe in the megawatt range. A reduction in phase shift is also observed at these low frequencies. As the reactor power increases into the megawatt range, this effect becomes slightly less pronounced. This may be due to the competing effects of fission power deposition in the graphite and the heat transfer to the fuel, however additional examination of transient runs with oscillating reactivity was not conclusive.

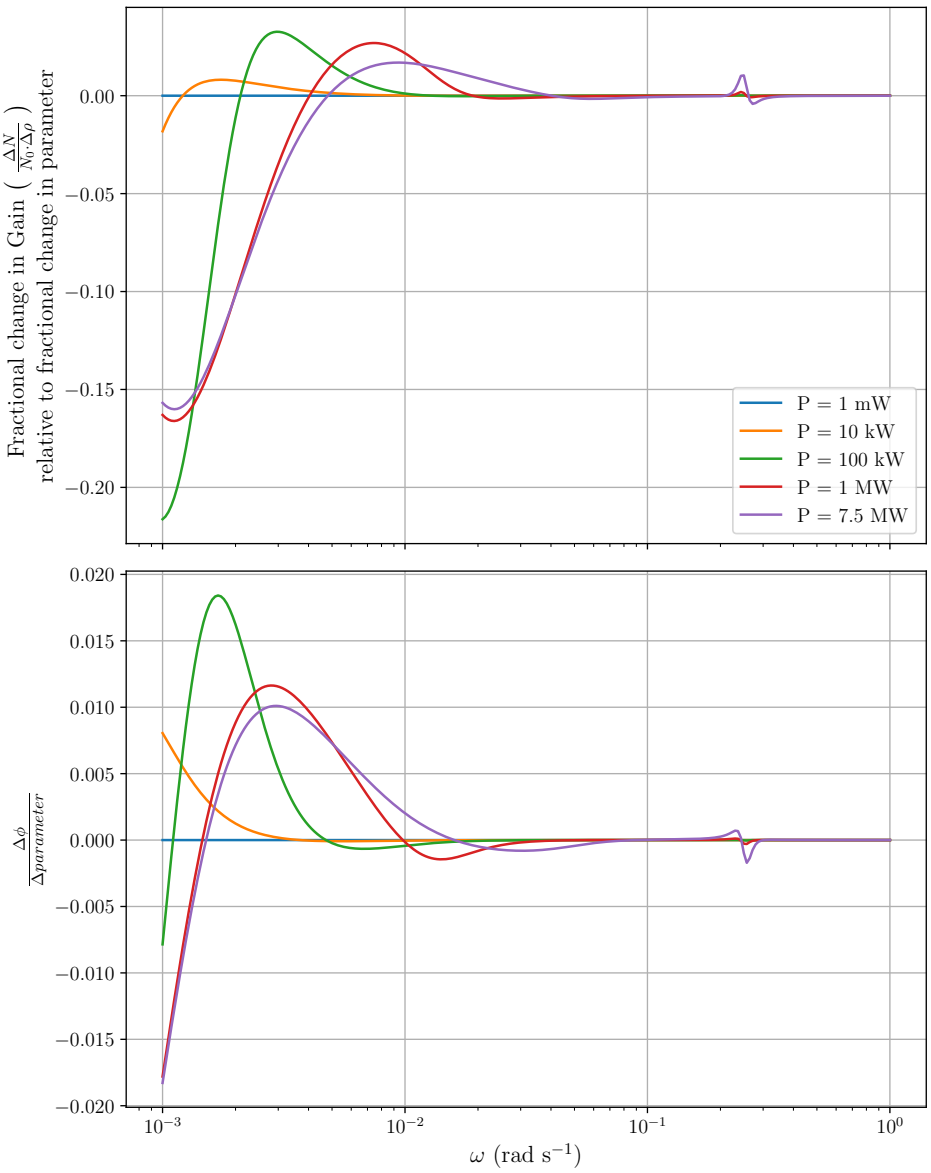

Figure 5.26: Frequency response sensitivity to change in $h_{f,g}$, with increasing reactor power. $\frac{\Delta \phi}{\Delta parameter}$ = absolute change in phase shift with respect to absolute change in parameter.

5.8.5 Sensitivity to Changes in Heat Exchanger Heat Transfer Coefficient ($h_{H.E.}$)

Figure 5.27 shows the sensitivity of the frequency response to changes in the heat exchanger heat transfer coefficient, $h_{H.E.}$. Increased heat rejection at the heat exchanger leads to a slower system temperature increase and smaller negative reactivity, permitting greater power increase

and therefore greater gain. This reduction in feedback causes the change in phase shift to be negative with respect to increased heat exchanger capacity. This relationship between core and heat exchanger is likely responsible for the abrupt change in gain and phase sensitivity close to the recirculation frequency.

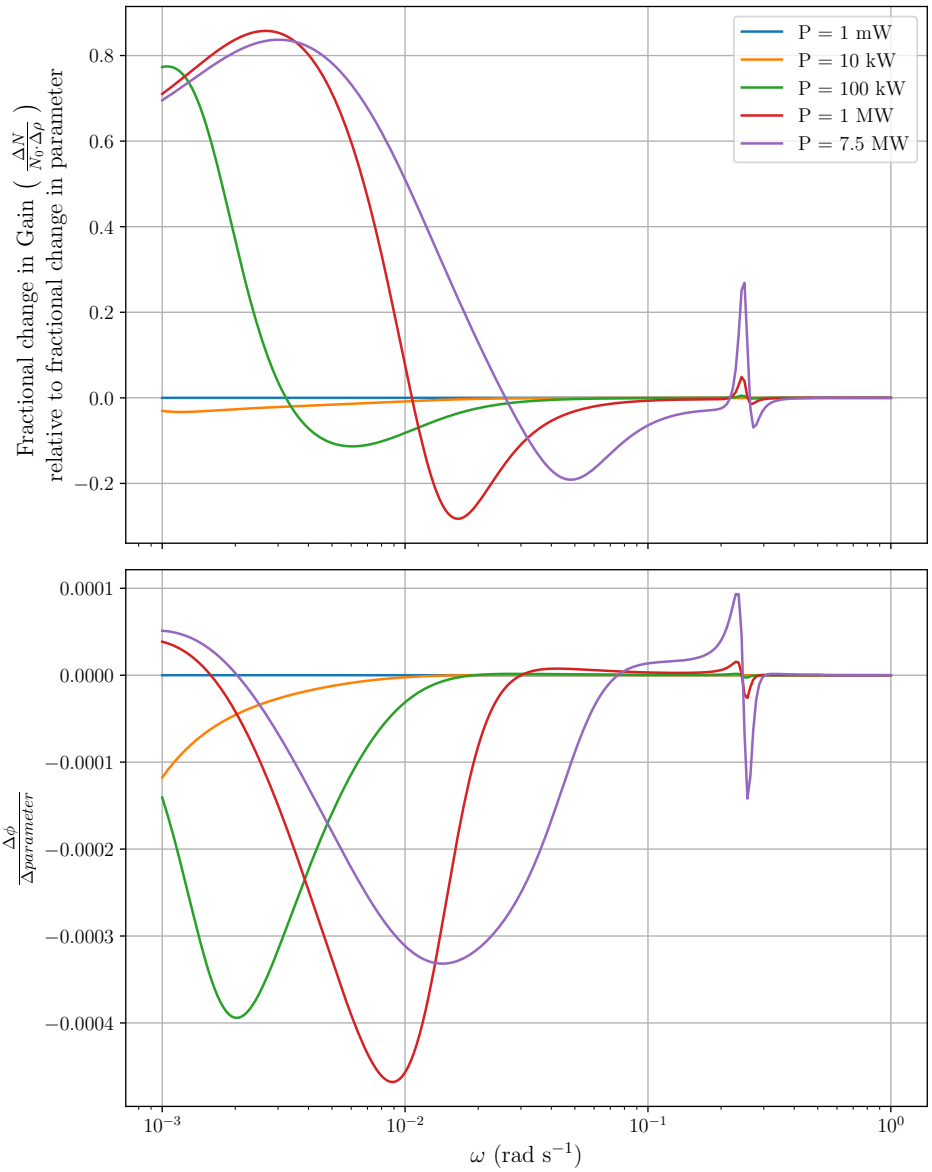

Figure 5.27: Frequency response sensitivity to change in $h_{H.E.}$, with increasing reactor power. $\frac{\Delta \phi}{\Delta parameter}$ = absolute change in phase shift with respect to absolute change in parameter.

5.8.6 Sensitivity to Changes in Deposited Power Fractions (p_f and p_g)

Figures 5.28 and 5.29 show the sensitivities of the frequency response to changes in the fraction of fission power deposited in the fuel (p_f) and graphite (p_g). They are closely related given the sum of deposited power fractions must sum to 1.0. An increase in power deposited in the graphite at very low frequencies leads to a decrease in gain. This may be due to the limited rate at which the graphite can lose heat to the fuel - if an increase in core power causes the graphite to heat up, it will remain hotter (and therefore exert negative reactivity) for a period of time before this energy can be transferred to the fuel and on to the secondary circuit. As discussed in Section 5.8.4, changes to the relative temperatures of fuel and graphite will be most apparent in the steady or quasi-steady state, hence the greatest sensitivity in the frequency responses at low frequencies.

At intermediate frequencies, there is a slight increase in gain and decrease in phase shift, though this effect is smaller in magnitude. A reduction in p_g (with corresponding increase in p_f) will cause a reduction in gain via greater heating of the fuel with its stronger temperature feedback coefficient.

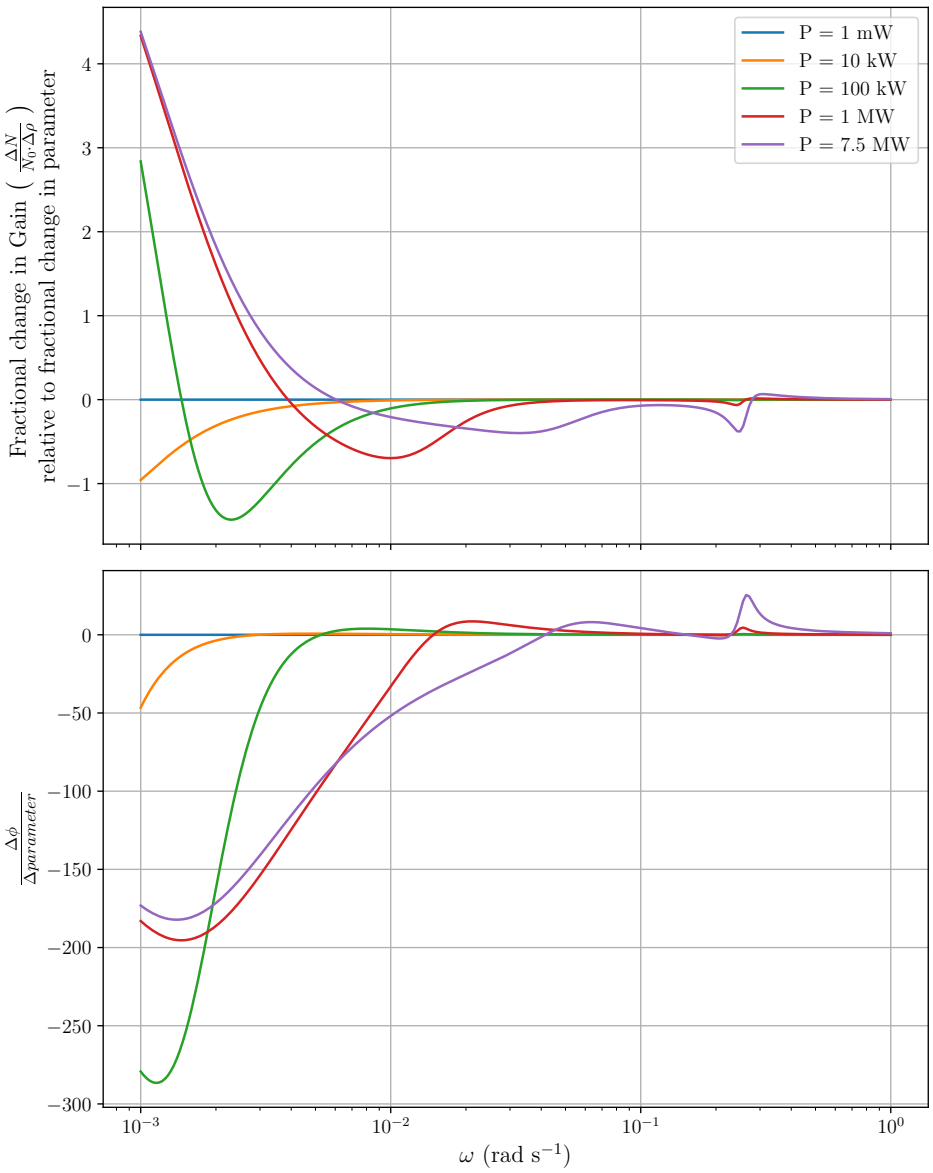

Figure 5.28: Frequency response sensitivity to change in p_f, with increasing reactor power. $\frac{\Delta \phi}{\Delta parameter}$ = absolute change in phase shift with respect to absolute change in parameter.

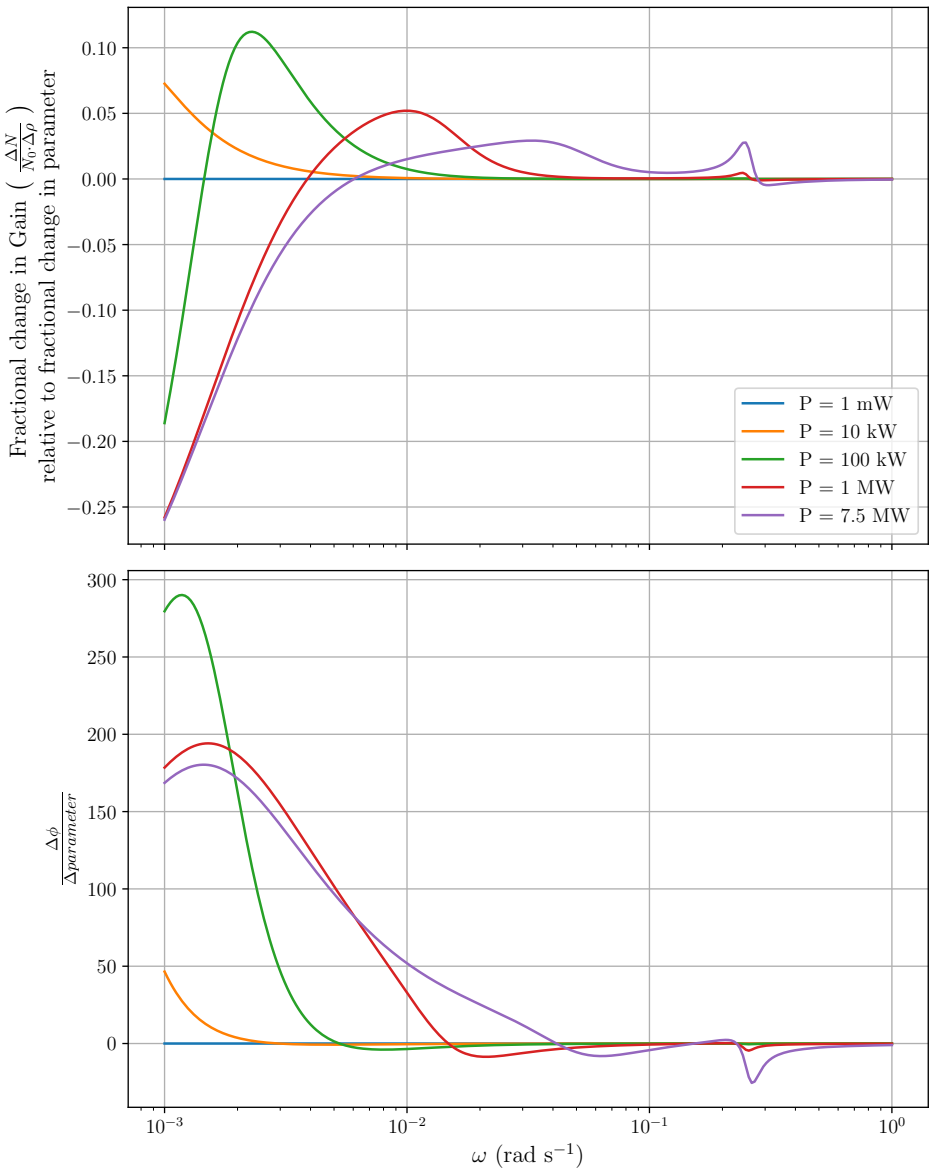

Figure 5.29: Frequency response sensitivity to change in p_g, with increasing reactor power. $\frac{\Delta \phi}{\Delta parameter}$ = absolute change in phase shift with respect to absolute change in parameter.

5.8.7 Sensitivity to Changes in the Mean Generation Time (Λ)

The effect of changes to the mean neutron generation time (Λ) is shown in Fig. 5.30. Increasing Λ leads to reduced gain and feedback at most frequencies and power levels, with the exception of mid frequencies in the megawatt range, though the magnitude of this effect compared to varying other model parameters is small. A longer mean generation time results in the reactor

power increasing at a slower rate in response to changes in reactivity with the effect becoming more pronounced at higher frequencies.

A distinct feature is visible at the primary circuit recirculation frequency in the sensitivity plots for gain and phase shift - a dip in gain at low powers and then an increase at higher powers. A slower increase in core heating rate due to the longer mean generation time may be combining with the increased reactivity due to cool fuel entering from the heat exchanger, leading to the decrease in sensitivity observed at the recirculation frequency (gain sensitivity returning closer to zero). A small change in phase shift is observed either side of the recirculation frequency, at the maximum power level.

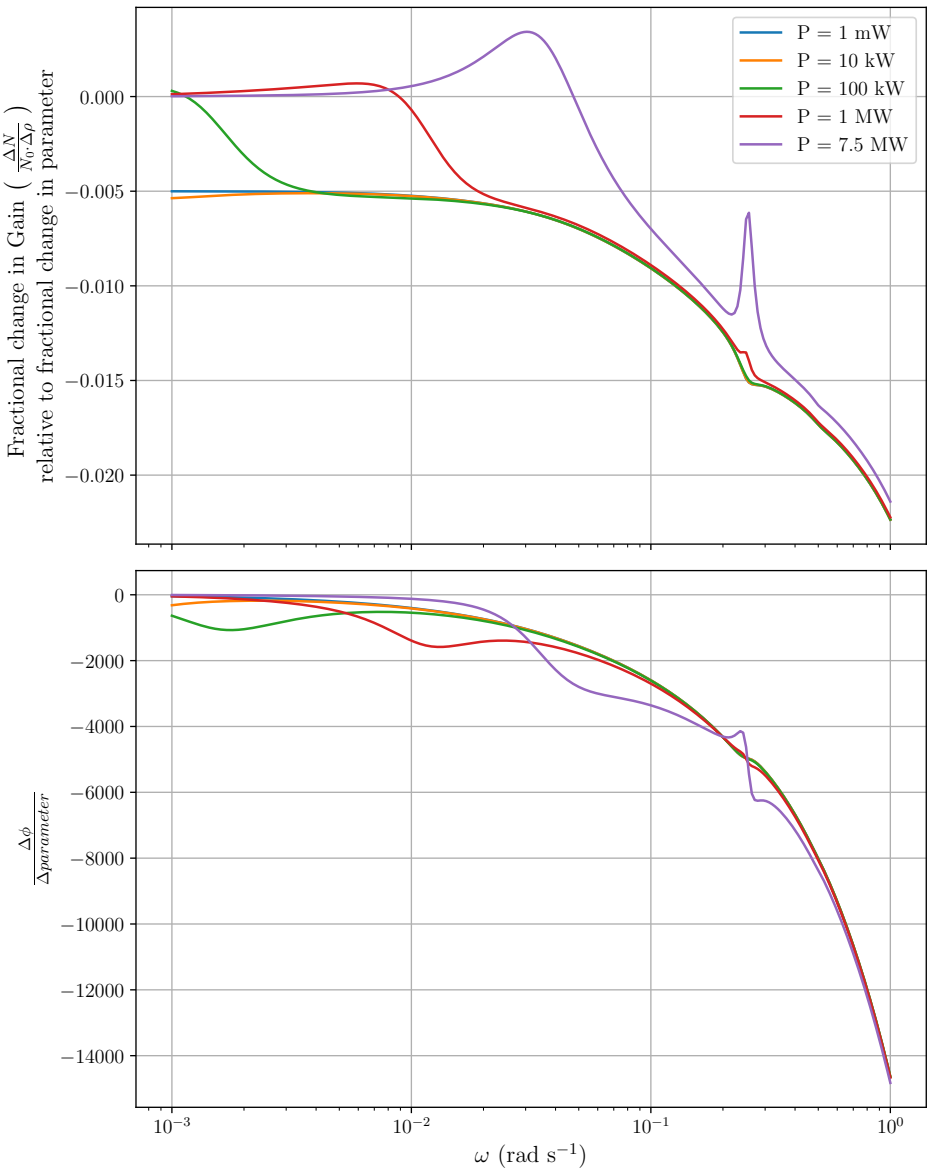

Figure 5.30: Frequency response sensitivity to change in Λ, with increasing reactor power. $\frac{\Delta \phi}{\Delta parameter}$ = absolute change in phase shift with respect to absolute change in parameter.

5.8.8 Discussion on Frequency Response Sensitivity Analysis

Generally the sensitivities presented above agree with previous investigations [33, 86], however two notable cases do not - the sensitivities of the frequency responses to changes in the temperature coefficient of reactivity for the fuel, α_f, and that of the graphite, α_g. In the cited works, at low frequencies the gain increases with respect to increases in the temperature feed-

back coefficients. According to the definitions of the sensitivities presented in [33] and [86], this implies that increasing α_f would increase the amplitude of power oscillations in response to driving external reactivity. This would contradict the physical understanding developed in this work and the sensitivities shown in Figure 5.23 - the ORNL sensitivities are similar in shape but mirrored in the frequency axis.

Figure 5.31 shows the frequency responses for the semi-analytical system with the standard α_f value (8.46×10^{-5} K^{-1}) plus two additional frequency response plots with 50% lower and and 50% higher fuel temperature feedbacks for comparison. At frequencies below $\sim 6 \times 10^{-2}$ rad s^{-1}, the trend of increased feedback causing lower gain is readily apparent. This supports the argument that the ORNL data may be plotted incorrectly as other sensitivities shown in Kerlin et al. (1971) [86] are similar, for example the sensitivity to fuel specific heat capacity, heat transfer coefficient at the heat exchanger and the mean generation time.

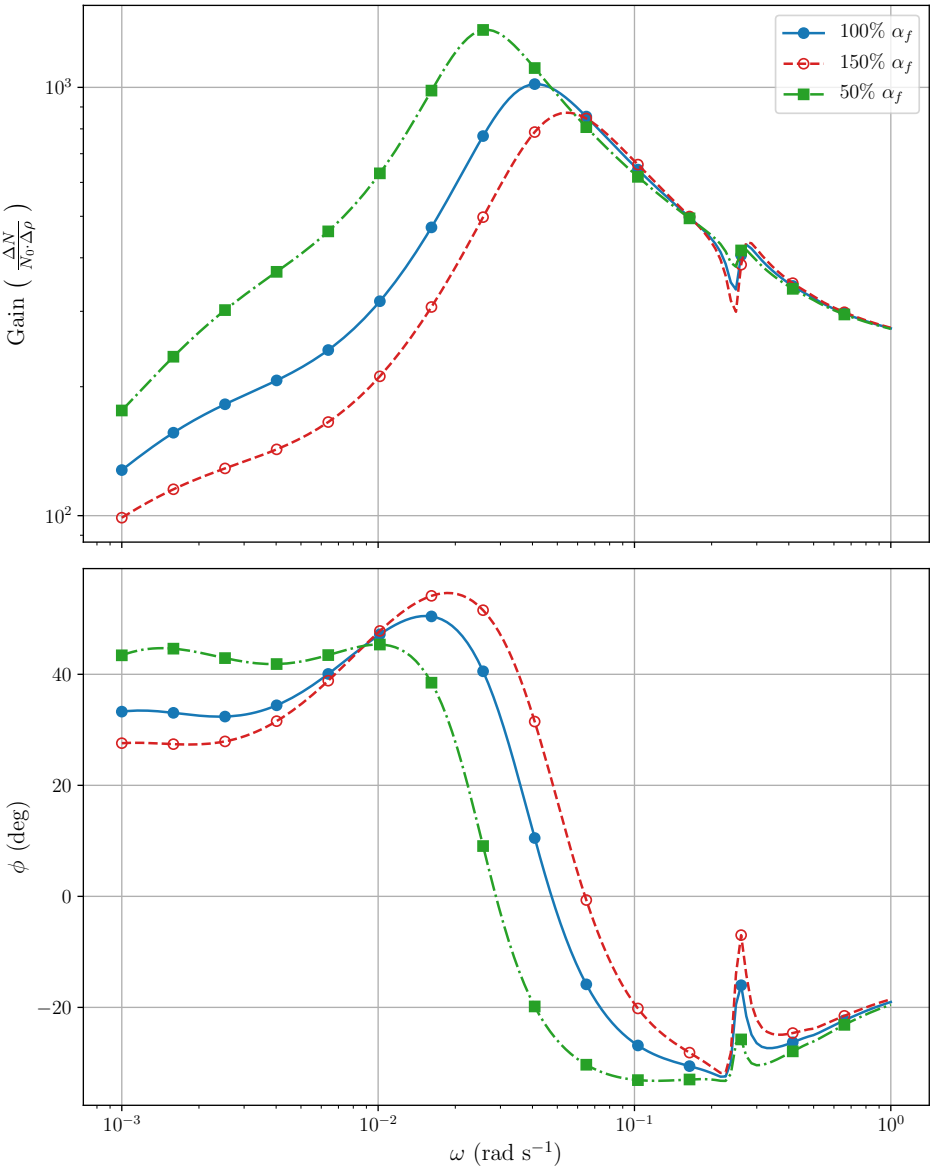

Figure 5.31: Frequency response for three models with 50%, standard (100%), and 150% α_f values.

5.9 Linear Stability Analysis

5.9.1 Introduction

An engineering system must be stable in order to be controlled and to avoid repeatedly stressing its components. For the purposes of this discussion, stability implies the tendency of a system,

initially in a steady state, to return to that steady state after some small perturbation in the initial condition. This is important for operation to ensure that small fluctuations in system variables such as power, pressure, temperature do not cause runaway positive feedbacks and large deviations which could damage the components in the system.

For linear time-invariant (LTI) systems, the eigenvalues of the Jacobian matrix must have negative real parts if the system is to be stable - this ensures that transient components decay to zero over long timescales, else the contribution of that mode will grow without bound (the Routh-Hurwitz stability criterion). Note that stability under this criterion does not eliminate the possibility of decaying oscillations that are of sufficient magnitude to damage the reactor. More complex self-driving oscillations and non-linear stability analysis will not be analysed in this section.

5.9.2 Example Stability Analysis

A small example is shown below for a simplified circulating fuel system with thermal feedbacks.

Equations

$$\frac{dN(t)}{dt} = \frac{\rho - \beta}{\Lambda} N(t) + \lambda C_{core}(t) m_{core}$$

$$\frac{dC_{core}(t)}{dt} = \frac{\beta}{\Lambda m_{core}} N(t) - \lambda C_{core}(t) + \frac{\dot{m}}{m_{core}} \Big(C_{external}(t) - C_{core}(t) \Big)$$

$$\frac{dC_{external}}{dt} = \frac{\dot{m}}{m_{external}} \Big(C_{core}(t) - C_{external}(t) \Big) - \lambda C_{external}(t)$$

$$\frac{dT(t)}{dt} = \frac{\chi_f N(t)}{\bar{\nu} \Lambda C_{p,f} m_{core}} - \big(T(t) - T_{sec} \big) r_{loss}$$

$$\rho = \rho_{external} - \alpha \Big(T - T_{ref} \Big)$$

Linearised Equations

$$\frac{d\delta N}{dt} = \frac{1}{\Lambda}\left[\rho_0 \delta N + \delta\rho N_0 - \beta\delta N\right] + \lambda\delta C_{core} m_{core}$$

$$\frac{d\delta C_{core}(t)}{dt} = \frac{\beta}{\Lambda m_{core}} N(t) - \lambda\delta C_{core}(t) + \frac{\dot{m}}{m_{core}}\left(\delta C_{external}(t) - \delta C_{core}(t)\right)$$

$$\frac{d\delta C_{external}}{dt} = \frac{\dot{m}}{m_{external}}\left(\delta C_{core}(t) - \delta C_{external}(t)\right) - \lambda\delta C_{external}(t)$$

$$\frac{d\delta T}{dt} = \frac{\chi_f \delta N}{\bar{\nu}\Lambda C_{p,f} m_{core}} - \delta T r_{loss}$$

$$\delta\rho = -\alpha\delta T$$

Eigenvalues as a Function of System Power

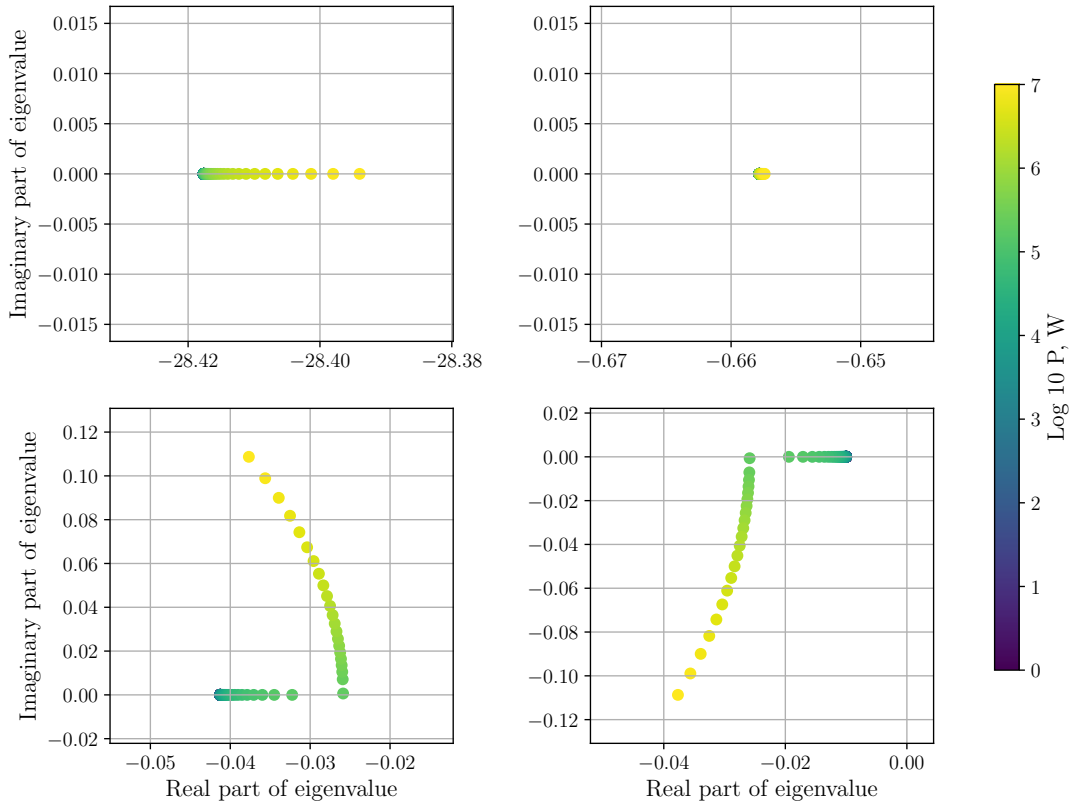

Figure 5.32: Real and imaginary components of the eigenvalues for the simplified circulating reactor system, against reactor power.

Above a power level of approx. 200 kW, the third and fourth eigenvalues become complex conjugates. This is indicated by their real parts becoming equal, and their imaginary parts becoming reflected in the real axis (Figure 5.33). Above this power level, the system oscillates as it settles back to steady state. Figure 5.34 shows the system behaviour when perturbed by a 0.5 K cooling of the system temperature. Note the rate of decay and frequency of the oscillations is consistent with the data from Figure 5.33, with an exponential fitted with the exponent equal to the real part of the complex conjugate eigenvalue at P= 10 MW.

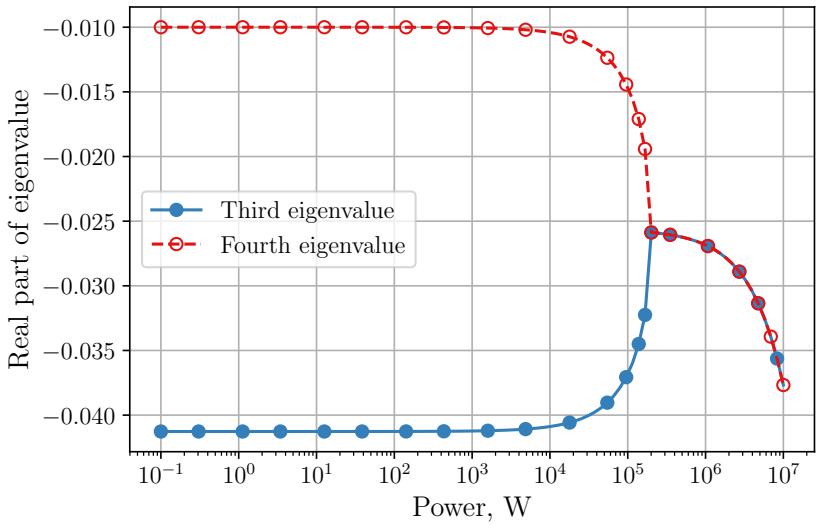

(a) Real parts

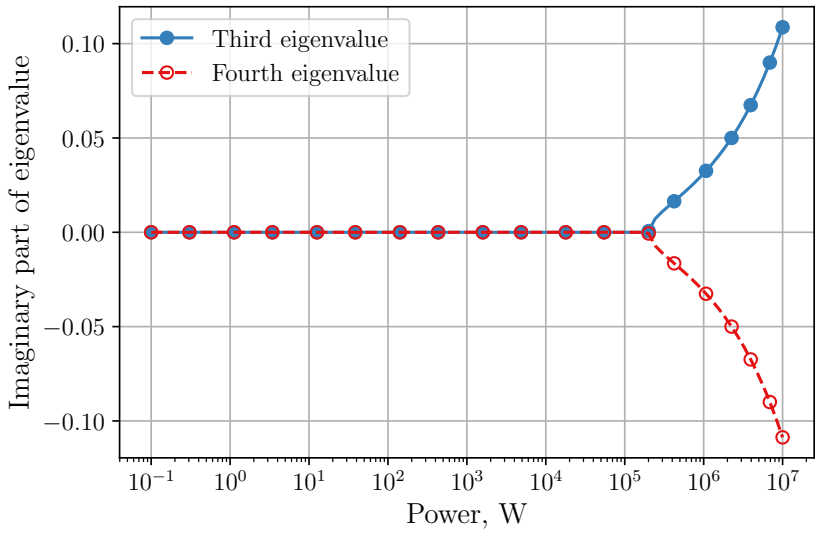

(b) Imaginary parts

Figure 5.33: Components of the complex third and fourth eigenvalues for simplified circulating fuel system with thermal feedbacks.

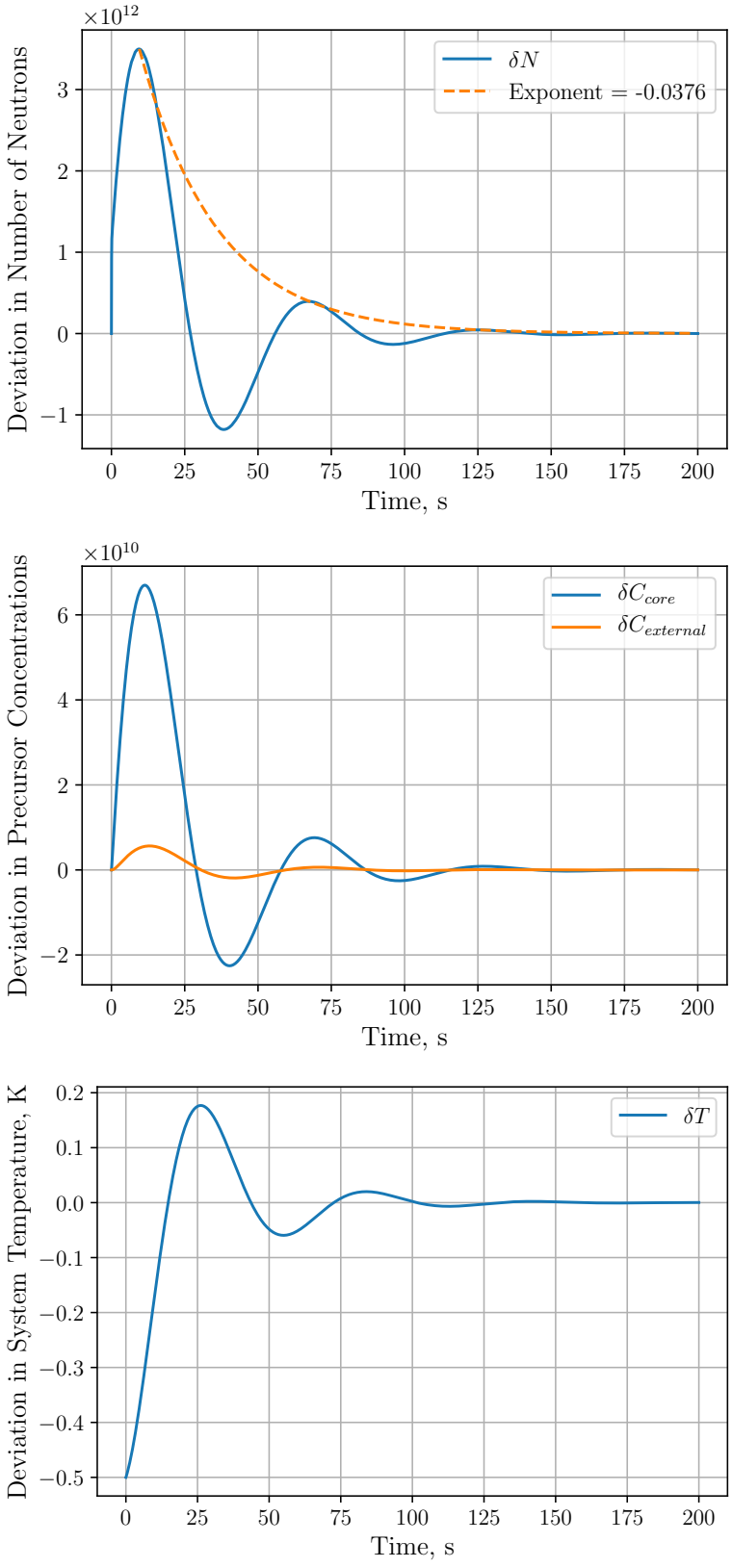

Figure 5.34: Transient response to 0.5 K system cooling, initial power 10 MW.

5.9.3 Larger Linearised System Representing MSRE Dynamics

The analysis methods described above will be applied to the more realistic system derived in Appendix A.5 with a larger number of equations. This model was designed to capture the physics of the numerical model in Ch. 2 but also be amenable to solution via semi-analytical methods.

Figure 5.35 shows the real parts of the eigenvalues of the linearised system which are negative both at very low power and at maximum design power, thus satisfying the criterion for system stability. Subsequent examination will focus on the eigenvalues with the smallest magnitudes, that is, the modes of the system that decay most slowly.

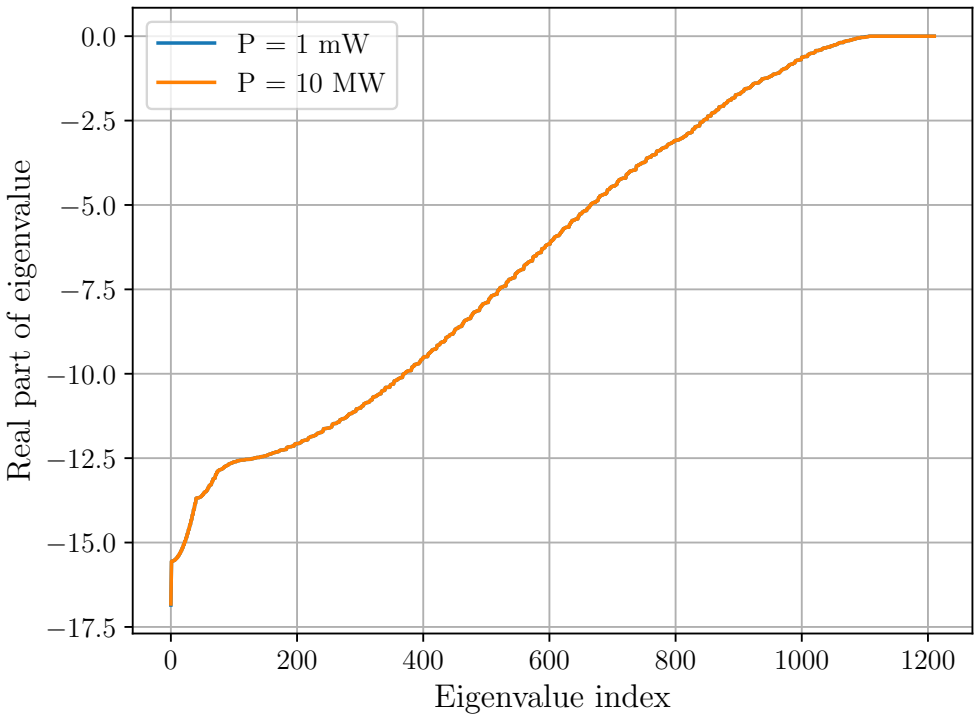

Figure 5.35: Real parts of eigenvalues for the linearised system, at very low power (P = 1 milliwatt) and maximum power (P = 10 MW). Note the P = 10 MW line is superimposed on the P = 1 mW line.

Figure 5.36 compares the characteristic decay time and period of oscillation of the system eigenvalues from zero power up to full operational power (approx. 7.5 MW). As the reactor

power increases, the characteristic decay time of the eigenvalue with largest real part (most relevant to stability) and the period of oscillation decrease. This indicates an increase in the stability of the system. Eigenvalues with real parts smaller than 10^{-6} were not plotted due to limits in solver precision and engineering relevance (a mode with decay time of weeks will in practice be represented as a reactivity bias).

Comparison with transients observed at the conclusion of frequency response tests in the MSRE program (Figs. 5.4 and 5.6 in Ch. 5) shows qualitative agreement but differences in the period of oscillation. For example, relaxation of the system to equilibrium after a transient at $P = 1$MW involved a damped sinusoid, maximum deviation in power approx. 10 percent, with a period of about 8 minutes (480 s). The analysis show in Fig. 5.36 shows the slowest-decaying eigenvalue with a period of 664 s, and a characteristic decay time of 154 s. After three periods (approx. corresponding to the period of the experimentally observed transient) the mode would have decayed to about 5 percent of its original power - this is consistent with the observed data, though the calculated period is longer.

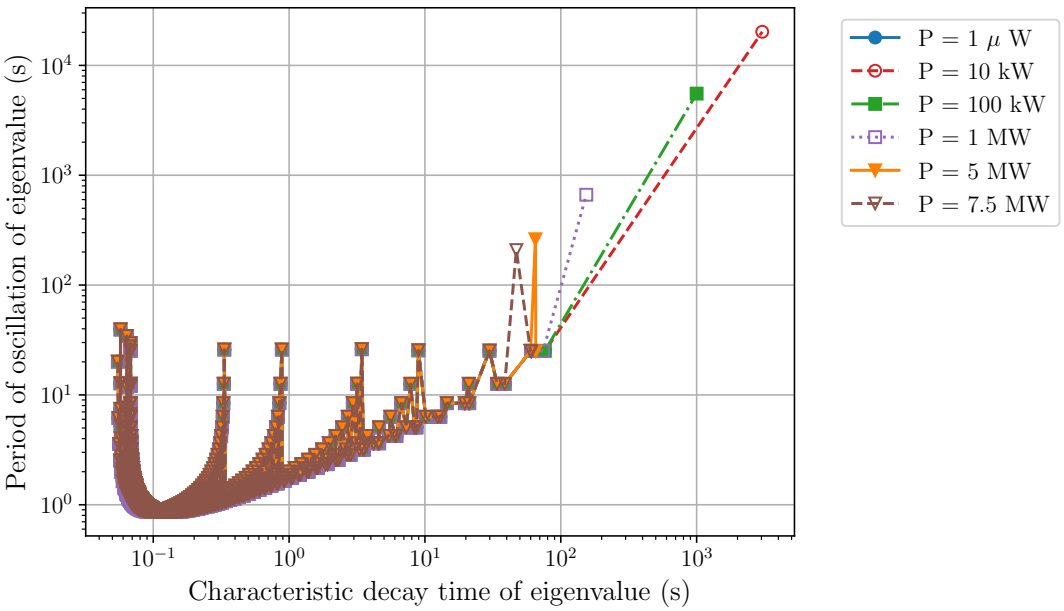

Figure 5.36: Characteristic decay time and period of oscillation of eigenvalues between 1 μW and 7.5 MW.

5.9.4 Discussion

Analysis of the MSRE system using a linearisation of the semi-analytical model contributes to the argument that the system is stable at all powers tested, based upon the Routh-Hurwitz criterion. This does not however rule out the possibility of oscillations of a large and damaging magnitude in the process of decaying to a steady state, the possibility of a steady state only existing at a damaging power or mechanical condition, nor the possibility of a self-driving oscillation.

Eigenvalue analysis must be paired with analysis of the transient behaviours of the system in order to assess the manner in which the system settles to a steady condition (as discussed at length in earlier chapters), if at all. An example transient in response to vessel inlet cooling is shown in Appendix A.5.

A future extension to the model might include radiation transport, for example using neutron diffusion. This would permit the modelling of gas bubbles which are known to circulate in the primary circuit and contribute to noise in the power level. Measurements showed that increased void fraction in the core resulted in increased neutron noise [44]. Voids in the core region reduce the local concentration of fissile material which may cause an increase or decrease in reactivity depending on whether or not the core is under- or over-moderated. In terms of stability this would manifest itself as a change in the eigenvalue related to the fundamental flux mode, i.e. k_{eff}.

Stability with respect to the presence of voids is important in other reactor types, notably the RMBK-1000. Coolant voids reduced the absorption of neutrons in the water, while fuel and moderator were retained in the core. This resulted in a positive reactivity feedback that contributed to the severe accident at the Chernobyl Nuclear Power Plant in 1986 [92].

Chapter 6

Modelling of MSR Startup Dynamics

This chapter expands the description of the molten salt reactor behaviour to include stochastic modelling of fission chains during reactor startup. The numerical model described in previous chapters was used to establish just-safe deterministic combinations of source strength and reactivity ramp rate that were compared against the CALLISTO-SPK (CALculation of Low Intensity STartup Operations - Stochastic Point Kinetics) code [93].

6.1 Stochastic Effects During Startup

6.1.1 Neutron Sources

Neutron sources in a reactor exhibit stochastic behaviour, that is, there is some uncertainty over the number of neutrons emitted in each emission event and the time at which those neutrons are released into the system. These events may only be described in a probabilistic fashion.

The number of neutrons released in each interaction may vary from zero (corresponding to absorption), one (corresponding to scattering or fission) up a maximum of about 7 neutrons. This variation in the number of progeny and their time of release (via the decay of delayed neutron precursors) contributes to fluctuations in the number of subsequent fissions and therefore fluc-

tuations in the reactor power. These fluctuations are known as 'zero power reactor noise' and are purely nuclear in origin.

Zero power reactor noise is distinct from 'power reactor noise' which is associated with mechanical issues in the core such as flow-structure interactions (FSI) between control rods, fuel rods and the coolant. In addition, the presence of dynamically-evolving voids within the coolant may induce random reactivity and power variations [94].

6.1.2 The Survival or Extinction of Fission Chains Sponsored by Neutron Sources

Initially, under subcritical or near-critical conditions, neutrons may initiate short-lived fission chains that die out after a limited number of generations. The neutron is the carrier of the chain reaction and so once all the neutrons have been absorbed or leak the chain reaction stops (also referred to as chain 'extinction'). Core power will remain zero until another source neutron is introduced.

A weak neutron source cannot sponsor many independent fission chains, so that when some are inevitably extinguished by neutron absorption or leakage, the fluctuations in the power level are large with respect to the mean. A high-intensity neutron source is capable of sponsoring many independent fission chains. These overlap leading to a leading to a large neutron population with fluctuations that are small with respect to the mean - the hallmark of a deterministic system. Deterministic kinetic equations may be used to describe the time evolution of the system, for example the point-kinetic equations from Chapter 2.

If the reactivity increases sufficiently for the system to become critical or supercritical, a persistent chain of fissions may emerge. Note that there remains a finite probability of a fission chain being extinguished even if the system is supercritical [94].

6.1.3 Ramp Reactivity Insertions with Low Source

For systems with weak sources, it is possible for significant time to elapse before persistent fission chains emerge. The later the time at which the persistent chains emerge, the higher the reactivity due to the ongoing ramp insertion. The neutron population may now increase at a

faster rate.

Large neutron populations are required in order to exert significant reactivity feedback and there is an associated time lag while components heat up and expand. This permits the power to rise to very high levels before the feedbacks kick in and end the transient. In addition, if the reactivity insertion ceases when the power burst is detected, a power rise that occurs later will have to deposit a larger amount of energy in the core in order to counteract the ramp having reached a later and correspondingly greater reactivity.

Thus, fluctuations in population at low power level can exert a significant influence on the time at which a power increase is observed, the rate of power increase, the magnitude of the peak power and energy deposited in the core during core startup [95].

The relationship between source strength and peak power is also observed in deterministic models though it is less pronounced. A startup transient where the number of neutrons at the end of the reactivity ramp is significantly lower than predicted by a purely deterministic model has been described as a 'rogue transient' [96].

6.1.4 Related Dangers During Reactor Startup

A core with a low intrinsic neutron source will have a small minimum shutdown power. Assuming a long shutdown period and neglecting any delayed neutron precursors, the shutdown power may be approximated using the following equation:

$$P = \frac{-S\Lambda}{\rho}, \tag{6.1}$$

where P = the core power level, S = the effective intrinsic neutron source (taking into account spatial extent), and ρ = the subcritical reactivity of the core.

A small shutdown power may not produce sufficient flux to register on the source range detectors which typically have a detection range of 1 to 10^6 counts per second at the detector location. This could impair the ability of the operator or automatic control system to determine the power level. This situation is referred to as a 'blind reactor start-up' [97] and is considered a

dangerous condition due to lack of indication from the detectors.

The operator or control system might withdraw the control rods in a bid to increase the core power, however no signal is detected due to extinction of the fission chains. The reactor could now be on a short period (the time taken for the fundamental flux mode to increase by factor e).

If an intrinsic source neutron were to be emitted at this point and sponsor a persistent fission chain it would cause a very rapid increase in reactor power before the safety systems are able to detect the burst and fully initiate a scram [98]. Control rods cannot be inserted instantaneously, instead taking some time to fall under gravity in most designs during which the power could still be rising. Excessive energy deposition on a short timescale will damage the core through overheating, either by sudden thermal expansion of core components or by boiling of the coolant with associated over-pressurisation of the primary circuit.

6.1.5 Countermeasures

Most nuclear reactors use an installed artificial startup neutron source (also referred to as an 'extrinsic' neutron source) to provide a sufficiently high source intensity to minimise the aforementioned stochastic fluctuations and ensure a reliable signal on the detectors even when the reactor is fully shut down. If this were not the case, the only source of neutrons wouid be those from the intrinsic neutron source and the resulting neutrons from subcritical multiplication within the core.

An additional precaution is to slow the rate of reactivity addition which permits the delayed neutron precursor population to build up. Each delayed neutron released by a precursor decay represents an independent opportunity to spawn overlapping fission chains. A controlled approach to criticality may be achieved using the pull-and-wait (also referred to as jog-and-wait) technique. This in practice slows the reactivity addition rate, permitting time for the rise in precursor population.

These techniques, independently or in combination, are used to reduce the risk of stochastic transients in nuclear power plant startup [96].

6.2 Modelling Stochastic Reactor Startup

Branching probability processes may be described using generating functions [99, 100]. These are a convenient mathematical representation from which statistical information can be easily obtained via differentiation.

The backwards Master equations are a system of coupled non-linear ODEs which are amenable to solution using a range of existing tools [101, 96]. This approach is used in the CALLISTO-SPK code [93] which is used for analysis in this chapter. CALLISTO-SPK can compute statistical information on the populations of neutrons and delayed neutron precursors for an arbitrary number of energy groups in a system undergoing a reactivity ramp, and return source multiplication factors (S_m), that is the increase in source strength required to reduce the probability of there being less than the mean number of neutrons in the system (and therefore potentially leading to a rogue transient) to a prescribed small probability, typically 10^{-8}.

6.3 Neutron Sources in MSRE

An intrinsic neutron source was present in the clean MSRE fuel salt due to spontaneous fissions, cosmic ray spallation neutron sources, and (α, n) reactions, primarily arising from α-decay of ^{234}U [47]. The original estimate of this source strength was approx. 4×10^5 n/s [102]. An intrinsic source calculation using the SOURCES-4C code [103] produced a value of 3.3×10^5 n/s. During MSRE commissioning, a comparison was made between the detected neutrons with a primary neutron startup source of intensity 10^8 n/s, and the counts from the intrinsic fuel source alone. Only 10 percent of the externally-supplied neutrons were expected to reach the core (estimated using the 2D diffusion code EQUIPOISE BURNOUT) [104], for an effective primary neutron startup source strength of 10^7 n/s. The intrinsic fuel source contributed 3 to 5 percent of the detected neutrons compared to the primary neutron startup source, yielding a total intrinsic neutron source strength of 3×10^5 to 5×10^5 n/s which is consistent with the calculations discussed above.

In addition, photoneutrons may be produced in ^{9}Be(γ, n) reactions when the photon energy exceeds about 1.67 MeV. This source is proportional to reactor power and runtime and can be significant many days after shutdown. The maximum photoneutron source in MSRE was of the

order of 10^{10} n/s [7].

6.4 Reactor Damage Criteria

Conventionally, reactor damage in a transient would be assessed in terms of fuel damage, for example by phase change. The boiling point of the molten salt used in MSRE is extremely high.

The reactivity insertion R_{max} required in order to raise the nuclear average fuel temperature by an amount ΔT_f^* is given by a rearrangement of the following equation,

$$R_{max} = \Delta T_f^* \alpha_f + \Delta T_g^* \alpha_g$$

$$\frac{R_{max} - \Delta T_g^* \alpha_g}{\alpha_f} = \Delta T_f^*$$

For very fast reactivity ramps, the contribution of the graphite may be neglected due to the large proportion of power deposited directly in the fuel to yield a working approximation for the reactivity insertion required.

$$\frac{R_{max}}{\alpha_f} = \Delta T_f^* \tag{6.2}$$

Maximum allowable vessel stresses for the MSRE design were determined on the basis of the ASME Unfired Pressure Vessel Code and long term creep rates. This limited the maximum operating temperature to approx. 977 K (1300 °F) [2]; however it was expected to maintain strength in short exposures to higher temperatures (maximum tested was 1255 K (1800 ° F) [105, 106, 107].

This was reduced in response to irradiation, therefore for this study the conservative maximum allowable transient temperature at the vessel exit was deemed to be 1088 K (1500 ° F). This also corresponds to the maximum temperature at which core materials were tested without

significant oxidation by the molten fluoride salt. The primary mechanism of chemical attack is by selective dissolution of elements from the alloy, notably chromium. The difference in Gibbs free energy (ΔG) between the metal phase and fluoride was a good predictor of the susceptibility of a particular element to fluoride salt attack at a given temperature [14, 32].

Assuming an initial hot zero power state at 922 K (1200 ° F) and rapid reactivity ramp, the reactivity insertion required to exceed the maximum allowed temperature is 0.014 or 2.1 Dollars.

A 'just-safe' combination of source strength and ramp rate was then determined to be the pair of inputs that did not exceed the maximum temperature as a result of the reactivity insertion. This pair can then be compared against the stochastically-safe pair generated by CALLISTO-SPK.

Example transient simulations of ramps with different source strengths and ramp rates are shown in Figures 6.1, 6.2 and 6.3. Initial conditions are minus \$0.5 subcritical. A reactivity ramp inserting 0.015 was initiated at $t = 250$s, to allow the system to equilibrate with the intrinsic source rate. A maximum ramp rate of approx. 5×10^{-4} per s was permitted without exceeding the maximum allowed temperature (indicated in the figure).

Figure 6.4 shows the maximum power obtained during the ramp for a range of different source strengths. In the first 250s of the simulation, the system equilibrates with the source under subcritical conditions. At the onset of the ramp, the power increases - a higher source will result in a lower peak power that occurs earlier due to an earlier onset of negative temperature feedbacks.

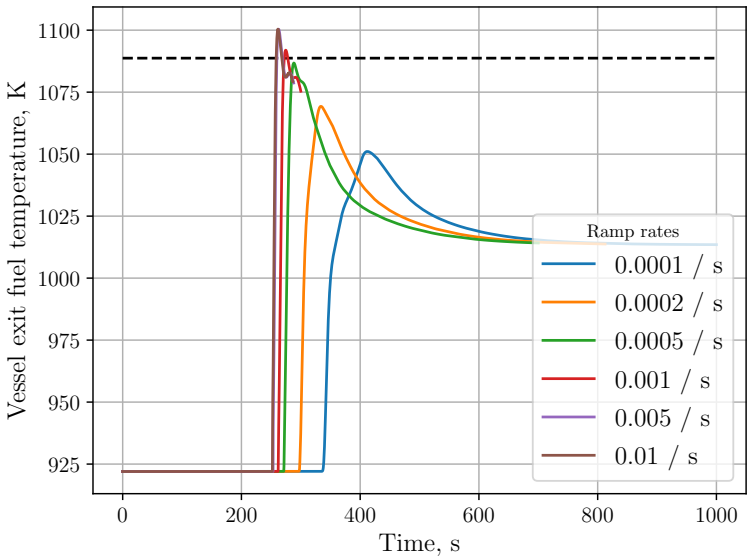

Figure 6.1: Fuel temperatures at vessel exit for a series of reactivity ramp rates between 1×10^{-4} and 1×10^{-2} with intrinsic source rate set to 3.3×10^{5} neutrons per second, corresponding to the intrinsic source level in the MSRE. The maximum permissible temperature, 1088 K is indicated by the dashed horizontal line.

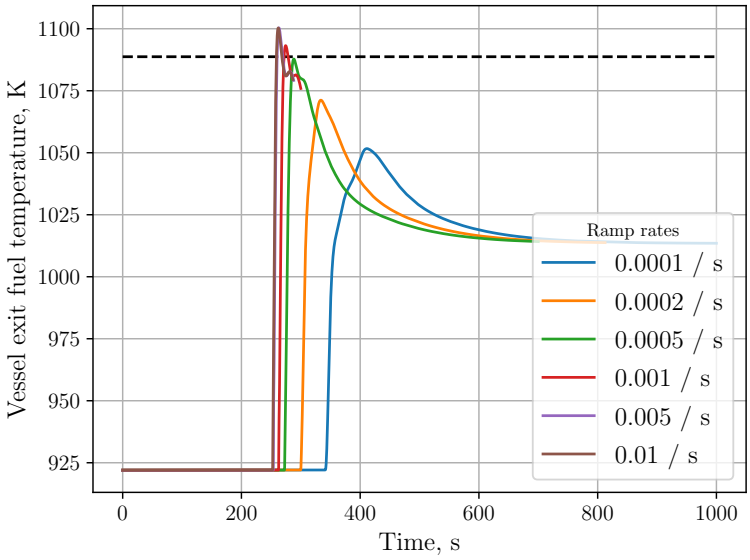

Figure 6.2: Fuel temperatures at vessel exit for a series of reactivity ramp rates between 1×10^{-4} and 1×10^{-2} with intrinsic source rate set to 10 neutrons per second. The maximum permissible temperature, 1088 K is indicated by the dashed horizontal line.

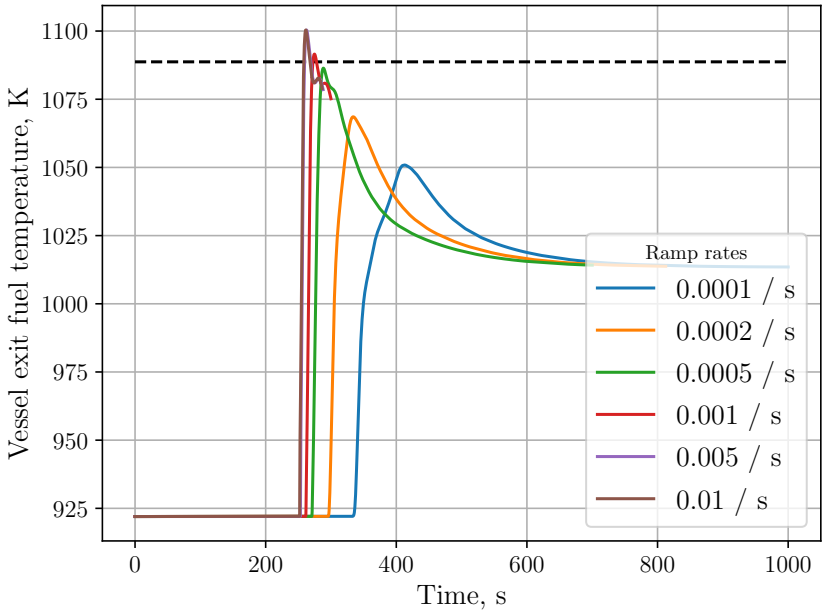

Figure 6.3: Fuel temperatures at vessel exit for a series of reactivity ramp rates between 1×10^{-4} and 1×10^{-2} with intrinsic source rate set to 10^7 neutrons per second. The maximum permissible temperature, 1088 K is indicated by the dashed horizontal line.

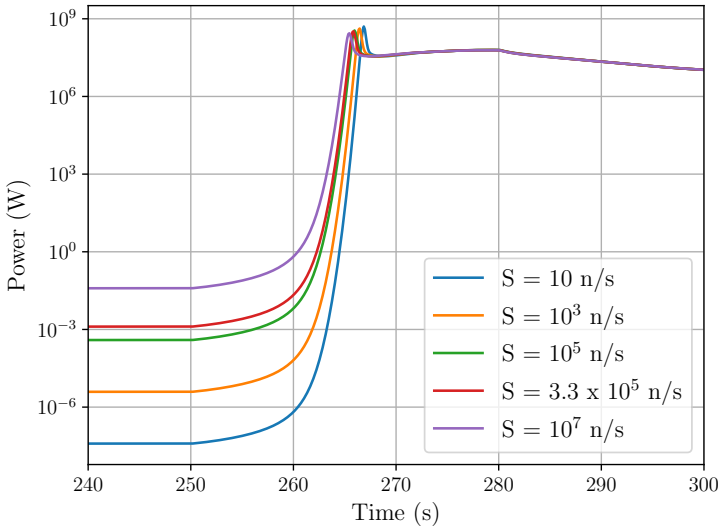

(a) Logarithmic power scale. Transients shown from 10 s prior to start of reactivity ramp.

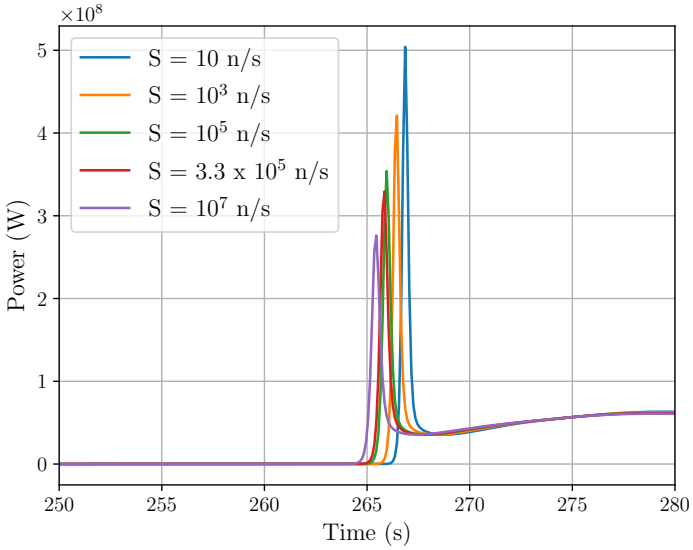

(b) Linear power scale. Transients shown from the start of the reactivity ramp.

Figure 6.4: Dependency of peak power in the ramp as a function of source strength. Reactivity ramp rate = 5×10^{-4} / s, ramp begins at $t = 250$ s.

Note that for this reactor type, the maximum permissible ramp rate appears to be quite insensitive to the source strength, changing by only a few kelvin.

6.5 CALLISTO-SPK Calculations for Stochastically-Safe Combinations of Source and Ramp rate

6.5.1 Fixed Ramp Rate with Varying Source Strength

The stochastically-safe combination of source and ramp rate for an MSRE-like design was assessed using the CALLISTO-SPK code. Cross sections derived from the original MSRE design study [7] and the MCNP model outlined in Appendix C were used to calculate the source multiplication factor for a range of source strengths undergoing the same reactivity ramp as described in the previous section (initially \$-0.5 subcritical followed by a 50 s ramp inserting \$2.239, corresponding to a ramp rate of 0.0448 \$ per s).

Figure 6.5 compares the effect of increasing source strength on the stochastically-safe source multiplication factor, S_m, for these data sets plus Hansen's 1960 [108] criterion for the source regime,

$$\Lambda S << \frac{\bar{\nu}}{2}\frac{\langle \nu(\nu-1)\rangle}{\bar{\nu}^2} \sim 1 \tag{6.3}$$

where Λ = the mean generation time [s], S = source strength [n/s], and $\frac{\langle \nu(\nu-1)\rangle}{\bar{\nu}^2}$ = Diven's factor, ~ 0.8.

Results using the ORNL and MCNP cross sections both show strong dependence of the stochastically-safe source multiplier on the source strength. S_m decreases rapidly as the source strength increases past 1000 neutrons per second, tending to the asymptote $S_m = 1.0$ (a deterministic system). These results agree with the criterion derived by Hansen, with the boundary demarcated by the shaded region. Systems with source strength significantly lower than $\frac{1}{\Lambda}$ (to the left hand portion of Fig. 6.5) are deemed to be in the stochastic regime and therefore a large source multiplier is required to reduce the likelihood of a rogue transient (Q) to a small value. For example, for the system with ORNL-derived generation time, the weakest intrinsic source (250 n/s) must be multiplied by 3×10^7 to reduce Q to 10^{-8}.

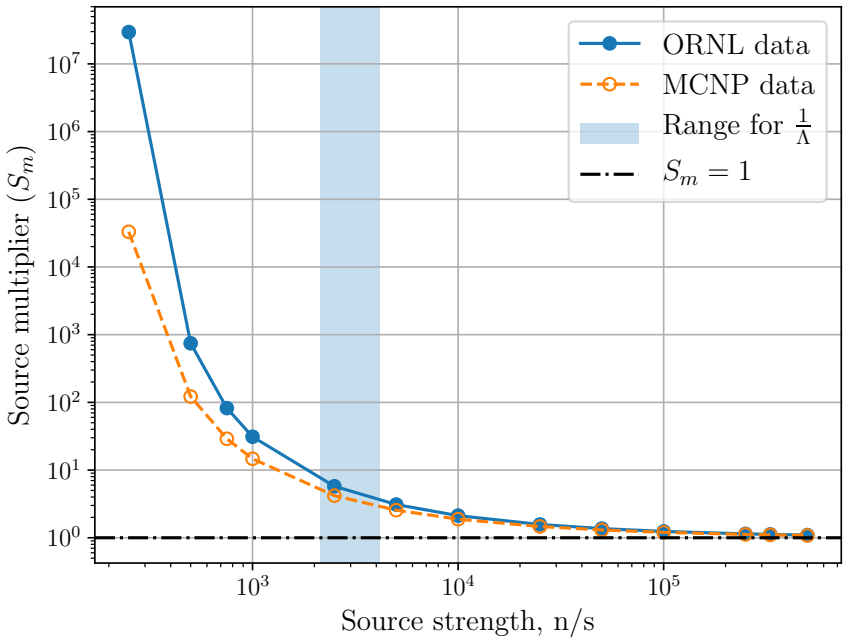

Figure 6.5: Source strength vs. source multiplier as calculated using CALLISTO-SPK for fixed ramp (0.0448 \$ / s) and Q value (10^{-8}). The blue shaded region indicates the range of source strengths that correspond to Hansen's low source criterion for each of the simulated systems.

For a source strength equivalent to that estimated for MSRE (330,000 n/s), the source multiplier was calculated to be between 1.10 and 1.12 (for the MCNP and ORNL-derived parameters, respectively). A reactor with intrinsic source of this magnitude is expected to be highly deterministic with extremely low probability of a rogue transient occurring.

For extremely high source rates, it may not be possible to adequately represent the value of the dummy variable z in the saddlepoint equations using the available numerical precision. Under such conditions the system will be highly deterministic and the value of z corresponding to the probability generating function for the system will be extremely close to 1.0, with evaluation of the derivatives with $z = 1.0$ corresponding to the moments of the distributions.

6.5.2 Fixed Source Strength with Varying Ramp Rate

A series of reactivity ramps with different reactivity insertion rates were simulated using a fixed source strength equal to that predicted for MSRE (330,000 n/s). The CALLISTO-SPK source

multiplier for these reactivity ramps is shown in Figure 6.6. For slow reactivity ramps the source multiplier is close to 1.0 indicating the system is highly deterministic with very small probability of a rogue transient occurring at the end of the ramp (as discussed in Section 6.5.1). For very fast reactivity insertions, the source multiplier is higher, tending to a value just under 2.0. Thus for this high source strength, S_m is not very sensitive to the rate of reactivity insertion.

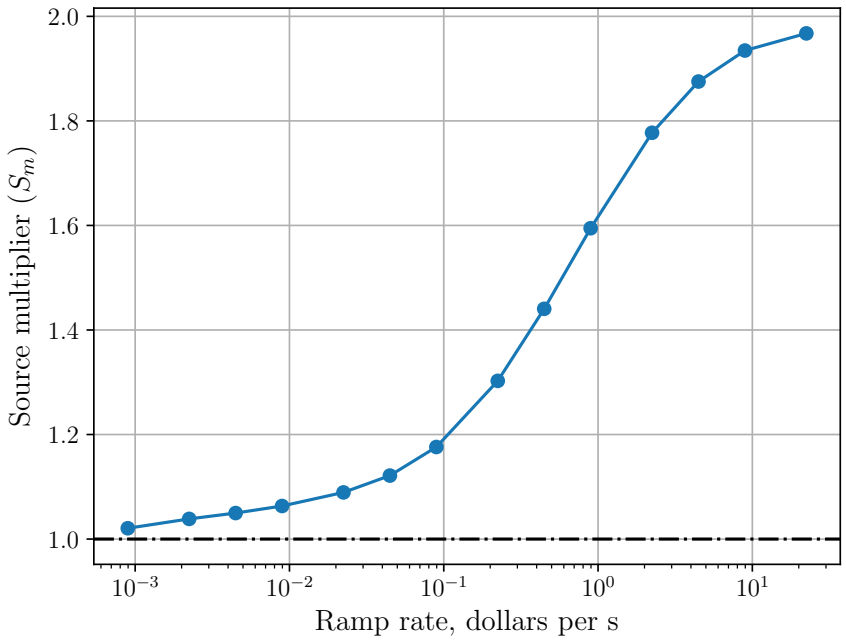

Figure 6.6: Source multiplier for reactivity ramps with fixed source strength (330,000 n/s) and varying ramp rates.

6.6 Discussion

The analysis above suggests that a molten salt reactor design similar to MSRE would exhibit limited stochastic behaviour due to the strong intrinsic source. The system is also predicted to have limited sensitivity to the rate at which the reactivity is inserted.

A further argument for limited stochastic behaviour is based on a result by Bell [109]. Analysis of the fission chain survival probability in a supercritical system with random intrinsic source of fixed average intensity yields a gamma distribution with shape parameter η. If η is less than 1, the probability distribution for number of neutrons as time t has a long tail. As η increases and

becomes greater than 1, the distribution rapidly becomes peaked with a mean that characterises the distribution adequately (a deterministic system).

Consideration of η values for an MSRE-like core under static reactivity conditions, using a different definition of η [94] reveals a slightly more stringent criterion than that suggested by Hansen [108]:

$$\eta = \frac{2S\tau_f}{\langle \nu(\nu-1) \rangle} \tag{6.4}$$

where S = source intensity [n/s], τ_f = prompt neutron lifetime and $\langle \nu(\nu-1) \rangle$ is approximately equal to 4.7.

Using the ORNL mean generation time (2.4×10^{-4} s), this results in a minimum source of 9800 n /s in order for η to exceed 1. The corresponding source strength using the MCNP generation time (4.68×10^{-4} s) is 5000 n/s.

Cooling et al. have demonstrated similar results using a coupled probabilistic-point kinetic model for a system undergoing a rapid reactivity ramp [95]. Systems with low source had wide distributions for the peak power (directly related to the power via Eq. 2.5 in Section 2.2) while those with a high source rate had narrow distributions. A reduced ramp rate had a marked effect on the distribution, with slower ramps resulting in more deterministic behaviour.

6.6.1 Other Molten Salt Systems

Examination of other plausible MSR mixtures suggests they too have strong intrinsic neutron sources, especially those containing ^{9}Be or ^{19}F due to the high (α,n) reaction cross sections. Strong α emission from fuel mixtures containing ^{233}U or plutonium isotopes (plus spontaneous fission from ^{240}Pu) will contribute to a strong intrinsic source in these fuel mixtures.

The predecessor to MSRE, the Aircraft Reactor Experiment, was fuelled by a NaF-ZrF_4-UF_4 mixture with a ^{235}U enrichment of 93.4%. An estimate of the intrinsic source strength in this fuel using the SOURCES-4C code [110] gives 1.23×10^{-2} neutrons/s/cm^3 - the low spontaneous fission rate of ^{235}U, lack of beryllium and lithium in the fuel contribute to an intrinsic source

strength lower than that calculated for MSRE, 2.317×10^{-1} neutrons/s/cm^3. The total fuel intrinsic source count scaled to the ARE fuel volume (0.0504 m^3), is relatively low, 620 n /s. This may have been increased slightly by ^{9}Be(n,2n)^{8}Be and ^{9}Be(n,α)^{6}Li reactions, both of which release α particles due to the rapid disintegration of the ^{8}Be nucleus. The released α particles could then contribute to the source via (α,n) reactions in the beryllium oxide moderating structure through which the fuel pipes were threaded [111]. The energy threshold for these reactions is high, and such additional sources were not modelled in this investigation.

A class of candidate MSR fuels with a low intrinsic source are those comprising of sodium chloride (NaCl) with uranium trichloride (UCl_3), especially if using highly enriched uranium in specialised applications [112]. A hypothetical compact reactor running on a 60:40 mole percent NaCl-UCl_3 fuel mixture with the same uranium enrichment as the ARE, same vessel fuel volume as MSRE (1.4188 m^3), and 99.9% enriched ^{37}Cl would have an intrinsic source strength of only 2280 n/s. Such a chloride-fuelled system is likely to be have an epithermal or fast neutron spectrum depending on core construction, therefore Hansen's criterion (the product of source strength and mean generation time, ΛS) may be significantly less than 1, placing it in the stochastic regime.

For most applications, it is not feasible to use highly enriched uranium (HEU) due to proliferation concerns. The maximum permitted ^{235}U enrichment for low enriched uranium (LEU) is 19.75 $\pm$ 0.2%. An MSRE-like design with the same 60:40 mole percent NaCl-UCl_3 mix, enriched to 19.75% ^{235}U would have an estimated intrinsic source of 9460 n/s and mean generation time of 60 microseconds. Using Hansen's criterion, $\Lambda S = 0.578$, therefore the system would be expected to show some stochastic behaviour.

In addition, recent research has shown a strong dependence of the stochastic reduction factor/source multiplier on source location in the core [113]. A more developed model of the stochastic behaviour of a circulating fuel reactor would incorporate the probability of a neutron being emitted by a precursor decay at location (r, z) with respect to some importance function that includes the transport of precursors outside of the moderated regions inside the vessel.

6.7 Conclusions of the MSRE Stochastic Analysis

This analysis supports the original assessment [104] that the intrinsic source in MSRE due to the materials in the fuel salt would be sufficient to reduce the likelihood of a rogue transient to a very small probability. Analysis of startup reactivity ramps with varying sources suggested the system was insensitive to source strength using the limiting fuel temperature damage criterion.

It is expected that future reactor designs incorporating fluoride salts of lithium and beryllium will exhibit strong intrinsic sources due to (α, n) reactions in the salt, particularly if the nuclear fuel is dissolved in it allowing close association of α source and low-Z target nuclei. Stochastic behaviours may be important in systems with a lower intrinsic neutron source, for example those with high ^{235}U enrichments.

Evidence of a stochastically-safe startup could be used to support a regulatory case for extrinsic source deletion in a reactor design. This provides advantages in avoiding having to procure the primary neutron startup source material. An example of a commonly-used primary neutron startup source is ^{252}Cf. An estimate of the cost of ^{252}Cf in the year 2000 was $60 million per gram [114]. There have been recent shortages of other specialist nuclear materials, for example ^{238}Pu which is used in radioisotope thermoelectric generators (RTGs) for deep space missions. After the closure of Cold War era infrastructure related to weapons production the U.S. Dept of Energy procured the isotope from other countries however this supply has ceased. A recent effort at ORNL has restarted production but only in limited quantities (1.5 kg per year) [115]. Source handling is complicated by the large size of the shielded transport casks, with associated planning to reduce worker dosage. Elimination of these procedures would represent a saving in time and cost due to reduced safety analyses and reduced reactor downtime.

Chapter 7

Conclusions

This thesis has developed a number of coupled point kinetic-thermal hydraulic models of an MSRE-like system, solved using numerical and semi-analytical methods, for the investigation of fundamental MSR physics under steady state and transient conditions. The models were used to evaluate the system performance, safety, and stability. A turbulent mixing term was introduced into the numerical model and this was augmented with uncertainty and sensitivity analysis on key model parameters. For the first time, within the literature, this enabled a detailed explanation of the differences between existing models and the experimentally observed behaviour of the MSRE frequency response. Overall good agreement, in a qualitative sense, was observed between the model frequency response and stability compared to the MSRE experimental data.

In this thesis, MSRE-like designs were shown to be stochastically safe for a variety of fuel mixtures and for varying reactivity ramp insertion rates due to the strong intrinsic source present in conventional MSRs. Other non-conventional molten salt mixtures, such as those with higher ^{235}U enrichment levels have been demonstrated to exhibit a lower intrinsic source strength. Examples of such MSRs include the predecessor to MSRE, the ARE reactor. Such MSRs may have application in compact nuclear power plants. These types of non-conventional molten salt mixtures have been demonstrated to require low neutron source startup analysis for safety assessment purposes. This is the first time that a detailed description of low neutron

source startup analysis has been provided for MSRs within the literature.

Chapter 3 showed the numerical model to exhibit similar steady state properties and distribution of delayed neutrons in the core compared to calculations performed for MSRE. Chapter 4 used a combination of Monte Carlo sampling and deterministic runs for bounding cases to elucidate aspects of MSR physics, for example the strong influence of the heat exchanger heat transfer coefficient ($h_{H.E.}$) on the steady-state condition, and the importance of fuel-graphite heat transfer rate ($h_{f,g}$) during a transient.

This knowledge was developed further in Chapter 5, which examined the frequency response and stability of the numerical model and a related semi-analytical model. Analysis of the frequency response and eigenvalues showed the models becoming more stable as the reactor power increased, in agreement with observations made on MSRE. A recirculation feature identified at $\omega \approx 0.25$ rad s^{-1} had been predicted by MSRE design models but did not appear in the experimental frequency response - greater than expected mixing in the primary circuit had been proposed as an explanation for this difference but had not been extensively tested.

A novel interpretation of the experimental frequency response was verified using a turbulent dispersion parameter that introduced extra mixing in the primary circuit in proportion to the local velocity. This parameter introduced sufficient mixing at the correct primary circuit locations to suppress the recirculation feature that had persisted in other numerical models. Possible explanations for the remaining differences between the models and experiment at very high and low frequencies were discussed.

Chapter 6 considered the effects of the stochastic behaviour inherent to multiplying systems with low neutron populations, when applied to an MSRE-like core and MSR fuel. Calculations of the fuel intrinsic neutron source gave a source strength sufficient to reduce the likelihood of a rogue transient during reactor startup to very small probability (less than 10^{-8}). This is likely to be the case for most candidate MSR mixtures with low atomic weight materials, particularly those containing lithium and beryllium fluorides. This bodes well for a potential future regulatory safety case recommending source deletion in a future 'Generation IV' MSR. This could potentially lead to significant cost savings for first startup of the reactor and reduced radiation worker dosage.

7.1 Future Work

Expansion of the model to include a secondary circuit is desirable as it may offer improvements to the frequency response and accuracy of the steady state condition. The secondary circuit could be modelled using a delay term, or for greater accuracy, heat transfer explicitly represented in a similar fashion to the primary circuit. It may be the case that the former is sufficient while incurring only a very small additional cost over the basic model derived in Chapter 2.

Linearisation of the equations developed in Ch. 2 would permit sensitivity and stability analysis with respect to the turbulent dispersion parameter and other geometric aspects of the circuit, for example the cross-sectional areas of the primary circuit that are treated as residence volumes in the semi-analytical model.

A model incorporating spatially-dependent nuclear reactor kinetics might improve the frequency response results at frequencies higher than that corresponding to the primary circuit recirculation, as well as permit more realistic stability analyses. This of course comes at a greater computational cost. A semi-analytical approach, akin to that used in Section 5.6 may be the most fruitful approach for this problem given the efficiency of the method (not requiring many independent, expensive in this case, transient runs in order to obtain the frequency response). Development of noise models of point kinetic models and spatially-dependent kinetic models, both coupled to thermal hydraulics is discussed in [94] and such methods were used to estimate the void fraction in the MSRE primary circuit [44].

An increase in the fidelity of the thermal hydraulic model of the MSRE would be desirable from the standpoint of the frequency response dynamics discussed in Ch. 5 and also the damage criterion for stochastic startup discussed in Ch. 6. The system was observed to be insensitive to the source strength when reactor damage was assessed in terms of maximum permissible fuel temperature. If additional physics were included, particularly the pressure in the primary circuit, it would permit an assessment of the just-safe combination of source and ramp rate that did not exert a dangerous pressure in the primary circuit. An additional more realistic, if undesirable, behaviour might include expansion of the fuel volume in the pump bowl to such an extent that the fuel was deposited in the overflow tank.

A more detailed numerical model incorporating the thermal shield that surrounded the MSRE vessel may improve the accuracy of k_{eff} values calculated for the MSRE-like core. A model with the thermal shield would be expected to increase k_{eff} due to backscatter and moderation of the neutrons in the cooling water. Comparison between neutron transport calculations with all vacuum boundary conditions, all reflecting boundaries and reflecting boundaries only at the sides may be found in Appendix C.

Thermal neutron scattering data for the molten salt and other reactor materials is a significant source of uncertainty in models of MSRs. Molecular motions in the liquid phase increase inelastic scattering with the relative contributions from coherent and incoherent scatter dependent on the specific molecular dynamics and chemical bonding within the material. First-principles modelling of thermal neutron scattering derived from molecular simulations of heterogeneous and soft-matter materials is an area of active research and can enable more accurate predictions of reactor physics parameters for both solid and liquid reactor materials [116]. A more detailed discussion may be found in Appendix Section C.2.1.

Bibliography

[1] W. B. Cottrell, H. E. Hungerford, J. K. Leslie, and J. L. Meem. Operation of the Aircraft Reactor Experiment, ORNL-1845. Technical report, Oak Ridge National Laboratory, 1955.

[2] R. C. Robertson. MSRE Design and Operations Report: Part I: Description of Reactor Design. Technical report, Oak Ridge National Laboratory, 1965.

[3] R. C. Steffy. Frequency-Response Testing of the Molten-Salt Reactor Experiment. Technical report, Reactor Division, Oak Ridge National Laboratory, 1970.

[4] W. C. Ulrich. *An Extended Hydraulic Model of the MSRE Circulating Fuel System.* PhD thesis, University of Tennessee, 1970.

[5] R. B. Briggs. Molten-Salt Reactor Program Semiannual Progress Report for Period Ending January 31, 1964, ORNL-3626. Technical report, Oak Ridge National Laboratory, 1964.

[6] B E Prince, S J Ball, J R Engel, P N Haubenreich, and T W Kerlin. Zero-Power Physics Experiments on the Molten-Salt Reactor Experiment, ORNL-4233. Technical report, Oak Ridge National Laboratory, 1968.

[7] P. N. Haubenreich, J. R. Engel, B. E. Prince, and H. C. Claiborne. MSRE Design and Operations Report: Part III. Nuclear Analysis, ORNL-TM-730. Technical report, Oak Ridge National Laboratory, 1964.

[8] T. B. Fowler, M. L. Tobias, and D. R. Vondy. EXTERMINATOR - A Multigroup Code for Solving Neutron Diffusion Equations in One and Two Dimensions. Technical report, Oak Ridge National Laboratory, 1965.

[9] B. E. Prince. Period Measurements on the Molten Salt Reactor Experiment During Fuel Circulation: Theory and Experiment, ORNL-TM-1626. Technical report, Reactor Division, Oak Ridge National Laboratory, 1966.

[10] T.W. Kerlin and S.J. Ball. Experimental Dynamic Analysis of the Molten-Salt Reactor Experiment. Technical report, Oak Ridge National Laboratory, 1966.

[11] M. W. Rosenthal, R. B. Briggs, and P. R. Kasten. Molten-Salt Reactor Program Semiannual Progress Report For Period Ending August 21, 1968, ORNL-4344. Technical report, Oak Ridge National Laboratory, 1969.

[12] W R Grimes. Molten Salt Reactor Chemistry. *Nuclear Applications & Technology*, 8:137–155, 1970.

[13] Melvin Tobias and T. B. Fowler. The EQUIPOISE Method — A Simple Procedure for Group- Diffusion Calculations in Two and Three Dimensions. *Nuclear Science and Engineering*, 12:513–518, 1962.

[14] H. E. McCoy. The INOR-8 Story. *Oak Ridge National Laboratory Review*, pages 35–49, 1969.

[15] Cecil B. Ellis. The Atomic-Powered Aircraft. Technical report, Reactor Technology Division, Oak Ridge National Laboratory, 1950.

[16] Wm. B. Cottrell. Reactor Program of the Aircraft Nuclear Propulsion Project, ORNL-1234. Technical report, Oak Ridge National Laboratory, 1952.

[17] M E Wheatley, L E McNeese, W L Carter, L M Ferris, and E L Nicholson. Engineering Development of the MSBR Fuel Recycle. *Nuclear Applications and Technology*, 1970.

[18] Paul N. Haubenreich. Two Years of HRE-2 Operation. *Nuclear Science and Engineering*,

8(6):467–479, 1960.

[19] R. C. Briant and Alvin M. Weinberg. Molten Fluorides as Power Reactor Fuels. *Nuclear Science and Engineering*, 2:797–803, 1957.

[20] J. A. Lane, H. G. MacPherson, and Frank Maslan, editors. *Fluid Fuel Reactors*. Addison-Wesley, 1958.

[21] D F Williams, L M Toth, and K T Clarno. Assessment of Candidate Molten Salt Coolants for the Advanced High-Temperature Reactor (AHTR). Technical report, Oak Ridge National Laboratory, mar 2006.

[22] J. Kopecky. Atlas of Neutron Capture Cross Sections. Technical report, International Nuclear Data Committee, IAEA, 1997.

[23] A. M. Perry and H. F. Bauman. Reactor Physics and Fuel-Cycle Analyses. *Nuclear Applications & Technology*, 8:208–219, 1970.

[24] Dunlap Scott, G. W. Alwang, E. F. Demski, W. J. Fader, E. V. Sandin, and R. E. Malenfant. A Zero Power Reflector-Moderated Reactor Experiment At Elevated Temperature. Technical report, Oak Ridge National Laboratory, 1958.

[25] W.K. Ergen, A.D. Callihan, C.B. Mills, and Dunlap Scott. The Aircraft Reactor Experiment - Physics. *Nuclear Science and Engineering*, 2:826–840, 1957.

[26] E.S. Bettis, W.B. Cottrell, E.R. Mann, J.L Meem, and G.D. Whitman. The Aircraft Reactor Experiment - Operation. *Nuclear Science and Engineering*, 2:841–853, 1957.

[27] F. C. Linn. Heat Transfer Reactor Experiment No. 3: Comprehensive Technical Report, General Electric Direct-Air-Cycle Aircraft Nuclear Propulsion Program, APEX-906. Technical report, Flight Propulsion Laboratory Department, General Electric Company, 1962.

[28] Comptroller General of the United States. Report to the Congress of the United States: Review of Manned Aircraft Nuclear Propulsion Program. Technical report, 1963.

[29] Paul N. Haubenreich and J R Engel. Experience with the Molten-Salt Reactor Experi-

ment. *Nuclear Applications and Technology*, 8:118–136, 1970.

[30] C. H. Gabbard. Reactor Power Measurement and Heat Transfer Performance in MSRE, ORNL-TM-3002. Technical report, Oak Ridge National Laboratory, 1970.

[31] R. J. Kedl and C. K. McGlothlan. Tube Vibration in MSRE Primary Heat Exchanger. Technical report, Oak Ridge National Laboratory, 1968.

[32] Roy E. Thoma. Chemical Aspects of MSRE Operations, ORNL-4658. Technical report, Oak Ridge National Laboratory, 1971.

[33] S. J. Ball and T. W. Kerlin. Stability Analysis of the Molten-Salt Reactor Experiment. Technical report, Oak Ridge National Laboratory, 1965.

[34] S.E. Beall, P.N. Haubenreich, R.B. Lindauer, and J.R. Tallackson. MSRE Design and Operations Report: Part V: Reactor Safety Analysis Report. Technical report, Oak Ridge National Laboratory, 1964.

[35] Paul N Haubenreich, J. R. Engel, C. H. Gabbard, R.H Guymon, and B.E. Prince. MSRE Design and Operations Report: Part V: A Safety analysis of operation with 233U. Technical report, Oak Ridge National Laboratory, 1968.

[36] M. E. Whatley, L. E. Mcneese, W. L. Carter, L. M. Ferris, and E. L. Nicholson. Engineering Development of the MSBR Fuel Recycle. *Nuclear Applications and Technology*, 8(2):170–178, 1970.

[37] R.C. Robertson, R.B. Briggs, O.L. Smith, and E.S. Bettis. Two-Fluid Molten-Salt Breeder Reactor Design Study (Status as January 1968) - ORNL-4528. Technical report, Oak Ridge National Laboratory, 1970.

[38] E.S. Bettis and R.C. Robertson. The Design and Performance Features of a Single-Fluid Molten-Salt Breeder Reactor. *Nuclear Applications and Technology*, 8(February):190–207, 1970.

[39] Thomas J. Dolan, editor. *Molten Salt Reactors and Thorium Energy.* Woodhead Pub-

lishing, 2017.

[40] Pre-Licensing Vendor Design Review - Canadian Nuclear Safety Commission.

[41] Hongjie Xu. Status and Perspective of TMSR in China. Seminar, 2017.

[42] J. Kópházi, M. Szieberth, S. Fehér, Gy. Csom, and P.F.A de Leege. MCNP Based Calculation of Reactivity Loss in Circulating Fuel Reactors. In *Nuclear Mathematical and Computational Sciences: A Century in Review, A Century Anew*, pages 1–7, 2003.

[43] T.W. Kerlin, S.J. Ball, and R.C. Steffy. Theoretical Dynamics Analysis of the Molten-Salt Reactor Experiment. *Nuclear Technology*, 10:118–132, 1971.

[44] D. N. Fry, R. C. Kryter, and J. C. Robinson. Measurement of Helium Void Fraction in the MSRE Fuel Salt using Neutron-Noise Analysis. Technical report, Instrumentation and Controls Division, Oak Ridge National Laboratory, 1968.

[45] M. W. Rosenthal, P. R. Kasten, and R. B. Briggs. Molten-Salt Reactors - History, Status, and Potential. *Nuclear Applications and Technology*, 8:107–117, 1970.

[46] P. N. Haubenreich. Prediction of Effective Yields of Delayed Neutrons in MSRE. Technical report, Oak Ridge National Laboratory, 1962.

[47] A Radkowsky, editor. *Naval Reactors Physics Handbook: Volume I: Selected Basic Techniques*. Naval Reactors, Division of Reactor Development, United States Atomic Energy Commission, 1964.

[48] Daniel Wooten and Jeffrey J. Powers. A Review of Molten Salt Reactor Kinetics Models. *Nuclear Science and Engineering*, 191(3):203–230, 2018.

[49] P. R. Bell and H. A. Straus. Electronic Pile Simulator. *Review of Scientific Instruments*, 21(8):760–763, 1950.

[50] Dalin Zhang, Suizheng Qiu, and Guanghui Su. Development of a safety analysis code for molten salt reactors. *Nuclear Engineering and Design*, 239(12):2778–2785, 2009.

[51] E. R. Mann. Analog Devices for Design of Reactor Controls. *IRE Transactions - Nuclear Science*, 3(2):760–763, 1956.

[52] J. MacPhee. The Kinetics of Circulating Fuel Reactors. *Nuclear Science and Engineering*, 4:588–597, 1958.

[53] S. Tamor. Note on the Non-Linear Kinetics of Circulating-Fuel Reactors. Technical report, Oak Ridge National Laboratory, 1952.

[54] William K. Ergen. Kinetics of the circulating-fuel nuclear reactor. *Journal of Applied Physics*, 25(6):702–711, 1954.

[55] B E Prince. Improved Representation of Some Aspects of Circulating-Fuel Reactor Kinetics. Technical report, Reactor Division, Oak Ridge National Laboratory, 1973.

[56] P. N. Haubenreich. Safety Calculations for MSRE, ORNL-TM-251. Technical report, Oak Ridge National Laboratory, 1962.

[57] O. W. Burke and F. H. S. Clark. Analyses of Transients in the MSRE System with U233 Fuel. Technical report, Instrumentation and Controls Division, Oak Ridge National Laboratory, 1969.

[58] T.W. W Kerlin, S.J. J Ball, R.C. C Steffy, and M.R. R Buckner. Experiences with Dynamic Testing Methods and the Molten-Salt Reactor Experiment. *Nuclear Technology*, 10:103–117, 1971.

[59] O.W. Burke. Hybrid Computer Simulation of the MSBR, ORNL-TM-3767. Technical report, Oak RIdge National Laboratory, 1972.

[60] Jiří Křepel, Ulrich Rohde, Ulrich Grundmann, and Frank Peter Weiss. DYN1D-MSR spatial dynamics code for molten salt reactors. *Annals of Nuclear Energy*, 32:1799–1824, 2005.

[61] Jiří Křepel, Ulrich Rohde, Ulrich Grundmann, and Frank Peter Weiss. DYN3D-MSR spatial dynamics code for molten salt reactors. *Annals of Nuclear Energy*, 34(6):449–462,

2007.

[62] Shisheng Wang, Andrei Rineiski, and Werner Maschek. Molten salt related extensions of the SIMMER-III code and its application for a burner reactor. *Nuclear Engineering and Design*, 236(14-16):1580–1588, 2006.

[63] Matteo Zanetti, Antonio Cammi, Carlo Fiorina, and Lelio Luzzi. A Geometric Multiscale modelling approach to the analysis of MSR plant dynamics. *Progress in Nuclear Energy*, 83(April):82–98, 2015.

[64] K. Zhuang, Y. Zheng, L. Cao, T. Hu, and H. Wu. Improvements and validation of the transient analysis code MOREL for molten salt reactors. *Journal of Nuclear Science and Technology*, 3131(August), 2017.

[65] Sandra Dulla, Ernest H. Mund, and Piero Ravetto. The quasi-static method revisited. *Progress in Nuclear Energy*, 50(8):908–920, 2008.

[66] Lawrence Shampine and Marilyn Gordon. *Computer Solution of Ordinary Differential Equations: The Initial Value Problem*. W.H. Freeman & Co Ltd, 1975.

[67] G. Taylor. The Dispersion of Matter in Turbulent Flow through a Pipe. *Proceedings of the Royal Society A: Mathematical, Physical and Engineering Sciences*, 223(1155):446–468, 1954.

[68] B. E. Prince and J. R. Engel. Temperature and Reactivity Coefficient Averaging in the MSRE. Technical report, Oak Ridge National Laboratory, 1962.

[69] R. J. Kedl. Fluid Dynamic Studies of the Molten-Salt Reactor Experiment (MSRE) Core. Technical report, Oak Ridge National Laboratory, 1970.

[70] J. R. Engel and P. N. Haubenreich. Temperature in the MSRE Core During Steady-State Power Operation. Technical report, Oak Ridge National Laboratory, 1962.

[71] V. Singh, A.M. Wheeler, M.R. Lish, O. Chvála, and B.R. Upadhyaya. Nonlinear dynamic model of Molten-Salt Reactor Experiment – Validation and operational analysis. *Annals*

of Nuclear Energy, 113:177–193, 2018.

[72] K.H. Knuth. Optimal Data-Based Binning for Histograms. *ArXiv Physics e-prints*, may 2006.

[73] The Astropy Collaboration, Thomas P. Robitaille, Erik J. Tollerud, Perry Greenfield, Michael Droettboom, Erik Bray, Tom Aldcroft, Matt Davis, Adam Ginsburg, Adrian M. Price-Whelan, Wolfgang E. Kerzendorf, Alexander Conley, Neil Crighton, Kyle Barbary, Demitri Muna, Henry Ferguson, Frédéric Grollier, Madhura M. Parikh, Prasanth H. Nair, Hans M. Günther, Christoph Deil, Julien Woillez, Simon Conseil, Roban Kramer, James E. H. Turner, Leo Singer, Ryan Fox, Benjamin A. Weaver, Victor Zabalza, Zachary I. Edwards, K. Azalee Bostroem, D. J. Burke, Andrew R. Casey, Steven M. Crawford, Nadia Dencheva, Justin Ely, Tim Jenness, Kathleen Labrie, Pey Lian Lim, Francesco Pierfederici, Andrew Pontzen, Andy Ptak, Brian Refsdal, Mathieu Servillat, and Ole Streicher. Astropy: A Community Python Package for Astronomy. *Astronomy and Astrophysics*, 33:1–9, 2013.

[74] T.W. Kerlin. *Frequency Response Testing in Nuclear Reactors*, volume 11. Academic Press, 1974.

[75] T W Kerlin. Stability Extrema in Nuclear Power Systems with Design Uncertainties. *Nuclear Science and Engineering*, 27:120–130, 1967.

[76] T. W. Kerlin and J. L. Lucius. The SFR-3 Code - A Fortran Program for Calculating the Frequency Response of a Multivariable System and its Sensitivity to Parameter Changes. Technical report, Oak Ridge National Laboratory, 1966.

[77] A. Cammi, V. Di Marcello, C. Guerrieri, and L. Luzzi. Transfer Function Modeling of Zero-Power Dynamics of Circulating Fuel Reactors. *Journal of Engineering for Gas Turbines and Power*, 133:1–8, 2011.

[78] T. W. Kerlin and J. L. Lucius. CABS - A Fortran Computer Program for Calculating Correlation Functions, Power Spectra and the Frequency Response from Experimental Data. Technical report, Oak Ridge National Laboratory, 1966.

[79] D. E. Fry. The Use of Cross-Correlation and Power SpectraI Techniques for the Identification of the Hunter Mk . 12 Dynamic Response. Technical report, Avionics Department, Royal Aircraft Establishment, Farnborough, 1969.

[80] R.C. Steffy and P. J. Wood. Theoretical Dynamic Analysis of the MSRE with 233U Fuel. Technical report, Oak Ridge National Laboratory, 1969.

[81] M Zanetti, L Luzzi, and A Cammi. An Innovative Approach To Dynamics Modeling and Simulation of the Molten Salt Rector Experiment. *Physor 2014*, (SEPTEMBER):1–14, 2014.

[82] Matteo Zanetti, Antonio Cammi, Carlo Fiorina, and Lelio Luzzi. A Geometric Multiscale modelling approach to the analysis of MSR plant dynamics. *Progress in Nuclear Energy*, 83(August):82–98, 2015.

[83] Jiri Krepel, Ulrich Rohde, Ulrich Grundmann, and Frank Peter Weiss. Dynamics of molten salt reactors. *Nuclear Technology*, 164(1):34–44, 2008.

[84] J. Kópházi, G. Légrádi, S. Fehér, and S. Czifrus. Effect of fuel mixing phenomena on the kinetic behavior of molten salt reactors. *Transport Theory and Statistical Physics*, 36(1-3):227–240, 2007.

[85] Matteo Zanetti, Antonio Cammi, Lelio Luzzi, Jiri Krepel, and Konstantin Mikityuk. Extension of the FAST Code System for the Modelling and Simulation of MSR Dynamics. In *ICAPP 2015*, pages 883–890, Nice (France), 2015.

[86] T W Kerlin, S J Ball, and R C Steffy. Theoretical Dynamics Analysis of the Molten Salt Reactor Experiment. *Nuclear Technology*, 10:118–132, 1971.

[87] J. Kópházi, D. Lathouwers, and J. L. Kloosterman. Development of a Three-Dimensional Time-Dependent Calculation Scheme for Molten Salt Reactors and Validation of the Measurement Data of the Molten Salt Reactor Experiment. *Nuclear Science and Engineering*, 163(2):118–131, 2009.

[88] K. Nagy, D. Lathouwers, C. G.A. T'Joen, J. L. Kloosterman, and T. H.J.J. Van Der

Hagen. Steady-state and dynamic behavior of a moderated molten salt reactor. *Annals of Nuclear Energy*, 64:365–379, 2014.

[89] Liangzhi Cao, Kun Zhuang, Youqi Zheng, Tianliang Hu, and Hongchun Wu. Transient analysis for liquid-fuel molten salt reactor based on MOREL2.0 code. *International Journal of Energy Research*, (June):1–15, 2017.

[90] Jiadong Bao. *Development of the model for the multi- physics analysis of Molten Salt Reactor Experiment using GeN-Foam code.* Masters thesis, Paul Scherrer Institut, 2016.

[91] M. R. Buckner and T. W. Kerlin. Optimum Binary Signals for Reactor Frequency Response Measurements. *Nuclear Science and Engineering*, 49(3):255–262, 1972.

[92] Bal Raj Sehgal, editor. *Nuclear Safety in Light Water Reactors.* Academic Press, 2012.

[93] C. M. Cooling, M. M. R. Williams, and M. D. Eaton. CALLISTO-SPK: A Stochastic Point Kinetics code for performing low source nuclear power plant start-up and power ascension calculations. *Annals of Nuclear Energy*, 113:319–331, 2018.

[94] M. M. R. Williams. *Random Processes in Nuclear Reactors.* Pergamon Press, 1974.

[95] C. M. Cooling, M. M.R. Williams, and M. D. Eaton. Coupled probabilistic and point kinetics modelling of fast pulses in nuclear systems. *Annals of Nuclear Energy*, 94:655–671, 2016.

[96] M. M.R. Williams and M. D. Eaton. A theory of low source start-up based on the Pál-Bell equations. *Annals of Nuclear Energy*, 102:317–348, 2017.

[97] J. Shaw. *Reactor Operation.* Pergamon Press Ltd., 1969.

[98] E. E. Lewis. *Nuclear Power Reactor Safety.* Wiley-Interscience, 1977.

[99] Herbert S Wilf. *generatingfunctionology.* Academic Press, 1994.

[100] Imre Pázsit and Lénárd Pál. *Neutron Fluctuations.* Elsevier, 2007.

[101] Anil K. Prinja. Notes on the Lumped Backward Master Equation for the Neutron Ex-

tinction/Survival Probability, LA-UR-12-22638. Technical report, Los Alamos National Laboratory, 2012.

[102] P. N. Haubenreich. Inherent Neutron Sources in Clean MSRE Fuel Salt, ORNL-TM-611. Technical report, Oak Ridge National Laboratory, 1963.

[103] W. B. Wilson, R. T. Perry, W. S. Charlton, and T. A. Parish. Sources: A code for calculating (alpha, n), spontaneous fission, and delayed neutron sources and spectra. *Progress in Nuclear Energy*, 51(4-5):608–613, 2009.

[104] J. R. Engel, P. N. Haubenreich, and B. E. Prince. MSRE Neutron Source Requirements, ORNL-TM-935. Technical report, Oak Ridge National Laboratory, 1964.

[105] R. B. Briggs. Molten-Salt Reactor Program Semiannual Progress Report for Period Ending July 31, 1964, ORNL-3708. Technical report, Oak Ridge National Laboratory, 1964.

[106] R. B. Briggs. Molten-Salt Reactor Program Semiannual Progress Report for Period Ending August 31, 1965, ORNL-3872. Technical report, Oak Ridge National Laboratory, 1965.

[107] J. T. Venard. Tensile and Creep Properties of INOR-8 for the Molten-Salt Reactor Experiment, ORNL-TM-1017. Technical report, Metals and Ceramics Division, Oak Ridge National Laboratory, 1965.

[108] G. E. Hansen. Assembly of Fissionable Material in the Presence of a Weak Neutron Source. *Nuclear Science and Engineeringc*, 8:709–719, 1960.

[109] George I. Bell. Probability Distribution of Neutrons and Precursors in a Multiplying Assembly. *Annals of Physics*, 21(2):243–283, 1963.

[110] W. B. Wilson, R. T. Perry, E. F. Shores, W. S. Charlton, T. A. Parish, G. P. Estes, T. H. Brown, E. D. Arthur, M. Bozoian, T. R. England, D. G. Madland, and J. E. Stewart. SOURCES 4C: A Code for Calculating (a,n), Spontaneous Fission, and Delayed Nuetron Sources and Spectra, LA-UR-02-1839. Technical report, Los Alamos National Laboratory, 2002.

[111] E. S. Bettis, R. W. Schroeder, G. A. Cristy, H. W. Savage, R. G. Affel, and L. F. Hemphill. The Aircraft Reactor Experiment - Design and Construction. *Nuclear Science and Engineering*, 2(6):804–825, 1957.

[112] A. W. Kramer. *Nuclear Propulsion for Merchant Ships*. U.S. Atomic Energy Commission, 1962.

[113] M. M. R. Williams and M. D. Eaton. Spatial effects in low neutron source start-up and associated stochastic phenomena. *Annals of Nuclear Energy*, 111:616–634, 2018.

[114] R. C. Martin, J. B. Knauer, and P. A. Balo. Production, distribution and applications of californium-252 neutron sources. *Applied Radiation and Isotopes*, 53(4-5):785–792, 2000.

[115] Mike Wall. New Supply Could Prevent Deep-Space Plutonium Shortage. *Scientific American*, mar 2017.

[116] Yuwei Zhu, Colby Sorrell, Cole Manring, Andrew Antony, and Ayman I. Hawari. Thermal Scattering Law Research and Development at North Carolina State University. In *Technical Program Review, Nuclear Criticality Safety Program, March 27-28, 2018, Oak Ridge, TN*, 2018.

[117] Barry N. Taylor and Peter J. Mohr. Fundamental Physical Constants from NIST. https://physics.nist.gov/cuu/Constants/index.html, 2014.

[118] C. R E de Oliveira. An arbitrary geometry finite element method for multigroup neutron transport with anisotropic scattering. *Progress in Nuclear Energy*, 18(1-2):227–236, 1986.

[119] M D Brough and C T Chudley. *Characteristic Ray Solutions of the Transport Equation*, pages 1–31. Springer US, Boston, MA, 1980.

[120] Y. Zhu and A. I. Hawari. Thermal neutron scattering cross section of liquid FLiBe. *Progress in Nuclear Energy*, 101:468–475, 2017.

[121] Ayman I. Hawari. Thermal Scattering Law (TSL) Data Generation Activities at North Carolina State University. In *OECD/NEA Meeting: WPEC SG42: "Thermal Scattering*

Kernel S(α,β): Measurement, Evaluation and Application", Paris, 2016.

[122] Longwei Mei, Xiangzhou Cai, Dazhen Jiang, Jingen Chen, Yuhui Zhu, Yafen Liu, and Xiaohe Wang. The investigation of thermal neutron scattering data for molten salt Flibe. *Journal of Nuclear Science and Technology*, 50(7):682–688, 2013.

[123] Zhifeng Li, Liangzhi Cao, Hongchun Wu, and Qingming He. The impacts of thermal neutron scattering effect and resonance elastic scattering effect on FHRs. *Annals of Nuclear Energy*, 97:102–114, 2016.

Appendix A

Model Parameters

A.1 Nuclear Reactor Physics Parameters for the Core

Parameter	Symbol	Value
Prompt neutron generation time (s)	Λ	2.4×10^{-4}
Average number of neutrons released per fission	$\bar{\nu}$	2.43
Delayed neutron fraction	β	0.0067
Delayed neutron group yields	β_1	2.211×10^{-4}
	β_2	1.4673×10^{-3}
	β_3	1.3132×10^{-3}
	β_4	2.6465×10^{-3}
	β_5	7.705×10^{-3}
	β_6	2.814×10^{-4}
Delayed neutron group decay constants (s^{-1})	λ_1	0.0124
	λ_2	0.0305
	λ_3	0.111
	λ_4	0.301
	λ_5	1.14
	λ_6	3.01
Component fission fractions	f_{core}	0.891
	$f_{U.H.}$	0.056
	$f_{L.H.}$	0.024
	$f_{D.C.}$	0.029
Energy released per fission event (J)	χ_f	3.15×10^{-11}
Thermal feedback coefficients (reactivity K^{-1}, non-Dollar units)	α_f	8.46×10^{-5}
	α_g	4.68×10^{-5}

Table A.1: Parameters from [7].

A.2 Nuclear Thermal Hydraulic Parameters

Parameter	Symbol/Component	Value
Component deposited power fractions	p_{core}	0.7972
	p_g	0.0671
	$p_{U.H.}$	0.06972
	$p_{L.H.}$	0.02988
	$p_{D.C.}$	0.03610
Core fuel volume fraction	$f_{vol,fuel}$	0.224
Core graphite volume fraction	$f_{vol,g}$	0.776
Core height (m)	H	1.6256
Fuel-graphite heat transfer coefficient ($\mathrm{W\,K^{-1}}$)	$h_{f,g}A_{f,g}$	3.6×10^4
Primary circuit length (m)	L	16.37
Core diameter (m)		1.4034
Upper head height (m)		0.22
Vessel to pump (m)		2.64
Pump path (m)		0.45
Pump to HE (m)		1.07
HE length (m)	$L_{H.E.}$	4.27
HE to vessel inlet (m)		4.19
Inlet & downcomer (m)		1.63
Lower head height (m)		0.27
Residence times (s)	core	9.4
	upper head	3.9
	vessel to pump	0.8
	pump	0.3
	pump to H.E.	2.3
	H.E.	2.3
	H.E. to vessel inlet	0.8
	vessel inlet and D.C.	3.6
	lower head	3.8
Fuel density ($\mathrm{kg\,m^{-3}}$)	ρ_{fuel}	2290.6
Graphite density ($\mathrm{kg\,m^{-3}}$)	ρ_g	1860.0
Specific heat capacities ($\mathrm{J\,kg^{-1}\,K^{-1}}$)	$C_{p,fuel}$	1967.8
	$C_{p,g}$	1760
Heat exchanger heat transfer coefficient [30] ($\mathrm{W\,m^{-2}\,K^{-1}}$)	$h_{H.E.}$	3.725×10^3
Heat exchanger surface area ($\mathrm{m^2}$)	$A_{H.E.}$	23.6
Secondary circuit temperature (K)	$T_{coolant}$	825

Table A.2: Unless otherwise stated, parameters from [2].

A.3 Flow times

	Core Entry	Core Centre	Core Exit	Upper Head Exit	Downcomer Entry	Lower Head Entry
Core Entry	25.18	20.51	15.83	11.9	7.37	3.74
Core Centre	4.68	25.18	20.51	16.58	12.05	8.42
Core Exit	9.35	4.68	25.18	21.26	16.73	13.1
Upper Head Exit	13.28	8.61	3.93	25.18	20.66	17.03
Downcomer Entry	17.81	13.14	8.46	4.53	25.18	21.56
Lower Head Entry	21.44	16.77	12.09	8.16	3.63	25.18

Table A.3: Flow times, in seconds, between key components in the model. *Note: Table is read region listed at top to region listed in the left hand column.*

A.4 Survey and Selection of Temperature Coefficients of Reactivity

Source	**Experimental / Theoretical**	**Value x 10^5**	**Comments**
Briggs (1961)	Theoretical	Total: -15.84 Fuel: -5.04 Graphite: -10.8	Two-group, bare reactor model. neutron temperature = graphite temperature. Negligible effect of changing reactor/fuel channel size. Fermi age is f(ρ_g) only. Resonance escape and η are independent of T.

Prince & Engel (1962) (1)	Theoretical	Fuel: -8.01 Graphite: -13.09	Based on 19 region, two group diffusion calculation and perturbation theory. Assumed thermal expansion higher than later experimental values. Resonance cross section variation with T deemed small, so neglected.
Prince & Engel (1962) (2)	Theoretical	Fuel: -7.43 Graphite: -12.46	Homogeneous reactor model, similar to that in ORNL-3215. Quoted also in progress report ORNL -3369. Deemed very sensitive to reactor size.
Haubenreich et al. (1964)	Theoretical	Fuel: -5.90 Graphite: -6.62	Homogeneous cylinder model. Acknowledged to be sensitive to energy cutoffs for thermal group.
Prince et al. (1968) (1)	Experimental	Total: -13.14	Slow system heating and observation of critical position of regulating control rod.
Prince et al. (1968) (2)	Experimental	Fuel: -8.82 ± 4.14	Fuel pump stopped, coolant (secondary) loop heated, then pump restarted. A noisy analog-digital converter limited accuracy of temperature measurements.

Prince et al. (1968) (3)	Experimental	Fuel: -8.46 ± 1.26	Hot secondary coolant stored and then released to H.E. More accurate T-measurement vs. previous experiment. Authors note potential limitation due to lag in T-measurement at the vessel outlet.
Krepel (2006)	Theoretical	Total: -10.9 Fuel: -6.9 Graphite: -4.0	Coupled neutronics-thermal hydraulics code DYN1D-MSR.
Krepel et al. (2007)	Theoretical	Total: -11.093 Fuel: -7.127 Graphite: -4.502	Used in DYN3D-MSR code. Ref. Lecarpentier et al. (2003) (original unavailable)
Kophazi et al. (2009)	Theoretical	Fuel: -9.77 Graphite: -6.31	Isothermal core.
Nagy et al. (2014)	Theoretical	Fuel: -8.85 Graphite: -5.98	No fuel movement or graphite expansion. Simplified geometry, no downcomer or control rods modelled.

Zhuang et al. (2017)	Theoretical	Total: -11.9 Fuel: -13.64 Graphite: -4.5	MOREL2.0 code. Fuel and graphite temperature assumed to be isotropic 923 K for this calculation, though predictions of T-distribution in hottest channel agree well with ORNL predictions.

Table A.4: Survey of temperature coefficients of reactivity from the literature. Note reactivity changes are quoted in absolute (non-dollar) units. Other values were encountered during the literature survey, those on other reactor designs or MSRE on ^{233}U fuel are not shown.

On the basis of a refined experimental result using the MSRE reactor, a fuel temperature coefficient of reactivity of $-8.46 \times 10^{-5} \pm 1.26$ K^{-1} was chosen. The graphite temperature coefficient of reactivity was assumed to comprise the remainder of the total thermal feedback, as measured using slower system heating. This resulted in a value of $-4.68 \times 10^{-5} \pm 1.26$ K^{-1}.

A.5 Semi-Analytical Model for Frequency Response and Stability Analysis

Transfer functions may be derived that describe the response of components or collections of components in dynamical systems. Useful information may be obtained, such as frequency response, transient behaviour and stability analysis in the vicinity of a steady state. A semi-analytical, simplified transfer function model of MSRE was derived in order to obtain such information.

A.5.1 Equations

Number of neutrons in the core:

$$\frac{dN(t)}{dt} = \frac{\rho - \beta}{\Lambda} N(t) + \sum_j \sum_i \lambda_i C_{i,j}(t) m_j \tag{A.1}$$

Concentration of precursors in core:

$$\frac{dC_{i,j}(t)}{dt} = \frac{\beta_i \psi_j}{\Lambda m_j} N(t) - \lambda_i C_{i,j}(t) + \frac{\dot{m}}{m_j} \Big(C_{i,j-1}(t) - C_{i,j}(t) \Big) \tag{A.2}$$

Concentration of precursors in primary circuit piping sections:

$$\frac{dC_{i,loop,j}}{dt} = \frac{\dot{m}}{m_{loop,j}} \Big(C_{i,loop,j-1}(t) - C_{i,loop,j}(t) \Big) - \lambda_i C_{i,loop,j}(t) \tag{A.3}$$

Concentration of precursors in HE sections:

$$\frac{dC_{i,HE,j}}{dt} = \frac{\dot{m}}{m_{HE,j}} \Big(C_{i,HE,j-1}(t) - C_{i,HE,j}(t) \Big) - \lambda C_{i,HE,j}(t) \tag{A.4}$$

Temperature of fuel in core:

$$\frac{dT_j(t)}{dt} = \frac{\chi_f \psi_j N(t) p_f}{\bar{\nu}\Lambda C_{p,f} m_j} + \frac{\dot{m}}{m_{core,j}}\left(T_{core,j-1} - T_{core,j}\right) + \frac{h_{f,g}A_{f,g}}{C_{p,f}m_{f,core}}\left(T_{g,j} - T_{f,core,j}\right) \quad \text{(A.5)}$$

Temperature of graphite in core:

$$\frac{dT_{g,j}(t)}{dt} = \frac{\chi_f \psi_j N(t) p_g}{\bar{\nu}\Lambda C_{p,f} m_{g,j}} + \frac{h_{f,g}A_{f,g}}{C_{p,g}m_g}\left(T_{f,core,j} - T_{g,j}\right) \quad \text{(A.6)}$$

Temperature of fuel in loop sections:

$$\frac{dT_{loop,j}(t)}{dt} = \frac{\dot{m}}{m_{loop,j}}\left(T_{loop,j-1} - T_{loop,j}\right) \quad \text{(A.7)}$$

Temperature of fuel in heat exchanger:

$$\frac{dT_{HE,j}(t)}{dt} = \frac{\dot{m}}{m_{HE}}\left(T_{HE,j-1} - T_{HE,j}\right) - \frac{h_{HE}A_{HE}}{C_{p,f}m_{HE}}\left(T_{HE,j} - T_{sec}\right) \quad \text{(A.8)}$$

Reactivity is defined by the following equation. Nuclear average temperatures are defined in the same fashion as the numerical model.

$$\rho = \rho_{external} - \alpha_f\left(T^*_{f,core} - T_{ref}\right) - \alpha_g\left(T^*_g - T_{ref}\right) \quad \text{(A.9)}$$

Additional notes:

Global $\dot{m}$ was adjusted to maintain the residence times in the respective sections according to experiment. The core residence time included the residence times of the upper and lower heads in order to capture all regions of significant fission activity.

A.5.2 Steady State Equations

The following set of equations were solved at low power (10^{-6} W) to find the external reactivity that compensated for loss of neutrons due to precursor decay outside of the core. With an

increasing number of component discretisations, the compensating reactivity converged on a value of approx. 2.7×10^{-3}.

$$-\alpha_f T_{ref}\frac{N_0}{\Lambda}-\alpha_g T_{ref}\frac{N_0}{\Lambda}+\beta\frac{N_0}{\Lambda}=-\alpha_f T_{core,av,0}\frac{N_0}{\Lambda}-\alpha_g T_{g,av,0}\frac{N_0}{\Lambda}+\rho_{external}\frac{N_0}{\Lambda}+\sum_j\sum_i \lambda_i C_{i,j} m_j$$

$$\frac{-\beta\psi_j N_0}{\Lambda m_j}=-\lambda_i C_{i,j,0}+\frac{\dot{m}}{m_j}\left(C_{i,j-1,0}-C_{i,j,0}\right)$$

At core entry,

$$\frac{-\beta_i\psi_1 N_0}{\Lambda m_1}=-\lambda_i C_{i,1,0}+\frac{\dot{m}}{m_1}\left(C_{i,external,0}-C_{i,1,0}\right)$$

At beginning of external loop,

$$0=\frac{\dot{m}}{m_{loop,1}}\left(C_{i,coreend,0}-C_{i,loop,1,0}\right)-\lambda_i C_{i,loop,1,0}$$

In middle of loop,

$$0=\frac{\dot{m}}{m_{loop,j}}\left(C_{i,loop,j-1,0}-C_{i,loop,j,0}\right)-\lambda_i C_{i,loop,j,0}$$

Steady state precursor concentrations in HE:

$$0=\frac{\dot{m}}{m_{HE,j}}\left(C_{i,HE,j-1,0}-C_{i,HE,j,0}\right)-\lambda C_{i,HE,j,0}$$

Core fuel temperature sections

$$-\frac{\chi_f\psi_j N_0 p_f}{\bar{\nu}\Lambda C_{p,f} m_{core,j}}=\frac{\dot{m}}{m_{core,j}}\left(T_{f,core,j-1,0}-T_{f,core,j,0}\right)+\frac{h_{f,g}A_{f,g}}{C_{p,f}m_{f,total}}\left(T_{g,j,0}-T_{f,core,j,0}\right)$$

Graphite temperature sections

$$-\frac{\chi_f \psi_j N_0 p_g}{\bar{\nu}\Lambda C_{p,g} m_{g,j}} = \frac{h_{f,g} A_{f,g}}{C_{p,g} m_{g,total}} \left(T_{f,core,j,0} - T_{g,j,0} \right)$$

Loop section temperature

$$0 = \frac{\dot{m}}{m_{loop,j}} \left(T_{loop,j-1,0} - T_{loop,j,0} \right)$$

Heat exchanger section temperature

$$-\frac{h_{HE} A_{HE}}{C_{p,f} m_{HE,total}} T_{sec} = \frac{\dot{m}}{m_{HE}} \left(T_{HE,j-1,0} - T_{HE,j,0} \right) - \frac{h_{HE} A_{HE}}{C_{p,f} m_{HE,total}} T_{HE,j,0}$$

A.5.3 Linearised Equations

The equations in Section A.5.1 were perturbed from their steady state values (neglecting $O(n^2)$ product terms) and the steady state condition subtracted to yield a set of linearised equations.

$$\frac{d\delta N}{dt} = \frac{1}{\Lambda} \left[\rho_0 \delta N + \delta\rho N_0 - \beta \delta N \right] + \sum_j \sum_i \lambda_i \delta C_{i,j} m_j$$

$$\frac{d\delta C_{i,j}}{dt} = \frac{\beta_i \psi_j}{\Lambda m_j} \delta N - \lambda_i \delta C_{i,j} + \frac{\dot{m}}{m_j} \left(\delta C_{i,j-1} - \delta C_{i,j} \right)$$

$$\frac{d\delta C_{i,loop,j}}{dt} = \frac{\dot{m}}{m_{loop,j}} \left(\delta C_{i,loop,j-1} - \delta C_{i,loop,j} \right) - \lambda_i \delta C_{i,loop,j}$$

$$\frac{d\delta C_{i,HE,j}}{dt} = \frac{\dot{m}}{m_{HE,j}} \left(\delta C_{i,HE,j-1} - \delta C_{i,HE,j} \right) - \lambda_i \delta C_{i,HE,j}$$

$$\frac{d\delta T_{f,core,j}}{dt} = \frac{\chi_f \psi_j \delta N p_f}{\bar{\nu} \Lambda C_{p,f} m_{f,j}} + \frac{\dot{m}}{m_{core,j}} \left(\delta T_{core,j-1} - \delta T_{core,j} \right) + \frac{h_{f,g} A_{f,g}}{C_{p,f} m_{f,total}} \left(\delta T_{g,j} - \delta T_{f,core,j} \right)$$

$$\frac{d\delta T_{g,j}}{dt} = \frac{\chi_f \psi_j \delta N p_g}{\bar{\nu} \Lambda C_{p,g} m_{g,j}} + \frac{h_{f,g} A_{f,g}}{C_{p,g} m_{g,total}} \left(\delta T_{f,core,j} - \delta T_{g,j} \right)$$

$$\frac{d\delta T_{loop,j}}{dt} = \frac{\dot{m}}{m_{loop,j}} \left(\delta T_{loop,j-1} - \delta T_{loop,j} \right)$$

$$\frac{d\delta T_{HE,j}}{dt} = \frac{\dot{m}}{m_{HE}} \left(\delta T_{HE,j-1} - \delta T_{HE,j} \right) - \frac{h_{HE} A_{HE}}{C_{p,f} m_{HE,total}} \delta T_{HE,j}$$

$$\delta \rho = -\alpha_f \delta T_{f,core,av} - \alpha_g \delta T_{f,core,av}$$

A.5.4 Transient Response

The transient response of the linearised model after a sudden cooling of the core inlet by 5 K is shown in Figure A.1. Initial conditions are steady state at 1 MW power. The core power initially rises due to increased reactivity, with smaller oscillations as the cool slug passes around the primary circuit, but later returns to the steady state condition (deviation equal to zero). In this case, each major section (core, core to H.E., HE, H.E. to core) was discretised into 8 regions.

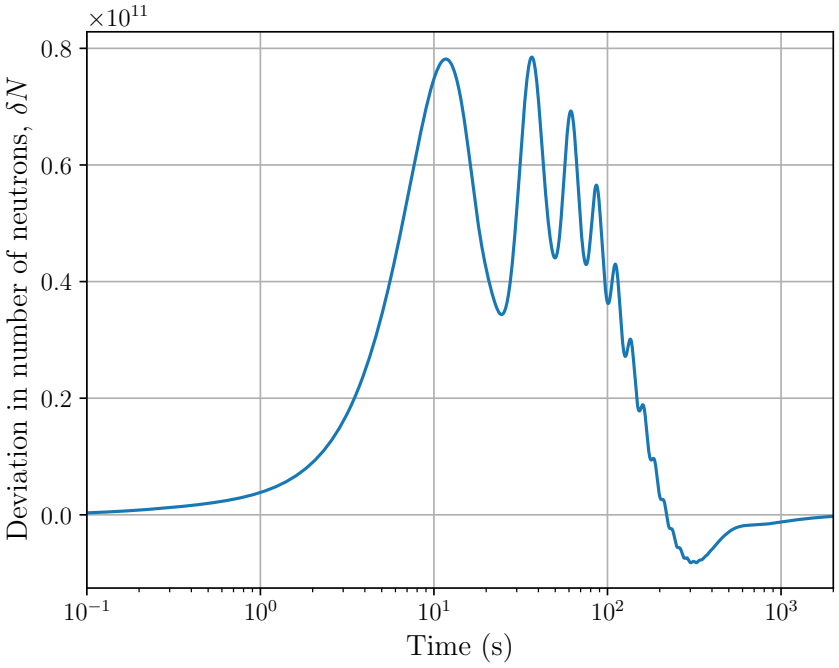

(a) δN

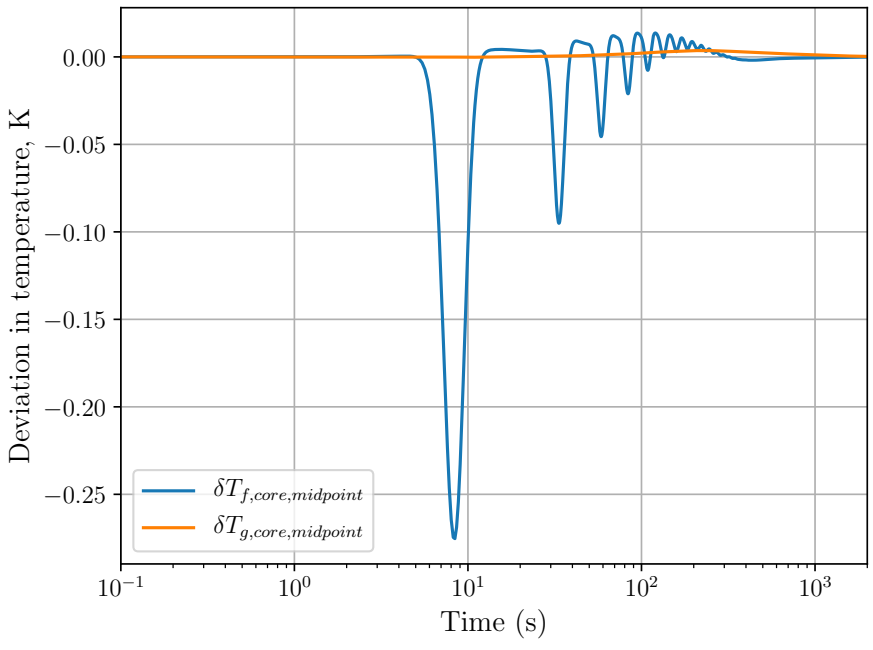

(b) δT_f and δT_g

Figure A.1: Deviations from steady state in response to a sudden 5 K cooling of the core inlet.

A.5.5 Transfer Function and Frequency Response

The linearised equations were Laplace transformed and the system solved for the deviation in power in s-space with a driving sinusoidal external reactivity source term to yield the system transfer function for $\delta\tilde{N}(s)$. The gain of the system was measured as the magnitude of δN relative to the original power N_0 and driving reactivity.

$$\frac{dX}{dt} = A(t) \tag{A.10}$$

Taking the Laplace transform of both sides and then subtracting the Laplace-transformed Jacobian matrix,

$$sI - \tilde{A}(s) = 0 \tag{A.11}$$

where I is the identity matrix. Substituting s for a complex sinusoid $i\omega$ and a source term containing the small perturbation amplitude $\delta\rho$ on the right hand side,

$$i\omega I - \tilde{A}(s) = \begin{bmatrix} \frac{\delta\rho N_0}{\Lambda} \\ 0 \\ \vdots \\ 0 \end{bmatrix} \tag{A.12}$$

The system is then solved for $\delta\tilde{N}(s)$ and the gain calculated as the magnitude of the change in power relative to the steady state power and amplitude of the driving signal, $\frac{\delta N}{\delta\rho N_0}$.

Convergence of Frequency Response with Increasing Circuit Discretisation

Figure A.2 shows the convergence of the frequency response of the model at P = 7.5 MW with decreasing mass per circuit section (and thus a higher number of sections and lower discretisation error). For investigations, a mass per section of 25 kg was chosen, offering a balance between error reduction and computational cost given the available resources.

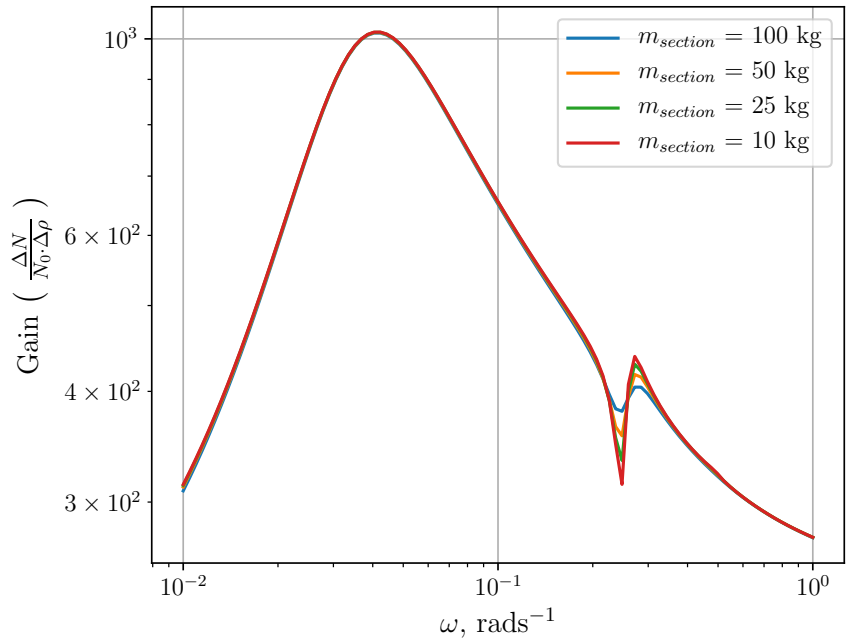

(a) Gain

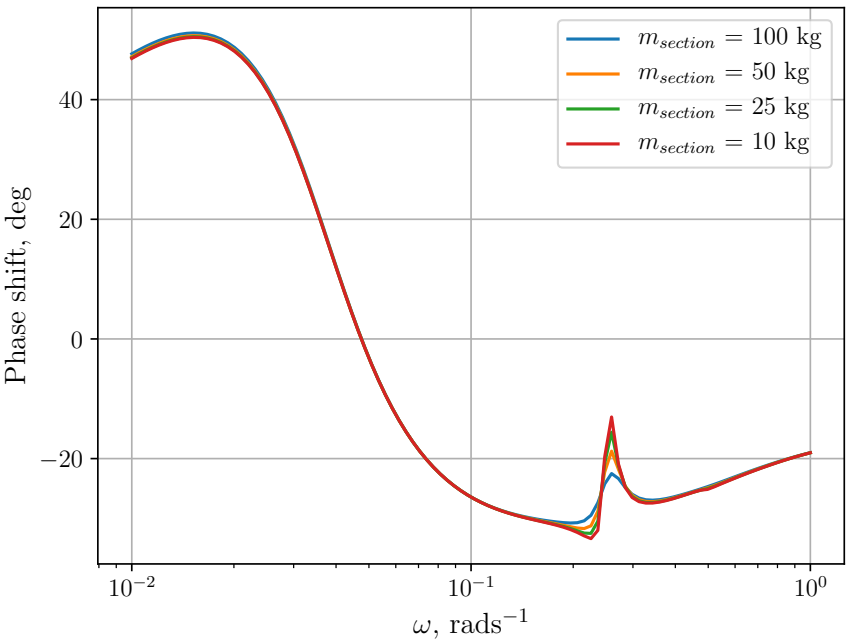

(b) Phase

Figure A.2: Convergence of gain and phase of semi-analytical model at 10 MW power, varying mass per circuit section from 100 kg to 5kg, in increasing resolution.

Appendix B

Overview of MSRE Frequency Responses

Figures B.1 and B.2 show the change in frequency response across the full range of MSRE operational powers, from zero power up to maximum of approx. 8 MW **??**. The system gains at all power levels are presented alongside one another for ease of comparison. This is repeated for system phase shifts. Also plotted are the responses from the MSFR code, used in the design phase of the programme [33].

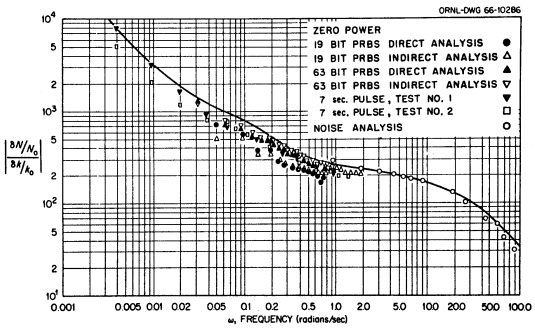

(a) Zero power, fuel circulating

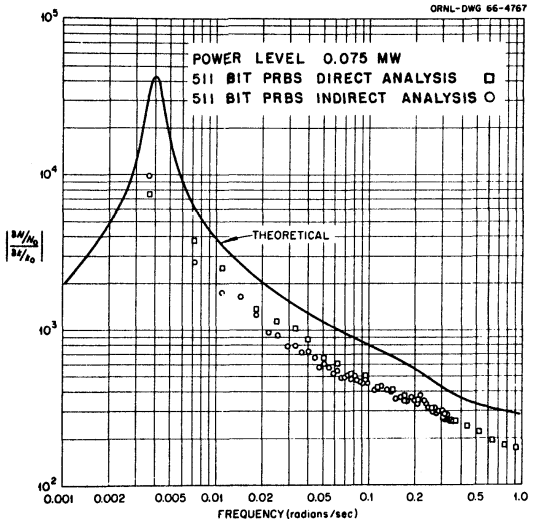

(b) 75 kW

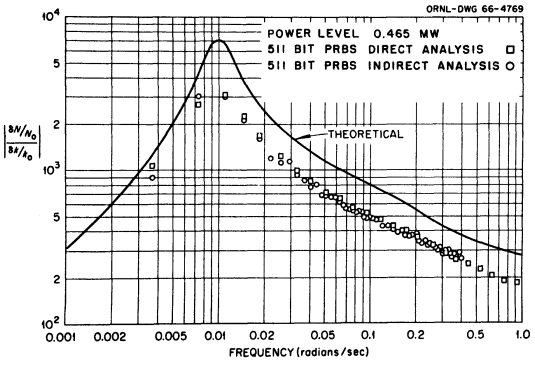

(c) 465 kW

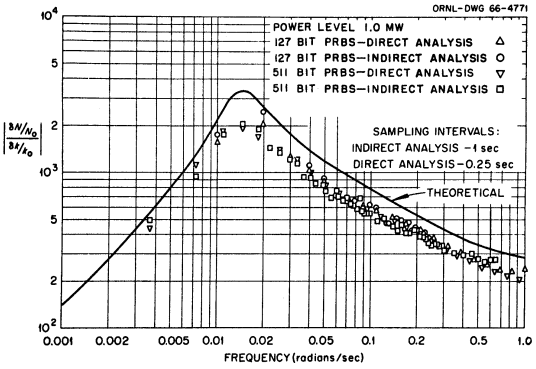

(d) 1 MW

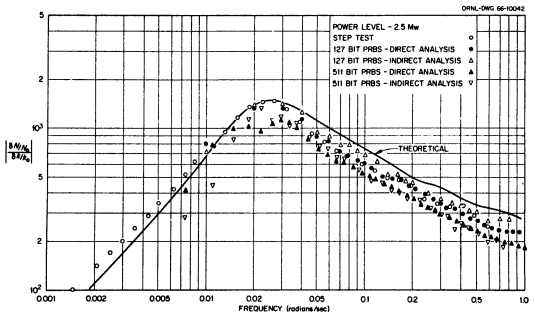

(e) 2.5 MW

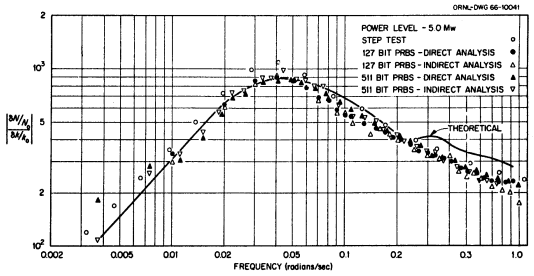

(f) 5 MW

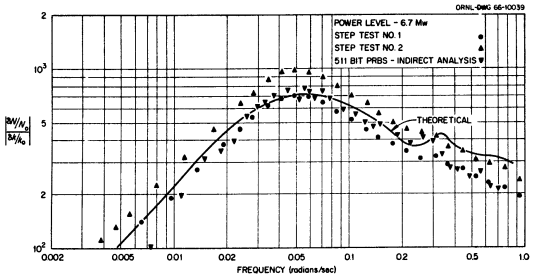

(g) 6.7 MW

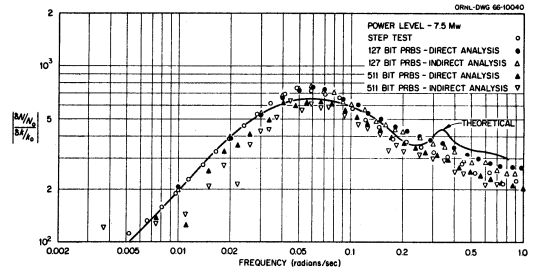

(h) 7.5 MW

Figure B.1: Experimental frequency response of ^{235}U-fuelled MSRE at various power levels, indicated by captions. Theoretical results generated by the MSFR code. Reproduced with permission, courtesy of the U.S. Dept of Energy [10].

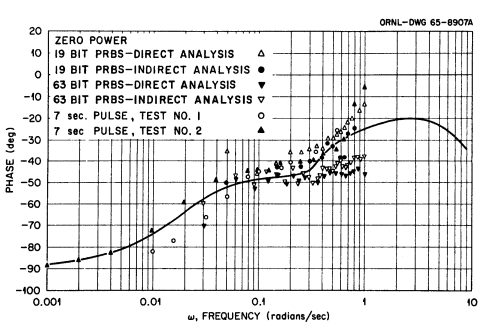

(a) Zero power, fuel circulating

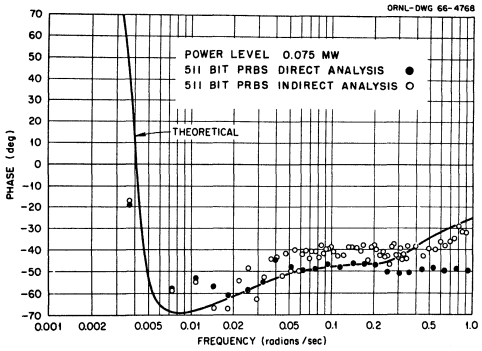

(b) 75 kW

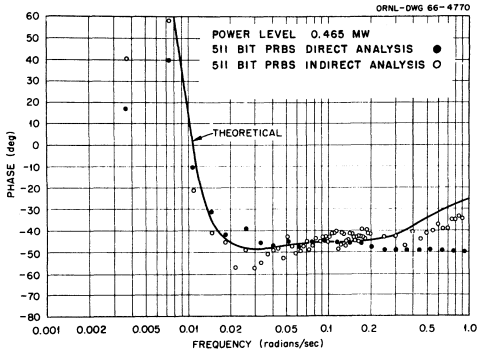

(c) 465 kW

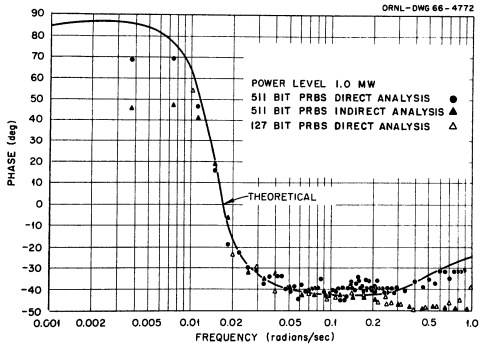

(d) 1 MW

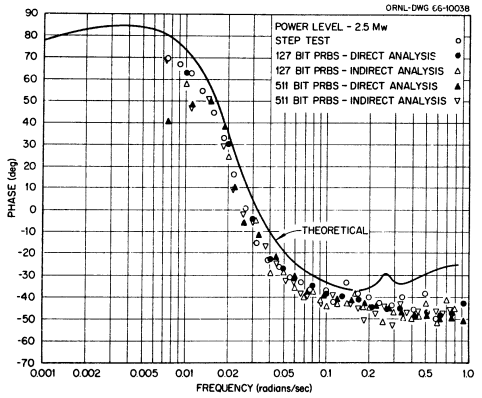

(e) 2.5 MW

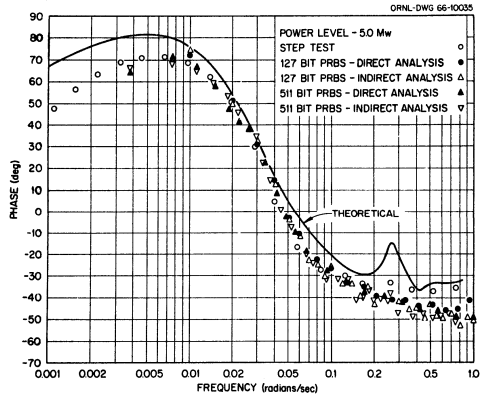

(f) 5 MW

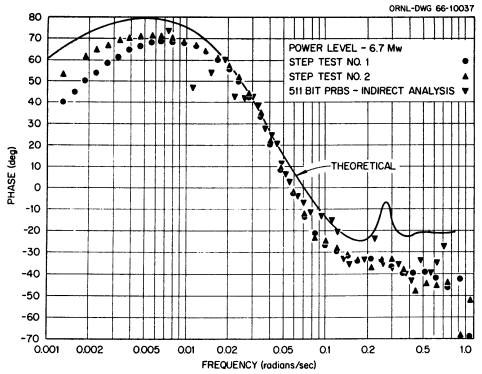

(g) 6.7 MW

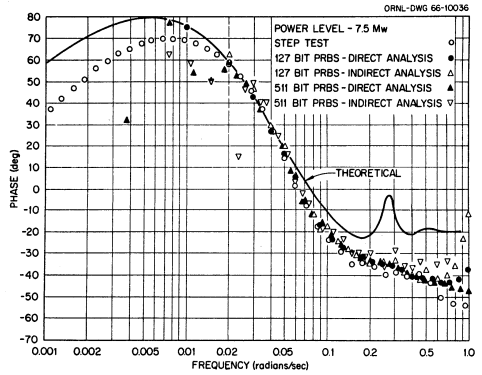

(h) 7.5 MW

Figure B.2: Experimental phase shift of ^{235}U-fuelled MSRE at various power levels, indicated by captions. Theoretical results generated by the MSFR code. Reproduced with permission, courtesy of the U.S. Dept of Energy [10].

Appendix C

MSRE Model for MCNP, WIMS and EVENT

A model was constructed in order to verify the parameters derived by Haubenreich *et al.* [7] in the MSRE design validation process. It consists of 20 regions of mixed material composition on the basis of component volume fraction in the reactor, in an un-rodded configuration with fresh fuel and a uniform temperature of 922.04 K (1200 °F). The model was used to construct input decks for the MCNP6 (Monte Carlo N-Particle) , WIMS (Winfrith Improved Multigroup Scheme) and EVENT (EVEn parity Neutral particle Transport) codes in order to compute macroscopic cross sections, mean generation times and flux distributions.

A python script was written to convert from the original Imperial measurements and chemical concentrations to SI units and number densities. Isotopic number densities are quoted to five significant figures for consistency of the total material amounts with the described reactor geometry. Physical constants and isotope abundances for unenriched materials, unless otherwise stated, were obtained from the National Institute of Standards and Technology (NIST) website [117].

C.1 Geometry

Figure C.1 shows a detailed cross sectional drawing of the MSRE vessel, core structures, piping and attachments at the top of the reactor cell to aid interpretation of the model.

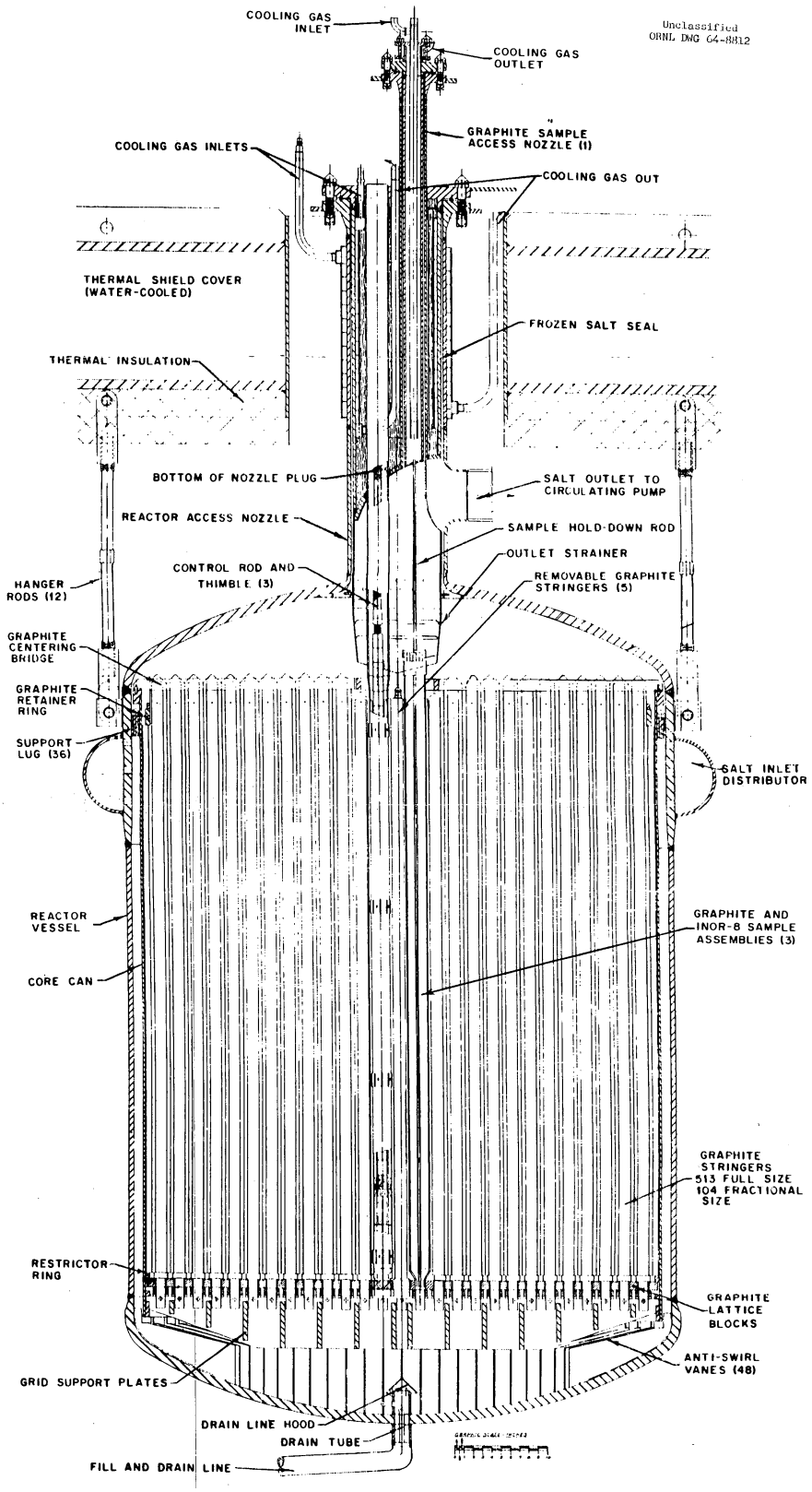

Figure C.1: Cross section through the MSRE vessel, reproduced with permission courtesy of the U.S. Department of Energy [2].

Region	Radius (m)		Height (m)		Volume Fraction			Density (kg m^{-3})	Description
	Inner	Outer	Bottom	Top	Fuel	Graphite	INOR-8		
A	0.	0.7508	1.9030	1.9314	0.	0.	1.	8775.0	Vessel top
B	0.7366	0.7508	-0.2322	1.9030	0.	0.	1.	8775.0	Vessel side
C	0.	0.7508	-0.2606	-0.2322	0.	0.	1.	8775.0	Vessel bottom
D	0.0762	0.7366	1.7137	1.9030	1.	0.	0.	2285.8	Upper head
E	0.0762	0.7112	1.6820	1.7137	0.937	0.035	0.028	2452.59	Graphite centering structure (1)
F	0.7112	0.7366	0.	1.7137	1.	0.	0.	2285.8	Downcomer
G	0.0762	0.7112	1.6645	1.6820	0.946	0.054	0.	2262.81	Top of graphite stringers
H	0.0762	0.7049	1.6406	1.6645	0.633	0.365	0.002	2143.36	Graphite centering structure (2)
I	0.7049	0.7112	0.	1.6645	0.	0.	1.	8775.0	Core can
J	0.0762	0.7049	0.1397	1.6406	0.225	0.775	0.	1955.81	Core including graphite moderator
K	0.0737	0.0762	0.1397	1.9030	0.	0.	1.	8775.0	Control thimbles
L	0.	0.0493	0.0508	1.6406	0.225	0.775	0.	1955.81	Central region
M	0.0493	0.7049	0.0508	0.1397	0.225	0.775	0.	1955.81	Lower part of core
N	0.	0.7049	0.	0.0508	0.237	0.763	0.	1960.91	Horizontal graphite stringers
O	0.	0.7366	-0.0358	0.	0.669	0.153	0.178	3375.73	Moderator support structure and stringer anchors
P	0.	0.7366	-0.2322	-0.0358	0.908	0.	0.092	2882.81	Lower head
Q	0.	0.0493	1.6820	1.9030	1.	0.	0.	2285.80	Vessel outlet
R	0.	0.0493	1.6645	1.6820	0.891	0.101	0.	2224.51	Top of graphite stringers
S	0.	0.0493	1.6406	1.6645	0.438	0.562	0.	2046.50	Centering structure (3)
T	0.0493	0.0737	0.1397	1.9030	1.	0.	0.	1051.47	Fuel and voids

Table C.1: Region dimensions, material volume fractions and descriptions. Dimensions are rounded to the nearest 0.1 millimetre, close to the precision quoted in the original source [7].

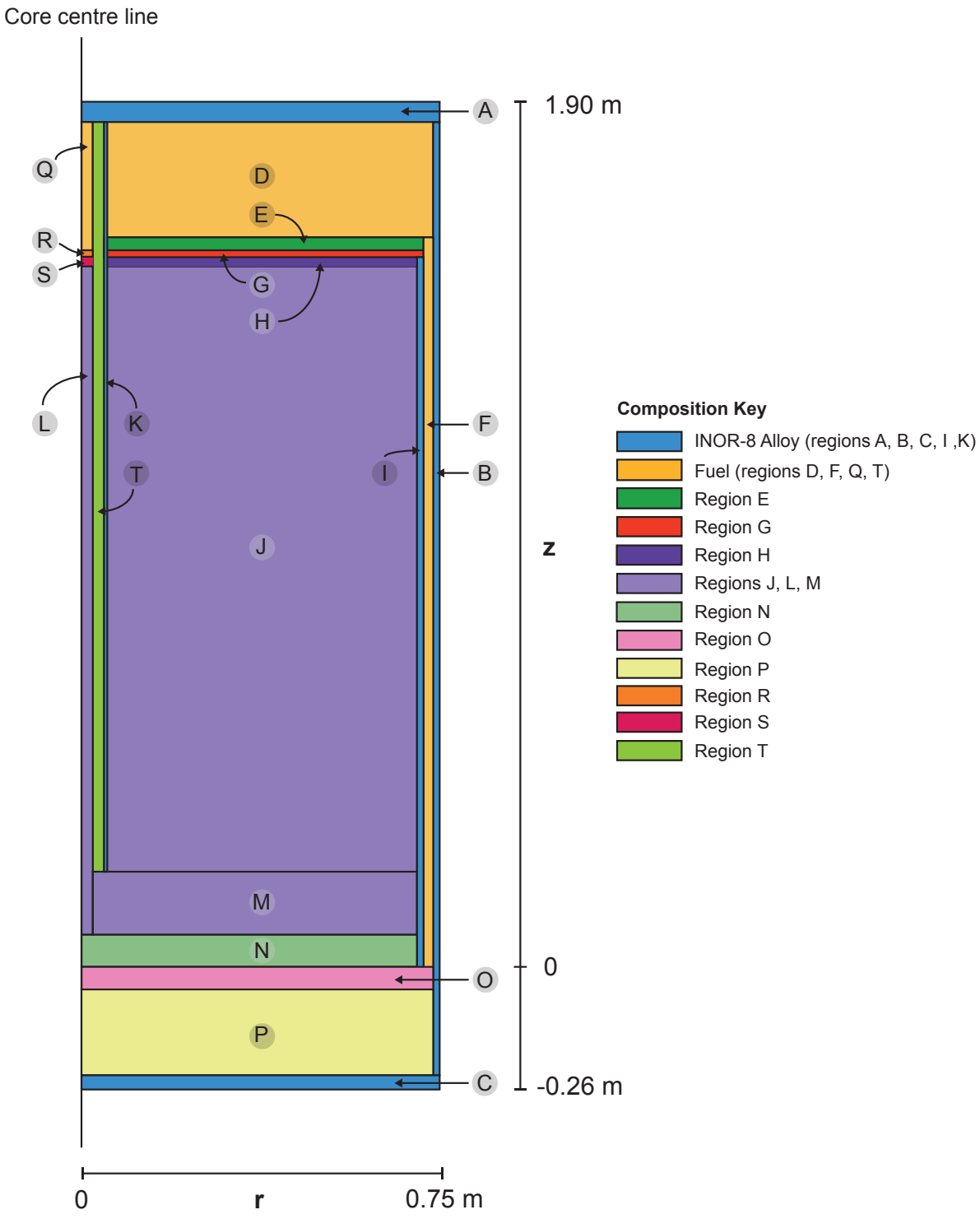

Figure C.2: Core schematic with approximate dimensions and region identifiers.

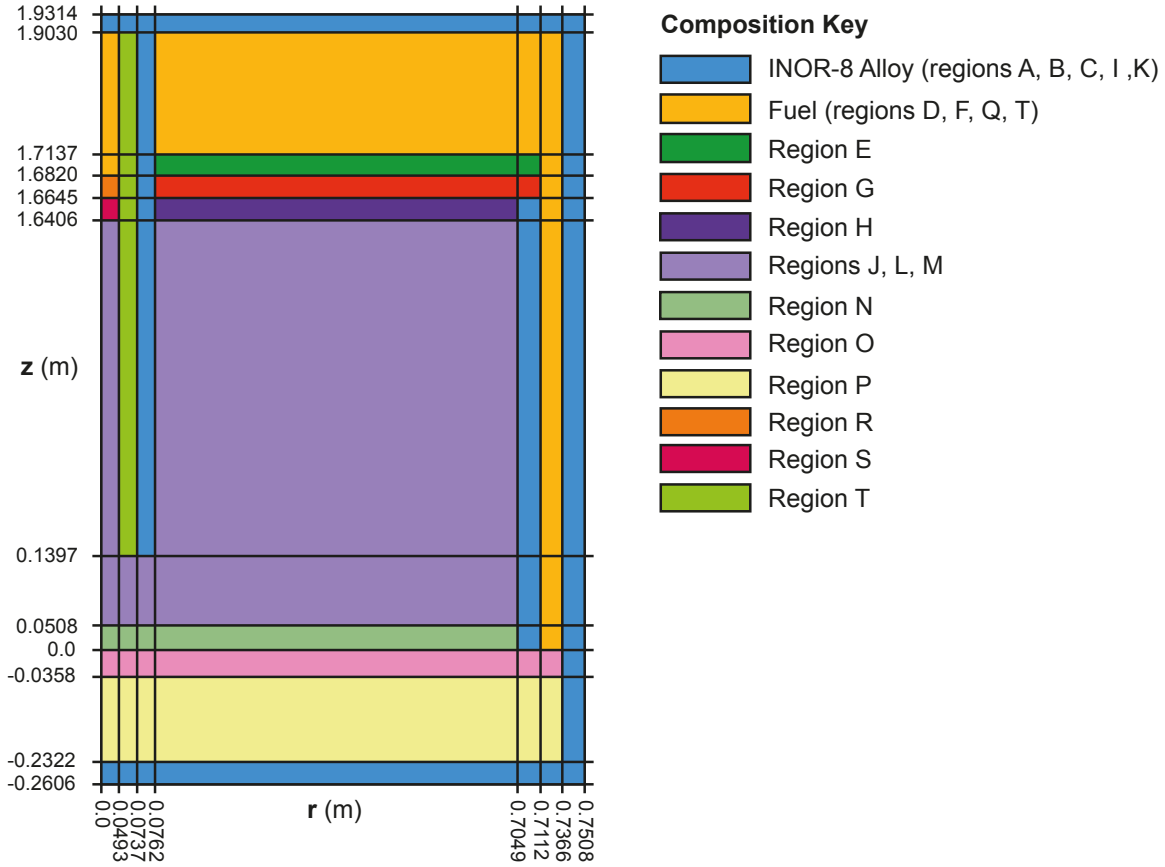

Figure C.3: EVENT cartesian mesh coloured by material, not to scale.

Material/Region	Group	Σ_t	Σ_a	$\nu\Sigma_f$	$\Sigma_{s0\ 1\to1}$	$\Sigma_{s0\ 1\to2}$	$\Sigma_{s1\ 1\to2}$	$\Sigma_{s1\ 1\to2}$
INOR-8	1	$1.04169 \cdot 10^{0}$	$1.3602 \cdot 10^{-2}$	$0.00000 \cdot 10^{0}$	$1.02648 \cdot 10^{0}$	$1.60493 \cdot 10^{-3}$	$2.58049 \cdot 10^{-2}$	$6.1236 \cdot 10^{-4}$
-	2	$1.43978 \cdot 10^{0}$	$1.58438 \cdot 10^{-1}$	$0.00000 \cdot 10^{0}$	$6.8633 \cdot 10^{-3}$	$1.27447 \cdot 10^{0}$	$4.15436 \cdot 10^{-3}$	$6.22908 \cdot 10^{-3}$
Fuel	1	$1.26136 \cdot 10^{-1}$	$1.06811 \cdot 10^{-3}$	$1.04895 \cdot 10^{-3}$	$1.24641 \cdot 10^{-1}$	$4.27228 \cdot 10^{-4}$	$9.88884 \cdot 10^{-3}$	$-1.05627 \cdot 10^{-4}$
-	2	$1.30438 \cdot 10^{-1}$	$1.21498 \cdot 10^{-2}$	$2.36824 \cdot 10^{-2}$	$5.65767 \cdot 10^{-4}$	$1.17723 \cdot 10^{-1}$	$4.4219 \cdot 10^{-5}$	$5.4855 \cdot 10^{-3}$
E	1	$1.62135 \cdot 10^{-1}$	$1.52563 \cdot 10^{-3}$	$1.04315 \cdot 10^{-3}$	$1.59995 \cdot 10^{-1}$	$6.14709 \cdot 10^{-4}$	$1.08342 \cdot 10^{-2}$	$-1.17449 \cdot 10^{-4}$
-	2	$1.79178 \cdot 10^{-1}$	$1.64844 \cdot 10^{-2}$	$2.28408 \cdot 10^{-2}$	$9.26818 \cdot 10^{-4}$	$1.61767 \cdot 10^{-1}$	$7.03285 \cdot 10^{-5}$	$5.77304 \cdot 10^{-3}$
G	1	$1.39859 \cdot 10^{-1}$	$1.14439 \cdot 10^{-3}$	$1.11232 \cdot 10^{-3}$	$1.38022 \cdot 10^{-1}$	$6.92453 \cdot 10^{-4}$	$1.06238 \cdot 10^{-2}$	$-1.66377 \cdot 10^{-4}$
-	2	$1.48327 \cdot 10^{-1}$	$1.18345 \cdot 10^{-2}$	$2.30611 \cdot 10^{-2}$	$9.17733 \cdot 10^{-4}$	$1.35575 \cdot 10^{-1}$	$-3.50913 \cdot 10^{-5}$	$5.8329 \cdot 10^{-3}$
H	1	$2.28217 \cdot 10^{-1}$	$9.34864 \cdot 10^{-4}$	$8.00105 \cdot 10^{-4}$	$2.25805 \cdot 10^{-1}$	$1.47692 \cdot 10^{-3}$	$1.56943 \cdot 10^{-2}$	$-3.41477 \cdot 10^{-4}$
-	2	$2.51424 \cdot 10^{-1}$	$8.29659 \cdot 10^{-3}$	$1.54026 \cdot 10^{-2}$	$3.34153 \cdot 10^{-3}$	$2.39786 \cdot 10^{-1}$	$-4.58688 \cdot 10^{-4}$	$7.85684 \cdot 10^{-3}$
JLM	1	$3.39612 \cdot 10^{-1}$	$4.74657 \cdot 10^{-4}$	$3.91556 \cdot 10^{-4}$	$3.3359 \cdot 10^{-1}$	$5.54788 \cdot 10^{-3}$	$2.29793 \cdot 10^{-2}$	$-1.2253 \cdot 10^{-3}$
-	2	$3.81345 \cdot 10^{-1}$	$2.9499 \cdot 10^{-3}$	$5.51366 \cdot 10^{-3}$	$5.98963 \cdot 10^{-3}$	$3.72405 \cdot 10^{-1}$	$-9.8407 \cdot 10^{-4}$	$1.03323 \cdot 10^{-2}$
N	1	$3.3988 \cdot 10^{-1}$	$4.52771 \cdot 10^{-4}$	$3.65721 \cdot 10^{-4}$	$3.35843 \cdot 10^{-1}$	$3.58367 \cdot 10^{-3}$	$2.23833 \cdot 10^{-2}$	$-8.12387 \cdot 10^{-4}$
-	2	$3.77107 \cdot 10^{-1}$	$3.05076 \cdot 10^{-3}$	$5.71586 \cdot 10^{-3}$	$6.43093 \cdot 10^{-3}$	$3.67625 \cdot 10^{-1}$	$-1.02733 \cdot 10^{-3}$	$1.06567 \cdot 10^{-2}$
O	1	$3.44154 \cdot 10^{-1}$	$4.03783 \cdot 10^{-3}$	$8.47155 \cdot 10^{-4}$	$3.38776 \cdot 10^{-1}$	$1.34003 \cdot 10^{-3}$	$1.49159 \cdot 10^{-2}$	$-5.80572 \cdot 10^{-5}$
-	2	$4.13837 \cdot 10^{-1}$	$3.72862 \cdot 10^{-2}$	$1.56828 \cdot 10^{-2}$	$2.77303 \cdot 10^{-3}$	$3.73778 \cdot 10^{-1}$	$4.09372 \cdot 10^{-4}$	$6.93538 \cdot 10^{-3}$
P	1	$2.15701 \cdot 10^{-1}$	$2.21624 \cdot 10^{-3}$	$8.95430 \cdot 10^{-4}$	$2.13074 \cdot 10^{-1}$	$4.11243 \cdot 10^{-4}$	$1.11116 \cdot 10^{-2}$	$-2.95017 \cdot 10^{-5}$
-	2	$2.506 \cdot 10^{-1}$	$2.5388 \cdot 10^{-2}$	$2.07533 \cdot 10^{-2}$	$1.26885 \cdot 10^{-3}$	$2.23943 \cdot 10^{-1}$	$3.96888 \cdot 10^{-4}$	$5.6021 \cdot 10^{-3}$
R	1	$1.5155 \cdot 10^{-1}$	$1.10592 \cdot 10^{-3}$	$1.06824 \cdot 10^{-3}$	$1.49586 \cdot 10^{-1}$	$8.58985 \cdot 10^{-4}$	$1.14336 \cdot 10^{-2}$	$-2.0449 \cdot 10^{-4}$
-	2	$1.62338 \cdot 10^{-1}$	$1.10613 \cdot 10^{-2}$	$2.15360 \cdot 10^{-2}$	$1.26116 \cdot 10^{-3}$	$1.50015 \cdot 10^{-1}$	$9.98313 \cdot 10^{-5}$	$6.11201 \cdot 10^{-3}$
S	1	$2.79168 \cdot 10^{-1}$	$6.16847 \cdot 10^{-4}$	$5.41135 \cdot 10^{-4}$	$2.76644 \cdot 10^{-1}$	$1.9064 \cdot 10^{-3}$	$1.89996 \cdot 10^{-2}$	$-4.41451 \cdot 10^{-4}$
-	2	$3.12288 \cdot 10^{-1}$	$5.50816 \cdot 10^{-3}$	$1.05681 \cdot 10^{-2}$	$4.84539 \cdot 10^{-3}$	$3.01935 \cdot 10^{-1}$	$7.35888 \cdot 10^{-4}$	$9.24688 \cdot 10^{-3}$
T	1	$5.78741 \cdot 10^{-2}$	$7.54379 \cdot 10^{-4}$	$7.11018 \cdot 10^{-4}$	$5.64746 \cdot 10^{-2}$	$6.45142 \cdot 10^{-4}$	$4.67564 \cdot 10^{-3}$	$-1.48738 \cdot 10^{-4}$
-	2	$6.01411 \cdot 10^{-2}$	$5.70128 \cdot 10^{-3}$	$1.11143 \cdot 10^{-2}$	$2.01396 \cdot 10^{-4}$	$5.42384 \cdot 10^{-2}$	$1.44983 \cdot 10^{-5}$	$2.52866 \cdot 10^{-3}$

Table C.2: Two group macroscopic neutron cross sections generated by WIMS for EVENT case with linearly anisotropic scattering.
χ_1 = 9.9999923E-01, χ_2 = 8.0000001E-07.

C.2 Flux Distributions and Reactor Physics Parameters

Flux distributions across the core were tallied using the KOPTS card in MCNP and renormalised to a power of 10 MW. 10^7 neutron histories per cycle were generated. Fast and thermal groups were treated as neutron energies between 20 MeV and 0.4 eV, and less than 0.4eV, respectively. The midpoint of the thermal group, 0.2 eV, was used to renormalise the flux for comparison with the ORNL model. Flux maps are shown in Figures C.5 and C.6. The depression in the thermal flux in the central region containing the control rod and sample thimbles is visible. In the fast spectrum, Region T exhibits higher flux than the surrounding regions and is visible.

Figures C.8 and C.9 compare the MCNP and EVENT flux distributions at specific axial and radial slices to ORNL data. A large disparity exists between the magnitude of the ORNL thermal flux distribution and the corresponding thermal flux distributions as calculated using MCNP and EVENT. In addition, there is a difference of a few cm in the location of flux peak in the axial distribution.

Haubenreich *et al*, in their original reactor physics analysis of MSRE [7], show flux distributions for 'Fuel C' (close to the operational mixture) with two vertical axes for fast and thermal fluxes on one plot. Other plots in their report do not use twin axes so it was investigated if this was a typographical error as use of the fast flux scale permitted the MCNP and EVENT thermal flux magnitudes to match those from ORNL more closely.

The MCNP model was re-run with 'Fuel B', a highly-enriched alternative fuel that was considered for use early in the MSRE programme, with no ambiguity in the flux axes. Use of this fuel mixture reduced the difference between MCNP and ORNL flux magnitudes however did not fully resolve the difference. The investigation was not conclusive.

During the MSRE program, monitoring of the axial neutron flux distribution outside the vessel was performed using steel wires which were later cut into segments and analysed. Gold and copper foils were also used for flux calibration [11]. These measurements (Figure C.4) show a broadly similar flux distribution to those presented in Fig. C.8, albeit with a slightly lower position corresponding to peak flux due to the position of the shim rods during the majority of the operating hours. In addition, neutron flux at the top of the core is depressed significantly

due to the insertion of the rods.

This data could be used to help resolve the differences in flux magnitudes identified above. It would require a model of the MSRE thermal shield in addition to the vessel and core in order to model the vessel leakage and reflection from the thermal shield materials. It is a cylindrical structure with walls approx. 40 cm thick, filled with a mixture of 25 mm steel balls and cooling water [2] which would likely reflect some neutrons back towards the vessel.

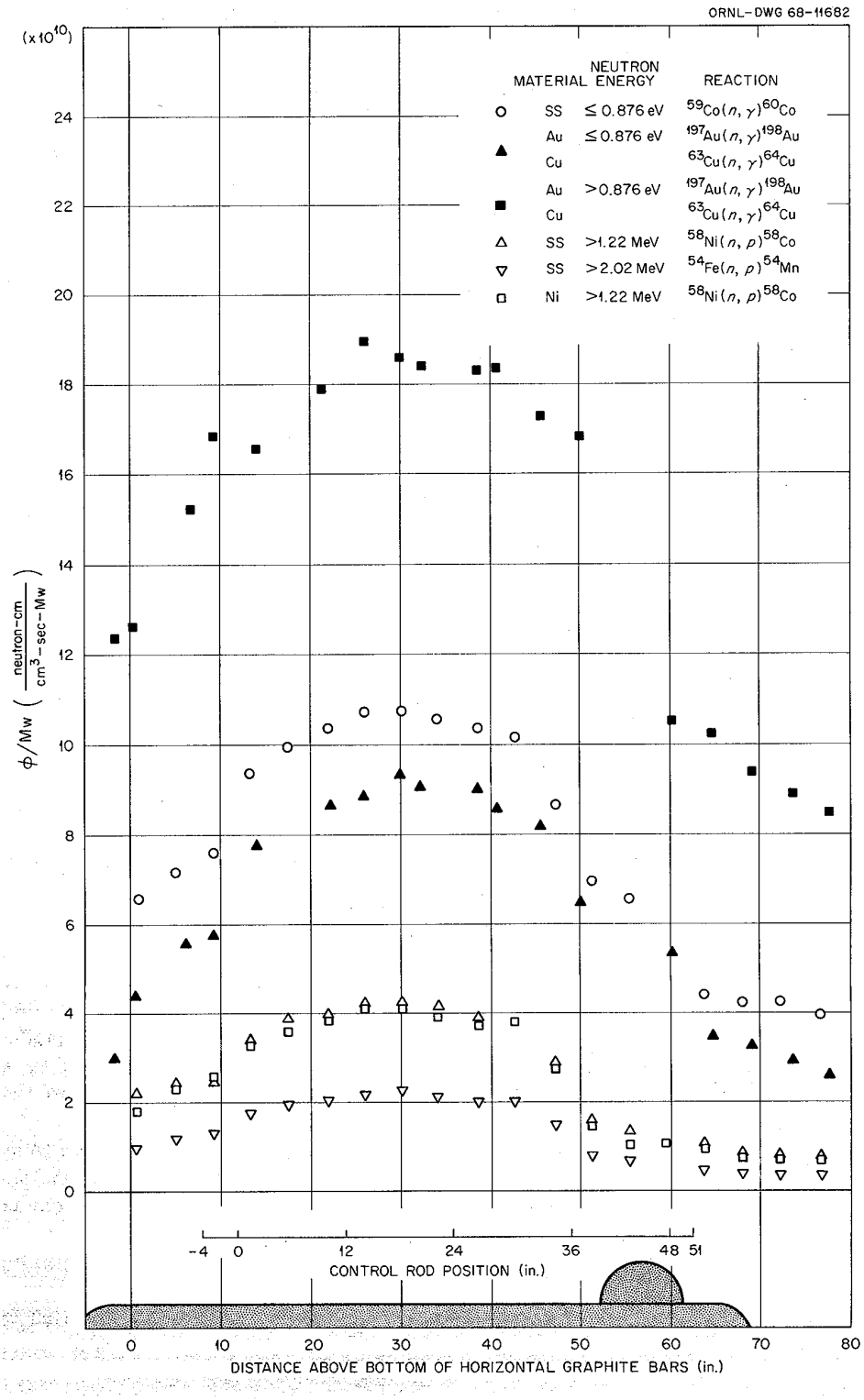

Fig. 1.12 Axial Neutron Flux in MSRE Reactor Furnace at Various Energies.

Figure C.4: Wire and foil flux measurements at various neutron energies from the exterior of the MSRE vessel. Reproduced with permission, courtesy of the US Department of Energy [11].

C.2.1 Discussion of the Effective Multiplication Factor k_{eff} and Thermal Scattering Cross Sections

Table C.3 shows a range of k_{eff} values computed by the MCNP, EVENT [118], WIMS10 CACTUS [119], WIMS11 SP_3 and MONK codes, each with different methods and combinations of boundary conditions.

k_{eff} Values			
Code	k_{eff}	Boundary condition	Comments
MCNP	0.97659	vacuum	MC, 10 million particle histories.
EVENT	0.8251	vacuum	86k elements, P_9 transport calculation.
WIMS11 CACTUSOT	0.81	vacuum	Method of Characteristics [1]
WIMS10 CACTUS	0.883133	reflective	190 x 75 subdivisions CACTUS3D mesh.
EVENT	0.93413	reflective	86k elements, P_9 transport calculation.
EVENT	0.91953	reflective sides with top/bottom vacuum	86k elements, P_9 transport calculation.
EVENT	0.93164	reflective	86k elements, SP_3 transport calculation.
MONK	0.92	reflective	MC, WIMS broad group cross sections [1]
WIMS11 SP_3	0.92	reflective	SP_3 approximated transport [1]

Table C.3: k_{eff} values for the MSRE vessel model. (Wood Plc ANSWERS Software Service[1])

A possible explanation for the difference between the values obtained for the WIMS, EVENT and MCNP k_{eff} is uncertainty in the thermal cross sections of the fuel salt. Scattering theory predicts a trend of highest inelastic cross sections for free-gas treatments, followed by the liquid phase, followed by the lowest contribution for crystalline molten salt.

An accurate prediction of the inelastic scattering cross section would have to take into account the coherent and incoherent contributions to the scattering in the molten salt. Correlated atomic motions contribute to coherent scattering while diffusion of nuclei contribute to incoherent scatter. Classical molecular dynamics simulations have predicted BeF_4^{2-} clusters (Be^{2+} ions coordinated in a tetrahedral fashion by F^-), surrounded by Li^+ ions that are more mobile [120]. Thus there will be contributions from bound and diffusive states in the dynamic structure factor, $S(\alpha, \beta)$, corresponding to the dynamics of the clusters and Li^+ ions, respectively.

This method has been used to refine the thermal scattering cross sections for nuclear graphite, taking into account the porous nature of the material compared to an ideal structure. Molecular models of the porous graphite exhibit a broader density of states (DOS) compared to the non-porous form, and so inelastic neutron scatter is enhanced. The adjusted cross sections were used to improve predictions in a slowing-down experiment in nuclear graphite compared to the ENDF/B-VII library [121].

Significant upscatter of neutrons from thermal energies is predicted in the FliBe molten salt which hardens the neutron spectrum in the reactor [122]. This will increase the fission reaction rate in the epithermal spectrum (5.0 eV to 0.22 eV), decrease the fission reaction rate in the thermal spectrum (0.22 eV to 10^{-5} eV), and increase resonance capture in ^{238}U. Analysis of a pebble-bed FLiBe-cooled design estimated a reduction in k_{eff} of up to 881 pcm [123]. A hardening of the spectrum will also increase leakage from the reactor, reducing k_{eff}.

Generalised theoretical predictions of thermal scattering in disordered materials is an area of active research [116]. Such methods could be used to improve estimates of thermal scattering cross sections for FLiBe with dissolved uranium fluoride fuel. The uranium cations will be coordinated by the fluoride anions altering the dynamics of the uranium nuclei. This may influence the doppler broadening of heavy nuclei resonance peaks.

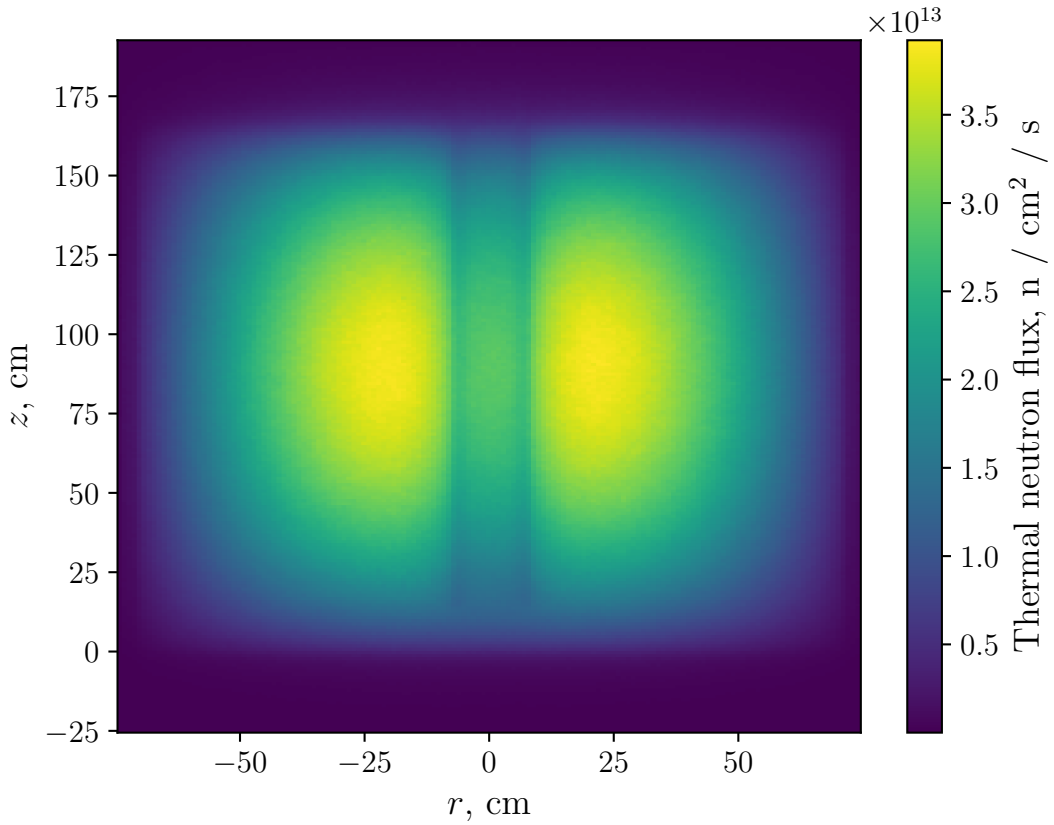

Figure C.5: Thermal neutron scalar flux map.

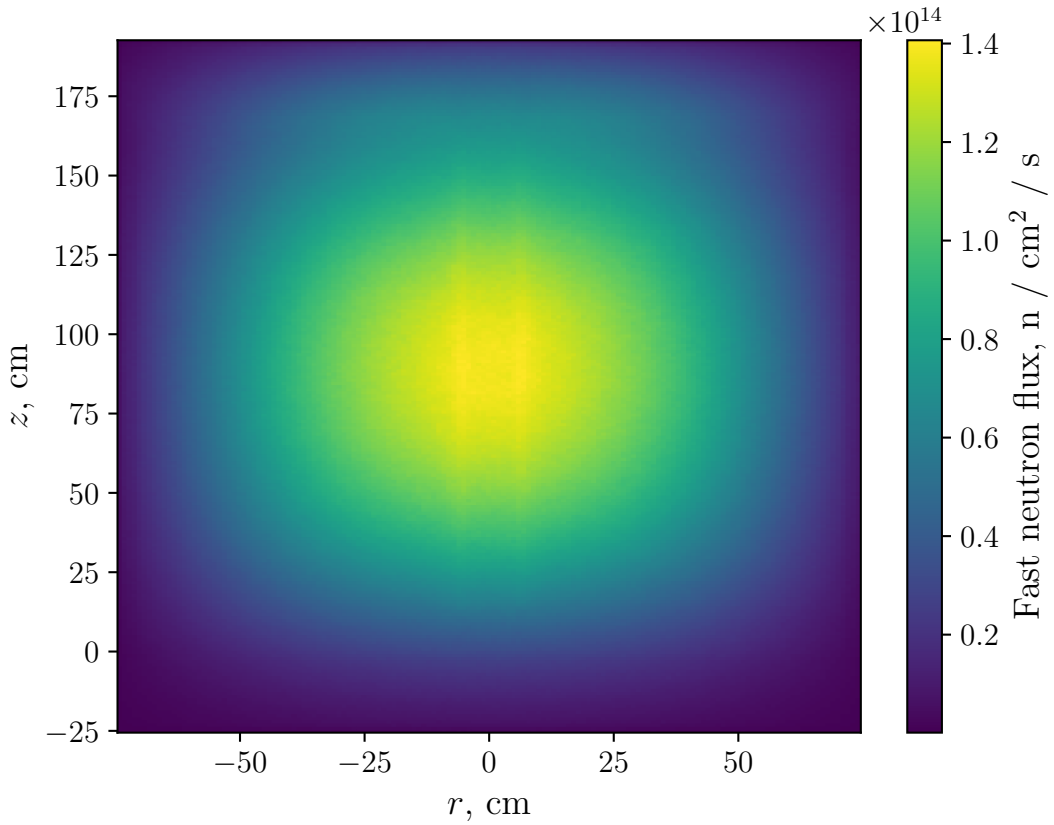

Figure C.6: Fast scalar neutron flux map.

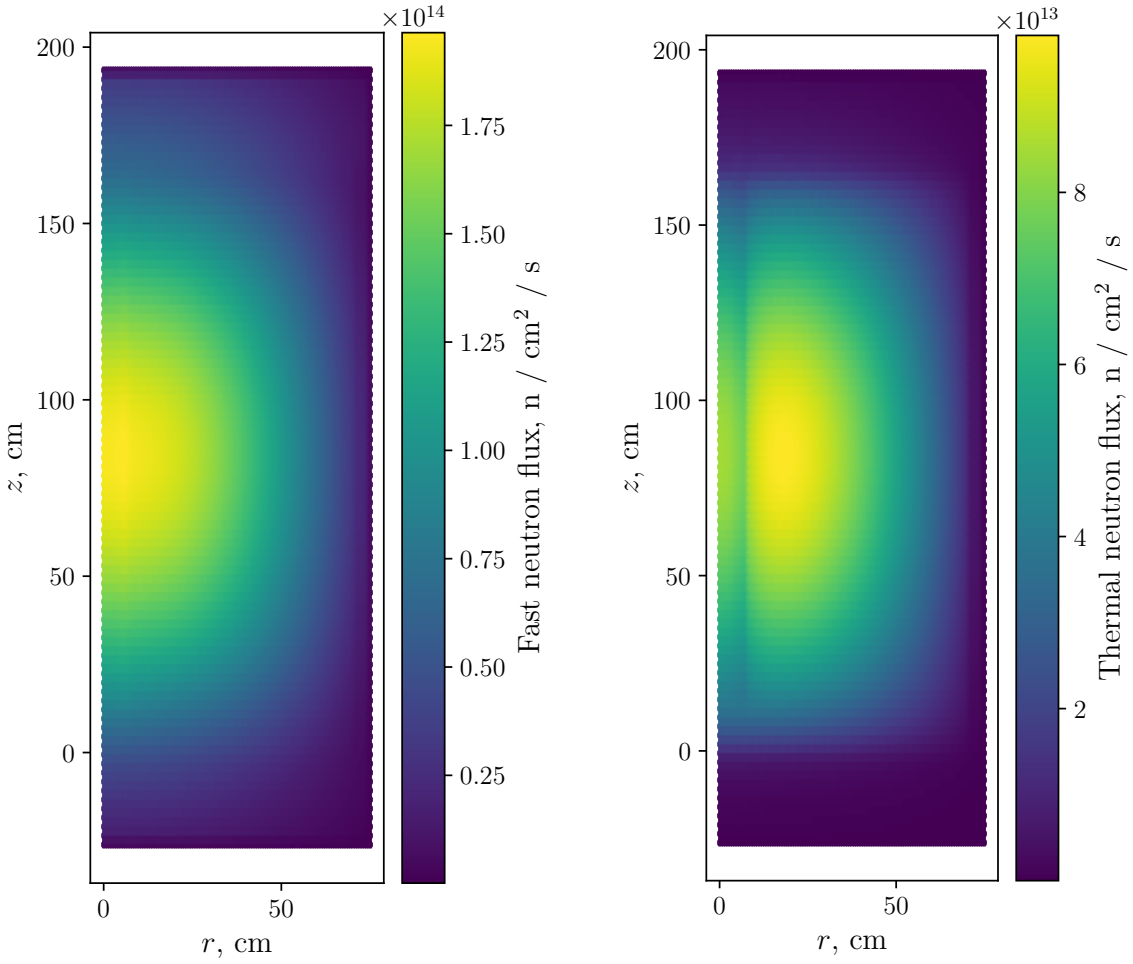

(a) Fast neutron scalar flux

(b) Thermal neutron scalar flux

Figure C.7: Flux maps from the two-group EVENT model.

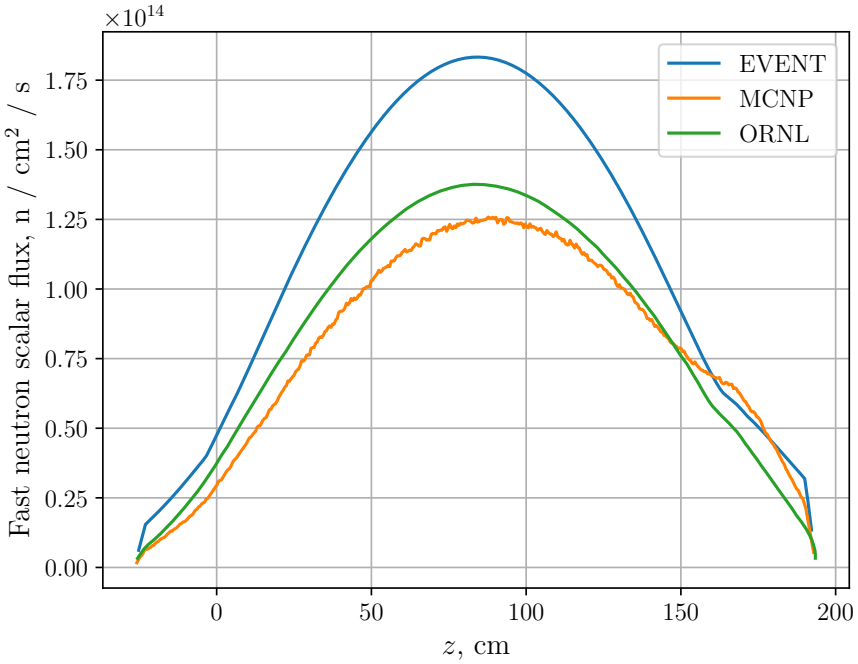

(a) Fast neutron scalar flux.

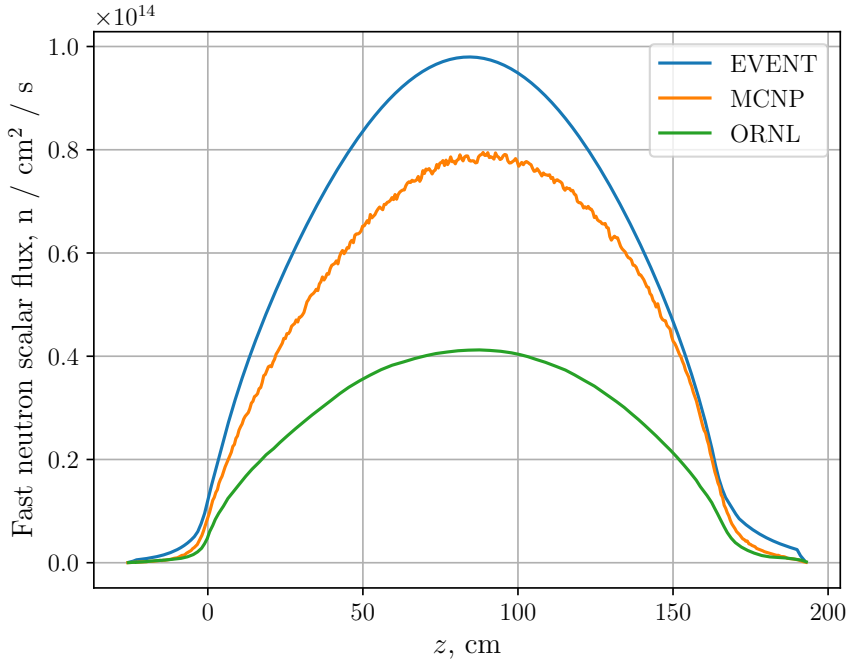

(b) Thermal neutron scalar flux.

Figure C.8: Comparison of axial flux distributions in the 'hottest' channel [7], corresponding to $r \sim 0.213$ m.

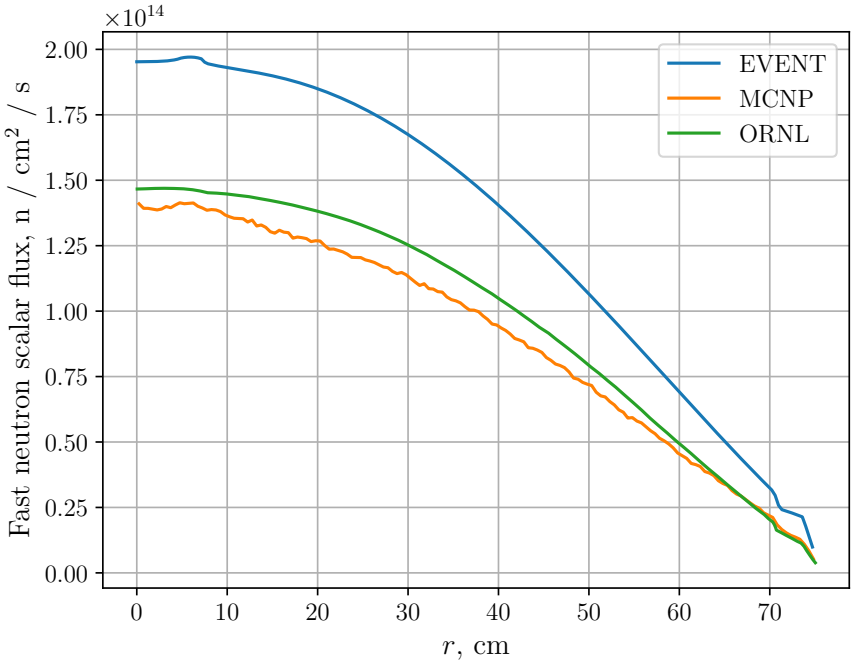

(a) Fast neutron scalar flux.

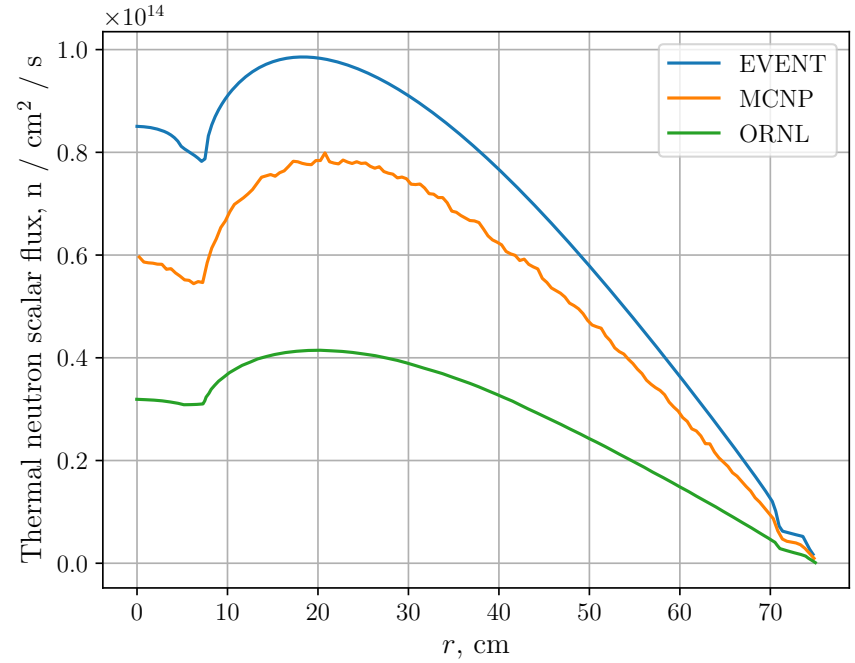

(b) Thermal neutron scalar flux.

Figure C.9: Comparison of radial flux distributions at $z = 0.85$m.

C.3 Material Compositions and Number densities

The model has 11 unique material compositions. Regions A, B, C, I and K consist solely of the INOR-8 alloy and may be defined in terms of mass fractions and natural isotopic compositions.

Element	Mass fraction
Ni	0.73
Mo	0.16
Cr	0.06
Fe	0.05

Table C.4: Elemental mass fractions for INOR-8 alloy, based on typical composition [14]
.

Isotope	Atoms (barn-cm)$^{-1}$
Ni	$6.57256 \cdot 10^{-2}$
Mo	$8.81197 \cdot 10^{-3}$
Cr	$6.09787 \cdot 10^{-3}$
Fe	$4.73134 \cdot 10^{-3}$

Table C.5: INOR-8 isotopic number densities for entry into WIMS.

Isotope	ZAID	Atoms cm^{-3}
Ni-58	28058	$4.4744 \cdot 10^{22}$
Ni-60	28060	$1.72352 \cdot 10^{22}$
Ni-61	28061	$7.49206 \cdot 10^{20}$
Ni-62	28062	$2.38886 \cdot 10^{21}$
Ni-64	28064	$6.0829 \cdot 10^{20}$
Mo-92	42092	$1.28038 \cdot 10^{21}$
Mo-94	42094	$8.06295 \cdot 10^{20}$
Mo-95	42095	$1.39582 \cdot 10^{21}$
Mo-96	42096	$1.46896 \cdot 10^{21}$
Mo-97	42097	$8.45949 \cdot 10^{20}$
Mo-98	42098	$2.14924 \cdot 10^{21}$
Mo-100	42100	$8.65336 \cdot 10^{20}$
Cr-50	24050	$2.64953 \cdot 10^{20}$
Cr-52	24052	$5.10935 \cdot 10^{21}$
Cr-53	24053	$5.79359 \cdot 10^{20}$
Cr-54	24054	$1.44215 \cdot 10^{20}$
Fe-54	26054	$2.76547 \cdot 10^{20}$
Fe-56	26056	$4.34119 \cdot 10^{21}$
Fe-57	26057	$1.00257 \cdot 10^{20}$
Fe-58	26058	$1.33424 \cdot 10^{19}$

Table C.6: INOR-8 isotopic number densities and ZAID codes for entry into MCNP.

Regions D, F, and Q are comprised exclusively of the molten fuel and have the following isotopic number density composition.

Species	**Mole %**	**Isotopic atom %**
LiF	65.0	
^{6}Li		0.0074
^{7}Li		99.9926
BeF_2	29.2	
ZrF_4	5.0	
UF_6	0.8	
^{234}U		0.3
^{235}U		35
^{236}U		0.3
^{238}U		64.4

Table C.7: Composition of clean MSRE fuel salt used for calculation of core physics parameters in this section.

Component	Atoms (barn-cm)$^{-1}$
Li6	$6.47145 \cdot 10^{-7}$
Li7	$8.74456 \cdot 10^{-3}$
Be	$3.92861 \cdot 10^{-3}$
U234	$3.229 \cdot 10^{-7}$
U235	$3.76716 \cdot 10^{-5}$
U236	$3.229 \cdot 10^{-7}$
U238	$6.93158 \cdot 10^{-5}$
F	$1.97238 \cdot 10^{-2}$
Zr	$6.72708 \cdot 10^{-4}$

Table C.8: Fuel isotopic number densities.

Isotope	ZAID	Atoms cm^{-3}
Li-6	3006	$6.47145 \cdot 10^{17}$
Li-7	3007	$8.74456 \cdot 10^{21}$
Be-9	4009	$3.92861 \cdot 10^{21}$
Zr-90	40090	$3.46108 \cdot 10^{20}$
Zr-91	40091	$7.54778 \cdot 10^{19}$
Zr-92	40092	$1.15369 \cdot 10^{20}$
Zr-94	40094	$1.16917 \cdot 10^{20}$
Zr-96	40096	$1.88358 \cdot 10^{19}$
U-234	92234	$3.229 \cdot 10^{17}$
U-235	92235	$3.76716 \cdot 10^{19}$
U-236	92236	$3.229 \cdot 10^{17}$
U-238	92238	$6.93158 \cdot 10^{19}$
F-19	9019	$1.97238 \cdot 10^{22}$

Table C.9: Fuel isotopic number densities and ZAID codes for entry into MCNP.

Component	Atoms (barn-cm)$^{-1}$
Li6	$6.06375 \cdot 10^{-7}$
Li7	$8.19365 \cdot 10^{-3}$
Be	$3.68111 \cdot 10^{-3}$
U234	$3.02557 \cdot 10^{-7}$
U235	$3.52983 \cdot 10^{-5}$
U236	$3.02557 \cdot 10^{-7}$
U238	$6.49489 \cdot 10^{-5}$
F	$1.84812 \cdot 10^{-2}$
Zr	$6.30327 \cdot 10^{-4}$
C	$3.26402 \cdot 10^{-3}$
Ni	$1.84032 \cdot 10^{-3}$
Mo	$2.46735 \cdot 10^{-4}$
Cr	$1.7074 \cdot 10^{-4}$
Fe	$1.32477 \cdot 10^{-4}$

Table C.10: Component number densities for Region E, for WIMS input.

Isotope	ZAID	Atoms cm^{-3}
Li-6	3006	$6.06375 \cdot 10^{17}$
Li-7	3007	$8.19365 \cdot 10^{21}$
Be-9	4009	$3.68111 \cdot 10^{21}$
Zr-90	40090	$3.24303 \cdot 10^{20}$
Zr-91	40091	$7.07227 \cdot 10^{19}$
Zr-92	40092	$1.08101 \cdot 10^{20}$
Zr-94	40094	$1.09551 \cdot 10^{20}$
Zr-96	40096	$1.76492 \cdot 10^{19}$
U-234	92234	$3.02557 \cdot 10^{17}$
U-235	92235	$3.52983 \cdot 10^{19}$
U-236	92236	$3.02557 \cdot 10^{17}$
U-238	92238	$6.49489 \cdot 10^{19}$
F-19	9019	$1.84812 \cdot 10^{22}$
C-12	6012	$3.22909 \cdot 10^{21}$
C-13	6013	$3.4925 \cdot 10^{19}$
Ni-58	28058	$1.25283 \cdot 10^{21}$
Ni-60	28060	$4.82586 \cdot 10^{20}$
Ni-61	28061	$2.09778 \cdot 10^{19}$
Ni-62	28062	$6.68882 \cdot 10^{19}$
Ni-64	28064	$1.70321 \cdot 10^{19}$
Mo-92	42092	$3.58506 \cdot 10^{19}$
Mo-94	42094	$2.25763 \cdot 10^{19}$
Mo-95	42095	$3.90829 \cdot 10^{19}$
Mo-96	42096	$4.11308 \cdot 10^{19}$
Mo-97	42097	$2.36866 \cdot 10^{19}$
Mo-98	42098	$6.01787 \cdot 10^{19}$
Mo-100	42100	$2.42294 \cdot 10^{19}$
Cr-50	24050	$7.41867 \cdot 10^{18}$
Cr-52	24052	$1.43062 \cdot 10^{20}$
Cr-53	24053	$1.62221 \cdot 10^{19}$
Cr-54	24054	$4.03801 \cdot 10^{18}$
Fe-54	26054	$7.7433 \cdot 10^{18}$
Fe-56	26056	$1.21553 \cdot 10^{20}$
Fe-57	26057	$2.8072 \cdot 10^{18}$
Fe-58	26058	$3.73586 \cdot 10^{17}$

Table C.11: Isotopic number densities and ZAID codes for Region E, for entry into MCNP.

Component	Atoms (barn-cm)$^{-1}$
Li6	$6.12199 \cdot 10^{-7}$
Li7	$8.27235 \cdot 10^{-3}$
Be	$3.71647 \cdot 10^{-3}$
U234	$3.05463 \cdot 10^{-7}$
U235	$3.56374 \cdot 10^{-5}$
U236	$3.05463 \cdot 10^{-7}$
U238	$6.55728 \cdot 10^{-5}$
F	$1.86587 \cdot 10^{-2}$
Zr	$6.36382 \cdot 10^{-4}$
C	$5.03592 \cdot 10^{-3}$

Table C.12: WIMS component number densities for Region G.

Isotope	ZAID	Atoms cm^{-3}
Li-6	3006	$6.12199 \cdot 10^{17}$
Li-7	3007	$8.27235 \cdot 10^{21}$
Be-9	4009	$3.71647 \cdot 10^{21}$
Zr-90	40090	$3.27418 \cdot 10^{20}$
Zr-91	40091	$7.1402 \cdot 10^{19}$
Zr-92	40092	$1.09139 \cdot 10^{20}$
Zr-94	40094	$1.10603 \cdot 10^{20}$
Zr-96	40096	$1.78187 \cdot 10^{19}$
U-234	92234	$3.05463 \cdot 10^{17}$
U-235	92235	$3.56374 \cdot 10^{19}$
U-236	92236	$3.05463 \cdot 10^{17}$
U-238	92238	$6.55728 \cdot 10^{19}$
F-19	9019	$1.86587 \cdot 10^{22}$
C-12	6012	$4.98203 \cdot 10^{21}$
C-13	6013	$5.38843 \cdot 10^{19}$

Table C.13: Isotopic number densities and ZAID codes for Region G, for entry into MCNP.

Component	Atoms (barn-cm)$^{-1}$
Li6	$4.09643 \cdot 10^{-7}$
Li7	$5.5353 \cdot 10^{-3}$
Be	$2.48681 \cdot 10^{-3}$
U234	$2.04396 \cdot 10^{-7}$
U235	$2.38462 \cdot 10^{-5}$
U236	$2.04396 \cdot 10^{-7}$
U238	$4.38769 \cdot 10^{-5}$
F	$1.24852 \cdot 10^{-2}$
Zr	$4.25824 \cdot 10^{-4}$
C	$3.40391 \cdot 10^{-2}$
Ni	$1.31451 \cdot 10^{-4}$
Mo	$1.76239 \cdot 10^{-5}$
Cr	$1.21957 \cdot 10^{-5}$
Fe	$9.46267 \cdot 10^{-6}$

Table C.14: WIMS Component number densities for Region H.

Isotope	ZAID	Atoms cm^{-3}
Li-6	3006	$4.09643 \cdot 10^{17}$
Li-7	3007	$5.5353 \cdot 10^{21}$
Be-9	4009	$2.48681 \cdot 10^{21}$
Zr-90	40090	$2.19087 \cdot 10^{20}$
Zr-91	40091	$4.77775 \cdot 10^{19}$
Zr-92	40092	$7.30288 \cdot 10^{19}$
Zr-94	40094	$7.40082 \cdot 10^{19}$
Zr-96	40096	$1.19231 \cdot 10^{19}$
U-234	92234	$2.04396 \cdot 10^{17}$
U-235	92235	$2.38462 \cdot 10^{19}$
U-236	92236	$2.04396 \cdot 10^{17}$
U-238	92238	$4.38769 \cdot 10^{19}$
F-19	9019	$1.24852 \cdot 10^{22}$
C-12	6012	$3.36748 \cdot 10^{22}$
C-13	6013	$3.64218 \cdot 10^{20}$
Ni-58	28058	$8.9488 \cdot 10^{19}$
Ni-60	28060	$3.44705 \cdot 10^{19}$
Ni-61	28061	$1.49841 \cdot 10^{18}$
Ni-62	28062	$4.77773 \cdot 10^{18}$
Ni-64	28064	$1.21658 \cdot 10^{18}$
Mo-92	42092	$2.56076 \cdot 10^{18}$
Mo-94	42094	$1.61259 \cdot 10^{18}$
Mo-95	42095	$2.79163 \cdot 10^{18}$
Mo-96	42096	$2.93791 \cdot 10^{18}$
Mo-97	42097	$1.6919 \cdot 10^{18}$
Mo-98	42098	$4.29848 \cdot 10^{18}$
Mo-100	42100	$1.73067 \cdot 10^{18}$
Cr-50	24050	$5.29905 \cdot 10^{17}$
Cr-52	24052	$1.02187 \cdot 10^{19}$
Cr-53	24053	$1.15872 \cdot 10^{18}$
Cr-54	24054	$2.88429 \cdot 10^{17}$
Fe-54	26054	$5.53093 \cdot 10^{17}$
Fe-56	26056	$8.68238 \cdot 10^{18}$
Fe-57	26057	$2.00514 \cdot 10^{17}$
Fe-58	26058	$2.66847 \cdot 10^{16}$

Table C.15: Isotopic number densities and ZAID codes for Region H, for entry into MCNP.

Component	Atoms (barn-cm)$^{-1}$
Li6	$1.45608 \cdot 10^{-7}$
Li7	$1.96753 \cdot 10^{-3}$
Be	$8.83938 \cdot 10^{-4}$
U234	$7.26525 \cdot 10^{-8}$
U235	$8.47612 \cdot 10^{-6}$
U236	$7.26525 \cdot 10^{-8}$
U238	$1.55961 \cdot 10^{-5}$
F	$4.43785 \cdot 10^{-3}$
Zr	$1.51359 \cdot 10^{-4}$
C	$7.22747 \cdot 10^{-2}$

Table C.16: WIMS component number densities for Regions J, L, M.

Isotope	ZAID	Atoms cm^{-3}
Li-6	3006	$1.45608 \cdot 10^{17}$
Li-7	3007	$1.96753 \cdot 10^{21}$
Be-9	4009	$8.83938 \cdot 10^{20}$
Zr-90	40090	$7.78744 \cdot 10^{19}$
Zr-91	40091	$1.69825 \cdot 10^{19}$
Zr-92	40092	$2.59581 \cdot 10^{19}$
Zr-94	40094	$2.63062 \cdot 10^{19}$
Zr-96	40096	$4.23806 \cdot 10^{18}$
U-234	92234	$7.26525 \cdot 10^{16}$
U-235	92235	$8.47612 \cdot 10^{18}$
U-236	92236	$7.26525 \cdot 10^{16}$
U-238	92238	$1.55961 \cdot 10^{19}$
F-19	9019	$4.43785 \cdot 10^{21}$
C-12	6012	$7.15014 \cdot 10^{22}$
C-13	6013	$7.73339 \cdot 10^{20}$

Table C.17: Isotopic number densities and ZAID codes for Regions J, L and M; for entry into MCNP.

Component	Atoms (barn-cm)$^{-1}$
Li6	$1.53373 \cdot 10^{-7}$
Li7	$2.07246 \cdot 10^{-3}$
Be	$9.31082 \cdot 10^{-4}$
U234	$7.65273 \cdot 10^{-8}$
U235	$8.92818 \cdot 10^{-6}$
U236	$7.65273 \cdot 10^{-8}$
U238	$1.64279 \cdot 10^{-5}$
F	$4.67454 \cdot 10^{-3}$
Zr	$1.59432 \cdot 10^{-4}$
C	$7.11556 \cdot 10^{-2}$

Table C.18: Isotopic number densities for Region N.

Isotope	ZAID	Atoms cm^{-3}
Li-6	3006	$1.53373 \cdot 10^{17}$
Li-7	3007	$2.07246 \cdot 10^{21}$
Be-9	4009	$9.31082 \cdot 10^{20}$
Zr-90	40090	$8.20277 \cdot 10^{19}$
Zr-91	40091	$1.78882 \cdot 10^{19}$
Zr-92	40092	$2.73426 \cdot 10^{19}$
Zr-94	40094	$2.77092 \cdot 10^{19}$
Zr-96	40096	$4.46409 \cdot 10^{18}$
U-234	92234	$7.65273 \cdot 10^{16}$
U-235	92235	$8.92818 \cdot 10^{18}$
U-236	92236	$7.65273 \cdot 10^{16}$
U-238	92238	$1.64279 \cdot 10^{19}$
F-19	9019	$4.67454 \cdot 10^{21}$
C-12	6012	$7.03943 \cdot 10^{22}$
C-13	6013	$7.61365 \cdot 10^{20}$

Table C.19: Isotopic number densities and ZAID codes for Region N, for entry into MCNP.

Component	Atoms (barn-cm)$^{-1}$
Li6	$4.3294 \cdot 10^{-7}$
Li7	$5.85011 \cdot 10^{-3}$
Be	$2.62824 \cdot 10^{-3}$
U234	$2.1602 \cdot 10^{-7}$
U235	$2.52023 \cdot 10^{-5}$
U236	$2.1602 \cdot 10^{-7}$
U238	$4.63723 \cdot 10^{-5}$
F	$1.31952 \cdot 10^{-2}$
Zr	$4.50042 \cdot 10^{-4}$
C	$1.42684 \cdot 10^{-2}$
Ni	$1.16992 \cdot 10^{-2}$
Mo	$1.56853 \cdot 10^{-3}$
Cr	$1.08542 \cdot 10^{-3}$
Fe	$8.42178 \cdot 10^{-4}$

Table C.20: WIMS component number densities for Region O.

Isotope	ZAID	Atoms cm^{-3}
Li-6	3006	$4.3294 \cdot 10^{17}$
Li-7	3007	$5.85011 \cdot 10^{21}$
Be-9	4009	$2.62824 \cdot 10^{21}$
Zr-90	40090	$2.31546 \cdot 10^{20}$
Zr-91	40091	$5.04947 \cdot 10^{19}$
Zr-92	40092	$7.71821 \cdot 10^{19}$
Zr-94	40094	$7.82172 \cdot 10^{19}$
Zr-96	40096	$1.26012 \cdot 10^{19}$
U-234	92234	$2.1602 \cdot 10^{17}$
U-235	92235	$2.52023 \cdot 10^{19}$
U-236	92236	$2.1602 \cdot 10^{17}$
U-238	92238	$4.63723 \cdot 10^{19}$
F-19	9019	$1.31952 \cdot 10^{22}$
C-12	6012	$1.41158 \cdot 10^{22}$
C-13	6013	$1.52672 \cdot 10^{20}$
Ni-58	28058	$7.96444 \cdot 10^{21}$
Ni-60	28060	$3.06787 \cdot 10^{21}$
Ni-61	28061	$1.33359 \cdot 10^{20}$
Ni-62	28062	$4.25218 \cdot 10^{20}$
Ni-64	28064	$1.08276 \cdot 10^{20}$
Mo-92	42092	$2.27908 \cdot 10^{20}$
Mo-94	42094	$1.43521 \cdot 10^{20}$
Mo-95	42095	$2.48455 \cdot 10^{20}$
Mo-96	42096	$2.61474 \cdot 10^{20}$
Mo-97	42097	$1.50579 \cdot 10^{20}$
Mo-98	42098	$3.82565 \cdot 10^{20}$
Mo-100	42100	$1.5403 \cdot 10^{20}$
Cr-50	24050	$4.71616 \cdot 10^{19}$
Cr-52	24052	$9.09464 \cdot 10^{20}$
Cr-53	24053	$1.03126 \cdot 10^{20}$
Cr-54	24054	$2.56702 \cdot 10^{19}$
Fe-54	26054	$4.92253 \cdot 10^{19}$
Fe-56	26056	$7.72732 \cdot 10^{20}$
Fe-57	26057	$1.78457 \cdot 10^{19}$
Fe-58	26058	$2.37494 \cdot 10^{18}$

Table C.21: Isotopic number densities and ZAID codes for Region O, for entry into MCNP.

Component	Atoms (barn-cm)$^{-1}$
Li6	$5.87608 \cdot 10^{-7}$
Li7	$7.94006 \cdot 10^{-3}$
Be	$3.56718 \cdot 10^{-3}$
U234	$2.93193 \cdot 10^{-7}$
U235	$3.42059 \cdot 10^{-5}$
U236	$2.93193 \cdot 10^{-7}$
U238	$6.29388 \cdot 10^{-5}$
F	$1.79092 \cdot 10^{-2}$
Zr	$6.10819 \cdot 10^{-4}$
Ni	$6.04676 \cdot 10^{-3}$
Mo	$8.10701 \cdot 10^{-4}$
Cr	$5.61004 \cdot 10^{-4}$
Fe	$4.35283 \cdot 10^{-4}$

Table C.22: Isotopic number densities for Region P.

Isotope	ZAID	Atoms cm^{-3}
Li-6	3006	$5.87608 \cdot 10^{17}$
Li-7	3007	$7.94006 \cdot 10^{21}$
Be-9	4009	$3.56718 \cdot 10^{21}$
Zr-90	40090	$3.14266 \cdot 10^{20}$
Zr-91	40091	$6.85339 \cdot 10^{19}$
Zr-92	40092	$1.04755 \cdot 10^{20}$
Zr-94	40094	$1.0616 \cdot 10^{20}$
Zr-96	40096	$1.71029 \cdot 10^{19}$
U-234	92234	$2.93193 \cdot 10^{17}$
U-235	92235	$3.42059 \cdot 10^{19}$
U-236	92236	$2.93193 \cdot 10^{17}$
U-238	92238	$6.29388 \cdot 10^{19}$
F-19	9019	$1.79092 \cdot 10^{22}$
Ni-58	28058	$4.11645 \cdot 10^{21}$
Ni-60	28060	$1.58564 \cdot 10^{21}$
Ni-61	28061	$6.8927 \cdot 10^{19}$
Ni-62	28062	$2.19775 \cdot 10^{20}$
Ni-64	28064	$5.59627 \cdot 10^{19}$
Mo-92	42092	$1.17795 \cdot 10^{20}$
Mo-94	42094	$7.41792 \cdot 10^{19}$
Mo-95	42095	$1.28415 \cdot 10^{20}$
Mo-96	42096	$1.35144 \cdot 10^{20}$
Mo-97	42097	$7.78273 \cdot 10^{19}$
Mo-98	42098	$1.9773 \cdot 10^{20}$
Mo-100	42100	$7.96109 \cdot 10^{19}$
Cr-50	24050	$2.43756 \cdot 10^{19}$
Cr-52	24052	$4.7006 \cdot 10^{20}$
Cr-53	24053	$5.3301 \cdot 10^{19}$
Cr-54	24054	$1.32678 \cdot 10^{19}$
Fe-54	26054	$2.54423 \cdot 10^{19}$
Fe-56	26056	$3.99389 \cdot 10^{20}$
Fe-57	26057	$9.22364 \cdot 10^{18}$
Fe-58	26058	$1.2275 \cdot 10^{18}$

Table C.23: Isotopic number densities and ZAID codes for Region P, for entry into MCNP.

Component	Atoms (barn-cm)$^{-1}$
Li6	$5.76606 \cdot 10^{-7}$
Li7	$7.7914 \cdot 10^{-3}$
Be	$3.5004 \cdot 10^{-3}$
U234	$2.87704 \cdot 10^{-7}$
U235	$3.35654 \cdot 10^{-5}$
U236	$2.87704 \cdot 10^{-7}$
U238	$6.17604 \cdot 10^{-5}$
F	$1.75739 \cdot 10^{-2}$
Zr	$5.99383 \cdot 10^{-4}$
C	$9.41903 \cdot 10^{-3}$

Table C.24: WIMS component number densities for Region R.

Isotope	ZAID	Atoms cm^{-3}
Li-6	3006	$5.76606 \cdot 10^{17}$
Li-7	3007	$7.7914 \cdot 10^{21}$
Be-9	4009	$3.5004 \cdot 10^{21}$
Zr-90	40090	$3.08382 \cdot 10^{20}$
Zr-91	40091	$6.72507 \cdot 10^{19}$
Zr-92	40092	$1.02794 \cdot 10^{20}$
Zr-94	40094	$1.04173 \cdot 10^{20}$
Zr-96	40096	$1.67827 \cdot 10^{19}$
U-234	92234	$2.87704 \cdot 10^{17}$
U-235	92235	$3.35654 \cdot 10^{19}$
U-236	92236	$2.87704 \cdot 10^{17}$
U-238	92238	$6.17604 \cdot 10^{19}$
F-19	9019	$1.75739 \cdot 10^{22}$
C-12	6012	$9.31824 \cdot 10^{21}$
C-13	6013	$1.00784 \cdot 10^{20}$

Table C.25: Isotopic number densities and ZAID codes for Region R, for entry into MCNP.

Component	Atoms (barn-cm)$^{-1}$
Li6	$2.8345 \cdot 10^{-7}$
Li7	$3.83012 \cdot 10^{-3}$
Be	$1.72073 \cdot 10^{-3}$
U234	$1.4143 \cdot 10^{-7}$
U235	$1.65002 \cdot 10^{-5}$
U236	$1.4143 \cdot 10^{-7}$
U238	$3.03603 \cdot 10^{-5}$
F	$8.63902 \cdot 10^{-3}$
Zr	$2.94646 \cdot 10^{-4}$
C	$5.24108 \cdot 10^{-2}$

Table C.26: WIMS component number densities for Region S.

Isotope	ZAID	Atoms cm^{-3}
Li-6	3006	$2.8345 \cdot 10^{17}$
Li-7	3007	$3.83012 \cdot 10^{21}$
Be-9	4009	$1.72073 \cdot 10^{21}$
Zr-90	40090	$1.51595 \cdot 10^{20}$
Zr-91	40091	$3.30593 \cdot 10^{19}$
Zr-92	40092	$5.05318 \cdot 10^{19}$
Zr-94	40094	$5.12095 \cdot 10^{19}$
Zr-96	40096	$8.25009 \cdot 10^{18}$
U-234	92234	$1.4143 \cdot 10^{17}$
U-235	92235	$1.65002 \cdot 10^{19}$
U-236	92236	$1.4143 \cdot 10^{17}$
U-238	92238	$3.03603 \cdot 10^{19}$
F-19	9019	$8.63902 \cdot 10^{21}$
C-12	6012	$5.185 \cdot 10^{22}$
C-13	6013	$5.60796 \cdot 10^{20}$

Table C.27: Isotopic number densities and ZAID codes for Region S, for entry into MCNP.

Component	Atoms (barn-cm)$^{-1}$
Li6	$2.97687 \cdot 10^{-7}$
Li7	$4.0225 \cdot 10^{-3}$
Be	$1.80716 \cdot 10^{-3}$
U234	$1.48534 \cdot 10^{-7}$
U235	$1.7329 \cdot 10^{-5}$
U236	$1.48534 \cdot 10^{-7}$
U238	$3.18853 \cdot 10^{-5}$
F	$9.07295 \cdot 10^{-3}$
Zr	$3.09446 \cdot 10^{-4}$

Table C.28: WIMS component number densities for Region T.

Isotope	ZAID	Atoms cm^{-3}
Li-6	3006	$2.97687 \cdot 10^{17}$
Li-7	3007	$4.0225 \cdot 10^{21}$
Be-9	4009	$1.80716 \cdot 10^{21}$
Zr-90	40090	$1.5921 \cdot 10^{20}$
Zr-91	40091	$3.47198 \cdot 10^{19}$
Zr-92	40092	$5.30699 \cdot 10^{19}$
Zr-94	40094	$5.37817 \cdot 10^{19}$
Zr-96	40096	$8.66448 \cdot 10^{18}$
U-234	92234	$1.48534 \cdot 10^{17}$
U-235	92235	$1.7329 \cdot 10^{19}$
U-236	92236	$1.48534 \cdot 10^{17}$
U-238	92238	$3.18853 \cdot 10^{19}$
F-19	9019	$9.07295 \cdot 10^{21}$

Table C.29: Isotopic number densities and ZAID codes for Region T, for entry into MCNP.